Development of bio-mimetic nano-compartments for solar energy capture

Anna Stikāne

Submitted in accordance with the requirements for the degree of

Doctor of Philosophy

The University of Leeds

Faculty of Biological Sciences

School of Biomedical Sciences

June 2020

The candidate confirms that the work submitted is their own, except where work which has formed part of jointly authored publications has been included. The contribution of the candidate and the other authors to this work has been explicitly indicated below. The candidate confirms that appropriate credit has been given within the thesis where reference has been made to the work of others.

The work in Chapter 4 of the thesis has appeared in publication as follows:

Publication (Journal article): A. Stikane, E. T. Hwang, E. V. Ainsworth, S. Piper, K. Critchley, J. Butt, E. Reisner and L. J. C. Jeuken. Towards Compartmentalized Photocatalysis: Multiheme Proteins as Transmembrane Molecular Electron Conduits. *Faraday Discussions*, **215**, 26-38, 2019

I was responsible for conducting the experimental work, processing and analysing the resulting data and writing the publication. The contribution of the other authors was discussions of results and writing of the publication.

In memory of my beloved brother for his bravery and insistence in following his own path

Acknowledgements

I would like to thank my supervisors, Prof. Lars Jeuken and Dr. Kevin Critchley, for their continuous advice and support, and the many opportunities offered for attending training courses and working in different universities across the world. You have provided strong foundations for advancing this work.

Thanks to my many collaborators for the support and the knowledge exchange supporting this work. Thanks to Prof. Julea Butt and her group at the University of East Anglia for providing proteins from *Shewanella oneidensis* MtrC and MtrCAB. My special thanks goes to Sam Piper, Dr. Emma Ainswort, Dr. Jessica van Wonderen and Simone Payne for contributing your experience of the purification and handling of the cytochrome proteins. I would also like to thank Prof. Erwin Reisner and his group at the University of Cambridge for providing light-harvesting nanoparticles, Dr. Gustav Berggren from the University of Uppsala for providing the HydA1 hydrogenase and Prof. Siddharth V. Patwardhan and his group at the University of Sheffield (especially, Dr Joseph Manning and Eleni Routoula) for the help with synthesis of porous bio-inspired silica particles.

Many thanks go to my collaborators at the Molecular Foundry and the Advanced Light Source of the Lawrence Berkeley National Laboratory, USA. Very special thanks to Dr. Corie Ralston, and Dr. Sayan Gupta for their expertise in x-ray protein footprinting and support with the work at the beamline. I am also very grateful to Prof. Caroline Ajo-Franklin and her group (especially, Lin Su, Dr. Moshe Baruch, Dr. Frankie Manea, Dr. Josh Atkinson, Dr. Sara Tejedor-Sanz) for their hospitality, productive discussions and making me feel at home during my brief research visits. In addition, I would like to express my gratitude to Dr Behzad Rad, Rita Garcia and Victor Mann for your invaluable technical and scientific support.

I am very grateful for the help of many people from different departments at the University of Leeds. These include Dr. James Ault and Dr. Rachel George from the University of Leeds Biomolecular Mass Spectrometry Facility and soon-to-be-doctor Owen Cornwell for sharing his expertise in oxidative protein footprinting, without which I would be lost within the uncertainties of peptide modifications. I would also like to thank Dr. Zabeada Aslam from Leeds Electron Microscopy and Spectroscopy centre and Dr. Rebecca Thompson from the cryo-electron microscopy facility at the Astbury

BioStructure Laboratory for their help with TEM and cryo-TEM imaging.

Thank you to the current and previous members of the Jeuken research group: Dr. Ee Taek Hwang for providing induction for this research; Dr. Theo Laftsoglou for your expertise and help with lipids and membrane proteins; Anushka Agrawal for the help with protein purification. My deepest gratitude for the continuous moral support provided from Dr. Matthias Gantner, Dr. Joseph Oram, Dr. Hope Adams, Dr. Huijie Zhang, Declan Kohl, Dr. Debajyoti Dutta, Emma Campbell and the many others, who I had the honour to work with. I would also like to thank our current and previous neighbours in the Bioincubator (especially, the Millner group and Rosamund Clifford for her precious lunchtime presence).

Very special thanks goes to all the brilliant scientists from the Molecular and Nanoscale Physics research group. Thanks to Dr. Sunjie Ye, Samuel Moorcroft and George Newham for your nanoparticle expertise and Ashley Hancock for the discussions on lipids, protein and light-harvesting and the frequent joyful presence at the Bioincubator. Thanks to Dr. Lucien Roach and Abiral Tamang for the many fruitful conversations on nanoparticles and beyond.

This work would be impossible without the unconditional support from my family and friends across the world. (You know who you are, and I am very grateful to have you around!) I do, however, what to add a special thanks to Dr. Kat Davies, Dr. Sîan Irvine and soon-to-be-doctor Sophie Hesketh (‘Da Ladiez’) for the invaluable tea-fueled conversations of science, life and work, which have taught me so much. Many thanks also to the amazing swing dance community (especially Michael Jones) and the peeps from the Leeds University Folk Society, that have brought so many joyful moments helping me to get through many obstacles during this PhD studentship.

And last, but not least, I would like to scknowledge the funding sources supporting this work. Tanks to the Biotechnology and Biological Sciences Research Council and the White Rose BBSRC Doctoral Training Partnership for sponsoring my PhD studentship and providing many great training opportunities (such as Professional Internships for PhD students). In addition, work at the Molecular Foundry was supported by the Office of Science, Office of Basic Energy Sciences, of the U.S. Department of Energy under Contract No. DE-AC02-05CH11231.

This page is intentionally left blank.

Abstract

A growing range of artificial cell-mimicking compartments (*e.g.*, liposomes) have been demonstrated as technological platforms for applications ranging from model systems in bottom-up cell biology to miniature chemical reactors. Here, I describe work on developing a liposomal compartment for capturing light-energy. The harvesting of light energy starts at a photoactive centre, where light-excited electrons are generated and then transferred to an electron acceptor. The efficiency of this electron transfer is often limited due to charge recombination (*i.e.*, re-assembly of photo-separated electrons and electron holes) within the photoactive chromophore. Inspired by natural photosynthesis, this study envisions a strategy to limit charge recombination by rapid transfer of the light-excited electrons away from the photoactive molecules (dye-sensitized TiO_2 nanoparticles or carbon dots) and across the liposome membrane via conductive transmembrane protein complex MtrCAB from *Shewanella oneidensis* MR-1. Furthermore, such compartment enables localisation of the oxidation and reduction processes in separate environments.

The assembly of the envisioned compartment begins with a study of the molecular interface between TiO_2 nanoparticles, a commonly used material for photocatalysis studies, and the MtrC(AB) conduit. This interface is mapped using an approach called protein footprinting, which involves protein labelling and subsequent analysis of the modified peptides by mass spectrometry. Understanding the molecular interactions at this bio-inorganic interface is crucial for engineering electronic communication between these materials. Then, a proof of concept is demonstrated of a half-reaction: light energy capture, charge separation across the membrane and use of the energy to drive a chemical reaction. Transmembrane electron transfer is achieved chemically and photochemically using dye sensitized TiO_2 nanoparticles or carbon dots located outside the liposomes. The electron transfer through MtrCAB conduit is confirmed optically by monitoring the destructive reduction of an encapsulated azo-dye Reactive Red 120. Finally, work on encapsulation of fuel evolving catalysts (*i.e.*, hydrogen producing Pt nanoparticles and a hydrogenase HydA1) within the lipid-enclosed compartment (*i.e.*, liposome lumen and porous silica support) is discussed alongside the challenges for combining different materials within ordered structures.

Abbreviations

AAS	atomic absorbtion spectroscopy
a-CD	amorphous carbon dots
AFM	atomic force microscopy
ALS	Advanced Light Source (Berkeley, California)
a-TiO_2	commercial anatase TiO_2 nanoparticles
CA	cardiolipin
CD	carbon dots
cryo-EM	cryogenic electron microscopy
CF	carboxyfluorescein
DGPE-CF	1,2-dioleoyl-sn-glycero-3-phosphoethanolamine-N-(carboxyfluorescein)
DHBA	3,4-dihydroxy-benzoic acid
DHBA-TiO2	DHBA functionalised TiO_2 nanoparticles
DHPE	1,2-Dihexadecanoyl-sn-Glycero-3-Phosphoethanolamine
DLS	Dynamic Light Scattering
DOPC	1,2-dioleoyl-sn-glycero-3-phosphocholine
DOPE	1,2-dioleoyl-sn-glycero-3-phosphoethanolamine
DOPG	1,2-dioleoyl-sn-glycero-3-phospho-(1'-rac-glycerol)
DPPC	1,2-dipalmitoyl-sn-glycero-3-phosphocholine
DT	sodium dithionite ($Na_2S_2O_4$)
EDTA	ethylenediaminetetraacetic acid
EIC	extracted ion chromatogram
EM	electron microscopy
ET	electron transfer
g-N-CD	graphitic carbon dots with core nitrogen doping
FPOP	fast photochemical oxidation of proteins
gSiO_2	bio-inspired ('green') silica
HDX	hydrogen deuterium exchange
HEC	hydrogen evolving catalyst
HER	hydrogen evolving reaction
His-tag	poly-histidine tag

ITC	Isothermal Titration Calorimetry
LC-MS/MS	liquid chromatography-tandem mass spectrometry
LDAO	N,N-Dimethyldodecylamine N-oxide
LHNP	light harvesting nanoparticle
LEMAS	Leeds Electron Microscopy and Spectroscopy Centre
LINAC	Linear particle accelerator
meSiO_2	mesoporous silica nanoparticles
MOPS	3-(N-morpholino)propansulfonic acid
MS	mass spectrometry
MV	methyl viologen
NP	nanoparticles
NPs/ml	nanoparticles within one mililiter (used as a unit of NP concentration)
NTA	nanoparticle tracking analysis
OG	n-octyl glucoside
•OH	hydroxyl radical
PEHA	pentaethylenehexamine
POPC	1-palmitoyl-2-oleoyl-sn-glycero- 3-phosphocholine
POPE	1-palmitoyl-2-oleoyl-sn-glycero-3-phosphoethanolamine
POPG	1-palmitoyl-2-Oleoyl-sn-Glycero-3-Phosphoglycerol
Pt_{com}	commercial Pt NPs
PTFE	polytetrafluoroethylene
Pt-gSiO_2	gSiO_2 NPs loaded with Pt
Pt_{syn}	in-house synthesized Pt NPsl
QCM-D	Quartz Crystal Microbalance with Dissipation
Q-TOF	quadrupole-orthogonal time of flight mass spectrometre
RR120	Reactive Red 120 azo dye
RT	retention time
RuP-TiO2	Ruthenium (Ru) dye sensitized TiO_2 anatase nanoparticles
SD	standard deviation
SDS	sodium dodecyl sulfate
SE	standard error
SED	sacrificial electron donor

SLB	supported lipid bilayer
TEAB	tetraethylammonium bromide
TEM	Transmission electron microscopy
Texas Red-DHPE	Texas Red fluorophore labelled DHPE
TFA	trifluoroacetic acid
TOF	turnover frequency
TX	Triton X100 detergent
XFMS	X-ray footprinting mass spectrometry
XF	X-ray footprinting

Contents

List of figures

List of tables

This page is intentionally left blank.

Chapter 1

Introduction

1.1 Bio-inspired compartments

Many crucial cell functions rely on a border separating compartments with different environments. Above all, the cell membrane sets the boundaries of a cell and regulates the transport of molecules in and out of the cell, thus creating and controlling the asymmetry between cytoplasm and the external medium. Furthermore, cells have evolved the use of compartments for optimal organization of simultaneous yet incompatible metabolic processes. [1, 2] For example, various protein compartments are used to assist in protein folding by providing a shielded hydrophobic environment (chaperones, see example in Figure 1.1a) [3] or storing and transporting minerals (ferritins, Figure 1.1b). [4] Similarly, organelles provide membrane-bound specialist environments for functions ranging from biomolecule degradation and recycling to energy assimilation and respiration. For example, lysosomes contain enzymes for cleaning-up the cell from obsolete nucleic acids, proteins, polysaccharides and material taken up for digestion from outside the cell (see Figure 1.1c). [5] The lysosomal membrane separates cell cytoplasm from the acidic pH environment maintained within lysosomes, optimal for the function of hydrolytic enzymes, and also stores these harmful enzymes shielded from the rest of the cell. [6] Compartments also allow the regulation and increase of local enzyme and substrate concentrations, thus optimizing conditions for successful reactions. [7] Finally, lipid membranes and the formation of ion gradients across them are fundamental to energy accumulation and storage in cells. [8]

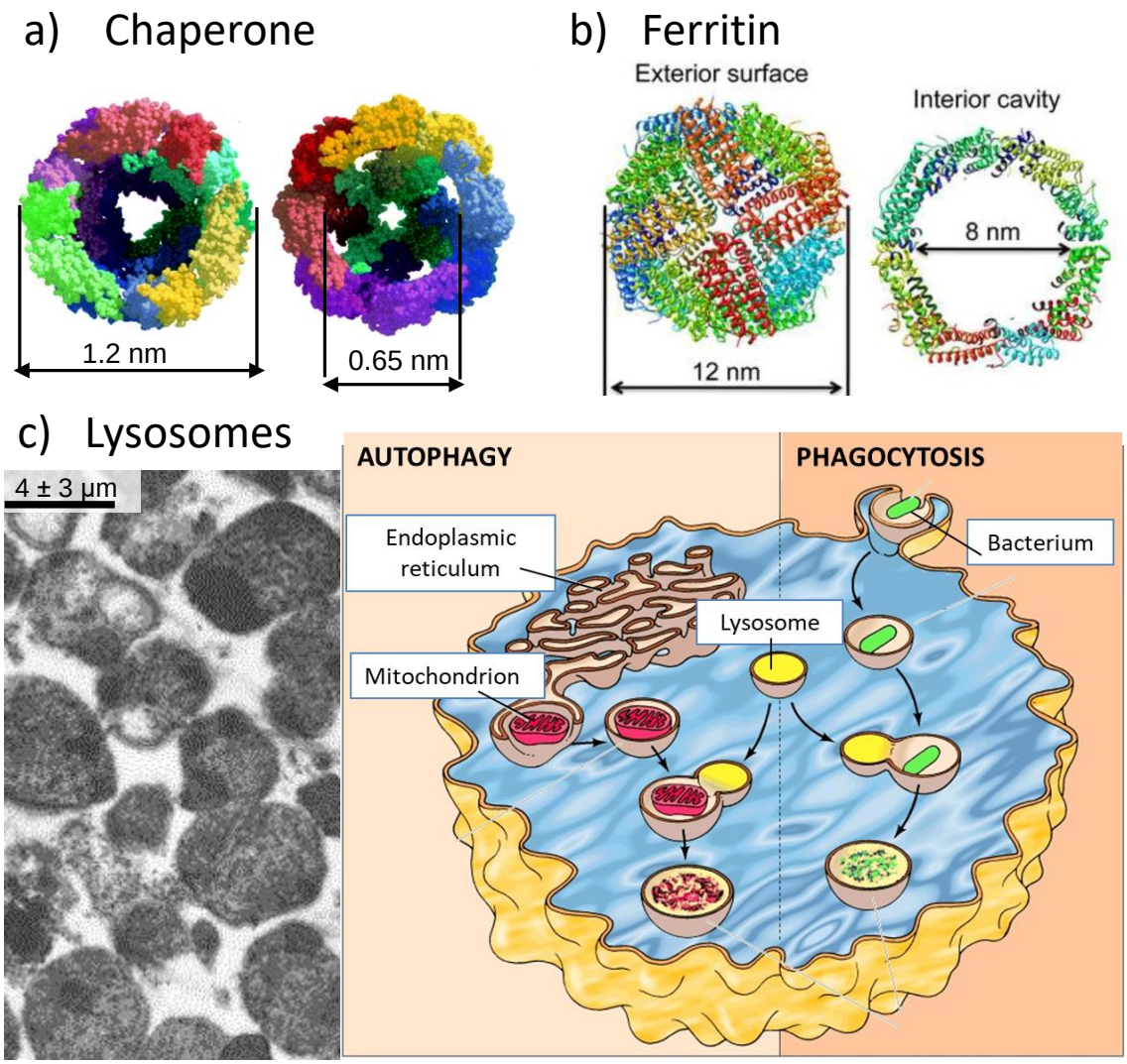

Figure 1.1: Examples of various natural compartments present within cells. (**a**) A cartoon depiction of a chaperone protein MjHSP16.5 belonging to the class of small heat-shock protein. The interior is viewed along the crystallographic three-fold axis (left) and four-fold axis (right). Different colours represent individual HSP 16.5 tetramers. Panel modified after ref. [9]. (**b**) A cartoon of the exterior surface and interior cavity of human heavy-chain ferritin (HFn). Figure panel modified after reference [10]. (**c**) An electronmicroscopy image of lysosomes reprined from [11] (left) and a schematic showing how lysosomes fuse with vesicles containing material (*e.g.*, old mitochondiron andd engulfed bacterium) to be digested (schematic modified after [5].)

Appreciation of the variety of roles membranes and compartments take in natural cells can also create curiosity of how similar cell-like compartments could be made artificially and what technological novelties these could bring. Over the years, much effort has been made to mimic biological compartments using a variety of available materials and methods, ranging from natural lipids to synthetic polymers. [12, 13] Applications including drug delivery, chemical microreactors and artificial cell model systems have been demonstrated and a variety of methods used to tailor these compartments for their potential use have been proposed. [2, 7, 14]

Artificial compartments can be created from a variety of materials including lipids, synthetic block copolymers, polyelectrolytes and proteins. [14, 15] The chosen material determines the chemical properties of the intended capsule and available methods for its formation. In particular, whether self-assembly or directed assembly could be used. Nevertheless, capsule size and shape, as well as the distribution of thereof within a sample, depends mainly on the preparation method used. For example, amphiphilic molecules like phospholipids self-assemble into various architectures within a solution. Meanwhile capsule formation from other materials (*e.g.*, polyelectrolytes) might require surfaces for deposition (*e.g.*, layer-by-layer assembly). [2]

The field of micro-compartmentalization has greatly increased in scope over the years. Thus this chapter will only introduce a selection of topics concerning compartment assembly, materials and concepts relevant for constructing an artificial compartment able to capture solar energy. However, the reader is provided with a selection of excellent reviews on liposome engineering and biomedical applications [13, 15–18], polymer and layer-by-layer capsules and their adaptation for different purposes [14, 19–24], multicompartments [6, 7, 25–27], compartment use as biomimetic model systems [1, 28] and biomimetic membrane use for sensor construction [29].

This chapter starts by describing self-assembly principles that underlay the formation of liposomes. Introduced later will be a few examples of the applications of liposome compartments. Next the motivation behind using liposomal compartments for solar energy capture is provided, followed by an introduction to some of the key materials used throughout this thesis. The chapter concludes with an overview of the work described in the following chapters.

1.2 Compartments created via self-assembly.

Most self-assembled structures are built from amphiphilic building blocks that contain hydrophilic and hydrophobic moieties. The dual nature of amphiphilic molecules causes them to self-organize in order to bury their hydrophobic chains while positioning their polar groups towards the surrounding aqueous medium. [15] This process has been used to create vesicles (originating from *vesicula*, small bubble, in the Latin) from biological membrane-forming lipids called liposomes. [15] Amphiphile self-assembly can also be applied to a range of other non-lipid molecules, such as polymersomes formed by amphiphilic block copolymers (where copolymer consists of hydrophobic and hydrophilic blocks) [15], dendrosomes assembled from amphiphilic branched polymers called Janus dendrimers [30], and amphiphilic polypeptide compartments, which are composed of hydrophobic (*e.g.*, poly-leucine) and charged (*e.g.*, poly-lysine) amino acid residues [1, 31–33].

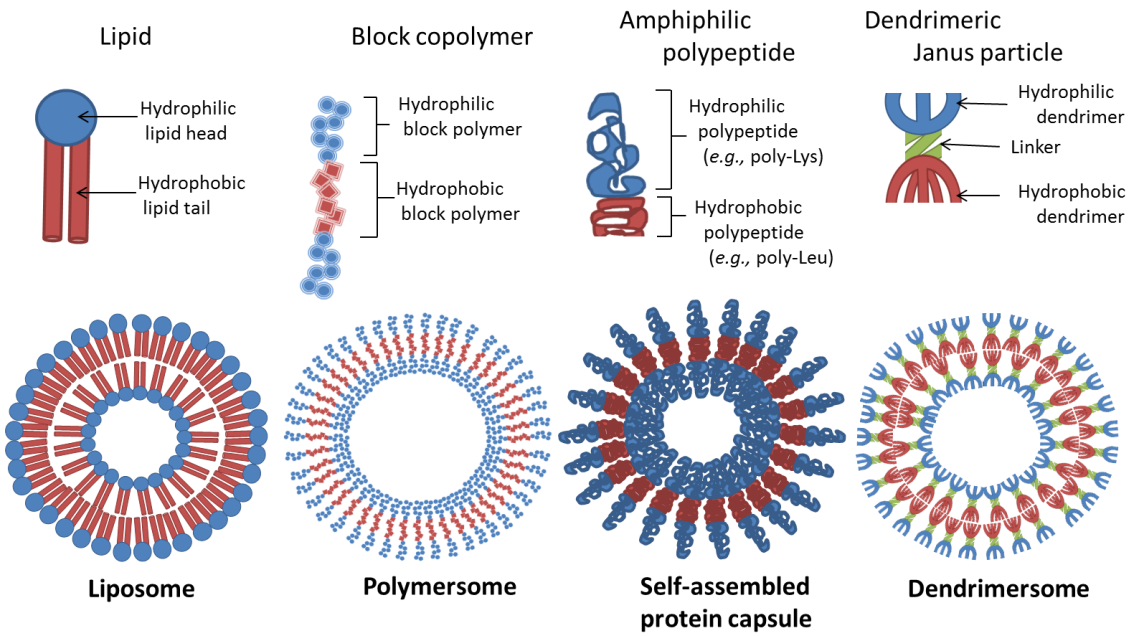

Figure 1.2: Schematic depiction of the variety of amphiphilic building blocks and types of capsules they can form. Hydrophilic and hydrophobic entities are coloured blue and red, respectively. Cartoon is not to scale.

Figure 1.2 illustrates some of the building blocks used to form self-assembled capsules. The parallel self-orientation of amphiphilic building-blocks, required for capsule formation, can also be achieved by other molecular interactions such as ligand binding,

hydrogen bonding, charge interaction (*e.g.*, poly-ion complexes termed PICsomes [34]), dipolar assembly or molecular complementarity (*e.g.*, DNA binding motifs). [15] This illustrates the flexibility in the range of materials and self-assembly interactions available for microcompartment construction.

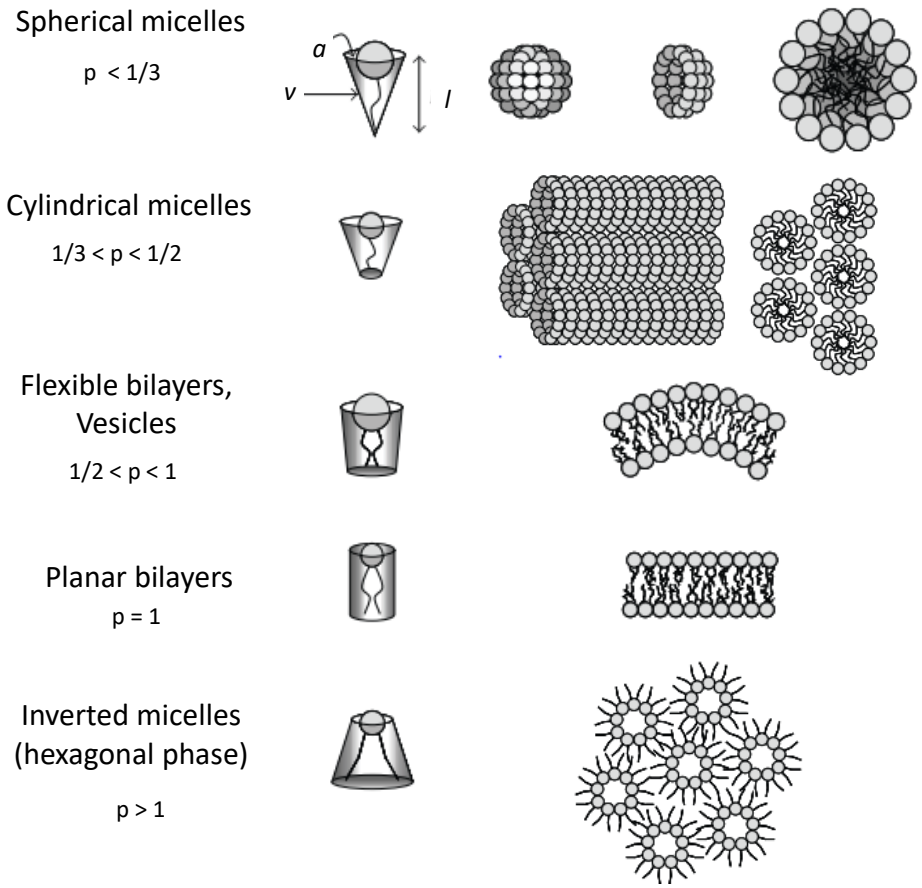

Figure 1.3: Different assembled structures predicted from the shape of the amphiphilic molecule using the packing parameter P. v is the volume of hydrophobic moiety, a - the interfacial area, l - length normal to the interface. Figure reproduced from ref. [35].

Amphiphilic molecules self-organize within aqueous solutions and form various structures such as micelles, planar lamellae, closed bilayer vesicles and even hexagonal and cubic structures of liquid crystal phase lipids. [17] The shape of the resulting structure is commonly described to depend on the geometry of the individual amphiphilic molecule. [15] This is conveniently illustrated by the surfactant packing parameter (p) defined as

$$p = \frac{v}{a * l},$$

where v is the volume of hydrophobic moiety, a - the interfacial area, l - length normal to the interface (see Figure 1.3). [15] The packing parameter is related to the curvature of a

vesicle and can be used to predict the aggregation structure within the solution. [15] Thus, for $p \approx \frac{1}{3}$ amphiphiles will assemble into a spherical micelle, whereas for $p \approx 1$ a molecular bilayer will be formed. [15] However, in practice the assembled end-structure depends on interactions between a variety of thermodynamic, biophysical and solution properties such as surfactant concentration, ionic strength and the preparation method. [15–18]

1.2.1 Liposomes

As biological cell membranes are built of phospholipids, lipids have been extensively studied since the mid-1960s. [17, 36] Hence, comprehensive knowledge has been accumulated on their biological, chemical and structural properties as well as their handling and synthesis. [17, 36, 37] Amongst the self-assembled structures mentioned above, lipid vesicles (liposomes) can be regarded as the simplest and most studied compartment systems that consist of an internal volume enclosed by self-assembled lipid double-layer. [2] Over the years, many different methods for liposome preparation have been reported. These are generally based on sonication, liposome extrusion, and removal of solvent or detergent. [36, 38] Thus liposome fabrication and functionalization (*e.g.*, by using chemically-modified lipids or membrane proteins) are well established processes. [2, 36] The advantages of liposomes are their fundamental biocompatibility and biodegradability resulting in low toxicity and immunogenicity – properties that make liposomes extremely attractive for pharmaceutical applications such as drug delivery. [13]

Although traditional liposome preparations are simple, their content is generally formed during lipid self-assembly by the random enclosure of surrounding media. [36] Therefore liposome size and content within a sample may vary. One example of a reproducible generation of liposomes with uniform size has been demonstrated by Takeuchi and colleagues (Figure 1.4). [39] They used a microfluidic device to deposit a lipid bilayer within a micrometre-scale well that is connected to the main microfluidic channel with a continuous fluid stream. Subsequent formation of a gas bubble within a narrow channel at the bottom of the well pushes the lipid membrane up into the main channel, where the membrane gets sheared off by the fluid flow. The diameter of liposomes created by this method varied around 16-17 μm, [39] which is large for biomedical applications, where the size governs particle distribution *in vivo* to different organs. [15] Yet, it might

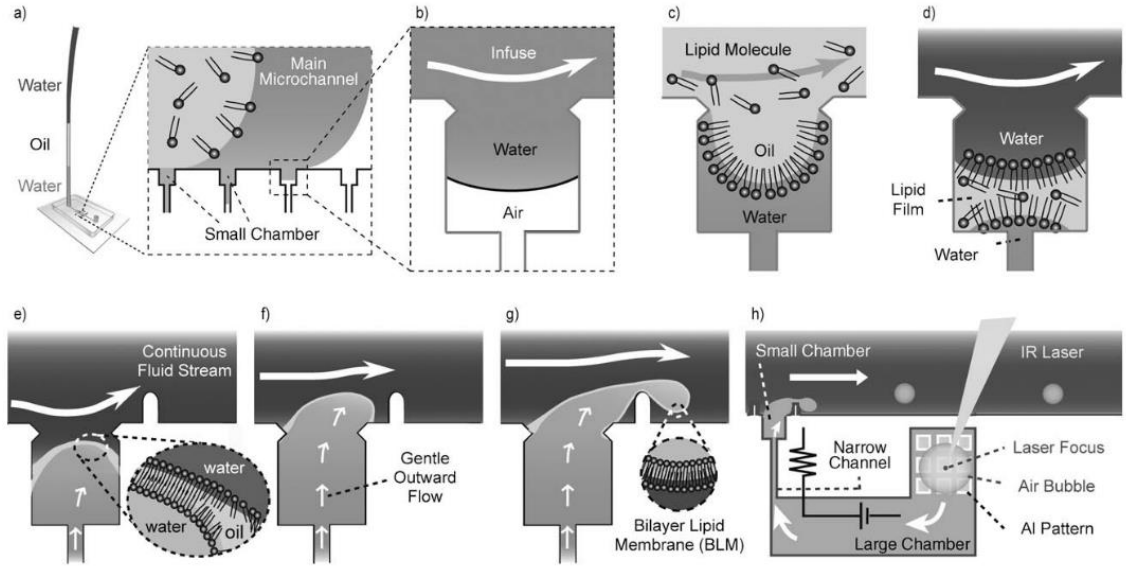

Figure 1.4: An example of a microfluidic process for liposome formation. a) The microfluidic device consists of a main channel with many micro-chambers within its walls. At first the device is infused in a step-wise manner with water, oil containing dissolved lipids and water. **b**) Water fills the device and simulteneously pushes air out of the channel. **c**) Oil displaces water from the main channel. The remaining water is confined within the chambers. **d**) Water is then used to again flush out the oil. Remaining oil residue form an oil film in which amphiphilic lipid molecules form two monolayers at the interface of water and oil. **e - g**) Schematic illustration of the vesicle formation. **e**) A cross flow from below the main compartment thins the lipid film and drives the contact of monolayers to form a bilayer. **f**) The bilayers are then further bent by a gentle outward flow. **g**) The continuous fluid stream within the main chamber create shear forcer that lead to the fission of the 'budding' bilayer, creating a unilamellar vesicle. **h**) The aqueous cross-flow is controlled using integrated system for optical generation of a microbubble. Figure reproduced from ref. [39].

be possible to tune the size of liposomes by adapting the dimensions of the microfluidic device and the applied flow rate. [39]

Besides size, limitations that impede liposome experimental analysis and practical use is the lack of control over liposome lifespan, due to their mechanical and chemical instability. [14] Several strategies have been proposed to improve the structural integrity of liposomes and reduce the leakage of encapsulated content. For example, chemically modified lipids have been used to coat liposomes with inert hydrophilic polymers like PEG. [17] Such coatings extend liposome circulation lifetime *in vivo* [40] by providing a barrier between the lipids and serum lipases and other proteins that can disrupt the lipid

membrane. [17] In addition, 'PEGylation' reduces liposome aggregation, thus reducing activation of immune response for biomedical applications. [41] However, increasing the PEG content above a critical point can destabilize lipid self-assembly, changing the liposome structure or increasing content leakage. [41]

1.3 Liposome applications

As introduced earlier, liposomes have been studied since the mid-1960s. [17, 36]. Since then, different liposome-based systems have been tested for a range of applications. First of all, as all microcompartments liposomes contain an internal space that is shielded from the surrounding environment and may thus be made chemically distinct. This can then be utilised to make liposomes a storage vessel for different loads, ranging from small compounds (*e.g.*, drugs, dyes, vitamins, flavours) and gas bubbles to larger assemblies such as proteins, DNA and nanoparticles. [13, 17, 28, 35, 42]

The idea of using capsules as drug delivery vehicles within the body has been around since the demonstration of the first liposomes in the1960s, while the first liposomes loaded with cancer chemotherapeutic doxorubicin were approved in the1990s. [36,41,43] Liposomes as pharmaceutical agents have many benefits. Firstly, they provide packaging that maintains a compound-favourable environment, *e.g.*, hydrophilic interior for water soluble doxorubicin and hydrophobic lipid layer for hydrophobic drugs like anti-fungal amphotericin B. [41] Liposomes also provide protection from premature degradation of the encapsulated drugs from, for instance, serum enzymes. [41] Secondly, drug release can be engineered to occur at the target site, which increases local drug concentration and optimises drug biodistribution and pharmacokinetics within the body. [41] This, in turn, allows reduction of drug dosage, which lowers risk of immunogenicity and side-effects. [41]

Liposomes can be used to encapsulate other cargo, such as enzymes and their substrates [44], which allows performing such reactions as PCR in liposomes. [42]. These demonstrations have helped to develop uses of synthetic microcontainers as chemical micro- or nanoreactors (previously referred as synthosomes). [45] These are often made from block co-polymers as the resulting capsules are more cost-effective and durable

than liposomes. [45] This approach of compartmentalizing reactions has benefits when an enzyme needs to be protected from surrounding proteases. [22] However, microreactors often need to overcome the limitation of small volumes in which substrate concentration can rapidly run low or an accumulation of product can inhibit the reaction. [22] A possible solution comes from functionalization of the compartment shell, *e.g.*, by engineering its permeability or reconstituting substrate importing membrane proteins to allow substrate and product exchange with the surrounding medium. [45]

Another set of interesting applications emerge when liposomes are engineered to act as artificial model-systems for biological membranes, or even cells. [46] Thus liposomes can be used to study membrane properties, interactions between membrane lipids, proteins and membrane supporting structures like cytoskeleton (*e.g.*, use supported liposomes or observe tubulin polymerisation within the liposome) as well as changes in membrane permeability and responsiveness to internal and external stimuli. [28, 46, 47] In addition, compartment-confined chemical reactions can be used to mimic cell metabolism (*e.g.*, enzyme reactions, sugar synthesis, DNA replication), thus providing a very interesting platform to study metabolic reaction dynamics and feed-back loops linking different reactions. [28, 48] For example, an artificial cell-like gene expression system was constructed to analyse fluctuations of gene expression present, even in clonal cell populations. [49] A cell-size liposome was loaded with an in vitro transcription and translation system and a plasmid containing genes for two fluorescent proteins (*e.g.*, blue and yellow) using the emulsion assembly method. The gene expression was assessed by monitoring the fluorescence of these synthesized proteins. Detected fluctuation of gene expression agreed well with a theoretical model of interactions between substrates, intermediate molecules and products.

Liposomes can also be used to explore biological processes associated with lipid membranes and membrane proteins such as energy storage and transformation across the membrane. Biological systems store solar or chemical energy, generated in photosynthesis and catabolism reactions respectively, in the form of transmembrane proton gradients, which is then utilised by the transmembrane ATP-synthase to synthesize the cellular energy ‘currency’ adenosine triphosphate (ATP). [50] Several groups have reported the reconstitution of functional ATPase in liposomes [51] and later also in other synthetic compartments [52, 53]. Furthermore, molecular systems establishing

a light-driven proton gradient across the membrane, have also been introduced in liposomes and polymersomes. [52, 54] These systems present artificial photosynthesis strategies, where light energy is captured by membrane-integrated artificial light-harvesting antennas [54] or bacterial light-responsive proton pump bacteriorhodopsin and converted to chemical energy in the form of ATP. [52] In a different approach, light energy is used to reduce NAD^+ to NADH by encapsulated TiO_2 nanoparticles. [55] Liposomes containing TiO_2 nanoparticles were illuminated with a UV light. The energised electrons were then transferred from TiO_2 nanoparticles to NAD^+ by a mediator, $Rh(bipyridine)_3^{+3}$. Generation of the reduced NADH was then confirmed spectroscopically and enzymatically. Thus light-energy was harvested within a compartment. These approaches demonstrate synergistic use of different materials to explore different aspects and strategies of energy transformation.

The work summarised within this PhD thesis uses nanocompartment architecture for synergic assembly of different materials. In particular, coupling of light-harvesting inorganic nanoparticles to a conductive membrane-spanning protein is explored in order to channel light energy insidde the compartment. There this energy could be used to drive such reductive chemical reactions as fuel synthesis, and demonstrate proof-of-concept compartment for artificial photo-synthetic nano-reactor. Such compartments can be used as bottom-up models exploring molecular arrangments for artificial photosynthesis reactions as well as potential ways to couple microorganisms with light harvesting nanoparticles or electrodes.

1.4 Motivation: bio-inspired liposomal compartments for solar energy capture

The conversion of light energy into other forms of energy (*e.g.*, electricity or chemical bonds) typically requires several steps. [56–58] Capture of light energy starts by initial light absorption at a chromophore. This absorbed energy is used to excite an electron to higher energy levels and the energised electron can then be transferred to an electron acceptor (*e.g.*, electrode for electricity or a chemical catalyst for fuel production) (Figure 1.5 a).

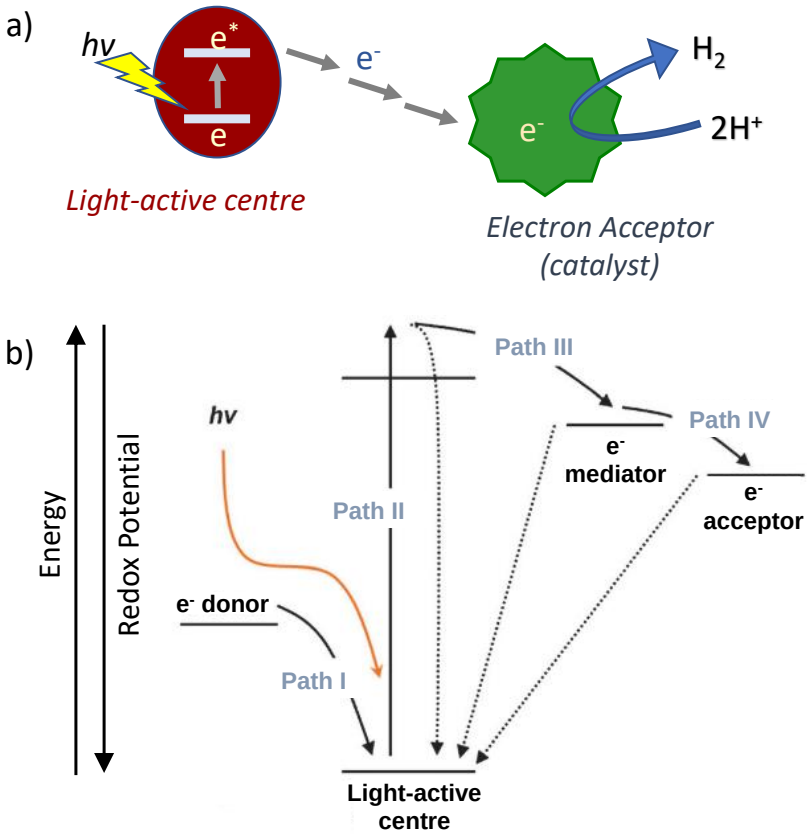

Figure 1.5: Overview of light-harvesting and the required electron transfer steps. **a**) Light energy is absorbed at the light-active centre and is used to excite an electron. The energised electron is then transferred to the electron acceptor, which in this case is a catalyst reducing hydrogen ions into gaseous hydrogen. **b**) Schematic of possible pathways of electron flow during light-harvesting. Light energy is used to eject an electron from the Light-active centre (Path II). The high energy electron then travels through electron mediator to an electron acceptor via Paths III and IV. The hole at the light-active centre is subsequently filled by electron donor (Path I). The dashed lines indicate that energised electrons can also be quenched and fall back to the ground state without leading to completed energy conversion. Figure **b**) adapted from [59].

For a thermodynamically favourable reaction, electrons are transferred along the energy gradient from compounds with more negative reduction-oxidation (redox) potential to compounds with more positive redox potential. [59] Thus for successful electron transfer the energy levels (*i.e.*, reduction potentials) of the excited chromophore (light active centre), the electron acceptor and any intermediate agents (*i.e.*, electron mediators) are required to be suitably placed along the energy gradient. [57, 59] This is shown in Figure 1.5 b, where pathways of electron flow associated with light absorption are

mapped. Despite global research efforts that are continuously advancing strategies for harnessing solar energy into sustainable electricity, solar fuels and solar chemicals [60–62], the light harvesting stage, *i.e.*, photo-induced charge separation and electron (or hole) transfer to electrode or catalyst, remains the principal efficiency limiting step in the proposed strategies. [62] This is primarily due to back-electron transfer and charge recombination (see the dashed lines in Figure 1.5 b). [57, 59] In contrast, biological photosynthesis is able to achieve near-unity charge separation [56] and resist the unfavourable charge recombination by rapid spatial charge separation along an electron transport chain embedded in photosynthetic membranes. [63–65]

The stunning efficiency of biological light-harvesting systems results from a very precise and sophisticated arrangement of photosynthetic components (organic photosensitizers, protein co-factors and electron mediators, redox biocatalysts), which are optimized in the dimensions of space (relative location of components), energy (light-excited state and redox properties) and kinetics (rates of competing processes). [56,66] The composition of biological photosynthetic assemblies allows efficient photon absorption at light harvesting antennae, which is then passed along series of chromophores to the reaction centres (*e.g.*, plant photosystems PSI and PSII), where this energy is used for electron excitation and water oxidation. [50] The excited electrons are then relayed along an electron transfer chain and ultimately stored as a transmembrane proton gradient and reduced redox-active molecules such as NADPH (Figure 1.6 a). [58]

Such features as near-unity quantum yield (defined as photon absorbtion leading to the formation of the charge-separated state despite competition between forward and back processes [56]) and environmentally friendly operation put biological light-harvesting systems above any other known system. [58] Hence, there is a lot of interest in directly exploiting natural or genetically modified organisms [62, 68–71] or their components for energy harvesting in artificial bio-hybrid systems. [72] Natural photosensitisers (PS) such as photosystem I, photosystem II and whole plant thylakoid membranes have been directly coupled to electrodes and inorganic catalysts in various photosynthetic devices to directly produce electricity, fuel (*e.g.*, molecular hydrogen) or evolve oxygen. [72–78] However, light-induced damage and degradation limits the use of pigment-protein complexes, isolated away from their natural repair mechanisms in their native environment (*e.g.*, the half-life of photoanodes containing isolated photosystem II is 20 min [79]). [72, 80]

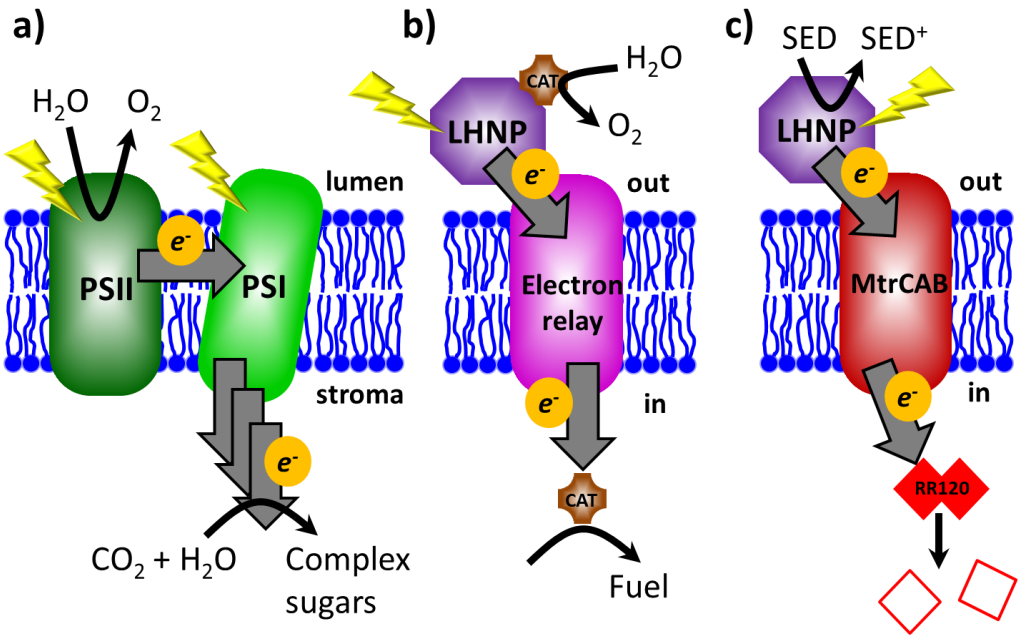

Figure 1.6: Schematic of light-driven electron transfer across the lipid membrane in nature (a), in the envisioned compartmentalised bio-mimicking system (b), and as presented in chapter 4(c). a) Photosystems I and II (PSI, PSII) are photo-excited and electrons are transferred via several electron acceptors across the membrane, where they are ultimately used for CO_2 conversion into complex sugars. **b**) External electrons are supplied photo-chemically from a light-harvesting nanoparticle (LHNP), which is regenerated by a water-oxidising catalyst (CAT). Electrons are relayed across the membrane to a catalyst leading to fuel generation within the compartment. **c**) Electron transfer across the lipid bilayer is ensured via transmembrane protein complex MtrCAB and monitored following reductive bleaching of an internalised red azo dye, Reactive Red 120 (RR120). SED – sacrificial electron donor. Figure adapted from [67].

An alternative approach is to mimic these natural systems using synthetic materials by devising and interfacing synthetic analogues of natural photosynthetic components: light harvesting antennae, reaction centres for charge separation, electron mediators, redox catalysts, electron donors and a supporting membrane to arrange components and physically separate the products. [56, 58] Reported systems include coupling of light-harvesting PS (*e.g.*, porphyrins, quantum dots) with various conductive materials ranging from graphene to peptide nanotubes to semi-conductor nanoparticles, fuel producing enzymes and electron mediators to regenerate cofactors for redox enzymes. [58, 81] Synthetic materials generally have longer lifespan. Thus the lifetime of a system consisting of dye-sensitised TiO_2 coupled with H_2 generating cobalt catalyst was limited

by the stability of the cobalt catalyst after 4 hours of illuminations and not the TiO_2 photosensitiser. [82] Efforts are also made to explore the effects of photosynthetic component spatial organisation by mimicking such natural systems as stacked plant thylakoid membranes [83] and chlorosomes of green sulfur bacteria [84].

The work described within this thesis aims to construct compartments mimicking another aspect of plant photosynthesis, *i.e.*, the use of a lipid membrane to arrange and spatially separate photosynthetic components between the different environments of thylakoid lumen and stroma (Figure 1.6 a). [50] Specifically, the objective is to spatially separate photo-oxidation and reduction reactions in the external and internal space of liposome compartments, respectively (Figure 1.6 b). Thus, the envisioned system combines several processes: 1) generation of light-excited electrons on the outside of liposomes, 2) transmembrane electron transfer, 3) storage of the excited electrons within chemical bonds within the liposome compartment and 4) regeneration of light-harvesting nanoparticles (LHNP). Thus use of liposomes provide means to direct spatial distribution of the involved molecules. Furthermore, these reactions occur at the liposome membrane (*i.e.*, inner and outer surface), thus in order to achieve more effective surface to volume ratio, focus is placed to utilise liposomes within the sub-micro scale.

1.5 Components required for the intended liposome compartment

The intended light-harvesting system involves assembly of suitable molecular components able to work together and perform the various tasks required for light energy harvest. These are:

- light-harvesting nanoparticles (LHNP) - to generate light-excited electrons on the outside of the liposome;
- electron conduit - to facilitate transmembrane electron transfer;
- reduction catalyst - to chemically store the excited electrons within the liposome compartment;

- oxidation catalyst or sacrificial electron donor (SED) - to regenerate the LHNPs;
- lipid membrane - to act as scaffolding and barrier, forming the compartment and separating the internal and external environment.

The next few sections will briefly introduce the components selected acros the space of biological and chemically synthesized materials. Many of the decisions concerning material selection were taken building on the previous work within the Jeuken group by Dr Ee Taek Hwang (see reference [63]) and the collaboration with Dr Emma Ainsworth from the University of East Anglia (for more information see the doctoral thesis at reference [85]).

1.5.1 Light-harvesting nanoparticles and SED

Synthetic LHNPs were chosen over their natural equivalents (*e.g.*, plant photosystems I and II) because they are simpler and cheaper to produce and because of their stability and chemical inertness. [59, 86, 87] Many of the compounds used within the field of artificial photosynthesis have been adopted from material development for solar panels, more specifically, dye-sensitised solar panel research. [57] Here, a molecular dye is absorbed onto a semi-conductor material, thus electrons from the photoexcited dye are injected into the conductive band of the semi-conductor (*e.g.*, TiO_2), which accumulate and transport multiple charge carriers to the electrode forming electric current. [57] This principle has been further explored in the field of solar fuels, where molecular dye and fuel-generating catalyst can be co-absorbed onto nanoparticles made of semiconducting materials such as TiO_2 NPs. [57] In this case the semiconducting particle functions both as a scaffold and as a solid-state electron mediator. [57] Figure 1.7 summarises some of the chromophores typically used for light absorption ranging from metal-based dyes, such as ruthenium poly-pyridine complexes (*e.g.* [Ru(2,20-bipyridine)3]$^{2+}$ derivatives (Figure 1.7a), porphyrins (Figure 1.7b), and organic dyes, such as Eosin-Y, donor–p–acceptor structures and chalcogenorhodamine dyes (Figure 1.7c–e). [57] In addition to these, carbon based nanoparticles such as carbon nitride and carbon dots have also been explored. [57]

The work described in this thesis tested and compared three LHNPs for solar energy

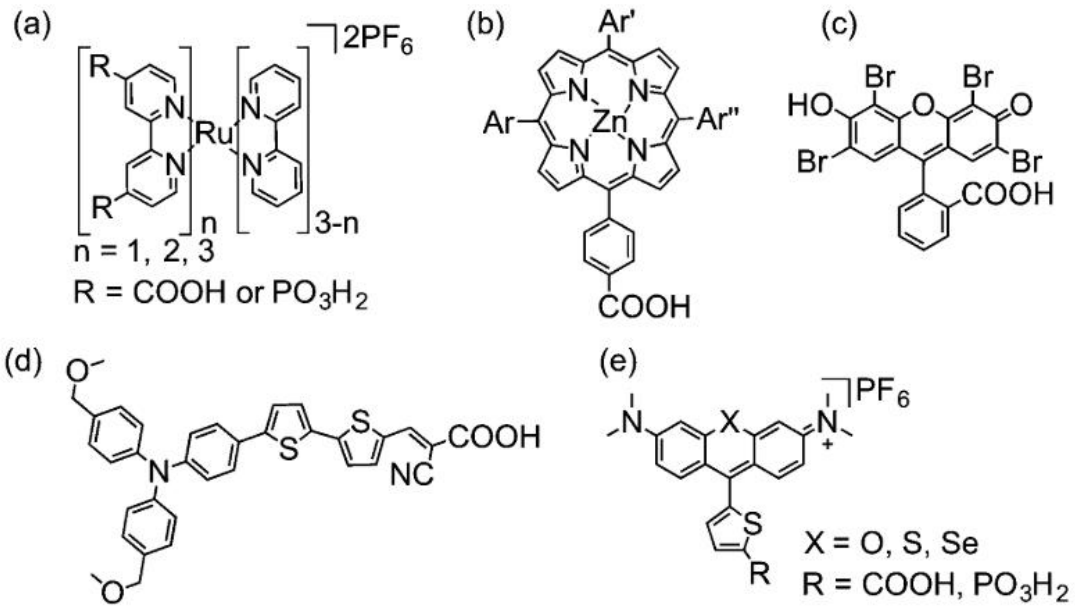

Figure 1.7: Chemical structures of dyes commonly used in dye-sensitised solar panel and dye-sensitised solar fuel research: (**a**) ruthenium bipyridine derivatives, (**b**) porphyrins (Ar = aryl groups), (**c**) Eosin-Y, (**d**) donor–p–acceptor type and (**e**) chalcogenorhodamine dyes. All dyes are shown in their fully protonated forms. Figure republished from reference [57].

capture. These were dye-sensitised TiO_2 nanoparticles and two types of carbon dots. Dye-sensitized TiO_2 nanoparticles are well-studied and are among the most active photocatalyst materials. [59] We used TiO_2 nanoparticles photosensitized with a Ru(II)(bipyridine)$_3$ dye in which one of the bipyridines is phosphonated in the 4,4'-position to enhance binding to TiO_2 (**RuP**-TiO_2, see Hwang *et al.* [63]). Carbon dots form another group of emerging light-absorbing nanomaterials showing remarkable photo-stability, water solubility, low toxicity and sustainable and cost-effective synthesis avoiding use of rare metals. [86–88] Here, we test amorphous carbon dots (*a*-CD) [86] and graphitic carbon dots with core nitrogen doping (*g*-N-CDs) [88, 89].

The choices made on LHNPs influenced the decisions on sacrificial electron donors (SED). SEDs are often used in photosynthesis test systems for their ability to regenerate the oxidised LHNP and also have the role in buffering the reaction solution. [57] Thus SEDs simplify the photo-oxidation reactions and allow to focus on developing and optimising photo-reduction reactions (*i.e.*, photo-electron excitation at the chromophore and subsequent electron trasfer leading to fuel generation). [57] Commonly used SEDs include tertiary amines (*e.g.*, triethanolamine, ethylenediaminetetraacetic acid,

triethylamine), alcohols, organic acids (*e.g.*, lactic acid, ascorbic acid, formic acid, oxalic acid) and inorganic ions such as sulfite. [57] Previous research on carbon dot photo-activity indicated that better photo-activity of carbon dot LHNPs were achieved using EDTA as the SED (supplementary information of references [86, 89]). Thus EDTA was used as the SED throughout the experiments.

1.5.2 Electron conduit and the lipid membrane

In the intended photo-synthetic compartment electrons generated from the light harvesting nanoparticles are transferred across the membrane. This is achieved using MtrCAB - a conductive transmembrane protein found in the bacterium *Shewanella oneidensis*. [90] This bacterium is able to support its anaerobic respiration by using a diverse range of extracellular electron acceptors. These include fumarate, nitrate, trimethylamine oxide (TMAO), dimethyl sulfoxide (DMSO), sulfite, thiosulfate, elemental sulfur and various metal oxides (insoluble iron and manganese minerals, *e.g.*, hematite, goethite, lepidocrite *etc*.) present either as soluble complexes or solid minerals. [90–92] The electrons are shuttled to the external minerals via outer membrane protein complexes such as MtrCAB and the closely related MtrDEF homologs. [90] These proteins form porin-cytochrome structures (Figure 1.8), which consist of a 20 haems assembled in a conductive molecular 'wire' made by MtrC (or homologus MtrF, OmcA) and MtrA (or homologus MtrD, DmsE). [90, 93, 94] This MtrC and MtrA conduit *i.e.*, molecular 'wire') spans the outer membrane through a pore formed by MtrB (or homologus MtrE and DmsF) [90, 93] The final stages of ET to these minerals are supported by MtrC (and its related homologues MtrF and OmcA) either by direct contact with the mineral or indirectly using soluble electron mediators as flavins. [90] Thus electrons from the periplasm of bacterium can be transferred across the outer membrane through the haem wire of MtrA and MtrC, which is supported within the membrne region by MtrB forming a protein pore (via structural β-barrel motif).

Purified MtrCAB has been shown to be used within liposomes, and have been observed to exhibit fast transmembrane electron transfer estimated as 10^3 – 10^4 electrons per second (measured by spectroscopic reduction of encapsulated methyl viologen). [91] In adddition, efficient electron exchange has been previously demonstrated between

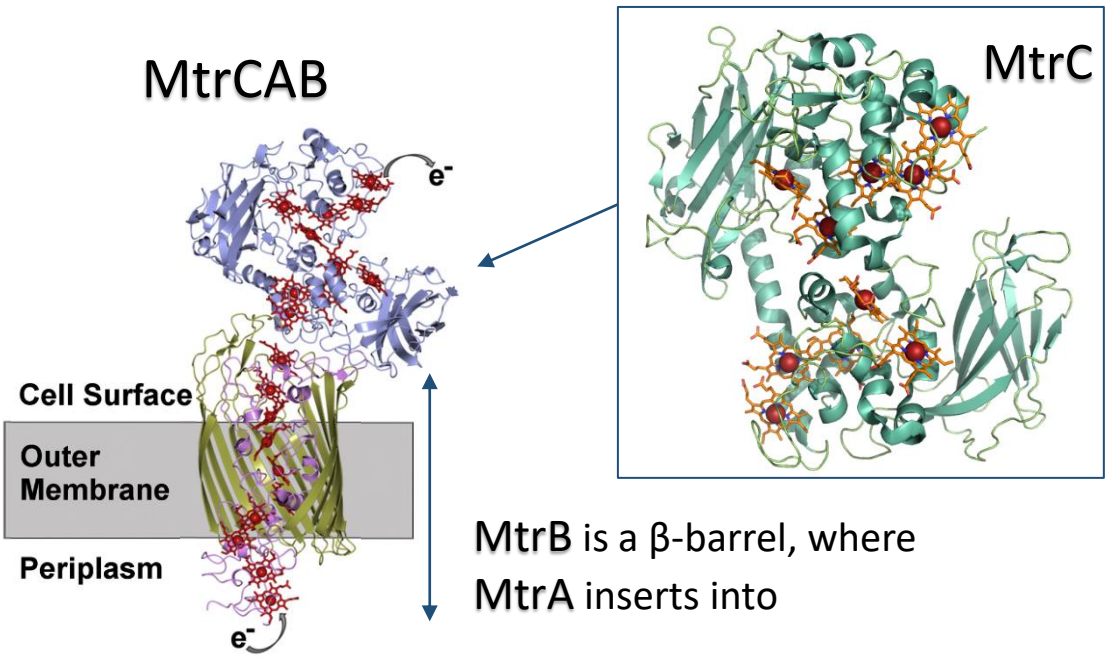

Figure 1.8: A diagram of the MtrCAB protein complex. Structure of a full MtrCAB complex from a closely related bacterium species *Shewanella baltica* OS185 [94] and an insert showing the structure of MtrC from *S. oneidensis* MR1 (PDB ID: 4LM8). Figure modified after [94].

the soluble decahaem subunit MtrC and LHNPs, in particular, with dye-sensitised TiO_2 nanoparticles. [95–97] Thus previous research has paved way for using MtrCAB as electron conduits for developing the light-harvest liposome compartment envisaged within this thesis.

Although many natural and synthetic lipids and lipid mixtures can be used to form liposomes, *Escherichia coli* polar lipid extract was chosen as a way to better mimic the natural outer membrane environment of the MtrCAB. This choice was made in order to minimise potential phospholipid-dependent changes in MtrCAB activity. [98] *Escherichia coli* polar lipid extract is estimated to primarily contain phosphatidyl ethanolamine (PE) at 70–80%, phosphatidyl glycerol (PG) at 20–25%, and cardiolipin (CL) at 5% or less. [99, 100]

1.5.3 Fuel-generating catalyst

There are many potential reduction reactions and compounds that could be used as proof for photocatalysis. These include H_2 evolution (*i.e.*, generation of gaseous

H_2 from water), carbon-based conversions such as fumarate to succinate reduction or CO_2 transformation to C_1 products (*e.g.*, CO, HCOOH, CH_3OH, CH_4), and nitrogen transformations like NH_3 generation from N_2 or reductions of N_3^- and NO_2^-. [101–103] Several reasons make hydrogen evolution (*i.e.*, production of hydrogen gas from water) attractive for the compartmentalised photocatalysis envisioned in this work. Firstly, H_2 evolution from H^+ present in water is a relatively simple two-electron reaction: $2H^+ + 2e^- \rightarrow H_2$ (E^0 = - 0.41 V vs NHE at pH 7). [101] Secondly, water (*i.e.*, hydrogen/hydronium ions) as a substrate is already abundant in the system. Thirdly, the reaction product (*i.e.*, H_2 gas) is able to diffuse across the compartment lipid membrane, thus simplifying reactant mass transport and reaction kinetics within the compartment. And finally, hydrogen evolution aligns well with the research interests of the field of solar fuels, where sustainable fuel generation from widely abundant and cheap raw materials (such as water or CO_2) is key. [101, 102]

Hydrogen evolving catalysts (HEC)

A variety of HECs have been reported and these can be broadly grouped as material (non-molecular) and molecular catalysts.

In material systems, hydrogen evolution reaction (HER) catalysis occurs on the surfaces of metals, semi-conductors and nano-structured materials. [101] Pt is long-known as the most efficient material for HER electrocatalysis, able to evolve H_2 very close to the reaction's equilibrium potential. [104] The superiority of Pt can be assigned to a near zero hydrogen binding (free) energy, and an optimal hydrogen bonding strength for facile hydrogen atom rearrangements and desorption. [105] However, the scarcity and cost of Pt [104, 106], makes it unsuitable for the needs of current and future industrial and photo-fuel applications. In this regard, many strategies are reported to reduce the size of Pt nanoparticles (*i.e.*, increase Pt surface area) [106] and to develop other materials for HER, such as semiconductors ranging from metal oxides (TiO_2, Cu_2O, WO_3, Fe_2O_3, $BiVO_4$) and metal sulphides (CdS, CdZnS) to chalcogenides (*e.g.*, $Cu(Ga,In)(S,Se)_2$, $CuGaSe_2$, Cu_2ZnSnS_4, ZnS-$AgInS_2$) and graphitic polymeric carbon nitride *g*-C_3N_4. [101] The strategies used for improving HER activity include material and surface nanostructuring to improve surface-to-volume ratio and adding interfaces

with electron accepting materials such as graphene or carbon nanotubes, as well as integrating co-catalysts such as Pt, RuO_2, NiO, MoS_2, MoS_2 composites and molecular catalysts as reviewed in [101]. Other strategies exploring photocatalytic HER also include material and surface nanostructuring to improve charge carrier transport properties and light absorption for photocatalysis, quantum and optical confinement. [101]

Molecular catalysts evolve hydrogen at specific catalytic sites, which usually comprise of one or more coordinated metals. The most efficient molecular hydrogen evolving catalysts (HEC) are hydrogenases. Hydrogenases are enzymes produced by bacteria, archea and lower eukaryotes, which use H_2 either as a source of low-potential electrons (*i.e.*, fuel) or as a way to eject excess electrons (*i.e.*, evolve H_2). [107] Three types of hydrogenases are distinguished and named after the metal composition in their active sites. [107, 108] These are [FeFe]- and [NiFe]- hydrogenases reversibly oxidising H_2 at their bimetallic centers coordinated by CO and cyanide ligands, and [Fe]-hydrogenases able only to split H_2 at a mononuclear iron-carbonyl centre. [107, 108] Most hydrogenases require only a minimal overpotential for H^+ interconversion into H_2 and demonstrate superiority over Pt in terms of single-site catalytic activity. [57, 107, 109] Unfortunately, the practical use of hydrogenases is limited due to their sensitivity to oxygen, instability, and the labour required for their isolation and purification. [57, 107, 108]

The exceptional activity of hydrogenases have inspired development of synthetic compounds mimicking features of the enzyme active centres. These efforts have also contributed to the development of synthetic earth-abundant metal complexes as catalysts for HER. Among the reported synthetic molecular catalysts are a few examples of Fe-, Mn-, Cu- and Mo- based complexes, as well as the more commonly used Co-based (*e.g.*, cobaloxime catalyst family) and Ni-complexes (*e.g.*, nickel phosphine complexes). [57, 110] However, these synthetic HECs are still far from demonstrating the catalytic activity of their biocatalytic counterparts. [102]

Catalysts used in this study

The aim for the work described within this thesis is to demonstrate a proof-of-concept HEC activity within the lumen of a liposome compartment.

As the main light-harvesting and electron transfer steps occur at the liposome membrane

(*i.e.*, inner and outer surface), it is advantageous to increase the amount of liposome surface versus the liposome volume. This can be achieved by preparing small unilamellar vesicles, such as sub-micro scale liposomes. Focus on higher liposome surface-to-volume ratios means that the liposome volume is quite small. For example, liposomes with an average diameter of 100 - 200 nm constitute only about 0.5 - 1 $\cdot 10^{-18}$ L per liposome.Thus the main challenge lies in encapsulating enough of a potent HEC to record a detectable signal. To mitigate the risk for missing the signal of hydrogen evolution within the liposomal compartment, this stuy focused on testing benchmark catalysts from both types of material and molecular catalysts (*i.e.*, Pt and hydrogenases).

Two types of Pt NPs were obtained - commercially purchased Pt NPs (Pt_{com}) and in-house synthesized Pt NPs (Pt_{syn}). The Pt_{com} consists of 99.9% pure Pt and have an average particle size of 3 nm (specified by the manufacturer). Pt_{syn} were synthesized as described in section 2.1 following previous work by Eklund and Cliffel, where glutathione was used as a capping agent to inhibit particle overgrowth and aggregation, and yield soluble NPs with an average size of about 2.5 nm. [111]

Hydrogenase HydA1 was provided by Dr. Gustav Berggren (Uppsala University). This small 48 kDa [Fe,Fe]-hydrogenase originates from an algae *Chlamydomonas reinhardtii*. [113] The HER occurs on the active site called the H-cluster, which consists of a [4Fe-4S] iron-sulphur cluster covalently linked to the catalytic [Fe,Fe]-subcluster by a cysteine thiolate. [114] Both irons in the binuclear [Fe,Fe]- subcluster are coordinated by bridging dithiolate ligand, three CO ligands and two CN^- ligands (Figure 1.9). [112, 114] A key step for the enzyme activity is the electron supply to the catalytic site buried within the enzyme, which can be improved with electron mediators (*e.g.*, methyl viologen) acting as remote, freely diffusing communication agents between the enzyme and electron source (*e.g.*, electrode, photosensitiser, light harvesting nanoparticle or ditihionite). [81]

HydA1 is able to convert H^+ into H_2 reversibly with a minimal overpotential even in the presence of H_2 (which is known to inhibit some other hydrogenases), but is also rapidly and irreversibly inactivated by even trace amounts of O_2. [114, 115] The production and purification of HydA1 has recently been facilitated in Berggren's group by heterologous expression of the apo-enzyme in *Escherichia coli* followed by an artificial *in vitro* maturation with a chemically synthesized mimic of the di-iron cluster. [112] The specific HER activity of the resulting HydA1 was reported as about 700 - 800 μmol H_2

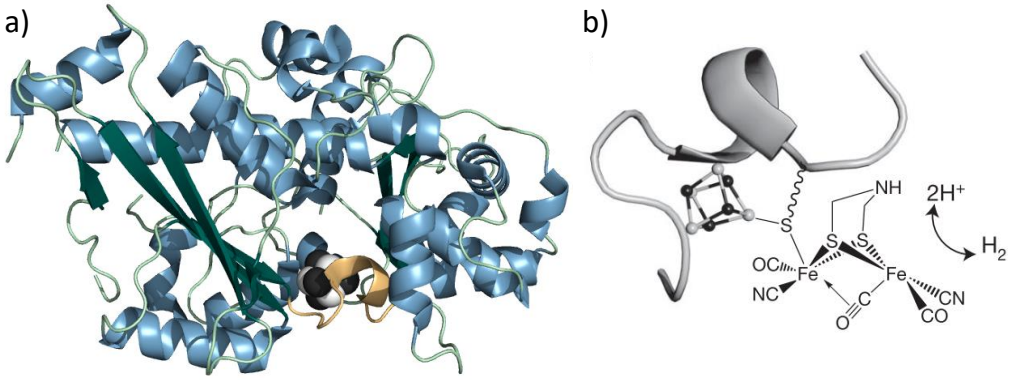

Figure 1.9: a) A cartoon representation of the HydA$^{\Delta EFG}$ hydrogenase from *Chlamydomonas reinhardtii* with a space-filling representation of the associated [4Fe-4S] cluster (Fe – white, S – dark grey). The $^{\Delta EFG}$ denotes potein expression devoid of the protein machinery responsible for the insertion of the [Fe,Fe]-subcluster, thus the [Fe,Fe]-subcluster (shown in **b**) is absent from this structure. Protein Data Bank ID, 3LX4. The protein representation is coloured according to the protein secondary structure (light green, loops; blue, α-helices; dark green, β-sheet). The light orange represent the protein loop represented in (**b**). **b**) The active centre of the HydA hydrogenase showing the chemical structure of the (Fe,Fe)-subcluster and the shematics of the protein loop containing [4Fe-4S] cluster (shown as balls and sticks with Fe and S shown as white and grey spheres, respectively). Figure republished from [112].

min^{-1} mg^{-1} [112], which is comparable to the reported activity of the wildtype enzyme (*e.g.*, ≈730 and 935 μmol H_2 min^{-1} mg^{-1} reported in [113] and [115], respectively).

1.6 Development of a light-harvesting compartment and chapter overview

This thesis describes work on developing light-energy harvesting compartments, where the liposomal membrane is used to spatially arrange and separate the key molecular components. This includes several ET steps across molecular interfaces: 1) light-harvesting nanoparticle (LHNP) to MtrCAB, 2) MtrCAB to H_2 evolving catalyst (HEC) and 3) sacrificial electron donor to the LHNP. Figure 1.10 summarises the key steps of the intended light-harvesting compartment and the chapters within this thesis, which focuses on particular molecular interfaces and interactions. At first, **Chapter 3** describes attempts to understand the interface between light harvesting nanoparticles (*e.g.*, dye

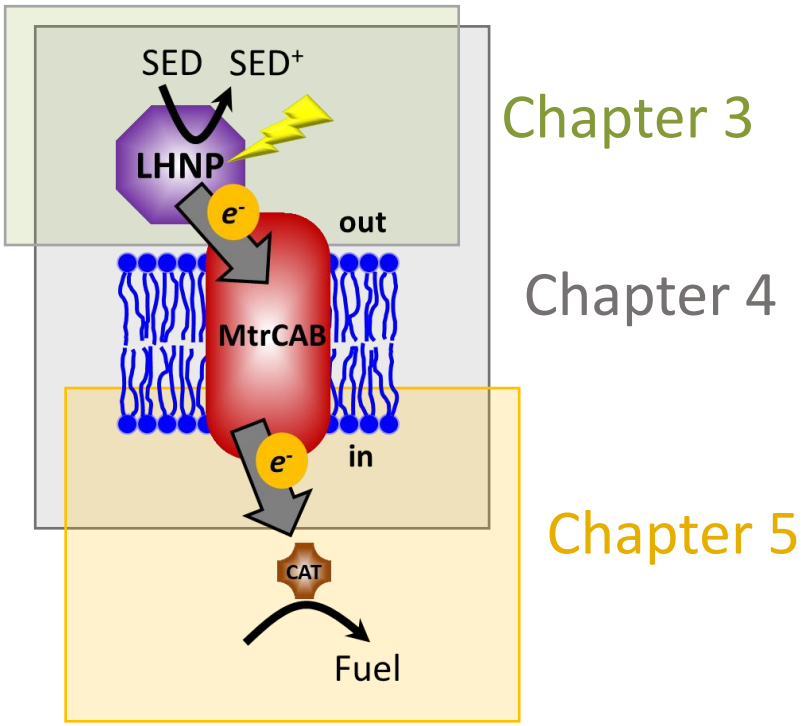

Figure 1.10: Overview of chapters describing work on developing light-harvesting compartments.

sensitized TiO_2) and the MtrC(AB) to aid with engineering of electron transfer from the light harvesting nanoparticles to the MtrC, which forms the soluble part of the MtrCAB. Then, **Chapter 4** explores photo-electron transfer across the liposome membrane. This is demonstrated using a liposomal compartment, where electrons from LHNPs are passed through the MtrCAB and use to bleach an incapsulated red dye. Finally, **Chapter 5** describes work attempting to finish the energy conversion across the membrane to a chemical entity (*e.g.*, hydrogen gas) by a catalytic electron acceptor (*e.g.*, platinum catalysts and a hydrogenase), thus separating and preventing oxidation and reduction process in time and space. **Chapter 6** summarises these approaches and suggests future research directions in this area.

This page is intentionally left blank.

Chapter 2

Materials and Methods

This chapter aims to describe in detail the materials and experimental techniques used throughout this thesis. At first, section 2.1 lists sources of main chemicals, lipids, proteins and nanoparticles. Then in sections 2.2 and 2.3 I describe generic methods used throughout the thesis to create and characterize liposomes and nanoparticles. The following sections 2.4, 2.5 and 2.6, along with 2.7.1 focus on specific experimental methods used for work described in Chapters 3, 4 and 5, respectively.

2.1 Materials

Unless stated otherwise, all chemical substances were obtained from commercial suppliers and used without further purification: 3-(N-morpholino)propansulfonic acid (MOPS, >99.5%), sodium sulphate (Na_2SO_4, analytical reagent grade), ammonium chloride (NH_4Cl, tested according to Ph Eur), ammonium bicarbonate (NH_4HCO_3, ≥99.0%), N,N-Dimethyldodecylamine N-oxide (LDAO, BioXtra, >99%), sodium hydrosulfite (DT, >82%), Reactive Red 120 azo dye (RR120), methyl viologen dichloride hydrate (MV), pentaethylenehexamine (PEHA) and sodium metasilicate pentahydrate were purchased from Sigma–Aldrich. Ethylenediaminetetraacetic acid disodium salt dehydrate (EDTA, >99.5%), n-octyl glucoside (OG, laboratory grade) and monobasic potassium phosphate (KH_2PO_4, ≥98.0%) were acquired from Melfors. Di-Potassium hydrogen phosphate (K_2HPO_4, 98.0%) was purchased from VWR Chemicals. Triton X100 (TX, electrophoresis grade) detergent was purchased from Fisher Chemicals. Milli-

Q system was used to generate ultrapure water (resistance 18.2 MΩ· cm) which was used throughout.

The majority of lipids were purchased from Avanti Polar Lipids. These were *Escherichia coli* polar lipid extract, 1-palmitoyl-2-oleoyl-sn-glycero-3-phosphocholine (POPC), 1-palmitoyl-2-oleoyl-sn-glycero-3-phosphoethanolamine (POPE), 1-palmitoyl-2-Oleoyl-sn-Glycero-3-Phosphoglycerol (POPG) and 1,2-dioleoyl-sn-glycero-3-phosphoethanolamine-N-(carboxyfluorescein) (DGPE-CF). 1,2-Dihexadecanoyl-sn-Glycero-3-Phosphoethanolamine (Texas Red-DHPE) and Alexa Fluor™488 hydrazide fluorescent dye were purchased from Molecular Probes (Thermo Fisher Scientific). Lipids were dissolved in chloroform, distributed in 5 mg aliquots in glass vials, dried first under a stream of nitrogen gas and subsequently under vacuum for 2h. Lipids were stored in dry aliquots under nitrogen atmosphere at -20°C.

Light Harvesting Nanoparticles (LHNPs) were a kind gift from Prof. Erwin Reisner from the University of Cambridge. Ruthenium (Ru) dye sensitized TiO_2 anatase nanoparticles (**RuP**-TiO_2) and Ru-free precursor 3,4-dihydroxy-benzoic acid (DHBA) functionalised TiO_2 anatase nanoparticles (DHBA-TiO_2, diameter 6.8 ± 0.7 nm) were synthesized and characterized by Prof. Reisner group at Cambridge as described previously. [63] Graphitic nitrogen doped carbon dots (*g*-N-CD; diameter 3.1 ± 1.1 nm) and amorphous carbon dots (*a*-CD; diameter 6.8 ± 2.3 nm) were also synthesized and characterized by Prof. Reisner group at Cambridge as described in [86]. Commercial Titanium Oxide (anatase) nanopowder (a-TiO_2, average particle size 5 nm) was purchased from Nanostructured & Amorphous Materials, Inc. (Katy, USA).

Shewanella oneidensis MR1 protein MtrC and MtrCAB were provided by Prof. Julea Butt (University of East Anglia). MtrCAB was also purified in-house using Triton X-100 to solubilise MtrCAB as described before. [116] The detergent was exchanged into 5 mM LDAO using size-exclusion chromatography (*i.e.*, Superdex 200 Increase, GE Healthcare) eluted with 5mM LDAO, 20 mM HEPES, pH 7.8. Final purity of the purified MtrCAB was confirmed by SDS-PAGE with protein visualized by Coomassie and haem stain. [117] The concentration of protein was routinely measured using BCA assay (ThermoFisher Scientific) according to the manufacturer's protocol. As MtrC and MtrCAB contain multiple haems (10 and 20, respectively), protein concentration and structural integrity was also routinely monitored via haem absorbance by light spectroscopy. Thus UV-visible

light spectroscopy of oxidized MtrC/MtrCAB displays a heme Soret (γ) absorption peak centered at 410 nm, a visible-region peak at 531 nm and a shoulder at 560 nm. Upon haem reduction the Soret (γ) peak shifts to ≈420 nm and two smaller a and b peaks can be distinguished at around 552 and 523 nm. [118] An example of MtrCAB absorbance spectrum is shown in Figure 2.8 a. All purified proteins were stored at -80 °C.

Commercial Pt (Pt_{com}) nanopowder water dispersion (3 nm in diameter, pH 7) was bought from US Research Nanomaterials, Inc. (Houston, USA). The dispersion contains 1000 ppm 99.99% Pt, which corresponds to a concentration of $3 \cdot 10^{15}$ nanoparticles per one mililiter (NPs/ml).

Soluble glutathione capped Pt nanoparticles (Pt_{syn}) were synthesized following a protocol by [111]. In short, 41.3 mg glutathione (reduced) and 101 mg chloroplatinic acid was dissolved in 25 mL water and stirred for 30 min. Then 73.3 mg sodium borohydride solution in 3 ml water was added dropwise to the platinum solution and stirred again for 30 min. Resulting particles were precipitated by mixing the sample with ethanol (1:3) and collected by centrifugation for up to 40 min at 18 000 RCF. The resulting pellet was re-suspended in deionised water (pH 8.8 - 11.0) and stored at 4 °C. In order to estimate the amount of Pt_{syn} in the samples, Pt was measured by atomic absorption spectroscopy (AAS). AAS is a technique commonly used to detect metals, which relies on observation of the specific interaction between atoms and electromagnetic irradiation. [119] The analytes are first atomised, then the applied light energy excites the valence electrons to the available empty orbitals. Although these electron transitions are unstable, these provide highly element specific radiative transitions, which are detectable optically. [119] In some cases, AAS was unsuitable for measuring Pt concentration (*e.g.*, sample volume was too small or sample was too dilute). In these situations Pt concentration was estimated spectroscopically at 280 or 368 nm using an optical absorbance-concentration calibration curve constructed manually using sample with known Pt NP concentration.

Mesoporous silica nanoparticles (further abbreviated as meSiO_2; 200 nm particle size, pore size 4 nm) were bought from Sigma Aldrich (Cat.no. 748161).

The [FeFe]-hydrogenase HydA1 was provided by Dr. Gustav Berggren (Uppsala University) in sealed anaerobic vials and stored at -80 °C.

2.2 Liposome preparations

2.2.1 Liposome and MtrCAB proteoliposome formation with simultaneous RR120 encapsulation by rapid dilution (Chapter 4)

5 mg dried *E. coli* polar lipid extract was resuspended by vigorous vortexing for up to 20 minutes in 294 μl MOPS buffer (20 mM MOPS, 30 mM Na_2SO_4, pH 7.4) containing 6.6 mM RR120 and 85 mM n-octyl glucoside (OG). 50.5 μL of 10 μM MtrCAB (or 5mM LDAO for control liposomes) was added to the lipid solution and kept on ice for further 10 min. The sample was then rapidly diluted while mixing in 50 mL ice-cold 20 mM RR120 in MOPS buffer. The sample was transferred to an ultracentrifuge tube (polycarbonate, 38 x 102 mm; Beckman Coulter) and centrifuged for 1h 40 min at 200 000 g (41 000 rpm) at 4°C using Beckman Coulter and type 45 Ti Rotor. The supernatant containing most of the non-encapsulated RR120 was discarded and the pellet was re-suspended in 500 μL MOPS buffer. The proteoliposome sample was then centrifuged at 5000 g for about 5 minutes to pellet any aggregates. Remaining non-encapsulated RR120 was removed by two consecutive rounds of 60 min sample incubation with 0.6 g Bio-Beads (Bio-Rad SM-2) per 1 ml of sample at 4°C on a rolling shaker. Experiments were performed within 2 days from liposome preparation.

The amount of reconstituted MtrCAB was determined using a Bicinchoninic Acid (BCA) assay [120] (ThermoFisher Scientific). This is a standart total protein concentration assay, where the peptide bonds reduce copper ions (*i.e.*, Cu^{2+} to Cu^{+}), which is then chelated by BCA. This reaction is accompanied with a sample color change from green to purple, which is proportional to protein concentration. Thus protein concentration can be be measured using colorimetric techniques. As the absorbance of encapsulated RR120 overlaps with BCA reagent absorbance, liposomes were first lysed with detergent (0.1% v/v Triton X100) and RR120 was removed by two consecutive desalting columns (0.5 ml Zeba™Spin, ThermoFisher). The effectiveness of the desalting columns was confirmed using a control sample of RR120 loaded liposomes without MtrCAB. MtrCAB recovery after desalting steps was estimated spectroscopically as more then 84%.

The concentration and size distribution of liposomes was determined by Nanoparticle Tracking Analysis (NTA) and DLS as described in section 2.3. The size and volume of liposomes were estimated by treating liposomes as spherical particles with the average diameter based on NTA data or DLS.

2.2.2 H_2 evolving catalyst encapsulation within liposomes by rapid dilution

Encapsulation of all H_2 evolving catalysts were attempted using a modified version of the protocol described in section 2.2.1.

For Pt_{com} encapsulation, 5 mg dried *E. coli* polar lipid extract was resuspended by vigorously vortexing for up to 20 minutes in 624 μl MOPS buffer (20 mM MOPS, 30 mM Na_2SO_4, pH 7.4) containing 125 μl Pt_{com} NP (100 mg Pt) and 55 mM n-octyl glucoside (OG). The sample was then rapidly diluted while mixing in 50 mL ice-cold MOPS buffer.

For Pt_{syn} encapsulation, 2.5 mg dried *E. coli* polar lipid extract was resuspended by vigorous vortexing for up to 20 minutes in 244 μl MOPS buffer (20 mM MOPS, 30 mM Na_2SO_4, pH 7.4) containing 100 μl Pt_{syn} NP (18.6 mg Pt) and 55 - 58 mM OG. Afterwards, 22.5 μL of 10 μM MtrCAB (or MOPS buffer for control liposomes) was added to the lipid solution and kept on ice for further 15 min. The sample was then rapidly diluted while mixing in 50 mL ice-cold MOPS buffer.

For [FeFe]-hydrogenase (HydA1) encapsulation, 5 mg dried *E. coli* polar lipid extract was resuspended by vigorously vortexing for up to 10 minutes in 181 μl MOPS buffer (20 mM MOPS, 30 mM Na_2SO_4, pH 7.4). The sample was brought into an anaerobic glovebox (O_2 <0.01 ppm, Labmaster, MBraun) and an additional 100 μl 250 mM OG and 17 μl HydA1 sample (4.8 nmol HydA1) were added. Then, 50.5 μL of 5 mM LDAO was added to the lipid solution and kept at 4°C for further 10 min. The sample was rapidly diluted while mixing in 50 mL ice-cold MOPS buffer.

After the rapid dilution step, samples were transferred to ultracentrifuge tubes and centrifuged for 1h 40 min to 2h at r_{av} of 125 000 - 140 000 g at 4°C using Beckman Coulter and type 45 Ti Rotor. After returning the centrifuge tubes back into the anaerobic glovebox (O_2 <0.01 ppm, Labmaster, MBraun), the supernatants were discarded and the

pellet was re-suspended in MOPS buffer. The resulting samples were then kept at 4°C. Experiments were performed within 2 days from liposome preparation.

2.3 Liposome and nanoparticle characterization

Several methods were used to gain understanding of particle size distribution in samples containing nanoparticles and liposomes. These were dynamic light scattering (DLS), nanoparticle tracking analysis (NTA), transmission electron microscopy (TEM) and cryogenic electron microscopy (cryo-EM).

2.3.1 DLS

DLS measures hydrodynamic radius of particles dispersed within solution using physical light properties. DLS relies on a beam of monochromatic laser, which is directed through the solution containing the dispersed colloidal particles (*e.g.*, macromolecules, nanoparticles, liposomes) of interest. [121] As the light moves through the colloid, light becomes scattered by the dispersed particles, and the resulting scattered light is detected. Subsequent analysis of the fluctuations in the scattered light intensity allows to determine the particle size. [121] DLS provides information of the average particle size within a homogenous samples within the range from 1 nm to 10 μm. However, DLS accuracy is limited in heterogenous samples, where presence of larger particles and small amounts of dust particles can lead to biased results and misinterpretations. [122, 123]

Although DLS is not the most precise of available techniques, DLS is one of the most accessible and easy-to-use method for obtaining an estimate of particle size within a solution. As such DLS was used to estimate the particle size distribution of samples containing different nanoparticles (*e.g.*, a-TiO_2, Pt_{com}, Pt_{syn}, silica nanoparticles) and liposome preparations. DLS was performed using Zetasizer Nano Z (Malvern Panalytical).

2.3.2 NTA

NTA allows sizing of individual particles within a sample ranging in size from ≈ 30-1000 nm. [123] Similarly to DLS, NTA also relies on light scattering, but couples the light scattering with a direct analysis of the Brownian motion of individual particles. [123] This is done utilising a special set-up, where laser light scattering microscopy is coupled with a charge-coupled device (CCD) camera able to capture and visualise nanoparticle movement in solution. The NTA software then identifies and tracks individual particles and calculates particle size from their movement. [122, 123]

As NTA measures individual particles, it provides more reliable estimate of particle size distribution and particle concentration. Unfortunately, NTA is not sensitive enough for very small particles (*i.e.*, ≤50 -100 nm), thus it was used for samples containing larger particles or particle aggregates such as commercial PT NPs (Pt_{com}), silica nanoparticles and liposomes. NTA was performed using Nanosight (NS300, Malvern Panalytical).

2.3.3 Electron microscopy

The most direct and practically more difficult techniques are TEM and cryo-EM. These rely on sample imaging by using electron beam passing through thin section of samples. [122] The sample irradiation with electron beam leads to excessive damage of organic matter. Thus TEM use for imaging of biological samples has been limited until the recent advances in cryo-EM, where the use of cryogenic temperatures reduces the effects of radiation damage. [124] At first, the sample is fixed by snap-freezing, which traps biomolecules within a thin vitrous layer of ice onto the imaging grid. Then the electron microscopy itself is performed under cryogenic temperatures using liquid nitrogen or liquid ethane. [124]

The TEM for nanoparticle (*i.e.*, Pt and silica NPs) imaging was performed as follows. 2 μl NP sample was drop-casted on 400 mesh copper EM grids with holey carbon film (Agar Scientific, S147-4). These copper grids use carbon film with holes for hosting and supporting the sample. The presence of holes within the carbon film provide areas on the grid with lower background noise. Grids were left to dry in room temperature for about 20 minutes. TEM was performed at Leeds Electron Microscopy and Spectroscopy

Centre (LEMAS) using FEI Tecnai TF20: FEGTEM Field emission gun TEM/STEM fitted with HAADF detector, Oxford Instruments INCA 350 EDX system/80mm X-Max SDD detector and Gatan Orius SC600A CCD camera. TEM of Pt_{com} and Pt_{syn} NPs were performed with the help of Dr Sunjie Ye. The diameters of Pt_{syn} particles were then measured manually using ImageJ [125]. Particle size distribution analysis was carried out by counting particles, and the average particle size was determined by fitting a lognormal distribution.

Cryo-EM as performed for liposome samples with and without **RuP**-TiO_2 at the Electron Microscopy unit of the Astbury Biostructure laboratory with the help of Dr Rebecca Thompson. Liposome or **RuP**-TiO_2 sample, or a sample containing both was placed onto lacey carbon grids with 200 μm mesh (Agar Scientific), blotted, and plunged frozen into liquid ethane. In this case lacey grids were used, which have even more open area (*i.e.* free from carbon film) as the holey grids used for TEM. Cryo-EM was performed as described elsewhere. [126] In short, cryo-EM was carried out at liquid nitrogen temperatures using an Oxford CT3500 holder and a FEI Tecnai-F20 electron microscope. Images were recorded at 50000 x magnification on a Gatan US4000 CCD camera under low-dose conditions (≈20 $e^-/Å^2$).

2.4 Experiments for MtrCAB footprinting (Chapter 3)

2.4.1 Monitoring binding between MtrC / MtrCAB and TiO_2 nanoparticles

Co-sedimentation assays

An aliquot of protein (MtrC or MtrCAB) stock sample was buffer-exchanged into 5 mM NH_4Cl (pH ≈8) with a desalting column (0.5 ml Zeba™Spin, ThermoFisher) according to manufacturer's instructions. MtrCAB samples contained also 5 mM LDAO detergent. The protein concentration of the sample before and after buffer-exchange was determined by a BCA assay, which indicated retention of ≈ 93% and ≈98% of MtrC and MtrCAB in samples, respectively. The protein samples were then diluted to 3-10 μM MtrC and 2-5 μM MtrCAB working protein stocks, which were used for co-sedimentation experiments.

A water suspension of 10 mg/ml commercial anatase TiO_2 nanoparticles (a-TiO_2) was further diluted to 1.8 mg/ml working stock solution. An appropriate amount of working anatase stock

solution was dispensed into polycarbonate centrifuge tubes (7 x 20 mm, Beckman Coulter), where then appropriate amount of protein and buffer (*e.g.*, MtrC in NH_4Cl) were added. The final solutions contained 160 nM MtrC and a-TiO_2, ranging from 0 – 130 μg/ml (total NP surface area of 0 - 7000 mm^2) in 5 mM NH_4Cl (total volume 190 μL). Samples containing MtrCAB were set up the same way and contained 80 nM MtrCAB, a-TiO_2, ranging from 0 – 80 μg/ml (total NP surface area of 0 - 4300 mm^2) in buffer containing 5 mM NH_4Cl and 5 mM LDAO. Samples monitoring co-sedimentation of MtrC samples without His-tag and a-TiO_2 in 5 mM NH_4Cl were set-up the same way, and contained 80 nM MtrC and a-TiO_2, ranging from 0 – 110 μg/ml (total NP surface area of 0 - 6000 mm^2) in 5 mM NH_4Cl (total volume 190 μL). Experiments involving DHBA-TiO_2 nanoparticles contained 100 nM MtrC and DHBA-TiO_2, ranging from 0 – 210 μg/ml (total NP surface area of 0 - 10000 mm^2) in 20 mM MOPS, 30 mM Na_2SO_4 buffer, pH 7.4 (total volume 200 μL).

Samples were then incubated in room temperature for about 20 minutes and ultra-centrifuged at 200,000 g, 6°C for 20 minutes using TLA-100 rotor (Beckman Coulter) in a tabletop ultracentrifuge (Optima MAX-TL, Beckman Coulter). 180 μl of supernatant was then carefully removed from the top and transferred to a 96-well plate (UV-star, Greiner Bio-One), where the absorbance of non-sedimented ('free') MtrC or MtrCAB was measured from 300 - 450 nm, step size 1 nm using Varioskan®Flash Spectral Scanning Multimode platereader operating SkanIt Software 2.4.5 RE for Varioskan Flash (Thermo Scientific).

In order to assess the MtrC and MtrCAB co-sedimentation with a-TiO_2, the amount of protein present in supernatant was first measured using half-maximum of the haem peak absorbance (*e.g.*, difference in absorbance between 413 nm and 423 nm or 412 nm and 423 nm). This method is less sensitive to background scattering of any non-sedimented a-TiO_2 particles. Then the relative protein amount was calculated by dividing with the average half-height heam absorbance from the control sample without a-TiO_2.

Protein recovery

The protein recovery from co-sedimented a-TiO_2 pellets was attempted using ammonium bicarbonate (NH_4HCO_3). The carbonate ions (CO_2^{2-}) bind TiO_2 surface, [127,128] and thus can be used to replace MtrC / MtrCAB from the a-TiO_2 surface. In order to do that, the ultra-centrifuged a-TiO_2 pellets (containing MtrC or MtrCAB) were dispersed in 180 μl 50 mM NH_4HCO_3 buffer (pH $\approx$ 8). Resulting samples were then ultra-centrifuged at 200 000 g, 6°C for 20 minutes as described before for co-sedimentation experiments. The supernatants containing the recovered

protein were transferred to a 96-well plate and the haem absorbance of MtrC and MtrCAB was measured as for co-sedimentation experiments. In addition, the absorbance of oxidised and reduced haems of the recovered MtrC and MtrCAB was assessed spectroscopically, and showed the same absorbance profile as the control, indicating that protein has not been damaged by interaction with a-TiO_2.

The amount of recovered protein was estimated relative to the initial protein amount used for co-sedimentation experiments. The half-maximum of the measured heam absorbance was divided with the average half-height heam absorbance from the control sample without a-TiO_2 used for co-sedimentation experiments. Then comparison of the amount of non-sedimented ('free') and the recovered MtrC/MtrCAB was made. This approach indicated that the amount of the recovered protein is influenced by the a-TiO_2 concentration. Thus a smaller fraction of the co-sedimented protein was recovered from samples containing higher a-TiO_2 concentration across all repeats. This observation can be explained by an increase in a-TiO_2 aggregation with increasing a-TiO_2 concentration, leading to more protein being trapped within the aggregates.

2.4.2 X-ray assisted protein labelling with Mass Spectrometry analysis (X-ray Footprinting Mass Spectrometry, XFMS)

Protein footprinting is a proteomics strategy where a change in the solvent accessibility of protein backbone and residues (*e.g.*, due to ligand binding) is monitored through their sensitivity to a chemical modification or proteolytic or chemical cleavage. As the result, solvent exposed protein areas become modified and chemically different from the native protein, and the imprint (or footprint) of these modifications can then be analysed using mass spectrometry (MS). [129] Different types of labelling can be used for protein footprinting, such as protease-cleavage of exposed protein backbone, deuterium exchange of amide protons in the protein backbone (hydrogen deuterium exchange, HDX), isotope-coded affinity tags to sample accessibility of specific amino acids (*e.g.*, cystein) as well as the use of oxidative hydroxyl radicals ($^{\bullet}OH$) to label solvent exposed amino acid side-chains. [129–131]

In this study $^{\bullet}OH$ labelling in used, as it provides non-specific (*i.e.*, all exposed residues can potentially be modified), fast and permanent modification, which allows greater flexibility in subsequent sample processing and use of different proteases. [129, 132] In this study TiO_2 NP binding to the protein is expected to shield this protein interface from water, thus comparison of peptide modification with and without TiO_2 NPs allows identification of protein residues involved in MtrC : TiO_2 interface. In short, the sample conditions and buffer composition is

optimised for radiolysis using a fluorescent dye, as described in X-ray irradiation dose-response assay. Then, protein samples with and without TiO_2 NPs are irradiated with X-rays. Water ionization generates hydroxyl radicals that label water exposed amino acid side chains even within buried protein cavities. [132] Resulting peptides typically contain covalent hydroxyl- (+16 Da or +32 Da) modifications, which subsequently are detected by liquid-chromatography tandem mass-spectrometry (LC-MS/MS). [129, 132, 133] The summary of XFMS approach is shown in Figure 2.1.

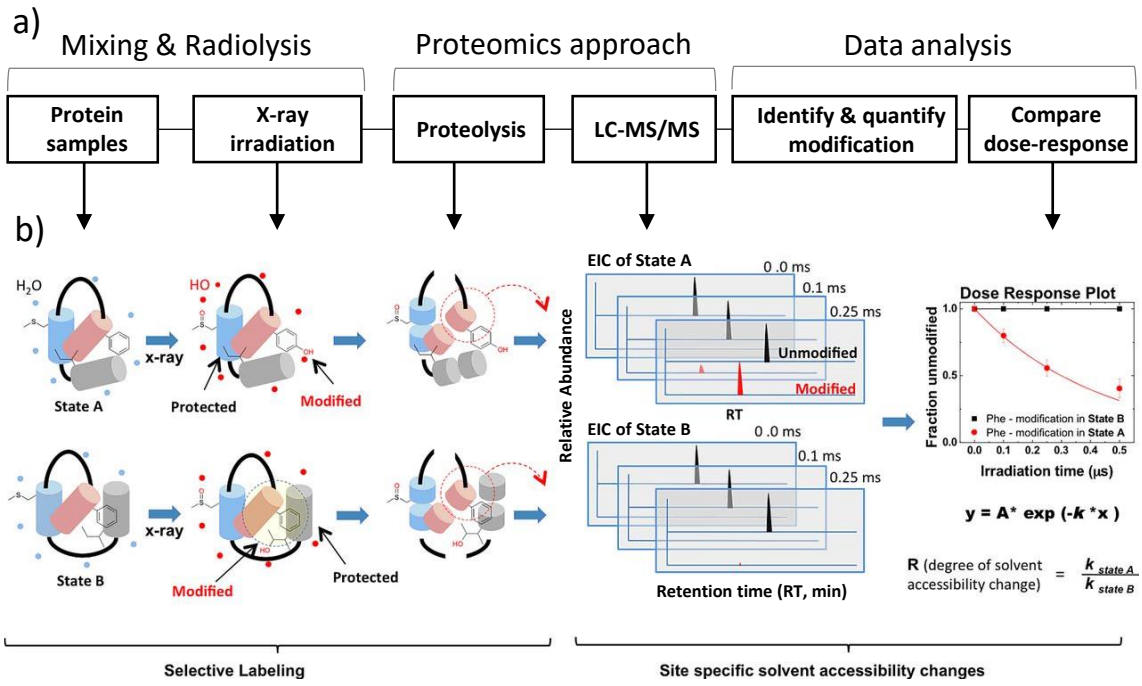

Figure 2.1: Overview of XFMS analysis. (**a**) Schematics showing main stages of XFMS approach. (**b**) Example of XFMS illustrating the water (blue dots) radiolysis and generation of hydroxyl- radicals (red dots), which then modify protein residues exposed to water. The conformational differences between protein in state A and state B lead to selective labelling of the identified phenylalanine (Phe). Protein is then digested with proteases and analysed using LC-MS/MS. LC quantitatively separate the peptides at different retention times (RT), which are then identified by the MS. MS/MS allows determination of the specific site of the modification. The quantification of the fractions of the unmodified peptide over exposure time (dose-response plot) allows determination of site-specific modification rate constants (k^{-1}). These rate constants are then compared between different sample conditions and their ratios (R) are used to describe the solvent accessibility changes due to any binding-interactions or conformational changes. The final result is mapped onto available structures. Figure reproduced and modified after [131].

XFMS experiments involved two conditions (*i.e.*, MtrC with and without a-TiO_2). Samples from

each condition were radiolysed for 5 different exposure times (*e.g.*, 0, 12.5, 25, 50 and 75 ms). MtrC from each sample was then proteolysed and the resulting native (*i.e.*, unmodified) and modified peptides were identified. Thus terms 'native' and 'modified' are used in regard to XFMS to describe whether a XF hydroxyl- modification (+16 Da) is detected on a peptide residue, peptide or protein. Then the amount and the distribution of hydroxyl- modifications were quantified across the 5 exposure times to produce a dose-response plot for each detected modification. A modification rate constants (k^{-1}) were then determined for each modification, which were compared between conditions as the modification rate ratio (R) of MtrC and MtrC : a-TiO_2 complex.

I performed the radiolysis experiments at the Beamline 3.2.1 at the Advanced Light Source (ALS) in Lawrence Berkeley National Lab (LBNL) working together with Dr Sayan Gupta, Dr Corie Ralston and Dr Caroline Ajo-Franklin as described in subsection on MtrC : a-TiO_2 NP sample radiolysis. The following LC-MS/MS analysis of modified proteins were performed by staff at the Biomolecular Mass Spectrometry Facility of the University of Leeds as described in subsection on Liquid chromatography-tandem mass spectrometry (LC-MS/MS) analysis. I analysed the resulting MS data as described in subsection on XFMS data processing and analysis.

X-ray irradiation dose-response assay

A key step in XF experiments is water ionization by x-ray irradiation, which generates $^{\bullet}OH$ that modify the side chains of protein residues [133]. Thus protein labelling is related to $^{\bullet}OH$ concentration, which in turn depends on X-ray exposure time and the flux density of an X-ray beam. [133] As the flux density of the X-ray beam is kept fixed, the dose of $^{\bullet}OH$ concentration is regulated by changing the duration of sample exposure. Many sample components such as buffering agents (*e.g.*, MOPS, Tris, HEPES), reducing agents and detergents used for membrane protein solubilisation react with $^{\bullet}OH$ (extrinsic radical scavengers) reducing the effective $^{\bullet}OH$ dose. [133] In addition, sample components (*e.g.*, macromolecular assemblies) can also react with $^{\bullet}OH$ (intrinsic scavengers). [133] Therefore, the duration of sample irradiation often has to be increased to overcome the radical scavenging processes [133], and the amount of $^{\bullet}OH$ scavenging was tested at the start of each radiolysis experiment.

The amount of hydroxyl radical formation and scavenging by different buffer and sample components was estimated indirectly - observing bleaching of irradiated fluorescent dye (Alexa Fluor 488), as reported in the supplementary information of [134] and in [133, 135]. Samples containing 40 μM Alexa Fluor 488 hydrazide were prepared with 0.2 - 0.3 mg/ml a-TiO_2 and/or

0.2 - 0.5 μM MtrC in a buffer containing 5 mM NH_4Cl (pH ≈8) or 50 mM phosphate buffer (pH ≈7). 10 μl aliquots were then subjected to 0 - 50 msec X-Ray irradiation at Beamline 3.2.1 at Advanced Light Source (ALS) of Lawrence Berkeley National Laboratory (USA) using a fixed stand set-up described in [136], where a microfuge tube containing the sample aliquot is placed in the sample holder and exposed one at a time. Samples were then diluted in 50 mM phosphate buffer (pH ≈7) and fluorescence (excitation at 496 nm, emission at 516 nm) was measured in a portable fluorimeter (Turner Biosystems TBS-380). The rate of hydroxyl radical formation was estimated from the dose-response plots, where fluorescence loss over x-ray irradiation time is fit to a single exponential function as described in [135]. The fit was made using GraphPad and apparent rate constants of the fluorophore modifications in various conditions were determined. Figure 2.2 provides an example of dose-response plots of MtrC with and without a-TiO_2.

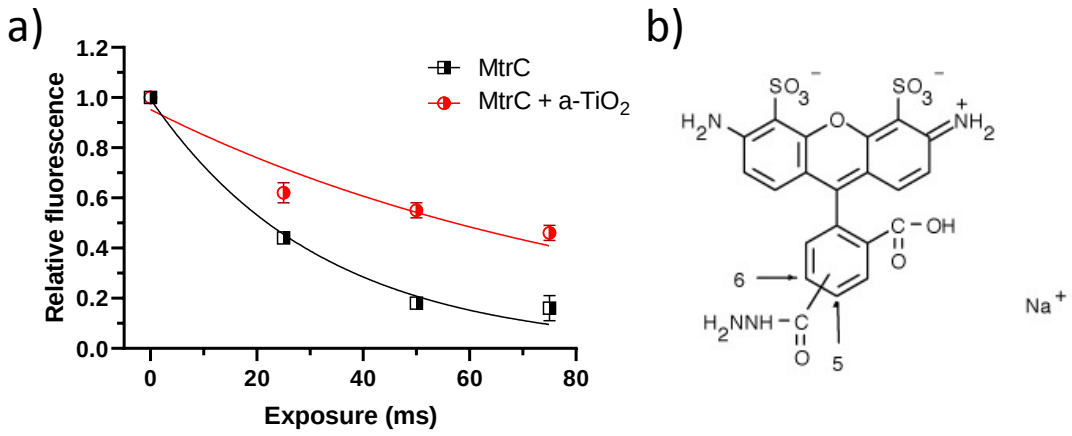

Figure 2.2: Determining hydroxyl radical dose for XFMS using fluorescent dye Alexa Fluor 488. (**a**) Example of a hydroxyl radical ($^{\bullet}$OH) dose-response plot of fluorophore decay after exposure to ionizing radiation. Experiments involved 40 μM Alexa Fluor 488 in 5 mM NH_4Cl buffer (pH ≈8) containing 0.2 μM MtrC with and without 0.2 mg/ml a-TiO_2 (black and red, respectively). The lines represent single exponential fit. Error bars indicate standard deviation, n=2. (**b**) Chemical structure of Alexa Fluor 488 hydrazide. Image obtained from the website of the commercial supplier (ThermoFisher, https://www.thermofisher.com/order/catalog/product/A10436#/A10436, accessed on 22/10/2019).

MtrC : a-TiO_2 NP sample radiolysis

MtrC samples with and without a-TiO_2 were radiolyzed by X-ray exposure at Beamline 3.2.1 at ALS as previously described [133, 134]. ≈0.4 nmol MtrC (0.2 μM) with and without 2 nmol a-TiO_2 nanoparticles (0.2 mg/ml, 1.1 μmol NP per litre, μmol NP/l) were mixed together in

5 mM NH_4Cl buffer. Total volume per sample was 1.85 ml. Samples were split in two parts and loaded in a flow set-up described in [133, 136] and irradiated with X-Rays for 0, 12.5, 25, 50 or 75 msec. Exposed samples were collected in a fresh tube containing 1M NH_4HCO_3 (final concentration 50 mM). The collection tube of one set of MtrC control samples without a-TiO_2 also contained 220 mM methionine amide (final concentration 11 mM) as a radical quencher to prevent secondary oxidation reactions [136]. Methionine amide was not used for other control samples and a-TiO_2 samples to avoid increasing the solute concentration and thus slow the a-TiO_2 precipitation. The samples containing a-TiO_2 were then immediately de-salted in 50 mM NH_4HCO_3 using Zeba™Spin columns (0.5 ml, 7k MWCO, ThermoFisher) according to manufacturer's instructions. Earlier sample turbidity measurements before and after the desalting step showed that a-TiO_2 binds to the de-salting column matrix (data not shown) and thus a-TiO_2 was effectively removed in this step. All exposed samples were then concentrated to about 70 - 100 μl using a spin concentrator (Amicon Ultra 4, 30k MWCO). Finally, samples were snap-frozen and kept at -80°C till LC-MS/MS analysis.

Liquid chromatography-tandem mass spectrometry (LC-MS/MS) analysis

Samples were proteolysed and run through LC-MS/MS by Dr Rachel George at the Biomolecular Mass Spectrometry Facility at the University of Leeds.

50 μL of sample was mixed with 50 μL SDS solubilisation buffer, which consisted of 5% sodium dodecyl sulfate (SDS), 50 mM tetraethylammonium bromide (TEAB), pH 7.55. To reduce and alkylate protein disulphide bonds, first DTT (dithiothreitol) was added to a final concentration of 20 mM and sample was heated to 95°C for 10 min with shaking. Then iodoacetic acid was added to a final concentration of 40 mM and sample was kept at 20°C for 30 min with shaking. The sample was acidified using 7.8 μL 12% phosphoric acid and 1200 μL of S-Trap binding buffer (90% methanol, 100 mM final TEAB, pH 7.1). 2 μg of protease Glu-C (reconstituted in 50 mM TEAB, Promega, UK) was added, and samples were transferred to a S-Trap™column (Protifi, NY, USA). As the total sample volume was higher than the volume of the spin column, the sample was loaded in parts onto the S-Trap column. The spin column was placed in a 2 mL Eppendorf tube and spun in a centrifuge at 4,000 g for 30 minutes to ensure all of the solution had passed through. The process was repeated until all of the sample had passed through the column and the protein was trapped within the protein-trapping matrix of the column. The captured protein was washed by adding 150 μL of S-Trap binding buffer (90% aqueous methanol containing 100 mM TEAB, pH 7.1) and centrifuged. This step was repeated three times. The S-Trap™column was moved

to a clean 1.7 mL sample tube then additional 0.5 μg of Glu-C in 25 μL of 50 mM TEAB was added to the top of the column ensuring that no bubbles were formed in the process. The column was capped loosely and incubated for 1 hr at 47°C in a thermomixer without shaking. Peptides were eluted with 40 μL of both 50 mM TEAB and then 0.2% aqueous formic acid. Sample was centrifugated for 30 seconds at 4,000 g. Hydrophobic peptides were eluted with 35 μL 50% acetonitrile, 0.2% formic acid. Eluted peptides were dried before being resuspended with 50 μL of 50 mM ammonium bicarbonate. 0.2 μg of protease ASP-N (reconstituted in water, Promega, UK) was added to the sample and then incubated at 37°C with shaking for 18 hours. The second digest reaction was quenched using 5 μL 1% trifluoroacetic acid (TFA). The sample was dried down prior to analysis on the mass spectrometer.

Samples were reconstituted in 100 μL 0.1% TFA, and an aliquot of 10 μL was used for LC-MS. LC separation of the peptide mixtures was performed on an ACQUITY M-Class UPLC (Waters UK, Manchester). 1 μL of each sample was loaded onto a Symmetry C18 Trap Column (180 μm inner diameter, 20 mm length) and washed with 1% acetonitrile/0.1% formic acid for 5 min at 5 μL min^{-1}. After valve switching, the peptides were then separated on a HSS T3 C18 analytical column (75 μm inner diameter, length 150 mm; Waters UK, Manchester) by gradient elution of 1-60% solvent B in A over 30 min at a flowrate of 0.3 μL/min. Solvent A was 0.1% formic acid in water, solvent B was 0.1% formic acid in acetonitrile.

The column eluant was directly interfaced to a quadrupole-orthogonal time of flight mass spectrometer (Xevo G2-XS Q-TOF, Waters UK, Manchester) via a Z-spray nanoflow electrospray source. The MS was operated in positive time of flight mode using a capillary voltage of 3.0 kV, cone voltage of 40 V, source offset of 80 V, backing pressure of 3.58 mbar. The source temperature was 80°C. Argon was used as the buffer gas at a pressure of $8.6 \cdot 10^{-3}$ mbar in the trap and transfer regions. Mass calibration was performed using [Glu]-fibrinopeptide (GFP) at a concentration of 250 fmol/μL. GFP was also used as a lock mass calibrant with a one second lock spray scan taken every 30 s during acquisition. 10 scans were averaged to determine the lock mass correction factor. Data acquisition was performed using data dependent analysis with a 0.2 s scan MS over m/z range from 350-2000, which was followed by five 0.5 s MS/MS taken of the five most intense ions in the MS spectrum. The applied collision energy was dependent upon charge state and mass of the ion selected. Dynamic exclusion of 60 s was used.

XFMS data processing and analysis

Peptides were de-novo sequenced and identified using PEAKS X software (Bioinformatics Solutions Inc., Waterloo, ON, Canada). The peptides with oxidation modifications were identified

Figure 2.3: Example of protein coverage and detected +16 Da modifications (small red squares) for unexposed MtrC control (without a-TiO_2) sample. Protein coverage 77%. Blue lines represent different identified peptides and are not a quantitative representation.

searching for +15.99 Da and 31.99 Da mass additions on each residue. The false discovery rate was set to 1%.

An example of obtained protein coverage and the identified +16 Da modifications of non-radiolysis MtrC control sample is shown in Figure 2.3. This figure provide an initial qualitative insight in the oxidation of MtrC by summarizing all different peptide versions identified across the protein.

The quantification of peptide modification was performed from extracted ion chromatograms (EIC), which extract elution profiles for a specified single m/z value. The abundance of native (*i.e.*, unmodified) and modified peptides were measured by integrating the peak area of the respective extracted ion chromatograms (EIC) as described in [130,133,134]. This was done using MassLynx v4.1 suite of software supplied with the mass spectrometer (Waters Ltd., Wilmslow, Manchester, UK). EICs were generated by extracting the signal of the m/z values for a selected native or modified peptides as a function of retention time (RT) for each observed charge state (*e.g.*, z = +2, +3 or +4). An example of EICs of a modified and unmodified peptide is shown in Figures 2.4 and 2.5. MS/MS data can then be used to identify the modified residues eluting at specific retention times (RT).

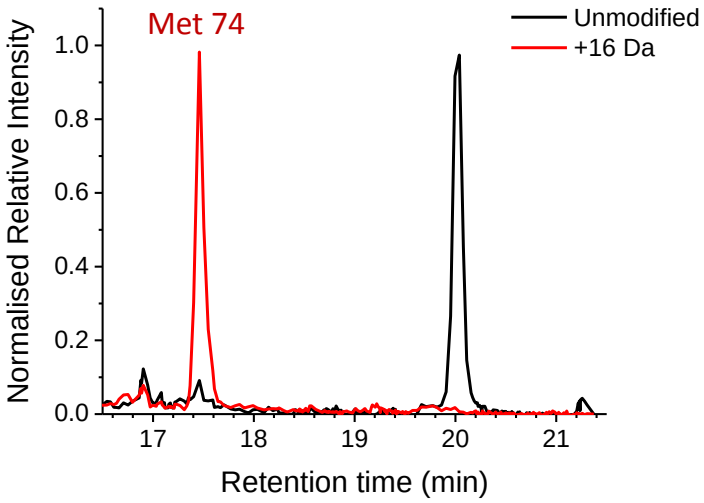

Figure 2.4: Example of XF labelling on peptide residues 73 - 83 (sequence: DMPVIGLANLE). Overlaid extracted ion chromatograms (EIC) of the native peptide (black, m/z 586.3, z=2) and +16 Da modified peptide (red, m/z 594.3, z=2). The intensity of native and modified peptides are normalised relative to the RT of the most abundant peptide within each EIC. EICs represent MtrC control sample (*i.e.*, without a-TiO_2) after 75 ms of radiolysis.

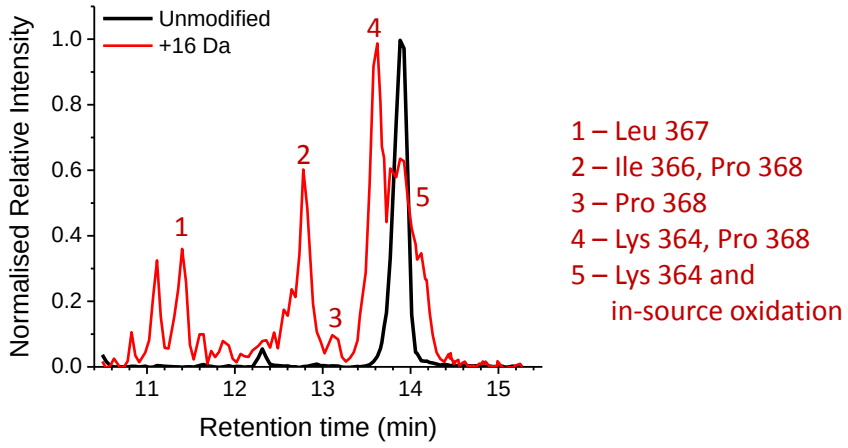

Figure 2.5: Example of XF labelling on peptide residues 362 - 374 (sequence: DLKTILPKVQRLE). Overlaid extracted ion chromatograms (EIC) of the native peptide (black, m/z 518.32, z=3) and +16 Da modified peptide (red, m/z 523.65, z=3). The labelled peaks represent identified peptide residues identified by MS/MS. Unlabelled peaks correspond to peptides with similar m/z signature, but not identified to be from this protein region. The intensity of native and modified peptides are normalised relative to the RT of the most abundant peptide within each EIC. EICs represent MtrC control sample (*i.e.*, without a-TiO_2) after 75 ms of radiolysis.

Some peptides, such as the one depicted in Figure 2.4 contained only a single XFMS modified residue and the corresponding XFMS analysis was straightforward. However, data analysis of other peptides was more convoluted. Figure 2.5 illustrates several common features of XFMS data analysis. Firstly, most modified peptides had shorter RT than the native peptide. Secondly, XF labelling of the same peptide residue can produce several oxidised products. For example, multiple residues can be modified on a single peptide [132]. Furthermore, some residues can be modified at different sites [129, 130] For example, the aromatic ring of phenylalanine can be attacked by a hydroxyl radical at *ortho*, *meta* and *para* positions, converting phenylalanine into three different stereoisomers of tyrosine [129]. Different oxidised products of the same native peptide typically elute at different times (*e.g.*, P368 and K364 in Figure 2.5). In some cases, EIC peaks corresponding to different versions of the oxidised peptide were poorly resolved, such as I366 and P368 with 12.6-13.1 min RT (peaks 2 and 3 in Figure 2.5), thus the quantification of these had to be performed cumulatively. Finally, peak 5 in Figure 2.5 has the same RT as the native peptide, which could be an in-source oxidation artefact formed during electrospray ionisation [137] and as a precaution would generally be excluded from the analysis. In this case, however, due to an overall overlap of peaks 4 and 5 in the EIC, peak area of both peaks were

pooled and quantified together. A summary of identified XFMS modifications and the criteria used to assign modified residues to individual EIC peaks are shown in Appendix, Table 1.

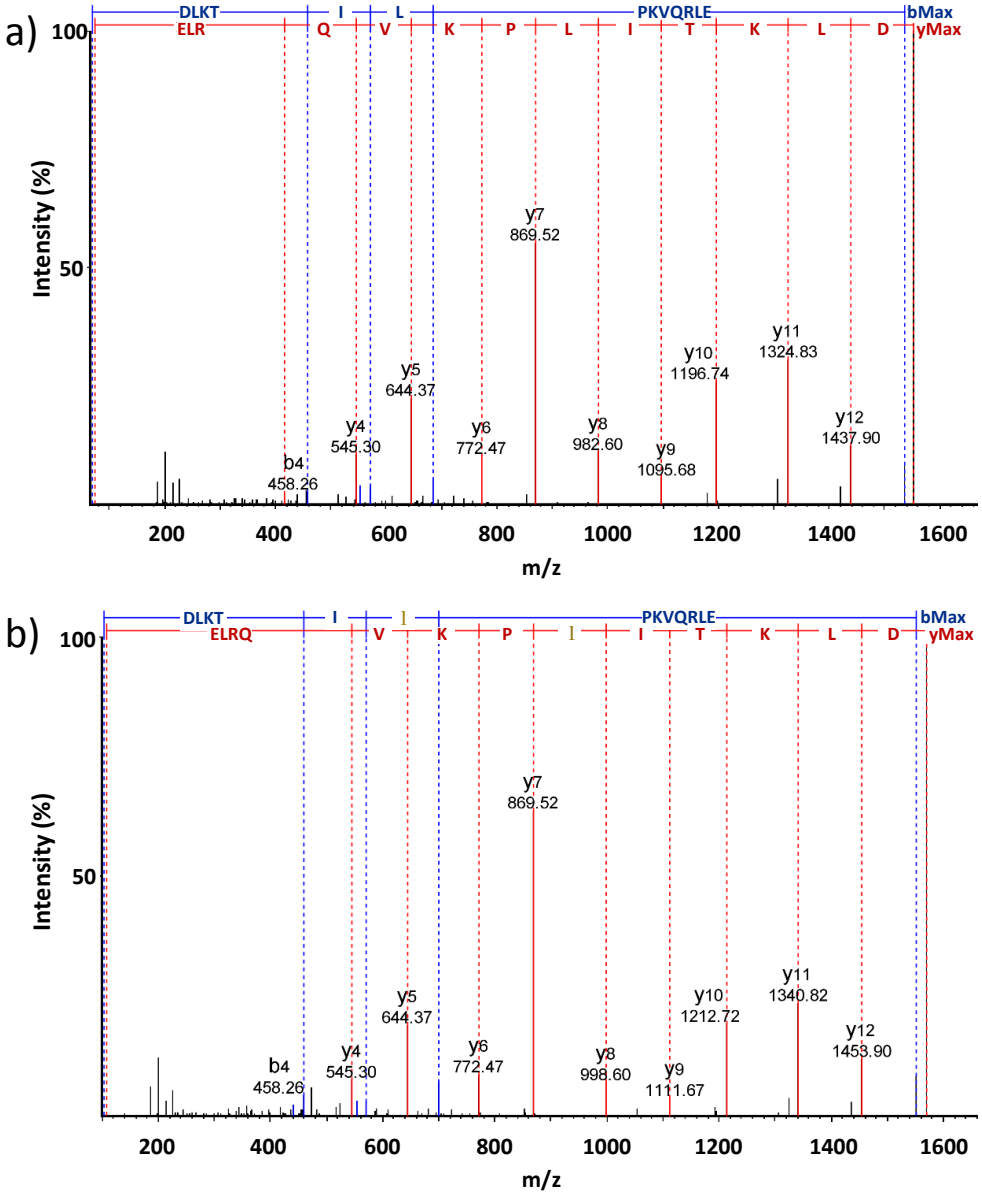

Figure 2.6: Example of MS/MS identification of a peptide residues 362 - 374 (sequence: DLKTILPKVQRLE). (**a**) Native peptide (1552.94 Da) was detected at 13.88 min retention time. (**b**) XF labelled peptide (1568.93 Da) bearing a +16 Da modification on L367 eluted at 11.40 min. Y-series ions (originate as MS/MS fragmentation of peptide's C-terminus) are shown in red and b-series ions (originate as MS/MS fragmentation of peptide's N-terminus) in blue. The location of XFMS modification is identified by observing +16 Da mass shift on peptides containing the L367 (*i.e.*, y8 - yMax in y-series ions and b5, b6, bMax in b-series ions).

Figure 2.6 shows an example of a MS/MS identification of a native (a) and modified (b) version of

the peptide from Figure 2.5. MS/MS fragmentation generates a nested set of peptide ions termed Y- and b- series ions. Y-series ions originate from MS/MS fragmentation of peptide's N-terminus (*i.e.*, appear to extend from the C-terminus), while b-series ions originate as MS/MS fragmentation of peptide's C-terminus. The location of XFMS modification is identified by observing +16 Da mass shift on peptides containing the L367 (labelled in small caps and gold in Figure 2.6b). Thus Y-series ions from y8 to Max and b5, b6, bMax of b-series ions are 16 Da heavier and appear right-shifted compared to the 'native' peptide (Figure 2.6a).

The modified fraction for each peptide (and residue, where the identification of the modified residues was possible) was calculated as described in [132]. In short, the ratio was calculated of the peak area corresponding to the modified peptide residue (or combined modification of a peptide) to the collective area of native and modified peptides, *i.e.*,

$$Fr.\,modified = \frac{\sum modified_{Peak}}{native + \sum modified_{All\ peaks}}.$$

Then a site-specific modification rate constant (k s^{-1}) was calculated by first calculating fraction of native site (*i.e.*, peptide or residue-level) as follows:

$$Fr.\,unmodified_{site} = 1 - Fr.\,modified.$$

This was then plotted over the duration of radiolysis to obtain a dose-response plot and rate constants (k^{-1}) of residue modification by a pseudo-first-order fit. [132] (Examples are shown in Figure 2.7). The extent of the residue modification depends on the specific residue reactivity and the local environment of the residue (*e.g.*, solvent accessibility) [132, 133]. To simplify analysis the changes in solvent accessibility (and hydroxyl-reactivity) of specific residues were estimated by calculating R, the ratio of the k^{-1} of free MtrC vs the k^{-1} of MtrC bound to a-TiO_2. Thus, in the case of modified residues reported in Figure 2.7, M74 (Figure 2.7a) is relatively unprotected by a-TiO_2 (R=2.4±1.0), while residues L367, I366+P368 and K364+P368 are shielded by a-TiO_2 (R=8.9±2.4, 6.6±1.3 and 11.0±4.1, respectively).

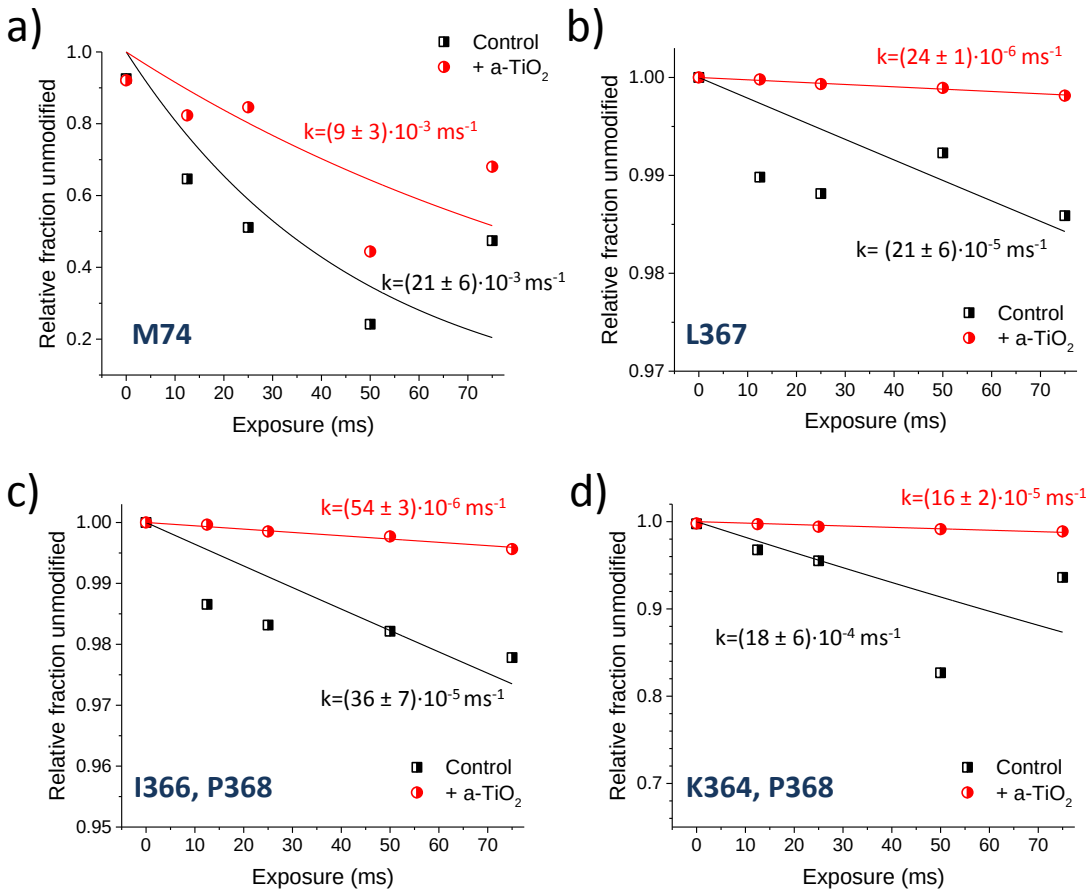

Figure 2.7: Examples of changes in hydroxyl-radical reactivity for selected MtrC residues: M74 (**a**), L367 (**b**), I366 with P368 (**c**), and K364 with P368 (**d**) with and without a-TiO_2 (red and black, respectively). Lines indicate a fit of a first order exponential ($y = A \cdot e^{-kt}$) used to determine the rate constants (k) of residue modification by hydroxyl-radicals. Error represents the standard error from the fit.

2.5 Reduction of RR120 encapsulated in MtrCAB proteoliposomes (Chapter 4)

Samples for photo-reduction experiments were assembled in nitrogen atmosphere (glovebox, LABmaster, MBrown, O_2 <0.01 ppm) to ensure anaerobic environment. MtrCAB proteoliposome sample (section 2.2.1) was diluted 10-fold in 20 mM MOPS, 30 mM Na_2SO_4, pH 7.4 buffer containing 50 mM sacrificial electron donor (EDTA). Appropriate amount of LHNP stock (27 μM **RuP**-TiO_2, 476 μM *g*-N-CD or 44 μM *a*-CD; mass of particles is estimated based on size determined by EM and density of material) was added to 1 μmol LHNP/L final concentration.

The cuvette was then sealed airtight and removed from the glovebox for UV-vis absorbance spectroscopy (Cary 5000 UV-Vis-NIR, Agilent) fitted with an integrating sphere (Internal DRA-900, Agilent). UV-vis absorbance spectra were measured after 10 sec, 50 sec, 60 sec, 120 sec or in some cases 300 sec of sample illumination using a cold light source holding a 150 W, 4.5 cm (15 V) halogen lamp (OSRAM) with a fibre optic arm (Krüss KL5125). The sample was placed 10 cm from the light source and illuminated from the side. The light intensity under these conditions is approximately (450 ± 40) mW/cm^2 at 400 nm. Afterwards, the chemical reductant DT was added (final concentration 27 mM) to monitor further possible reduction of RR120. Finally, Triton X100 detergent was added (final concentration 0.045% v/v) to break the lipid vesicles and observe reduction of any remaining RR120. Control experiments testing reduction by DT (*i.e.*, without LHNPs) were also performed. Photo-reduction control experiments with non-encapsulated RR120 were performed as above, but with 10 μM RR120, 50 mM EDTA and 1 μmol NP/L LHNPs in MOPS buffer. The recovery yield of MtrCAB was observed to vary between proteoliposome preparations. To account for this, comparisons of encapsulated RR120 (photo)reduction by DT and LHNPs were made with proteoliposomes from the same preparation.

2.5.1 Treatment of UV-visible spectroscopy data

Spectroscopy data were corrected for sample dilution and for variations in background absorbance (by setting absorbance at 750 nm as the zero for each spectrum). The changes in RR120 absorbance over time were monitored using absorbance at 539 nm, because it is less influenced by the absorbance of reduced MtrCAB (α- and β- haem peaks at 552 and 522 nm).

In order to correct for the contribution of light scattering by (proteo)liposomes, the sample absorbance was measured outside the RR120 absorbance peaks (*i.e.*, 440 nm and 610 nm) and used to estimate the optical density by comparing absorbance of intact and lysed (*i.e.*, after addition of TX) liposomes. *I.e.*, *Scattering*$_{440}$ = $A440_{finalDTspectrum} - A440_{finalDTandTXspectrum}$, and *Scattering*$_{610}$ = $A610_{finalDTspectrum} - A610_{finalDTandTXspectrum}$. The scattering contribution at 539 nm was then estimated as an average of scattering at 440 and 610 nm. This estimate of light scattering was then subtracted from all absorbance values at 539 nm values arising from liposome photo-reduction and DT reduction. Relative absorbance values were calculated setting sample absorbance at 0 minute as 100%.

2.5.2 Observations of haem reduction state from the UV-visible spectroscopy data

The absorbance spectrum of MtrCAB contains a heme Soret (γ) absorption peak centered at 410 nm, a visible-region peak at 531 nm and a shoulder at 560 nm. Upon haem reduction the Soret (γ) peak shifts to ≈420 nm and two smaller α and β peaks can be distinguished at around 552 and 523 nm. [118] An example of MtrCAB absorbance spectrum is shown in Figure 2.8**a**.

Unfortunately, the other compounds (*e.g.* LHNPs, liposomes) present in MtrCAB proteoliposome samples used for photoreduction experiments hinder the observation of haem absorbance. In order to better observe the change in MtrCAB haem oxidation, a 1^{st} derivative (*i.e.*, A') was calculated for each spectrum. This allowed to observe presence of inversed peak ('dip') of oxidised haems at ≈ 416 nm, which gets shifted to ≈ 426 nm upon haem reduction. Figure 2.8**b** shows the A' for purified MtrCAB. The haem reduction was assessed then by calculating the difference in A' between the selected wavelengths (*i.e.*, ΔA' = A'418 - A'426)). In the case shown in figure 2.8**b** ΔA' is -0.0035 and 0.02 for oxidised and reduced MtrCAB, respectively. The peak maximum (and minimum) was determined for each condition containing different LHNP and MtrCAB proteoliposome sample as shown in Figure 2.8**c,d** for *g*-N-CDs and **RuP**-TiO_2. The calculated ΔA was then plotted over time, to show better the change from oxidised to reduced MtrCAB haems.

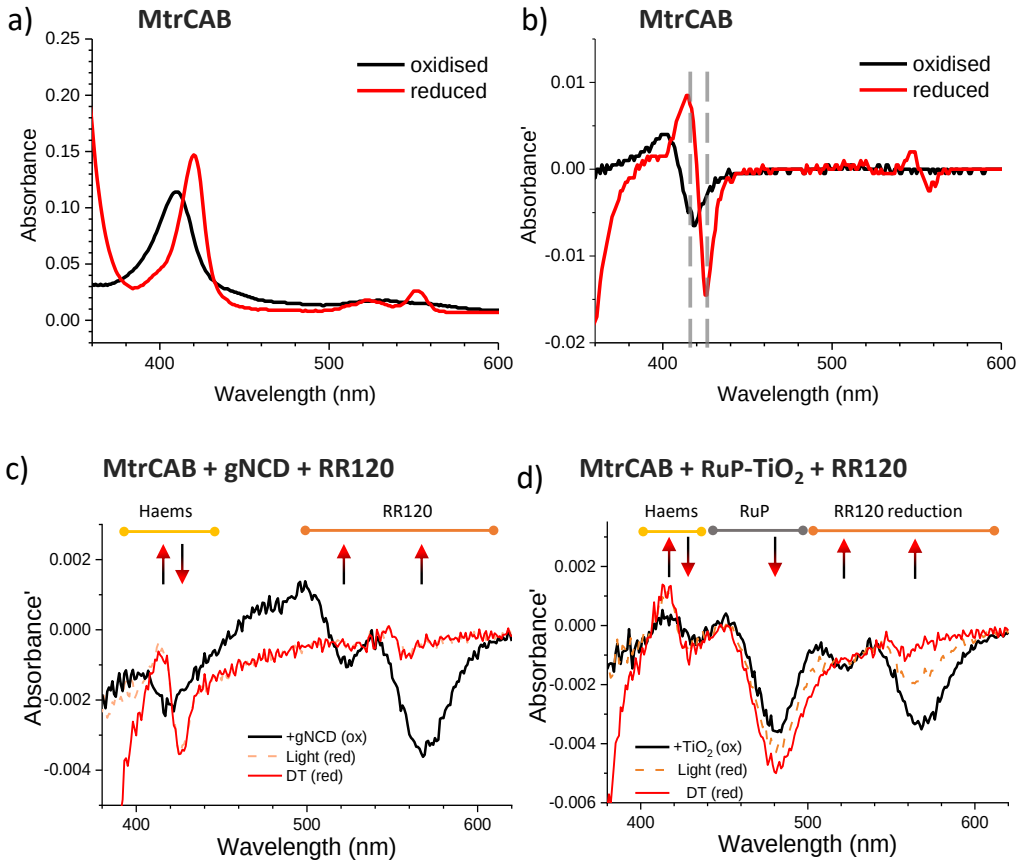

Figure 2.8: Observing reduction of MtrCAB haems using UV-vis spectroscopy. (**a**) Absorbance spectrum of MtrCAB under oxidising aerobic conditions (black) and reduced by dithionite (red). (**b**) The 1st derivative of MtrCAB absorbance (A'). Black – oxidised MtrCAB, Red – MtrCAB reduced by dithionite. Dashed lines indicate wavelengths selected to assess haem reductionby calculating the difference between them (*i.e.*, ΔA' = A'418 - A'426)). In this case ΔA' is -0.0035 and 0.02 for oxidised and reduced MtrCAB, respectively.(**c**) Example of the 1st derivative taken of the absorbance spectra (A') from *g*-N-CDs photoreduction of MtrCAB proteoliposomes containing RR120. Oxidised and reduced haems have different signatures, and the haem reduction is estimated by calculating the A' difference at the wavelengths corresponding the oxidised and reduced haem minima (416 nm and 426 nm, respectively). At the start of the experiment MtrCAB is oxidised (dark red line) and gets reduced during illumination (dashed line); Red line – reduced sample after addition of DT. DT – dithionite is included as indicator of fully reduced haems. (**d**) Example of the 1st derivative taken of the absorbance spectra from **RuP**-TiO_2 photoreduction of MtrCAB proteoliposomes containing RR120. Although **RuP** absorbance partially masks the signal of oxidised and reduced haems, the haem reduction was still estimated by calculating the A' difference at 416 nm and 426 nm. Coloured line segments indicate spectral areas and the main chromophores responsible for the signal.

2.6 H_2 detection (Chapter 5)

2.6.1 Clark electrode setup and calibration

The hydrogen evolution was assessed by constant potential chronoamperometry (set potential 0.6 V vs Ag/AgCl, current sampled every second) using a Clark type electrode disc (Hansatech) adapted for H_2 measurements [138, 139]. The electrode system consisted of a Pt anode (2 mm in diameter) and a concentric silver reference cathode connected via a thin layer of saturated KCl electrolyte solution (Figure 2.9). The electrode system was enclosed and separated from the reaction chamber with a polytetrafluoroethylene (PTFE) membrane (0.0125 mm x 25 mm x ≈ 2 cm, Hansatech) held in place by an O-ring (Figure 2.9). The potential was regulated by a potentiostat (PGSTAT30, Metrohm Autolab) controlled by Nova software (Metrohm Autolab). The experiments were performed anaerobically placing the Clark type electrode in a Faraday cage within the glovebox (LABmaster sp, MBraun, N_2 atmosphere, <0.1 ppm of O_2).

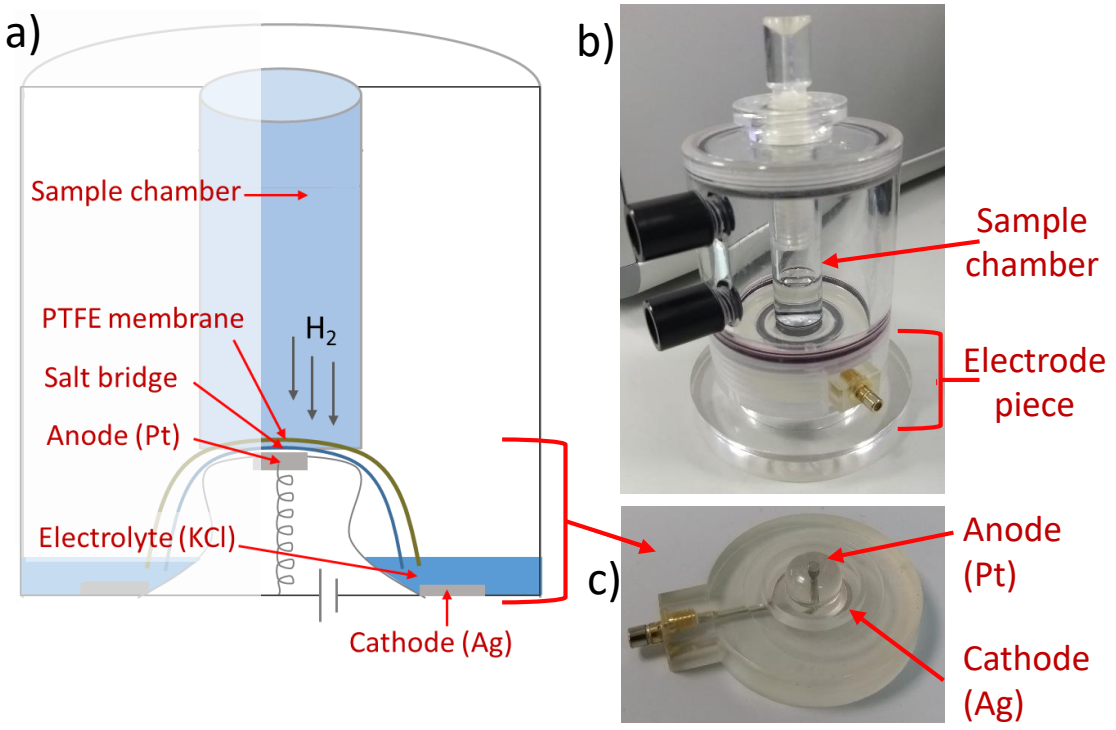

Figure 2.9: The Clark electrode. a) A schematic of the Clark electrode used for H_2 detection. **b)** An image of the fully assembled system, where the electrode piece is fitted and sealed with O rings below the reaction chamber. **c)** The electrode piece consists of a dome containing Pt anode, surrounded by an Ag/AgCl counter electrode.

In this system, H_2 as a non-ionized small molecule penetrates the PTFE membrane and is oxidised

at the Pt anode. [140] The measured current is directly proportional to the concentration of dissolved H_2 and is limited to the rate of mass transport across the PTFE membrane, which in turn is dependent on the H_2 concentration in the sample chamber. [139, 140] Fresh PTFE membrane was fitted daily and the Clark electrode was calibrated before each experiment using 5%-95% H_2 - N_2 gas (BOC). The electrode calibration was performed by polarising the electrode at 0.6 V vs Ag/AgCl for ≈10 minutes. Then 5% H_2 calibration gas was flushed through the sample using mass flow controllers (Sierra Instruments, accuracy ± 1%; typical flow rate 10 ml per minute) till signal started to saturate. For practical considerations the duration of calibration was limited to ≈ 10 - 20 min. The final measured value was considered to represent the sample saturated with 5% H_2 gas. Finally, H_2 was removed by flushing the sample with 100% N_2 gas (BOC) using mass flow controllers as before. A standard calibration curve is shown in Figure 2.10.

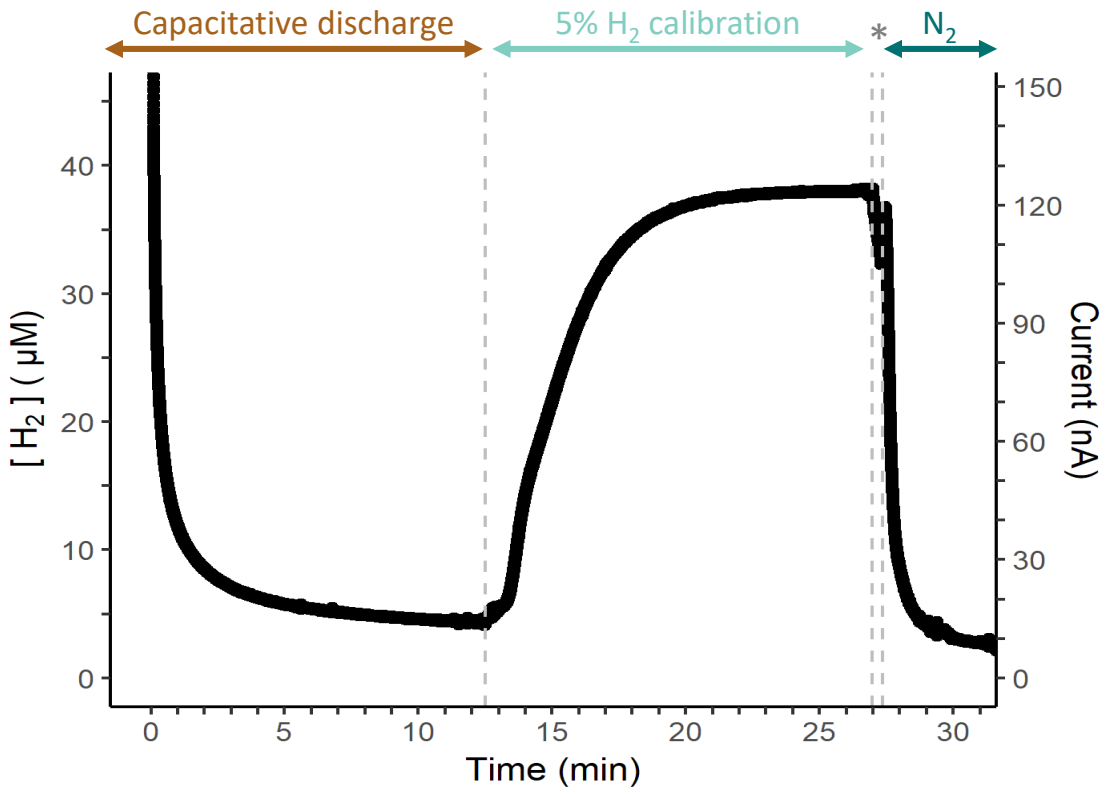

Figure 2.10: Calibration of the Clark electrode. First electrode is polarised for ≈10 min, then the reaction chamber is flushed with 5% H_2 calibration gas, followed by H_2 removal by flushing the sample with 100% N_2 gas. The asterisk ($\star$) indicates time period switching from H_2 to N_2 flush, when H_2 stream was stopped, but N_2 had not been started yet. The measured electrochemical current (scale on right) is converted into H_2 concentration (scale on left) by approximating the final calibration signal to represent the sample saturated with 5% H_2 gas (*i.e.*, 38μM).

The H_2 concentration of the sample saturated with 5% H_2 was calculated using the Henry's Law constant $H^{cp} = 7.9 * 10^{-6}[\frac{mol}{m^3 * Pa}] = 7.9 * 10^{-4}[\frac{mol}{L * atm}]$. [141] H^{cp} was used for Henry's volatility K_H^{pc} defined as

$$K_H^{pc} = \frac{p}{c_a} = \frac{1}{H^{cp}},$$

where p is the partial pressure of H_2 in the gas phase and C_a is the concentration of H_2 in the aqueous phase. [142] Thus the concentration of solution saturated with 5% H_2 is:

$$c_a = \frac{p}{K_H^{pc}} = \frac{0.05\,atm}{1300\,\frac{atm*L}{mol}} = 3.8 * 10^{-5} M \approx 38\,\mu M.$$

This value was then used to convert the measured current into H_2 concentration.

2.6.2 Chronoamperometry experiments

A typical experiment involved: Clark electrode calibration as described above, injection of a catalyst containing solution (*e.g.*, Pt NPs, Pt-Silica NPs, HydA1, liposomes) and injection of an electron donor (typically 20 μL 0.57 M DT or *g*-N-CD as photosensitiser, followed by, for example, addition of an electron mediator (methyl viologen, MV), a detergent to break lipid bilayer (*e.g.*, 1% v/v TX) or 50 μl 0.5 M OG or a sacrificial electron donor (50 mM EDTA) and sample illumination. For the experiments assessing photocatalytic hydrogen evolution reaction (HER), samples were illuminated using the same cold light source as for RR120 reduction experiments in section 2.5. The light source contains a flexible fibre optic light conductor arm, which was introduced within the Faraday cage and used to illuminate the sample sideways from about 10 cm distance. Given the high variability of experimental conditions tested, the precise details are given in the figure legend of each reported experiment.

2.6.3 Chronoamperometry data analysis

The measured current data was processed post-experiment to normalise it against changes in sample volume (*i.e.*, current was multiplied with sample volume in ml). In addition, data corresponding to the time of chemical addition (up to 30 sec before and 60 sec after) has been deleted to remove noise (spikes in current) caused by increased sample mixing. The catalytic activity of the detected H_2 evolution was assessed by fitting a line to the initial increase in signal. The range for the linear fit was judged manually, to identify the longest available linear range of the signal and limit such influences as current changes due to sample mixing or signal saturation. In some cases, signal saturated so quickly that it was not possible to identify a reliable linear activity. In these cases, data was used only for qualitative observation of H_2 evolution activity.

2.7 Trapping Pt_{syn} NPs into porous silica nanoparticles (Chapter 5)

2.7.1 Trapping Pt nanoparticles into preformed commercial $meSiO_2$ NPs

10 mg/ml $meSiO_2$ stock solution in water was sonicated, centrifuged and resuspended to 80 mg/ml. 265 μl of Pt_{syn} nanoparticle solution was added to 50 μL of the 80 mg/ml $meSiO_2$. Samples was diluted to 500 μl in MOPS buffer (20 mM MOPS, 30 mM Na_2SO_4, pH 7.4) containing 2 mM MV. Pt_{syn} and $meSiO_2$ solution was incubated on a rolling shaker overnight (4°C). Samples were then bath sonicated (Fisher Scientific) for 30 min and kept on rolling shaker till use.

2.7.2 Loading Pt nanoparticles while synthesizing $gSiO_2$ NPs

Pt loaded bio-inspired "green" SiO_2 ($gSiO_2$) NPs were synthesized with simultaneous loading of Pt_{syn} nanoparticles in collaboration with Prof. Siddharth Patwardhan from the University of Sheffield. [143] In short, 310 μL 94 mM pentaethylenehexamine (PEHA) solution was mixed with 310 μL of 0.95 M sodium metasilicate (Na_2OSiO_2) and Pt_{syn} NPs (estimated concentration 0.6 mg/ml). Particles were formed after lowering the pH by adding 380 μL of 1 M HCl. Reaction was carried out for 10 minutes. Particles were then washed by two cycles of sample centrifugation (8000 g, 1min) followed by the pellet re-suspension in 2 ml of 1 M HCl to remove PEHA. Finally, the particles were pelleted and the pellet was dried in oven (+ 40°C) overnight.

2.7.3 Forming supported lipid bilayer on SiO_2 NPs

Lipid mixtures were mixed by dissolving and mixing lipids in chloroform, drying under a stream of nitrogen and vacuum (for ≈2 hours) and finally storing dry aliquots in nitrogen atmosphere as described in section 2.1. The lipid mixtures contained: fluorescently labelled lipids (*e.g.*, 1% wt/wt DGPE-CF or 0.4% Texas Red - DHPE) mixed with POPC, *E. coli* polar lipids, 2:1 *E. coli* polar lipids : POPC and 5:3:1:1 *E. coli* polar lipids : POPC : POPG : POPE. Lipids were used to form liposomes by rehydration by adding MOPS buffer (20 mM MOPS, 30 mM Na_2SO_4, pH 7.4) at a typical concentration of 5 mg/mL. The lipid suspension was then extruded through a Mini-Extruder (Avanti Polar Lipids), passing through a polycarbonate track-etched membrane (pore

sizes 100 or 200 nm, Whatman) 11 times. 100 nm membrane was used for POPC, and 200 nm for all experiments involving or comparing with lipid mixtures containing *E. coli* polar lipid extract.

Testing different lipid mixtures for forming supported lipid bilayer on meSiO$_2$

Liposomes containing 1% wt/wt DGPE-CF combined with POPC, *E. coli* polar lipids, 2:1 *E. coli* polar lipids : POPC or 5:3:1:1 *E. coli* polar lipids : POPC : POPG : POPE were mixed with meSiO$_2$ at a 12% wt/wt ratio of lipid bilayer to meSiO$_2$. The lipid bilayer was then formed on silica particles after protocol described in [144]. The lipid-silica sample was vigorously vortexed for 2 min, followed by incubation on a rolling shaker for 1 h at 4°C. The nanoparticles were collected by centrifugation (17 000 g, 1 min, 4°C). These were then re-suspended in buffer and again subjected to another round of vigorous vortexing and incubation on rolling shaker for 1 h at 4°C. Sample was then diluted 10x and transfered to a black 96-well plate (polystyrene, flat-bottom μCLEAR®, Greiner Bio-One). The DGPE-CF fluorescence was measured using plate reader (Hidex Chameleon, Driver Version: 4.48) by exciting fluorophore at 485 nm and reading emission at 535 nm.

Forming supported lipid bilayer on Pt-loaded meSiO$_2$ NPs

Pt$_{syn}$ was trapped in meSiO$_2$ as described in section 2.7.1. The resulting sample was mixed with 1 : 2 *E.coli* : POPC liposomes at a 17% wt/wt ratio of lipids to meSiO$_2$ in the final volume of 130 μl MOPS buffer with 0.2 mM MV. The supported lipid bilayer was formed as described in [144] and section 2.7.3. Prepared samples were tested for hydrogen production using Clark electrode and the set-up described in section 2.6.

Forming supported lipid bilayer on gSiO$_2$ NPs

Silica and silica/Pt NPs were suspended in the MOPS buffer and sonicated in bath sonicator for about 30 - 40 minutes. Then liposomes consisting of POPC-1% DGPE-CF or POPC-0.4% DHPE-Texas Red in MOPS buffer (20 mM MOPS, 30 mM Na_2SO_4, pH 7.4) were mixed with silica particles at lipid:silica ratios ranging from 0 to 2 wt/wt. Samples were then sonicated at room temperature in bath sonicator for about 10 minutes. Then samples were washed to remove free liposomes by two cycles of sample centrifugation at 8000 g (18°C for 1 minute), removal of the supernatant and re-suspention of the pellet in water. The fluorescence of lipids associated

with $gSiO_2$ and free liposomes was determined using black 96-well plate (polystyrene, flat-bottom μCLEAR®, Greiner Bio-One) and a fluorescence microplate reader (Fluorostar optima or VarioskanFlash) with excitation : emission at 485 : 517 nm for DOPE-CF labelled lipids and 595 : 615 nm for DHPE-Texas Red labelled lipids. Prepared samples were tested for hydrogen production using Clark electrode and the set-up described in section 2.6.

Chapter 3

Interfacing inorganic nanoparticles with conductive MtrC

3.1 Introduction

A key process for light-harvesting is electron transfer (ET) from one molecule to another. This depends on multitude of parameters ranging from thermodynamic properties of electron donating and accepting molecules, environmental conditions (*e.g.*, temperature, pH) and the geometry of the ET interface. [57, 145] One of the key ET interfaces for the liposomal light-harvesting compartment introduced in Chapter 1 is between the LHNP and MtrCAB. This chapter aims to map the molecular interface between TiO_2 (common material used for light-harvesting in solar cells and solar fuel cells) and the decahaem cytochrome MtrC, which forms the soluble part of the MtrCAB conduit. This allows to identify the protein residues interacting with TiO_2 at one terminus of the MtrCAB conduit in the absence of other interfering compounds such as detergent or liposomes, which are needed to stabilise the membrane region of MtrCAB. Previous research has indicated binding interaction between MtrC and TiO_2 NPs [146], but not much is known about the binding interface. Identification of the protein residues at this binding interface will provide basis for better understanding of the molecular interactions and forces between TiO_2 particles and MtrC. This can then pave ways to improve ET by directed site-specific protein and nanoparticle engineering.

The chapter starts with a brief introduction in the current understanding of binding interactions between MtrC(AB) and metal oxides (section 3.1.1), the binding interactions between TiO_2 and peptides (section 3.1.2) and the main methods used to probe interactions between biological

and inorganic materials (section 3.1.3) and reasoning why an experimental technique termed 'protein footprinting' was chosen to map the molecular interface between TiO_2 and MtrC. This is section follows with an introduction to the method (XFMS, X-ray footprinting Mass Spectrometry) chosen for this study. Section 3.2 describes the considerations and experiments made for sample optimization. The chapter then continues with the experimental results and a discussion.

3.1.1 Binding of MtrC to metal oxides

As described in Chapter 1, MtrCAB is a conductive, transmembrane protein complex isolated from the bacterium *Shewanella oneidensis*. [90] The biological function of outer membrane protein complexes such as MtrCAB is to support the anaerobic growth of the bacterium by shuttling electrons out of the cell to extracellular electron acceptors, for example, insoluble iron and manganese minerals, *e.g.*, hematite (α-Fe_2O_3), goethite (α-FeO(OH)), lepidocrite (γ-FeO(OH)) *etc*. [90–92]. The final stages of ET to these minerals is supported by MtrC and the closely related proteins MtrF and OmcA either by direct contact with the mineral or indirectly using soluble electron mediators as flavins. [90] Figure 3.1 shows the structure of MtrC and the putative location of MtrC within MtrCAB complex. Observations indicating active localisation of *S. oneidensis* proteins (including MtrC and OmcA) at the mineral interface, suggest that MtrC is evolved to specifically bind and exchange electrons with such metal oxides as iron minerals. [147]

Several studies have attempted to characterize *in vitro* the interaction between hematite and all three closely related protein homologs: MtrC, OmcA and MtrF. [134, 147, 149] These studies report of a stable and specific interaction between hematite and all three extracellular cytochromes. [134,147,149] The redox state of the protein as well as the binding interaction can induce structural rearrangements of OmcA and MtrC. [147,149,150] In addition, hematite binding to MtrC changes between purified MtrC and MtrC *in vivo*. Thus, the binding affinity of MtrC *in vivo* was influenced by both the redox state and the concentration of hematite particles, whereas purified MtrC showed a constant binding affinity. [150] As for the location of hematite binding, MtrC and OmcA contain a proposed hematite binding amino acid sequence (Ser/Thr-Pro-Ser/Thr) near their haem 10 (C-terminus). [151] Such sequence, however is absent from MtrF, and the specific MtrF- hematite binding has been attributed to complementary electrostatic interactions with protein region near haems 6 and 7. [134] In this case, no large conformational changes were observed upon hematite binding. [134]

As MtrC and OmcA have also been identified as involved in reduction of other metal ions such as Mn(IV) and V(V) [152–154], it is possible that these proteins are adapted to accommodate a broad

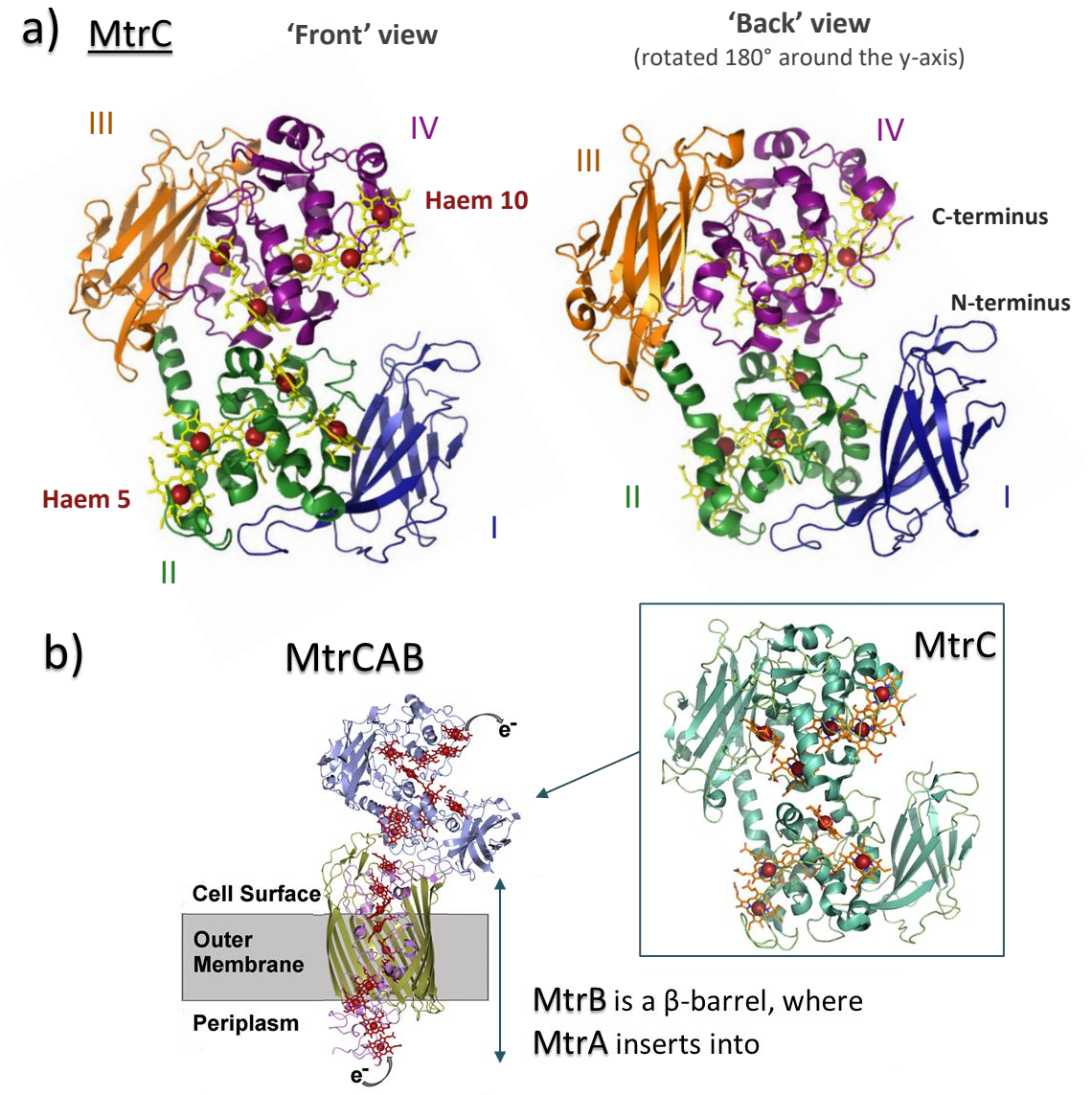

Figure 3.1: The structure of MtrC, which forms a soluble, conductive part of the MtrCAB conduit. (**a**) A cartoon representation of MtrC structure (PDB ID: 4LM8 [148]). The 10 haems are identified as yellow sticks, where the central iron atoms are shown as red spheres. In this representation 4 protein regions (domains) are distinguished as primarily forming β-strands or haem-containing α-helices. These are numbered and colour-coded according to their position within the primary protein sequence, where blue corresponds to residues 44 to 175, green - from 176 to 331, orange - from 332 to 485 and purple - from 486 to 669. The beginning (first 43 residues) and end of the protein are absent from the published crystal structure. (**b**) Structure of a full MtrCAB complex from a closely related bacterium species *Shewanella baltica* OS185 [94]. as published in [94] and an insert showing the structure of MtrC (PDB ID: 4LM8). Figure modified after [94].

range of metal oxide materials. Thus it could be possible to interface these proteins to a range of natural and engineered metal oxide surfaces. For example, light-active dye-sensitised TiO_2 nanoparticles (**RuP**-TiO_2) have been reported to bind OmcA and MtrC immobilised on a template stripped gold electrode modified with a self-assembled monolayer, made up of various mixtures of alkanethiols. [63, 146] The binding was estimated to occur at 1:1 ratio between the TiO_2 NP and MtrC. [63] In addition, these observations were accompanied with a decrease in electroactive coverage of MtrC, which has been attributed to changes in the mobility and/or orientation of MtrC. [63, 146] The binding of TiO_2 NP to immobilised monolayer of MtrC varied also among different nanoparticles. Thus amino-capped TiO_2 NP showed less binding compared to the ones capped with carboxyl- groups (*i.e.*, DHBA), whereas no binding was observed for the two commercial TiO_2 NPs. [146]

To summarize, MtrC seems to be able to bind several different metal oxides; but many questions remain about the binding interactions and surface parameters, as well as the changes in MtrC conformation and activity. The work described in this chapter aims to identify MtrC residues involved in the binding interface with a commercial TiO_2 NP and discuss any insights these could provide about the forces governing the interface.

3.1.2 Binding of TiO_2 to biological molecules.

TiO_2 is found in several natural minerals, including rutile, anatase and brookite. [155] Numerous experimental and theoretical molecular dynamics studies have been reported for interactions between TiO_2 surface and various small (bio)molecules. [155] These indicate that the nature of bio-molecular interactions with TiO_2 surface is primarily electrostatic. The surface of bare TiO_2 normally reacts with water molecules, which results in surface hydroxylation, typically ranging from 0.3 to 10 OH/nm^2. [155] This surface hydroxylation then leads to hydrogen bonding with water molecules and formation of an ordered water interface. [155]

Different types of surface hydroxyl groups are present on TiO_2 surface (*e.g.*, basic and acidic, bridged and terminal OH groups), which determine the electrostatic interactions and adsorption of amino acids. [155] Thus, charged amino acids (*i.e.*, Arg/R, Lys/K, Glu/E, Asp/D) show the highest affinity, followed by polar amino acids (*i.e.*, Ser/S, Thr/T, Asn/N, Gln/Q, Tyr/Y), while hydrophobic amino acids (*i.e.*, Val/V, Leu/L, Ile/I, Phe/F) show limited or zero affinity. [155] Charged and polar amino acids are also present within TiO_2 binding peptides identified via phage-display (*e.g.*, RKLPDA, FATDSLIK, GHTHYHAVRTQT, CHKKPSKSC). [155, 156] In addition, peptides utilised for TiO_2 precipitation and engineering of cell interactions with TiO_2 surface

(*e.g.*, RGD and $(RKK)_4D_8$) also contain primarily charged amino acids. [155] The importance of the charge of the amino acids, was tested in a point mutation study of the TiO_2 binding peptide CHKKPSKSC. [156] In this study, each individual amino acid residue was probed and replaced by K, A or R. [156] Interestingly, the three lysines were essential for binding to TiO_2, but additional lysines actually lowered the binding affinity. Further theoretical exploration suggested that the binding affinity is determined not only by the electrostatic interaction of the three Lys residues, but also by the context of other surrounding amino acids, which can reduce the peptide's conformational flexibility and thus promote favourable binding interactions. [156]

Although several studies have explored TiO_2 binding to small peptides, very little is known about TiO_2 binding interactions and interface with larger protein molecules. [155] Proteins contain a range of different exposed amino acid residues, which can change with changes in protein conformations. Furthermore, the surrounding environment (*e.g.*, water and buffer molecules) could also play role to modulate the binding affinity. [155] The answering of these questions starts with understanding the interface between TiO_2 and different proteins. Thus the aim of this chapter - determining the molecular interface between TiO_2 and MtrC- is a step towards building a dataset for further exploration of forces and interactions within this bio-inorganic interface.

3.1.3 Structural studies of protein-NP interaction

Several techniques can be used to study protein interaction with inorganic nanoparticles. These include absorbance and fluorescence spectroscopy, circular dichroism, dynamic light scattering, surface plasmon resonance, TEM, chromatography, electrophoresis, isothermal titration calorimetry, infrared spectroscopy, nuclear magnetic resonance (NMR), small angle X-ray scattering, mass spectrometry (MS) based proteomics, as well atomic force microscopy (AFM) and theoretical studies *in silico*. [147, 157, 158] Most of these techniques provide an insight in the general characteristics of the binding event, but the structural resolution of the molecular interface often is limited. For example, protein monolayers have been probed with metal modified AFM-tips. [147] This allowed to estimate that the binding strength of OmcA-hematite was about twice that of the MtrC-hematite bond and is strongly correlated to hematite binding with the whole bacterial cell. Other techniques must be used to gain further molecular and structural information about the binding interface. For example, information about broad changes in protein secondary structure can be gained through circular dichroism spectroscopy [150,157,158], whereas monitoring of finer structural details at the binding interface can be gained with NMR (typically limited to small proteins, <35 kDa in size) and various MS based proteomics

approaches. [129, 157]

The aim to locate TiO_2 binding interface on the MtrC requires the of use techniques providing high structural resolution. As MtrC is too big for standard NMR studies, proteomics approach termed protein footprinting was used. Protein footprinting is a strategy where a change in the solvent accessibility of protein backbone and residues (*e.g.*, due to ligand or NP binding) is monitored through their sensitivity to a chemical modification or backbone cleavage. As the result, solvent exposed protein areas become modified and chemically different from the native protein, and the imprint (or footprint) of these modifications can then be analysed using mass spectrometry (MS). [129] Different types of labelling can be used for protein footprinting, such as protease-cleavage of exposed protein backbone, deuterium exchange of amide protons in the protein backbone (hydrogen deuterium exchange, HDX), isotope-coded affinity tags to sample accessibility of specific amino acids (*e.g.*, cysteine) as well as the use of oxidative hydroxyl radicals ($^{\bullet}$OH) to label solvent exposed amino acid side-chains. [129–131] Each of these have their own advantages and disadvantages. For example, proteases can be used in wide-range of sample conditions, but often are specific to certain residues and are limited to protein areas that are sterically exposed and accessible to a large enzyme. [129, 134] HDX assesses non-specific protein backbone accessibility to solvent, but the nature of deuterium labelling is reversible, which constrains options for further sample processing and handling. [129, 130, 132] The resolution of isotope-coded affinity tags to sample accessibility of specific amino acids (*e.g.*, cysteine) are limited to the presence of these specific amino acids. [129] In this study $^{\bullet}$OH labelling was used, as it provides fast, permanent and non-specific modification (*i.e.*, all exposed residues can potentially be modified), which allows greater flexibility in subsequent sample processing and use of different proteases. [129, 132]

There are several methods to produce $^{\bullet}$OH in solution for oxidative footprinting. These include methods involving specialised facilities, for example, electron pulse radiolysis, where electron pulses are accelerated by a linear accelerator (LINAC) to megaelectronvolt scale and are able to ionize water. [129] Similar process is synchrotron radiation footprinting, where radiolysis of water is achieved using photons in the kilovolt X-ray range (x-ray footprinting, XF). [129] Other reported strategies for $^{\bullet}$OH generation that involve facilities with easier access, are UV-light laser photolysis of hydrogen peroxide (fast photochemical oxidation of proteins, FPOP), use of chemical oxidants (*e.g.*, Fenton-like reactions, tethered metal chelates, peroxynitrite) or high voltage electrical discharge, which takes advantage of electrospray ion source used in mass spectrometry. [129]

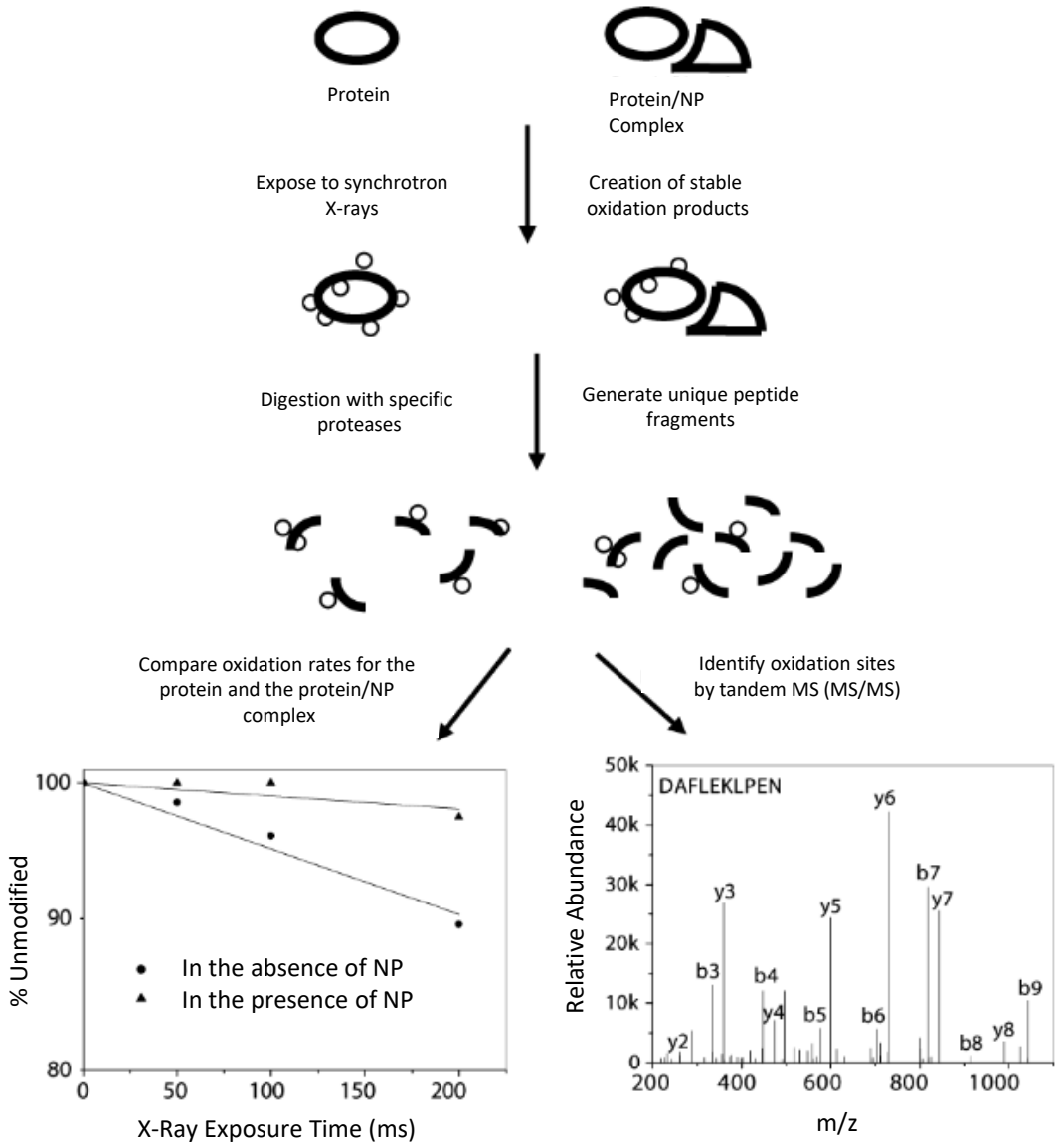

Figure 3.2: Schematic representation of $^{\bullet}$OH footprinting. A protein and its complex with a nanoparticle are exposed to hydroxyl radical source (*e.g.*, synchrotron beam radiolysis). These $^{\bullet}$OH radicals modify the side chains of the protein. Afterwards, the protein samples are digested with proteases creating a pool of different peptides with and without modifications. MS is then used to quantify the extent of modification through measuring the amount of modified and unmodified peptides. This step allows to observe the solvent accessibility of each peptide in both the isolated and complexed states. The exact modification sites are identified by tandem MS (MS/MS). The dose-response example shows a slower rate of modification for the peptide in the presence of NP compared to the condition of peptide in the absence of NP. This indicates that this peptide contains reactive side chain residues, which have been shielded by the binding process. Figure reproduced and modified after [129].

X-ray Footprinting - Mass Spectrometry (XFMS) analysis

The work described in this chapter uses XF and was performed in consultation with Dr Caroline Ajo-Franklin (Molecular Foundry), Dr Corie Ralston and Dr Sayan Gupta (Advanced Light Source, ALS) from the Lawrence Berkeley National Lab (LBNL). I designed my experiments based on their recent work mapping the MtrF binding interface with hematite [134] and I performed XFMS experiments based on their extensive XFMS expertise and using their facilities at the LBNL. Use of synchrotron radiation for $^{\bullet}$OH footprinting confers several advantages over other $^{\bullet}$OH footprinting methods. In XF $^{\bullet}$OH radicals are generated *in situ* without addition of chemical reagents (*e.g*, Fe-EDTA an H_2O_2), that could affect the protein conformation or damage/unfold the protein. [132] In addition, the timescale of radical production is faster in XF (milliseconds) than the microseconds used in laser photochemical methods such as FPOP. [132] This advantage of speed allows to control the radical dose received by protein samples and limit sample unfolding and conformational changes caused by residue modification and any secondary radical oxidation reactions. [132]

In this approach protein samples from two conditions (*i.e.*, with and without TiO_2 NPs) are irradiated with X-rays. Water ionization generates hydroxyl radicals that label amino acid side chains exposed to aqueous environment even within buried protein cavities. [132] Resulting protein typically contain covalent hydroxyl- (+16 Da or +32 Da) modifications, which are subsequently detected by liquid-chromatography tandem mass-spectrometry (LC-MS/MS). [129, 132, 133] The binding with TiO_2 NP is expected to shield the bound protein interface from water, thus comparison of peptide modification with and without TiO_2 NPs allows identification of protein residues involved in MtrC : TiO_2 interface. The summary of XFMS approach is shown in Figure 3.2.

3.2 Sample optimisation for XFMS

Hydroxyl radicals are a useful probe for protein footprinting because these provide fast, permanent and non-specific modification of any exposed protein residues. [129] The modification rate of a protein residue depends on the specific reactivity and the local context of that residue. For example, cysteine, tryptophan, tyrosine and methionine react readily with $^{\bullet}$OH radicals, while asparagine and glycine do not. [129] Challenge is to find sample conditions that permit generation of optimal $^{\bullet}$OH dose and generate enough protein modifications to be later analysed with LC-MS. This requires considerations of the sample composition, including, what buffer and how much

protein and TiO_2 NP to use and in what concentrations.

3.2.1 Buffer composition

A key step in XF experiments is water ionization by x-ray irradiation, which generates $^{\bullet}OH$ that modify the side chains of protein residues [133]. Thus protein labelling is related to $^{\bullet}OH$ concentration, which in turn depends on X-ray exposure time and the flux density of an X-ray beam. [133] As the flux density of the X-ray beam is kept fixed, the dose of $^{\bullet}OH$ concentration is regulated by changing the duration of sample exposure. Many sample components such as buffering agents (*e.g.*, MOPS, Tris, HEPES), reducing agents and detergents used for membrane protein solubilisation react with $^{\bullet}OH$ (extrinsic radical scavengers) reducing the effective $^{\bullet}OH$ dose. [133] In addition, sample components (*e.g.*, macromolecular assemblies) can also react with $^{\bullet}OH$ (intrinsic scavengers). [133] Therefore, the duration of sample irradiation often has to be increased to overcome the radical scavenging processes. [133]

In light of this, the many common buffers (*e.g.*, 20 mM MOPS, 30 mM Na_2SO_4) were not suitable due to reported radical scavenging. [136] Unfortunately, other inorganic compounds commonly used for XF experiments (*e.g.*,Na-KPO_4 buffer, $NaHCO_3$, NH_4HCO_3) were also not suitable, as these have high affinity to TiO_2 surface and would compete with protein binding. [159–161] Instead, NH_4Cl was selected as a buffering agent for the XF experiments.

3.2.2 Amount of MtrC and TiO_2 nanoparticles

X-ray assisted protein footprinting requires quite large amounts of protein. Each sample must contain enough protein for peptide detection with LC-MS/MS and to cover potential protein losses during sample processing stage between sample radiolysis and the LC-MS/MS step. In addition, multiple samples are required for each condition (*i.e.*, with and without TiO_2) to be able to measure the rate of residue modification (*i.e.* the amount of residue modification has to be quantified over increasing duration of radiolysis). The work described in this chapter used 0.3 mg MtrC for a single experiment with 2 experimental conditions (with and without TiO_2) and 5 different radiolysis exposure times (*i.e.*, 0, 12.5, 25, 50 and 75 ms).

High amounts of protein require even more TiO_2 NPs. An excess amount of TiO_2 is required in these experiments to make sure that nearly all of proteins are bound to TiO_2 nanoparticles. This then simplifies the subsequent data analysis, where the fraction of modified versus unmodified peptide is estimated for each modified residue in both control and +TiO_2 conditions. To satisfy the

requirement of having large amounts of TO_2 NPs, XF experiments used commercial anatase TiO_2 nanoparticles (a-TiO_2). These nanoparticles have a similar size (≈5 nm) to the dye-sensitised TiO_2 (*i.e.*, **RuP**-TiO_2; 6.8 nm in size) provided by Dr Reisner for the use as LHNP.

The caveat for using a-TiO_2 is that these nanoparticles have different surface chemistry. The differences in the nanoparticle surface is schematically illustrated in Figure 3.3. Commercial a-TiO_2 have no surface modification and thus likely have water hydroxylated TiO_2 surface (Figure 3.3a). In comparison, **RuP**-TiO_2, which are used as LHNPs, are surface-stabilized with DHBA (dihydroxy-benzoic acid) and photosensitized with **RuP** (Figure 3.3c). These particles were first synthesized as DHBA-TiO_2 (Figure 3.3b), which have been previously estimated to contain ≈1.4 DHBA-molecules present per square nanometre of the DHBA-TiO_2 surface. [63] Then **RuP** was bound to the DHBA-TiO_2 via the phosphate groups of **RuP** with an estimated efficiency of 90 ± 20 nmol **RuP** per mg of DHBA-TiO_2. [63]

To summarize the main difference in the surface chemistry of a-TiO_2 and DHBA-TiO_2 and **RuP**-TiO_2 is that the surface of a-TiO_2 primarily contains hydroxyl groups resulting from interaction with water molecules, whereas DHBA-TiO_2 and **RuP**-TiO_2 contain carboxylic acid functionality (due to DHBA) and **RuP**-TiO_2 also has the **RuP** complex. These differences in surface chemistry are also going to cause differences in the interaction between MtrC (and MtrCAB) and the different TiO_2. For example, carboxyl-groups are more negative than hydroxyl groups, DHBA-TiO_2 will bind stonger to the positive amino acids such as Lys and Arg. This is an important caveat for using a-TiO_2 compared to the use of the light-harvesting **RuP**-TiO_2, which unfortunately were not available in the quantities required for the XF experiments.

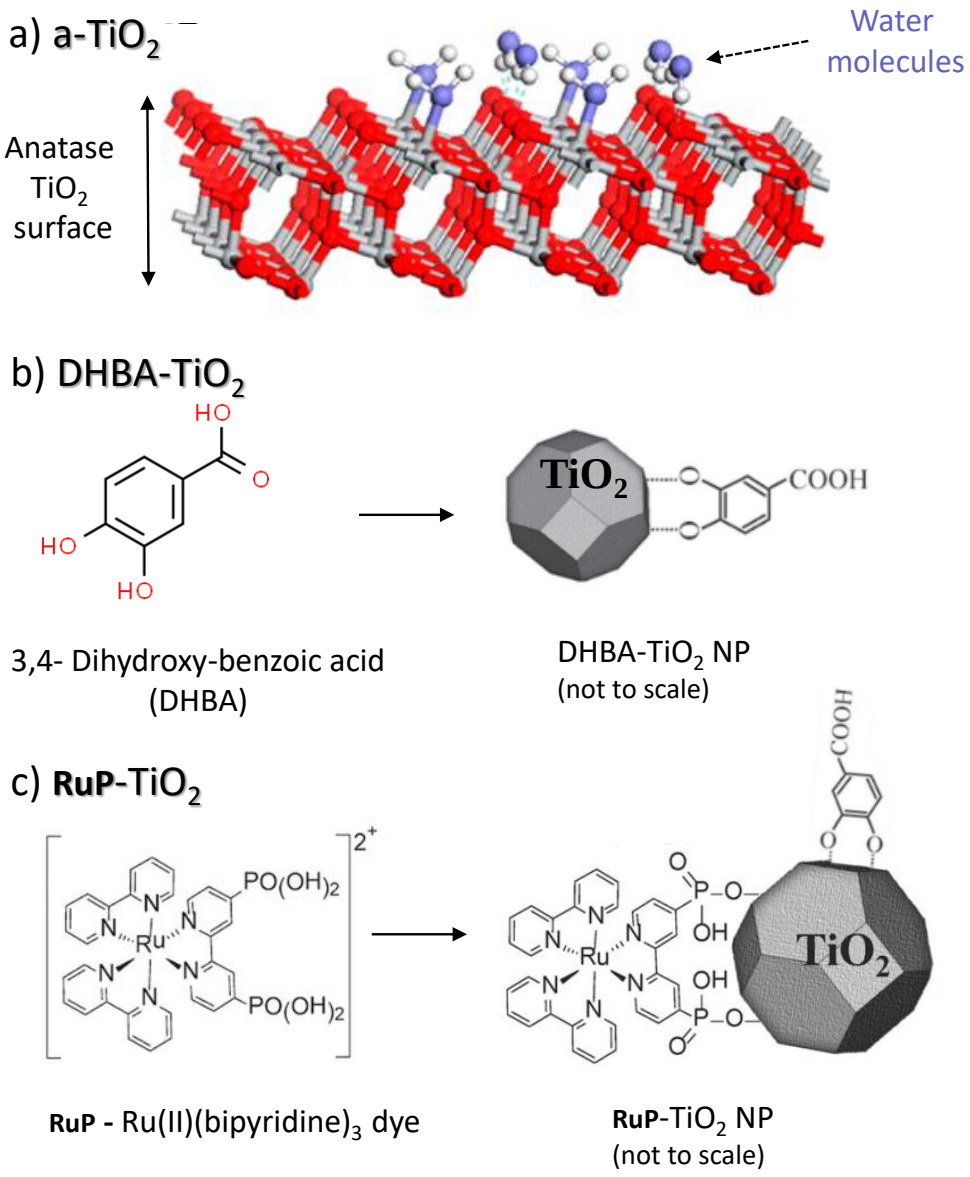

Figure 3.3: The surface differences between TiO_2 nanoparticles. (**a**) The bare surface of a-TiO_2 gets hydroxylated in aqueous solutions. Panel modified after [155]. (**b**) DHBA-TiO_2 NPs are surface-functionalised with DHBA to increase the solubility of nanoparticles. (**c**) **RuP**-TiO_2 NPs are DHBA-TiO_2, which have been additionally light-sensitized with **RuP** dye. Panels (**b**) and (**c**) have been modified after [63]. The chemical structure of DHBA was obtained from the internet (https://www.chemspider.com/Chemical-Structure.71.html; accessed on 03/05/2020).

The lack of surface modifications make a-TiO_2 more prone to aggregation as was seen in DLS (Figure 3.4), where introduction of NH_4Cl resulted in particle aggregation. Further addition of similar amounts of MtrC seemed to slow the a-TiO_2 aggregation, resulting in stable particle

aggregates of 100-200 nm in size. In order to minimise the effect of particle aggregation, a-TiO_2 NPs were added to the buffered protein sample immediately before experiments.

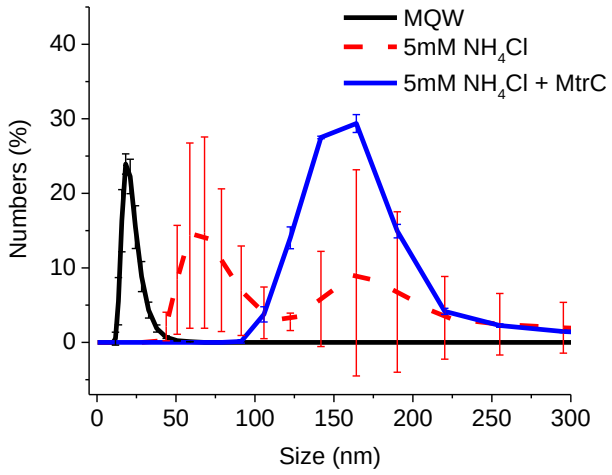

Figure 3.4: DLS of a-TiO_2 nanoparticles in water (MQW, black), in 5 mM NH_4Cl (pH≈8, dashed red line) and in 5 mM NH_4Cl with 50 nM MtrC (blue line). Approximately 11 μg (≈70 nmol NP/ml) a-TiO_2 NPs were used. Error bars represent standard deviation, where n≥3.

3.2.3 Estimating the binding ratio of MtrC and TiO_2 NPs.

A key feature for XFMS is to determine the optimal concentration and ratio of MtrC and a-TiO_2. As mentioned earlier, a-TiO_2 should be in excess so that all (or nearly all) of MtrC would be interacting with the surface of a-TiO_2. In order to do that, the binding stoichiometry between MtrC and a-TiO_2 was characterised using co-sedimentation assay as described in section 2.4.1. Protein was mixed with different amounts of a-TiO_2 NPs and incubated at room temperature for about 20 min. Bound proteins were then pelleted together with TiO_2 NPs by ultracentrifugation, and the amount of non-sedimented ('free') protein was determined optically by measuring the absorbance of supernatant (Figure 3.5 a and b). Then ammonium bicarbonate (NH_4HCO_3) was added to the MtrC-TiO_2 pellet. In this case, the binding of carbonate ions (HCO_2^- and CO_2^{2-}) to a-TiO_2 is exploited to displace MtrC from the a-TiO_2 surface. [127, 128] The a-TiO_2 was then removed again by ultracentrifugation as described in section 2.4.1. The amount of MtrC recovered from a-TiO_2 was again measured optically (Figure 3.5 c and d).

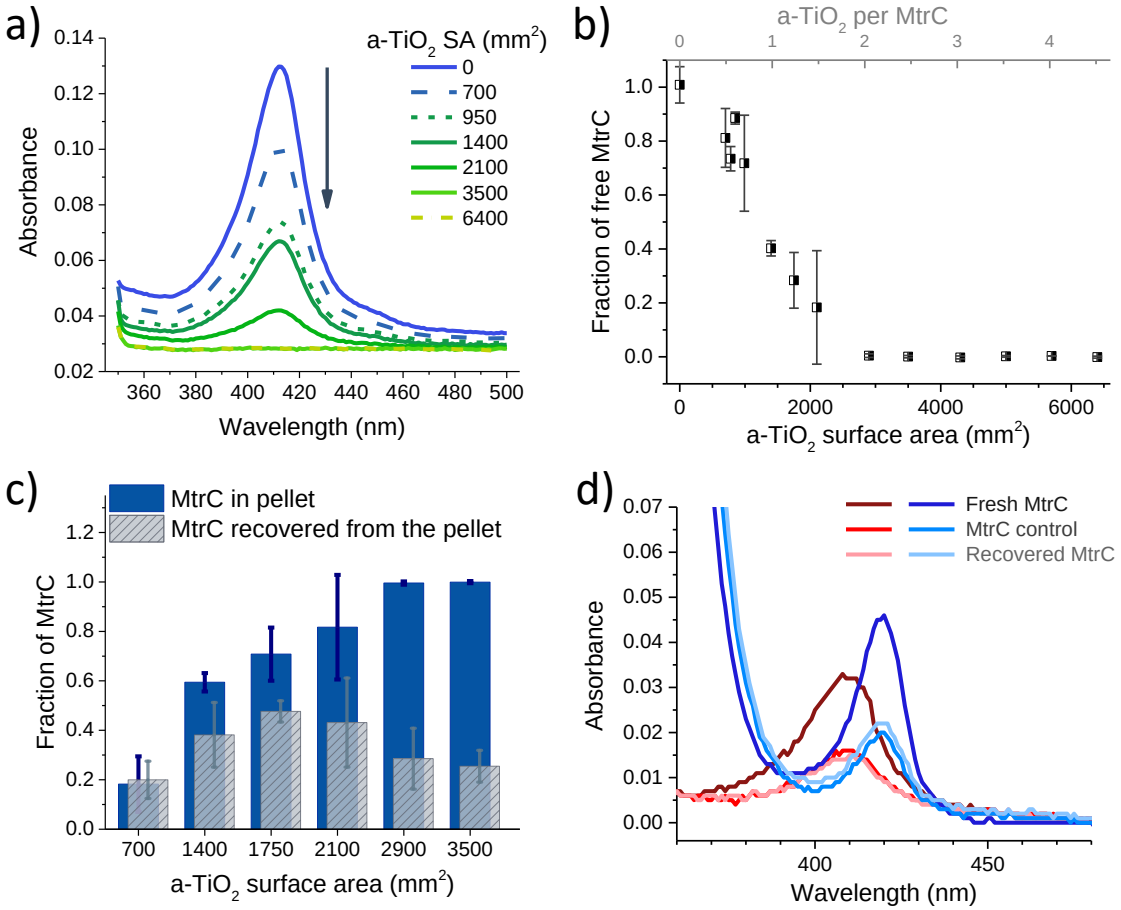

Figure 3.5: MtrC binding to and recovery from a-TiO_2 nanoparticles. (**a**) Representative example of a co-sedimentation assay showing a decreasing concentration of free MtrC (initial concentration ≈160 nM) in supernatant after protein sedimentation with increasing concentration of a-TiO_2 (0 – 120 μg/ml) in 5 mM NH_4Cl buffer, pH ≈8. (**b**) Co-sedimentation of a-TiO_2 with MtrC in 5 mM NH_4Cl, pH ≈8. Error bars represent standard deviation, where n≥3. (**c**) The amount of MtrC bound and pelleted together with a-TiO_2 (blue) is compared to the amount of recovered MtrC (grey) displaced from a-TiO_2 by carbonate ions. MtrC amount is shown relative to the initial amount of protein present in sample before co-sedimentation and recovery assays. n=3 (**d**) The haem absorbance of oxidised (red) and reduced (blue) MtrC exhibit identical characteristics before ('control') and after binding a-TiO_2 ('Recovered MtrC').

These experiments demonstrate 100% MtrC binding, when the total a-TiO_2 surface area was around 3000 mm^2 (Figure 3.5b) and particle ratio was about 2:1 a-TiO_2 : MtrC (50% MtrC binding at 1:1 particle ratio). (For convenience, the condition when all (or half) of the initial MtrC was sedimented is described as '100%' (or '50%') MtrC binding.) Thus, a particle ratio higher than 2:1 should be used for XFMS experiments to ensure conditions that nearly all MtrC are bound to

a-TiO_2.

It has been reported before that protein interactions with nanoparticles can lead to changes in protein structure and even protein unfolding [155, 157, 158, 162]. Experiments on MtrC recovery from co-sedimented MtrC : a-TiO_2 pellets aimed to test if MtrC binding to a-TiO_2 leads to irreversible protein conformation changes. The amount of recovered protein was estimated relative to the initial protein amount used for co-sedimentation experiments. Figure 3.5c compares the amount of recovered protein to the estimate of the fraction of MtrC sedimented as MtrC :a-TiO_2 complex. This approach indicated that the protein recovery is influenced by the concentration of a-TiO_2 during co-sedimentation (seen in Figure 3.5c, where the blue bars indicate how much MtrC was co-sedimented with a-TiO_2, and the overlapping grey bars indicate the amount of subsequently recovered MtrC). Thus all co-sedimented MtrC was recovered from the experiment involving a-TiO_2 with the total surface area of 700 mm^2 (1:2 particle ratio of a-TiO_2 :MtrC), whereas only a fraction of MtrC was recovered from samples containing higher a-TiO_2 concentration. This could be explained by an increase in a-TiO_2 aggregation at higher a-TiO_2 concentration leading to protein entrapment within the a-TiO_2 aggregates. It is also possible that MtrC gets not only entrapped but also damaged and unfolded at higher a-TiO_2 concentrations.

Protein absorbance of the recovered MtrC was measured (Figure 3.5d) under oxidative and reductive conditions, and showed the same absorbance profile as the control, indicating that the interaction with a-TiO_2 did not cause changes in the local haem environment. As the 10 haems of MtrC span the whole protein, this is a strong indication that the recovered MtrC have maintained structural integrity. This is important because following x-ray irradiation, the protein must be recovered and separated from a-TiO_2 for further sample processing and MS analysis.

Exploring interaction between MtrC and TiO_2 NPs in broader context.

So far binding interaction and ratio has been explored only between MtrC and commercial a-TiO_2 in 5 mM NH_4Cl. In order to estimate how this interaction relate to the full membrane protein complex, another set of co-sedimentation assays was performed with MtrCAB solubilised in detergent (LDAO) (Figure 3.6). MtrCAB showed similar binding to a-TiO_2 as MtrC, showing 50% and 100% binding at approximately 2:1 and 1:1 MtrCAB : a-TiO_2 ratios, respectively. The observation of similar affinity between a-TiO_2 and both MtrC and MtrCAB, suggests that MtrC interaction with MtrAB does not change MtrC binding capacity to a-TiO_2. A less likely scenario would be that MtrAB does shield some of MtrC binding interface with a-TiO_2, but in that case MtrAB provides complementary interactions with a-TiO_2.

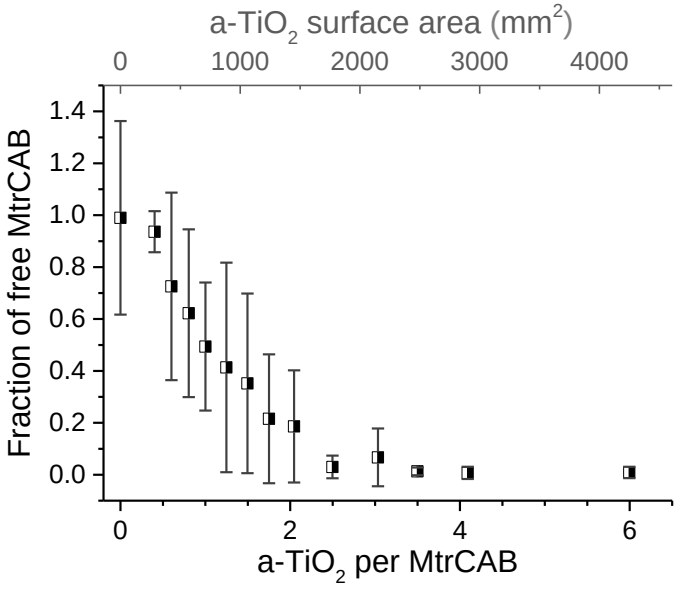

Figure 3.6: Detergent solubilised MtrCAB binding to a-TiO_2 nanoparticles. Co-sedimentation of a-TiO_2 with MtrCAB in 5 mM NH_4Cl, 5 mM LDAO, pH ≈8. Error bars represent standard deviation, where n≥3.

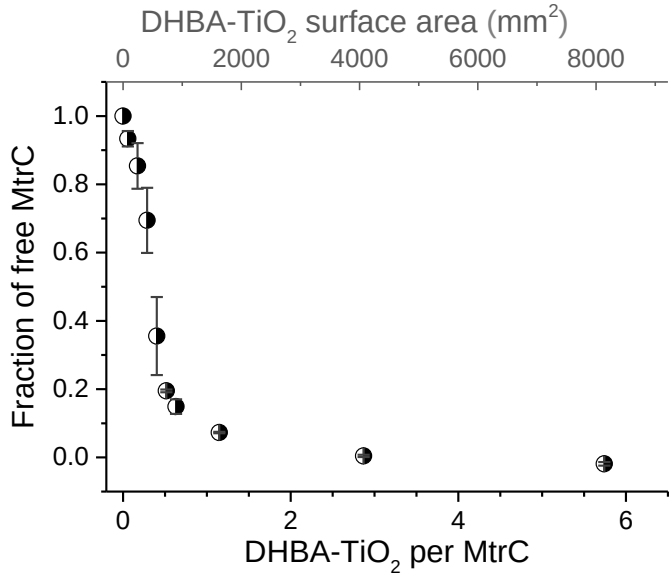

Figure 3.7: MtrC binding to DHBA-TiO_2 nanoparticles. (Co-sedimentation of DHBA-TiO_2 with MtrC in 20 mM MOPS, 30 mM Na_2SO_4, pH ≈7.4. Error bars represent standard deviation, where n≥3 with the exception of sample containing 2000 mm^2 DHBA-TiO_2 in (**d**), where n =2.

Another set of experiments was performed to gain an insight how binding interaction might change with TiO_2 NPs with different surface modifications. For this a co-sedimentation assay was performed with DHBA-TiO_2 NPs (Figure 3.7. DHBA-TiO_2 were chosen as these are precursor

NP for the light-harvesting **RuP**-TiO_2 NPs. **RuP**-TiO_2 were not suitable for this assay due to the spectral overlap of the absorbance of the photosensitiser dye (**RuP**) and MtrC haems.

The data in Figure 3.7 indicate that almost all MtrC was co-sedimented with DHBA-TiO_2, when the total TiO_2 surface area was around 1100 mm^2. This equates to particle ratio of about 1:1 DHBA-TiO_2 : MtrC and observation that 50% of available MtrC were sedimented at around 1:3 particle ratio. This relatively high MtrC : DHBA-TiO_2 ratio suggests that several MtrC molecules might be able to bind to a single DHBA-TiO_2. Comparison of these results to a-TiO_2, it can be noted that MtrC has lower binding affinity to a-TiO_2 than DHBA-TiO_2. This is most likely due to the different surface chemistries between these particles, where a-TiO_2 should have exposed hydroxyl groups, whereas DHBA-TiO_2 contain exposed carboxyl groups (see Figure 3.3). This observation of change in binding affinity due to difference in particle surface chemistry might hint that this particle interface is at least partly governed by electrostatic interactions. One caveat to comparing these co-sedimentation experiments between a-TiO_2 and DHBA-TiO_2 is that experiments with DHBA-TiO_2 were performed in a buffer with higher ionic strength. In order to estimate the effect that increased charge screening due to higher ionic strength has on MtrC binding to these different TiO_2 particles, it would be useful to perform co-sedimentation experiments with DHBA- TiO_2 in 5 mM NH_4Cl (or co-sedimentation with a-TiO_2 in the MOPs buffer, 20 mM MOPS, 30 mM Na_2SO_4, pH ≈7.4).

3.2.4 Estimation of the required x-ray irradiation dose.

After considering the initial sample conditions (*i.e.*, buffer, TiO_2 NPs, the ratio of MtrC and a-TiO_2 NPs), these experimental conditions were tested at the synchrotron beamline. The influence of different sample components on $^{\bullet}OH$ dose is commonly estimated indirectly - observing bleaching of irradiated fluorescent dye (Alexa Fluor 488), as reported in section 2.4.2. Figure 2.2 provides an example of dose-response plots of MtrC with and without a-TiO_2. The apparent rate constants of the fluorophore decay in various buffer and a-TiO_2 conditions are summarised in Table 3.1. These results indicate that MtrC was not scavenging $^{\bullet}OH$, whereas a-TiO_2 appeared to scavenge $^{\bullet}OH$ in 5 mM NH_4Cl. Interestingly, the $^{\bullet}OH$ scavenging was not influenced by a-TiO_2 concentration as the rate constant was essentially the same for samples containing 0.2-3 mg/ml a-TiO_2. Upon closer investigation, it was noticed the fluorescent dye (Alexa Fluor 488, Figure 2.2b) has a carboxylic and hydrazide groups, which could interact with a-TiO_2 surface. The resulting binding between fluorophore and a-TiO_2 could lead to enhanced fluorophore protection from oxidative $^{\bullet}OH$. To test this hypothesis, a similar $^{\bullet}OH$ dose-response assay was performed in 50 mM phosphate buffer

with and without a-TiO_2 (see Table 3.1). In this case, phosphate ions (similarly to carboxyl-groups used for MtrC recovery from co-sedimentation experiments) bind the a-TiO_2 surface and prevent binding of the fluorescent Alexa dye. The result showed no $^{\bullet}$OH scavenging by a-TiO_2 in phosphate buffer. Thus, it was concluded that these sample components (*i.e.*, 5 mM NH_4Cl, MtrC and a-TiO_2) were not significant scavengers of $^{\bullet}$OH. The estimated rate of ≈30 s^{-1} indicates that sample could be effectively radiolysed and modified with $^{\bullet}$OH radicals using x-ray exposure times ranging fom 0 to ≈70-80 ms (determined by Dr. Sayan Gupta based on his extensive experience with XFMS).

Initially, XFMS analysis of detergent solubilised MtrCAB complex interaction with a-TiO_2 were also intended. Unfortunately, this proved to be impractical as the $^{\bullet}$OH scavenging of the detergent (5 mM LDAO) was too high (Table 3.1).

Table 3.1: Summary of $^{\bullet}$OH modification rate constants from fluorophore dose-response assays

Buffer	**Protein**	**a-TiO_2**	**Rate ± SD (s^{-1})**	**n**
5 mM NH_4Cl	-	-	35 ± 6	2
5 mM NH_4Cl	0.2 μM MtrC	-	31 ± 2	2
5 mM NH_4Cl	0.2 μM MtrC	0.2 mg/ml	11 ± 1	2
5 mM NH_4Cl	-	0.3 mg/ml	8	1
5 mM NH_4Cl	-	3 mg/ml	10	1
50 mM Pi buffer	-	3 mg/ml	23	1
50 mM Pi buffer	-	-	26	1
5 mM NH_4Cl, 5 mM LDAO	-	-	12	1
5 mM NH_4Cl, 5 mM LDAO	0.4 μM MtrCAB	-	11	1
5 mM NH_4Cl, 5 mM LDAO	-	0.3 mg/ml	10	1

Pi - phosphate buffer; n - number of experimental repeats

3.2.5 Summary of sample conditions derived for XFMS experiments.

The previous few sections list a number of considerations and experiments aimed to optimize sample conditions for XFMS. The final conditions and the reasoning for them are summarized below:

1. 5 mM NH_4Cl buffer:
   (a) NH_4CL does not bind a-TiO_2 and is not scavenging $^{\bullet}OH$;
   (b) low concentration to minimise a-TiO_2 aggregation;
2. 0.3 mg MtrC used per a single XFMS experiment (2 experimental conditions, *i.e.*, with and without TiO_2, and 5 different radiolysis exposure times):
   (a) enough to detect peptides by LC-MS/MS despite large potential losses during sample processing;
   (b) large sample volume to keep MtrC in concentration comparable to conditions in co-sedimentation experiments (*i.e.*, ≈0.2 μM);
3. commercial a-TiO_2:
   (a) available in bulk to satisfy the requirements for large amounts of TiO_2 NPs;
   (b) main caveat is the difference in surface chemistry to the light-harvesting **RuP**-TiO_2 NPs;
4. particle ratio of 5:1 between a-TiO_2 and MtrC:
   (a) higher than 2:1, to make sure that all (or almost all) MtrC is bound to a-TiO_2;
   (b) increased even more to compensate a-TiO_2 aggregation in buffer, which effectively reduce the particle ratio between a-TiO_2 and MtrC;
   (c) the excess of a-TiO_2 over MtrC might lead to higher prevalence of non-specific binding and will have to be accounted for during XFMS data analysis;
5. radiolysis exposures ranging from 0-≈70-80 ms:
   (a) determined from Alexa fluorophore dose-response rate constant assay results by Dr. Sayan Gupta.

3.3 MtrC : a-TiO_2 XFMS analysis

MtrC : a-TiO_2 samples in 5 mM NH_4Cl were radiolysed at ALS based on work published in [133, 134] as described in section 2.4.2. Resulting proteins were then proteolysed and analysed using LC-MS/MS analysis at the Biomolecular Mass Spectrometry Facility of the University of Leeds as described in section 2.4.2. The summary of XFMS approach is shown in Chapter 2 Figure 2.1 and for convenience is reproduced here as Figure 3.8.

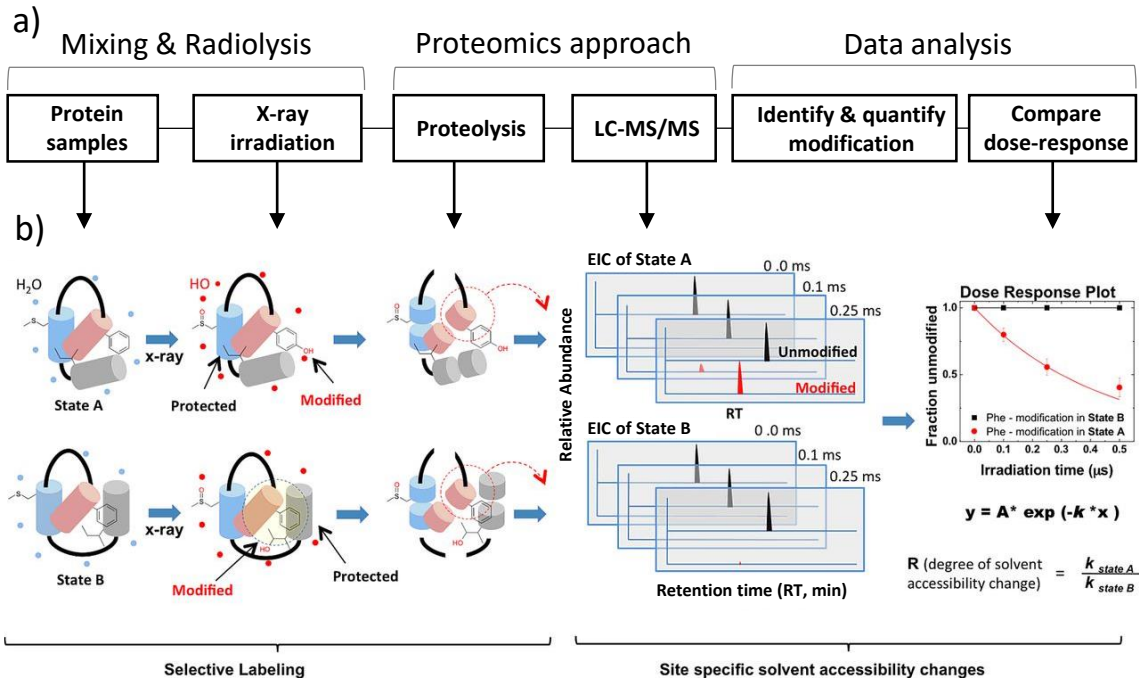

Figure 3.8: Overview of XFMS analysis. (**a**) Schematics showing main stages of XFMS approach. (**b**) Example of XFMS illustrating the water (blue dots) radiolysis and generation of hydroxyl- radicals (red dots), which then modify protein residues exposed to water. The conformational differences between protein in state A and state B lead to selective labelling of the identified phenylalanine (Phe). Protein is then digested with proteases and analysed using LC-MS/MS. LC quantitatively separate the peptides at different retention times (RT), which are then identified by the MS. MS/MS allows determination of the specific site of the modification. The quantification of the fractions of the unmodified peptide over exposure time (dose-response plot) allows determination of site-specific modification rate constants (k^{-1}). These rate constants are then compared between different sample conditions and their ratios (R) are used to describe the solvent accessibility changes due to any binding-interactions or conformational changes. The final result is mapped onto available structures. Figure reproduced and modified after [131].

XFMS experiments involved two conditions (*i.e.*, MtrC with and without a-TiO_2). Samples

from each condition were radiolysed for 5 different exposure times (*e.g.*, 0, 12.5, 25, 50 and 75 ms). MtrC from each sample was then proteolysed and the resulting native (*i.e.*, unmodified) and modified peptides were identified. Thus terms 'native' and 'modified' are used within this chapter to describe whether a XF hydroxyl- modification (+16 Da) is detected on a peptide residue, peptide or protein. Then the amount and the distribution of hydroxyl- modifications were quantified across the 5 exposure times to produce a dose-response plot for each detected modification. A modification rate constants (k^{-1}) were then determined for each modification, which were compared between conditions as the modification rate ratio (R) of MtrC and MtrC : a-TiO_2 complex.

3.3.1 Protein coverage.

Overall, MS/MS identified peptide fragments covering around 68% of the MtrC sequence (Figure 3.9) across exposed samples from both conditions (*i.e.*, with and without a-TiO_2). The missing peptides are generally located at the beginning and the end of the MtrC sequence, as well as the areas containing haem-groups. The 10 haems of MtrC are covalently attached via two cysteines in a CXXCH polypeptide motif, where X denotes unconserved amino acid within the motif [163] and are depicted red in Figure 3.9. It has been noted before that haem-containing fragments are more difficult to identify by MS/MS due to such properties as differing charge state of the haem iron and atypical peptide fragmentation. [164] *De novo* peptide sequencing by MS/MS also identified which peptides and peptide residues contained hydroxyl- modifications. The examples of obtained protein coverage and the identified +16 Da modifications of XF modified MtrC with and without a-TiO_2 are shown in Figure 3.10. This Figure provide an initial qualitative insight in the differential XF labelling of samples with and without a-TiO_2 (*i.e.*, Figure 3.10 a and b, respectively) by summarizing all different peptide versions identified across the protein. For instance, it is easily observed that more modifications (and more different peptide versions) are detected in the exposed MtrC control sample (without a-TiO_2) in peptides corresponding to residues 300-480 (highlighted with the yellow frame in Figure 3.10. Interestingly, the 0 ms radiolysis MtrC control sample (data shown in Chapter 2, Figure 2.3) shows that some peptides in unexposed control also contain oxidised residues. These are at or near Trp (W), Tyr (Y), Met (M), Phe (F) and His (H), which are among the most reactive amino acid residues towards $^{\bullet}OH$, thus likely represent protein oxidation during sample storage and handling. [129]

```
  1 MKFKLNLITL ALLANTGLAV AADGGGSDGN NGNDGSDGGE PAGSIQTLNL
 51 DITKVSYENG APMVTVFATN EADMPVIGLA NLEIKKALQL IPEGATGPGN
101 SANWQGLGSS KSYVDNKNGS YTFKFDAFDS NKVFNAQLTQ RFNVVSAAGK
151 LADGTTVPVA EMVEDFDGQG NAPQYTKNIV SHEVCASCHV EGEKIYHQAT
201 EVETCISCHT QEFADGRGKP HVAFSHLIHN VHNANKAWGK DNKIPTVAQN
251 IVQDNCQVCH VESDMLTEAK NWSRIPTMEV CSSCHVDIDF AAGKGHSQQL
301 DNSNCIACHN SDWTAELHTA KTTATKNLIN QYGIETTSTI NTETKAATIS
351 VQVVDANGTA VDLKTILPKV QRLEIITNVG PNNATLGYSG KDSIFAIKNG
401 ALDPKATIND AGKLVYTTTK DLKLGQNGAD SDTAFSFVGW SMCSSEGKFV
451 DCADPAFDGV DVTKYTGMKA DLAFATLSGK APSTRHVDSV NMTACANCHT
501 AEFEIHKGKQ HAGFVMTEQL SHTQDANGKA IVGLDACVTC HTPDGTYSFA
551 NRGALELKLH KKHVEDAYGL IGGNCASCHS DFNLESFKKK GALNTAAAAD
601 KTGLYSTPIT ATCTTCHTVG SQYMVHTKET LESFGAVVDG TKDDATSAAQ
651 SETCFYCHTP TVADHTKVKM KGELKLEGKP IPNPLLGLDS TRTGHHHHHH
```

Figure 3.9: Average coverage of identified peptides in MtrC sequence. Protein areas covered by MS/MS identified peptides are in bold. Grey indicates peptides found in majority of samples (across different exposures and conditions). Orange indicates areas that were identified in at least two exposures within each condition (*i.e.*, control and with a-TiO_2). Red 'CXXCH' motifs indicate location of the covalently-bound haems.

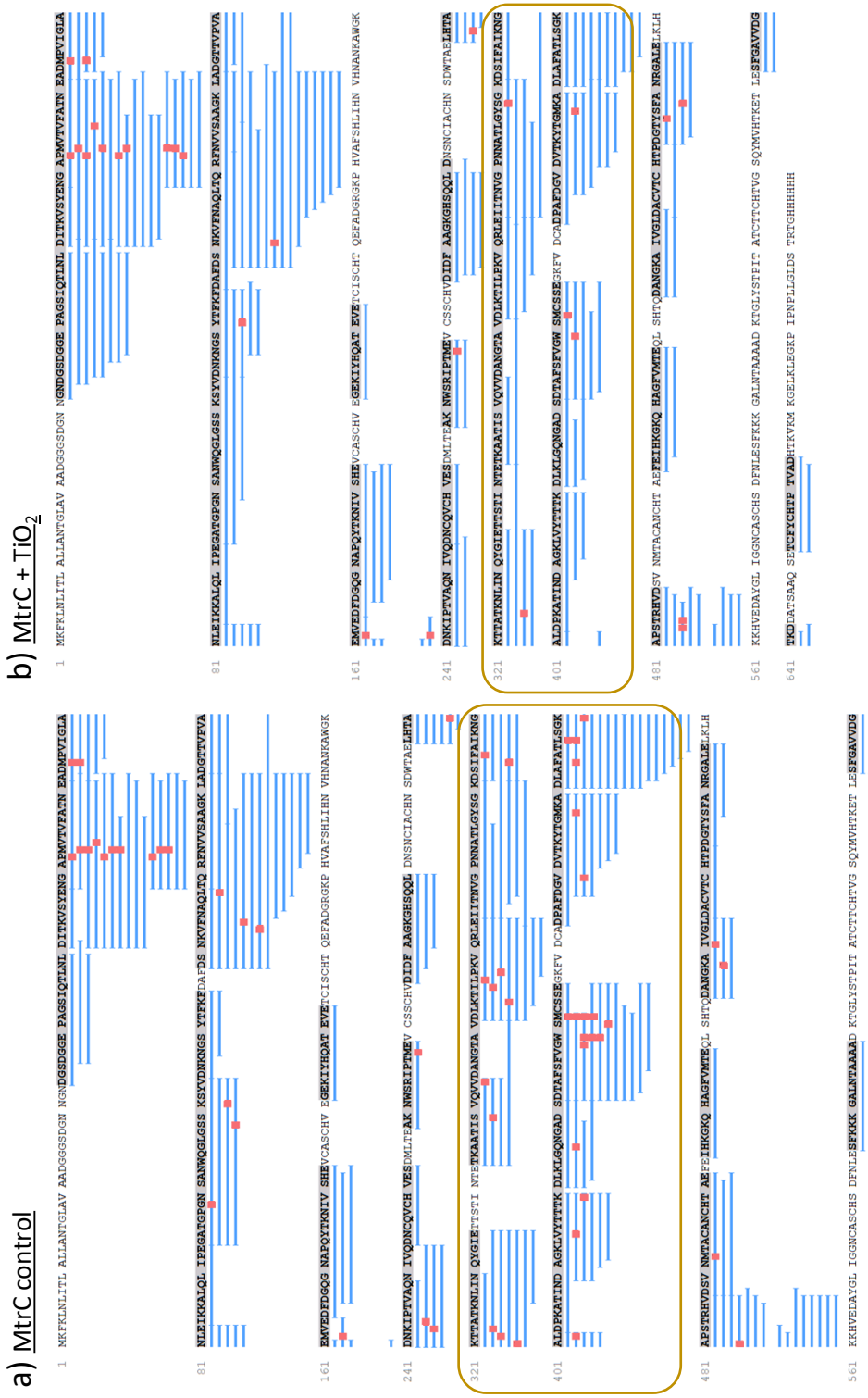

Figure 3.10: Examples of protein coverage and detected +16 Da modifications (small red) for MtrC control (a) and with a-TiO_2 (b) samples radiolysed for 50 ms. (**a**) Protein coverage 67%. (**b**) Protein coverage 64%. Blue lines represent different identified peptides and are not a quantitative representation. Golden rectangles encircle areas, were main differences can be readily observed between samples with and without a-TiO_2.

3.3.2 XFMS results

Overall about 41 peptides have been identified as showing potential +16 Da modifications caused by XF. The peptides eluting at specific retention times (RT) were identified by MS/MS and the quantification of peptide modification was performed from extracted ion chromatograms (EIC) as described in section 2.4.2. A summary of peptides with identified XFMS modifications and the criteria used to assign these modifications to specific modified amino acid residues are shown in Appendix, Table 1. The extent of the residue modification depends on the specific residue reactivity and the local environment of the residue (*e.g.*, solvent accessibility) [132, 133]. To simplify analysis the changes in solvent accessibility (and hydroxyl-reactivity) of specific residues were estimated by calculating R, the ratio of the k^{-1} of free MtrC vs the k^{-1} of MtrC bound to a-TiO_2. Thus, M74 is relatively unprotected by a-TiO_2 (R=2.4±1.0), while residue L367 is shielded by a-TiO_2 (R=8.9±2.4). The summary of the progress and results of XFMS modification processing and analysis to the date of writing this thesis is shown in Appendix, Table 1. Although the majority of data has been processed, a fraction of identified peptides remains unanalysed due to time constrains of this PhD. This work is intended to be continued by a postdoc or a future PhD student within the Jeuken lab.

The results of processed XFMS data analysis were evaluated in the context of MtrC structure published as PDB entry 4LM8 (shown earlier in Figure 3.1) [148]. The analysed XFMS peptides are shown in Figure 3.11.

The protein surface area is coloured according to the presence of detected $^{\bullet}$OH modifications (*i.e.*, grey, blue to yellow and red) and the areas of lack of information (black) due to undetected peptides and peptides that to date of writing this thesis have yet to be processed. In this type of studies, 1.5-3 fold increase (or decrease) of modification rate is regarded as significant identification of increased residue protection (or increased solvent accessibility). [132–134, 165, 166] Here, the difference of residue modification between condition with a-TiO_2 and the control is indicated using a colour scale from blue (no difference) to yellow (some residue protection by a-TiO_2) and dark red (strong residue protection from modification by a-TiO_2). As XFMS experiments used a-TiO_2 in excess, some of the detected modifications might represent non-specific binding events. These are expected to show lower fold increase of modification rate than areas of specific binding and would be shown in Figure 3.11 lighter (*e.g.*, light yellow to light orange).

To the date of writing this thesis majority (but not all) of the modified peptides have been analysed and is shown in Figure 3.11. In some cases, it was impossible to identify the precise location of the modified residue, thus peptide sequences corresponding to the closest reliable localisation of

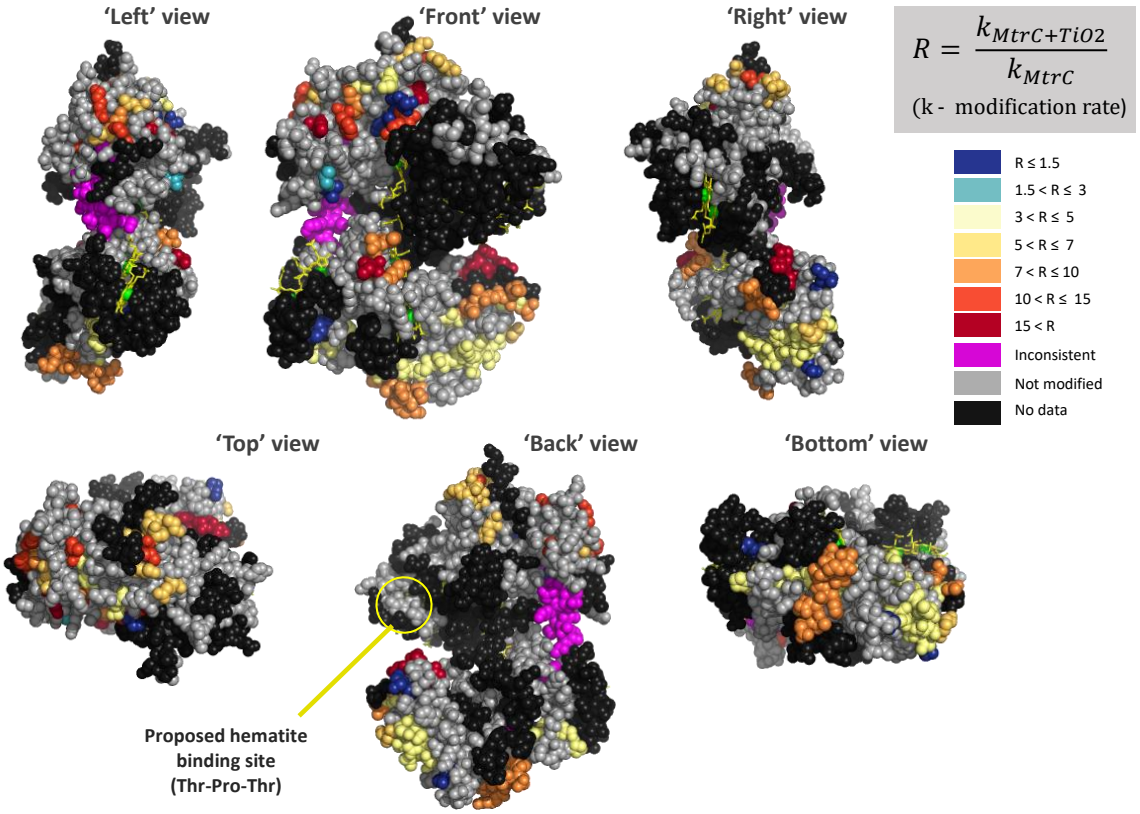

Figure 3.11: The available XFMS results mapped onto the surface of MtrC structure (PDB ID: 4LM8 [148]). Haems are shown as yellow sticks with green spheres as the central irons.+16 Da modified residues are coloured according to the ratio (R) of residue modification in MtrC control sample vs. sample with a-TiO_2. Residues modified similarly with and without a-TiO_2 (low R) are dark blue. Higher R (*i.e.*, residue modification are increasingly different between +/- a-TiO_2) is shown as progressive colour change from light blue to yellow, orange and dark red. Thus, dark red indicates residues showing highest detected shielding from $^{\bullet}$OH radicals by a-TiO_2. Magenta - inconsistent modifications (*i.e.*, data too noisy for a reliable fit or error >60%). Grey - residues with no detected modifications. Black - protein areas with no information due to missing peptides or peptides not analysed within the timeframe of writing this thesis. 'Left' and 'Right' view indicate sideways rotation of the structure in 'Front' view -90°and 90°around the y axis. The 'back' view is 180°around the y axis. Similarly, 'top' and 'bottom' views are -90°and 90°rotation around the x axis. Yellow circle indicates a proposed hematite binding sequence (Thr-Pro-Thr). [90, 151]

the detected modification are shown. More detail of each identified residue (or peptide area) are found in the Appendix, Table 1. The regions with peptides not detected in LC-MS/MS are shown black in Figure 3.11. Unfortunately, these correspond to areas around all 10 haems and the C-terminus of the peptide, which has been suggested to play role in protein orientation on self-assembled monolayer modified gold electrode [146]. The region around haem 10 has been identified as involved in binding to α-Fe_2O_3 (hematite) nanoparticles in MtrF (a closely related protein homologue of MtrC). [134] In addition, MtrC contain a proposed hematite binding sequence (Thr-Pro-Thr, yellow circle in Figure 3.11) near its haem 10 (residues 559-661) [90,151]. In current study the peptide containing these residues did not carry any detected modifications, which might be influenced by the low coverage of the entire domain IV. It is possible that the amounts of modified peptides at this region was present in not high enough amounts and thus was not picked-up with the tandem MS/MS. Further experiments probing the missing protein areas are required to provide better comparison between binding sites of a-TiO_2 and hematite, the natural binding partner of MtrC.

Most detected modifications are located primarily on the same haem-facing ('Front') side of the MtrC, with very few modifications in the 'Back'. This is unexpected because hydroxyl radicals should be able to modify all water accessible areas. It is possible that most modifications on the 'Back' of MtrC are located in the missing peptide areas. Alternatively, protein might be self-assembling in a structure, sequestering its back from the aqueous environment. Further experiments using different proteases or protein footprinting probes might help to address these possibilities. Overall, modification showing low or no difference between conditions with and without a-TiO_2 are present on the membrane-interfacing protein domains (domains I and II, see Figure 3.1). In few cases, data was too noisy for a reliable fit of exponential decay and these residues were marked inconsitent (magenta in Figure 3.11). Often these cases involved tryptophan (*e.g.*, W104, W272, W440), which showed high levels of oxidation modifications even in control samples without exposure to X-ray irradiation. Tryptophan is the second most reactive residue (after cystein) to be modified by hydroxyl radicals. [129] As, some of these residues were buried within the protein structure, these residues seem to be in some way more susceptible to oxidation. Further work is needed to test if these residues in their oxidised or reduced form play any specific role (*e.g.*, as a safety mechanism for radical quenching).

The most a-TiO_2 protected residues (having larger R and coloured intensive orange, red and dark red) are located on top of domain III and in the areas where domains I, II and III interface the largely missing domain IV. Interestingly, one modification (*i.e.*, Ile376, Ser389) is located near haem 7 among on domain III and near the interface with domain IV. These residues show no

difference with and without a-TiO_2 despite being surrounded by other a-TiO_2 protected areas. In this case, the LC-MS/MS identification of the modified Ser389 was ambiguous (see assignment criteria in Appendix, table 1) due to poor peptide fragmentation in MS/MS. Ile376 in turn is located in a buried cavity, thus water present within the cavity would be able to modify the residue irrespective of presence of a nearby a-TiO_2. In contrast, Ser389 is a surface exposed residue and surrounded by areas protected by a-TiO_2, which seems contradictory for a residue with no contact with a-TiO_2. Given the ambiguous identification of this residue by LC-MS/MS, analysis of additional XFMS samples and repeats is required to confirm the status of this modification. If this residue is indeed not-associated with a-TiO_2, this might be an indication for structural conformation changes caused by a-TiO_2 binding, such as potential rotation of the loop containing Ser389 to bury Ser389 within the same cavity as Ile376.

3.4 Discussion

To the time of writing this chapter the majority (but not all) of the collected XFMS data has been processed. It has been possible to identify multiple protein residues showing different modification rates with $^{\bullet}OH$ in conditions with and without a-TiO_2 (Figure 3.11). These can be used to hypothesize on putative a-TiO_2 binding sites and the properties leading to the binding interaction. The current understanding of MtrF binding to hematite [134] and several peptide binding to TiO_2 suggest a role of electrostatic interactions and a contribution of 3D peptide conformation [155, 156]. To address these in the context of MtrC, the properties of protein surface surrounding the residues identified in XFMS were examined (Figure 3.12). Although, a-TiO_2 protected residues are scattered around the MtrC, I focus on three areas showing highest residue protection by a-TiO_2 (*i.e.*, highest R and coloured more intensely red in Figure 3.12). This approach allows to disregard areas of possible non-specific a-TiO_2 binding events caused by the a-TiO_2 in excess. More detailed analysis for each detected modification together with further acquisitions of XFMS data and data refinement is necessary for better and more thorough data interpretation.

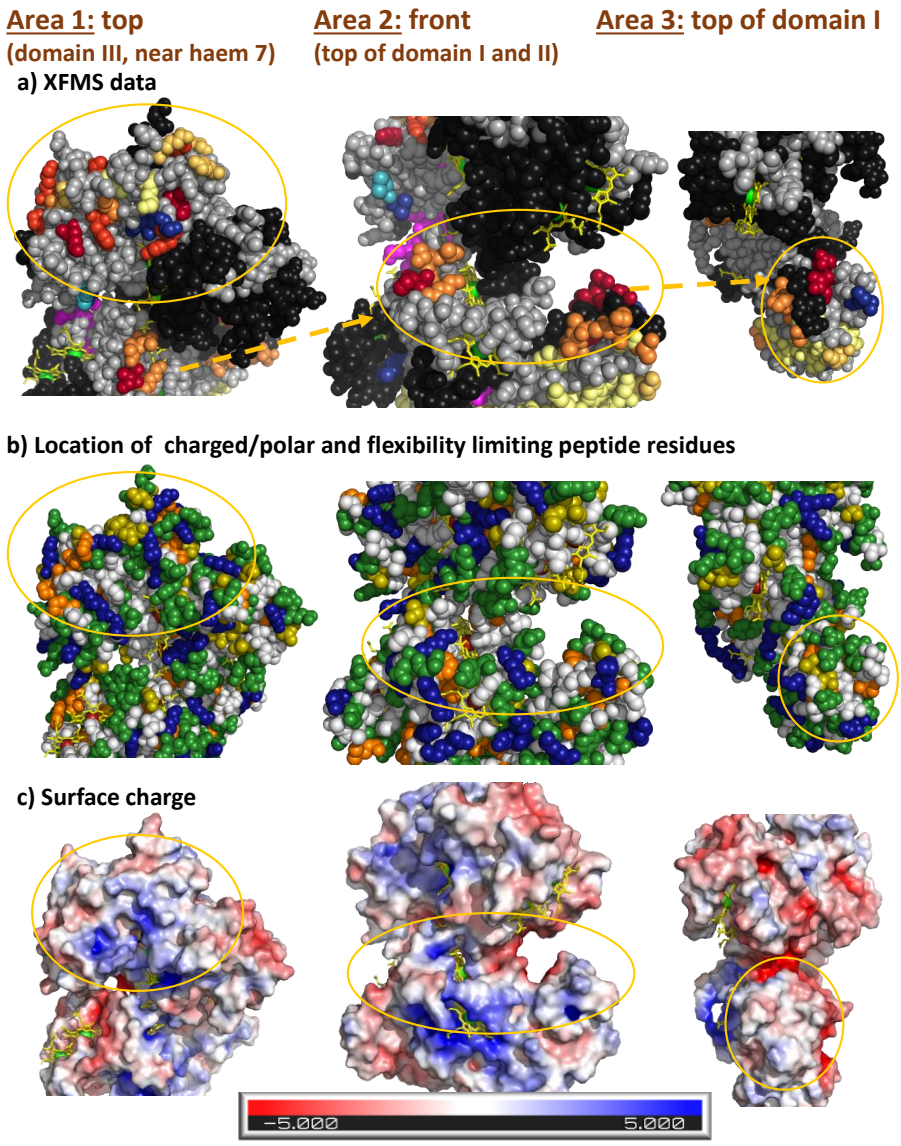

Figure 3.12: MtrC properties of three putative a-TiO_2 binding areas: area 1, near haem 7 (left), area 2, in near haem 1 (middle) and area 3, 'top' of the domain I (right). (**a**) XFMS data mapped on MtrC structure (PDB ID: 4LM8 [148]), coloured as described in Figure 3.11, where haems are identified as yellow sticks with green spheres. Modified residues are coloured according to the ratio (R) of residue modification, where low, moderate or high shielding by a-TiO_2 is shown as progressive colour change from blue to yellow to orange and red. Grey - non-modified residues. Black - areas where XFMS information is absent. (**b**) Location of polar and charged residues, as well as bulky residues, which increase local peptide rigidity. Blue - positive residues (*i.e.*, K and R), Green - charged (*i.e.*, E, D) and polar (*i.e.*, S, Q, N, Y) residues, Olive - T (polar and bulky residue), Orange - bulky residues (*i.e.*, P, W, L). Yellow sticks represent haem groups with the iron coloured as red sphere. (**c**) The surface charge of MtrC calculated using the APBS plugin within the Pymol. [167, 168] Colour transition from red to blue identifies surface charge from -5 to +5 kT/e (≈130 mV). Yellow sticks represent haem groups. Yellow circle highlights the boundaries of XFMS areas 1, 2 or 3.

The three areas selected for this initial data interpretation are: 1) 'top' of MtrC (domain III) and near heam 7 (further referred as Area 1), 2) an area in 'front' of MtrC near haem 1 (top of domains I and II around Lys243 - Thr246; further referred as Area 2) and a closer look on area on the 'top' of protein domain I (residues from P41 to L48; further referred as Area 3). Although area 1 mostly belong to an individual domain (domain III in Figure 3.12), these are all located near the domain interface with domain IV.

The panel c in Figure 3.12 shows distribution of electrostatic charge on the MtrC surface. No clear common properties can be seen between the three areas, as Area 1 is mostly positively charged, Area 2 contains both positively and negatively charged residues and Area 3 is mainly neutral. It is well-accepted that charged and polar amino acids have the greatest affinity for adsorption to TiO_2. [155] These include positive residues (Lys and Arg) that have been observed as essential for peptide binding to TiO_2 [156] In addition, the rigidity of peptide is also reported to promote interactions with TiO_2 [156] and other minerals as quartz, calcium carbonates [169, 170] and pure Ti [171]. Panel in Figure 3.12 aims to provide a summary of the distribution of charged and bulky amino acids within areas 1, 2 and 3. Thus positively charged residues (Lys, Arg) are shown blue, other charged and polar residues (Glu, Asp, Ser, Asn, Gln, Tyr) are green, Thr, which is both polar and bulky, is olive, but the distribution of bulky residues (Pro, Trp, Leu) restricting the local peptide conformation are shown as orange. In this context, it can be observed that Area 1 contains charged residues, including several positively charged Lys lining a pocket near haem 7. This pocket in turn is surrounded by several bulky amino acids restricting the conformational flexibility of the protein, and potentially facilitating a contact with a-TiO_2. Area 2 contains a charged Lys243 and Thr246, and the bulky Thr246 is located right next to another rigid residue - Pro245. The right side of area 2 (top of domain I) is closer observed as Area 3, which consists of charged and polar residues surrounded by positive residues and a bulky threonine, which might help to orient the charged residues towards a-TiO_2 surface. Thus, no single property can be identified as being common for all three MtrC areas explored in detail. They all contain charged residues able to form complementary electrostatic interactions with the hydroxylated surface of a-TiO_2 surface. In addition, presence of protein flexibility limiting amino acids is also observed, which could promote the stability of a complex formed by complementary electrostatics. Further experiments using mutations to replace the identified Lys and Pro/Leu/Trp/Thr at these interfaces could help to clarify how these amino acids and their properties affect the binding affinity. In addition, computational studies could be carried out to see how the flexibility and surface charge of MtrC in areas 1, 2 and 3 compare to other areas identified in contact or in absence of contact with a-TiO_2.

Another aspect of identifying the interface of MtrC binding to a-TiO_2 is to think about the

dimensions of both particles and how this interface would help or hinder electron transfer from a-TiO_2 and MtrC. Both particles are similar in size, where the diameter of a-TiO_2 is about 5 nm and the size of MtrC is approximately 8 nm × 7 nm × 4 nm [93]. Thus it is likely that the binding interface might also span large areas of MtrC. In fact, all tree areas explored in Figure 3.12 seemingly surround domain IV, where, unfortunately, the peptide coverage detected by MS/MS was very low. Nevertheless, one might speculate that a-TiO_2 forms a large interface with the 'front' side of MtrC's haem containing domain IV. In a way, this is supported by the current knowledge of the structural orientation of MtrC, where MtrC is suggested to form a membrane facing interface with MtrAB via the 'bottom' side of domains I and II (see Figure 3.1) [93]. In this scenario, the closest haems to the interface with MtrA would be either haem 2 or haem 5, and other terminal haems (*i.e.*, haem 7 and 10) would be positioned away from the membrane and closer to external electron acceptors. Such arrangement would also provide interpretation for the observation that both MtrC and MtrCAB had very similar binding affinity to a-TiO_2 in the co-sedimentation assays. This can be explained as follows, metal binding occurs through exposed MtrC areas near haem 7 ad domain IV, which are also accessible within detergent-solubilised MtrCAB, and that MtrAB do not have additional metal binding sites.

All of the three MtrC areas explored in detail in Figure 3.12 are located close to a haem group, which could lead to a direct ET between MtrC and a-TiO_2. For instance, area 1 is near haem7, area2 - near heam 1 and area 3 is not too far from haem 10. Similar areas have also been identified in the binding interface between hematite and the MtrC-homolog MtrF. [134] Fukushima and colleagues attributed the binding being governed by complementary electrostatic interaction between negatively charged hematite and positively charged pocket near haem 7 (*i.e.*, corresponding to area 1 of MtrC). In addition, mutational studies of residues located within this pocket lead to changes in the binding affinity to hematite. [134] The fact that MtrC also has a similar positively charged binding pocket near haem 7 could suggest a more universal binding strategy between these cytochromes to a range of metal oxide minerals. In addition, haem 7 has the highest redox potential of all haems (*i.e.*, 0.07 V for haem 7, the second highest potential being 0.01 V for haem 5, while the lowest redox potential is -0.28 V for haem 9) as has been identified in a molecular dynamics simulation. [172] These observations highlight a possibility that the haem 7 could be the main route for direct ET out of the cell and to the mineral. Unfortunately, lack of MtrC coverage and resolution in the current XFMS study limits our abilities to address these questions. One way to further explore these questions is to perform a wide range of protein footprinting assays. For example, different sent of proteases could be used to gain peptide coverage of the missing domain IV. In addition, these XFMS assay could be coupled with FPOP and HDX assays

to probe changes in the solvent accessibility of protein and, perhaps, further increase the resolution of protein footprinting. Other assays such as mutational analysis coupled with electrochemical assays are required to assess how mutations in protein around haems 1, 7 and 10 change electron transfer properties within MtrC and between MtrC and a-TiO_2.

The original question for the work described in this chapter was to map where and how MtrC binds to a-TiO_2. This was done to identify protein areas and strategies how these areas or particles could be modified to optimise ET from a-TiO_2 to MtrC. Unfortunately, XFMS experiments yielded incomplete protein coverage with many crucial protein areas being missing (*i.e.*, surrounding haems). Nevertheless, the available data identify multiple peptide residues scattered around the protein, with highest protected areas being nearby haem 1, 7 and 10. The scattered results of X-ray footprinting also reinforce assumption that this binding interface is relatively non-specific and guided by complementary electrostatic interactions. Thus particles with different surface modifications (*e.g.*, a-TiO_2, DHBA-TiO_2 and **RuP**-TiO_2) will have different binding properties to MtrC. This was indeed observed in co-sedimentation experiments comparing binding between MtrC and a-TiO_2 and other TiO_2 modified with DHBA. DHBA-TiO_2 showed superior binding affinity and were able to bind 50% of MtrC with half as much TiO_2 particles as a-TiO_2 (50% binding of a-TiO_2 occurred at 1:1 particle ratio). A key question for future work is to understand how the current results of a-TiO_2 binding interface with MtrC relate to the interface with dye-sensitised light-harvesting version of TiO_2 particles (*e.g.*, **RuP**-TiO_2). As the work described in this chapter identified protein areas similar to those identified by Fukushima *et al.* [134] using MtrC homolog protein MtrF and hematite nanoparticles, it is possible that the interface between these decahaem proteins and inorganic nanoparticles is qualitatively similar irrespective to the differences in particle surface. Further experiments are needed to address this and could involve measuring and mapping the MtrC binding interface and affinity with TiO_2 NPs of different sizes and with different surface modifications, as well as comparing the MtrC binding affinity for a-TiO_2 to that of hematite. In addition, other assays including mutational analysis, molecular dynamics simulations and circular dichroism spectroscopy could be used to probe changes in protein structure and potential binding interactions between a mineral and the protein. This would also clarify the contrasting observations where structural rearrangements of OmcA and MtrC were reported for binding with hematite, though no major structural changes were observed upon binding of MtrF and hematite. [134, 147, 149, 150]

3.5 Conclusion and future work

The work described in this chapter explores the interaction between MtrC and a-TiO_2, identifying particle binding within 1:1 and 3:1 binding between MtrC and a-TiO_2 and DHBA-TiO_2, respectively. The main question was to identify the interface of MtrC and a-TiO_2 nanoparticles. Overall these aims were achieved only partially due to incomplete MtrC coverage in XFMS analysis. Despite this several MtrC areas were identified to be involved in the binding interface with a-TiO_2. Closer analysis of the protein structure and the protein surface charge within these areas did not provide conclusive insights into the nature of the interaction, but adds to the growing evidence suggesting the necessity of complementary electrostatic interactions and the role of bulky and rigid peptide residues able to facilitate beneficial conformation of the peptide binding site. The chosen approach of protein footprinting provided a 'map' for protein areas interacting with the a-TiO_2, however this approach must be coupled with other functional assays to determine the strength of interaction. In this work, co-sedimentation assays provided insight in some of these aspects (*e.g.*, indicating higher affinity to DHBA-TiO_2 than a-TiO_2). Futher experiments using other techniques (*e.g.*, isothermal titration calorimetry, quartz crystal microbalance with dissipation) are required.

This work illustrates the power protein footprinting approaches have to gain understanding of the interface between biomolecules and metal oxide material. These interfaces are of great importance for many applications involving ET, such as protein-electrode and microbial-electrode interfaces used to explore strategies for light-harvesting, improving microbial fuel cells or advancing such fields as microbial synthesis. [57,59,80,97,159,173] Similar interfaces are also relevant to medical settings, where nanoparticles could be used for different therapeutic and diagnostic applications, as well as assessing the environmental impact of nanoparticle pollution, created by increasing use of nanoparticles in cosmetics, textiles, paints, coatings and food packaging. [174] Understanding the interplay of physical forces and interactions behind these bio-mineral interfaces can lead to further engineering of both nanoparticles and proteins, which in turn could promote more effective and safer use of these nano-materials. However, in order to achieve detailed understanding of these bio-mineral interactions, complementary experimental assays and theoretical simulations should be used, such as protein footprinting to identify the binding interface together with assays quantifying the binding affinity (*e.g.*, co-sedimentation, isothermal titration calorimetry, quartz crystal microbalance with dissipation (QCM-D), DLS *etc.*) and mutational assays to validate hypothesis formed through these observations.

The next chapter focuses on next steps the couple light-harvesting TiO_2 (*e.g.*, **RuP**-TiO_2) with full

MtrCAB protein complex and to construct light-harvesting compartment.

Chapter 4

MtrCAB as a transmembrane molecular electron conduit for compartmentalized photocatalysis

4.1 Chapter introduction

Chapter chap1 introduced the vision for demonstrating and liposomal compartment for solar energy capture. Figure 4.1 a provides a recap of the envisioned system, where light energy is captured by a light-harvesting nanoparticle (LHNP) located externally from liposomes. This energy is then used to excite an electron, which is then transferred across the membrane to the final electron acceptor (*e.g.*, catalyst producing fuel). This chapter introduces such compartment (Figure 4.1 b), where electrons from three different LHNPs are transferred across the membrane via integral membrane protein MtrCAB and used to reductively bleach an encapsulated red azo dye, Reactive Red 120 (RR120). The work behind this chapter aimed to demonstrate and assess the photo-electron transfer across the membrane using MtrCAB as an electron-conductive 'wire' (conduit) across the membrane. More specifically, it was aimed to test two key assumptions: 1) the ability to improve electron separation fom LHNP by using MtrCAB as a route for electron relay away from LHNP; 2) the ability to use the environmental separation by liposomes (*i.e.*, interior and exterior environment) to optimise such light-harvesting oxidation-reduction reactions.

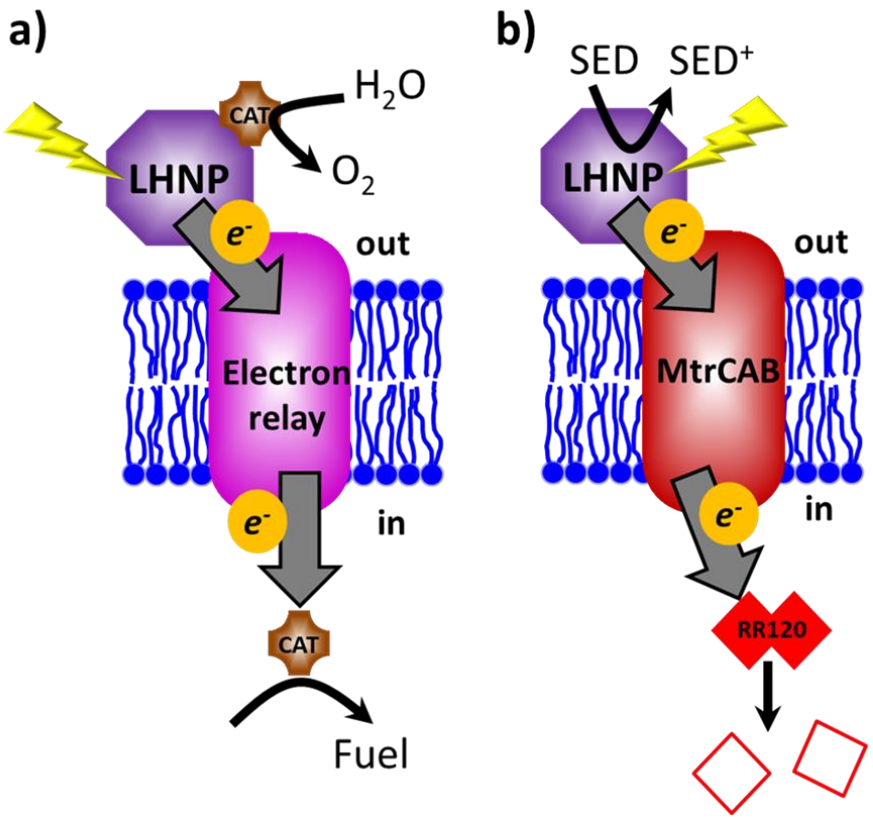

Figure 4.1: Schematic of light-driven electron transfer across the lipid membrane in the envisioned compartmentalised bio-mimicking system (a), and as presented in the model system in this chapter(b). **a**) External electrons are supplied photo-chemically from a light-harvesting nanoparticle (LHNP), which is regenerated by a water-oxidising catalyst (CAT). Electrons are relayed across the membrane to a catalyst (CAT) leading to fuel generation within the compartment. **b**) Electron transfer across the lipid bilayer is ensured via transmembrane protein complex MtrCAB and monitored following reductive bleaching of an internalised red azo-dye, Reactive Red 120 (RR120). SED – sacrificial electron donor. Figure adapted from [67].

In the envisioned compartment, electrons are transferred via MtrCAB to the liposome lumen, where they could generate fuel (such as hydrogen) by a fuel-generating catalyst. This chapter focuses on the proof-of-concept compartment, where the electron transfer across the membrane is optically monitored at 539 nm by a destructive reduction of an encapsulated azo dye, Reactive Red 120 (RR120, Figure 4.2). [175–177] RR120 contains two azo bonds (R–N=N–R'), each of which requires a transfer of four electrons in order to be cleaved to a colourless (pale yellow) product (Figure 4.2 c), *i.e.*, 8 electrons per RR120. [176] The optical signatures revealing the redox status of MtrCAB haems (Figure 4.3) are also monitored.

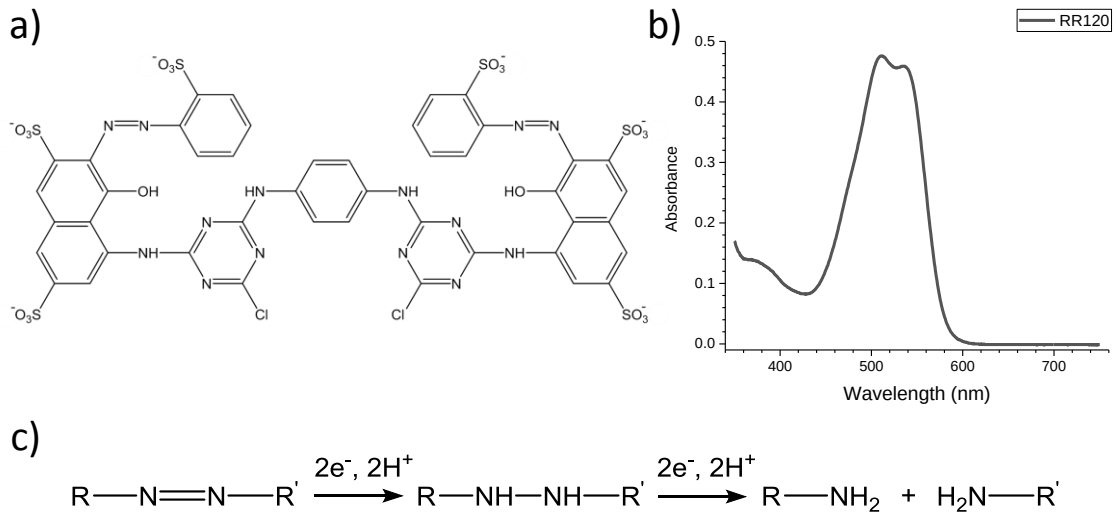

Figure 4.2: Characteristics of the RR120 azo-dye and its reactivity. The chemical structure of RR120 (**a**) and absorbance spectrum of 15 μM RR120 (**b** in MOPS buffer (20 mM MOPS, 30 mM Na_2SO_4, pH 7.4). (**c**) Schematics of the reduction reaction of an azo group.

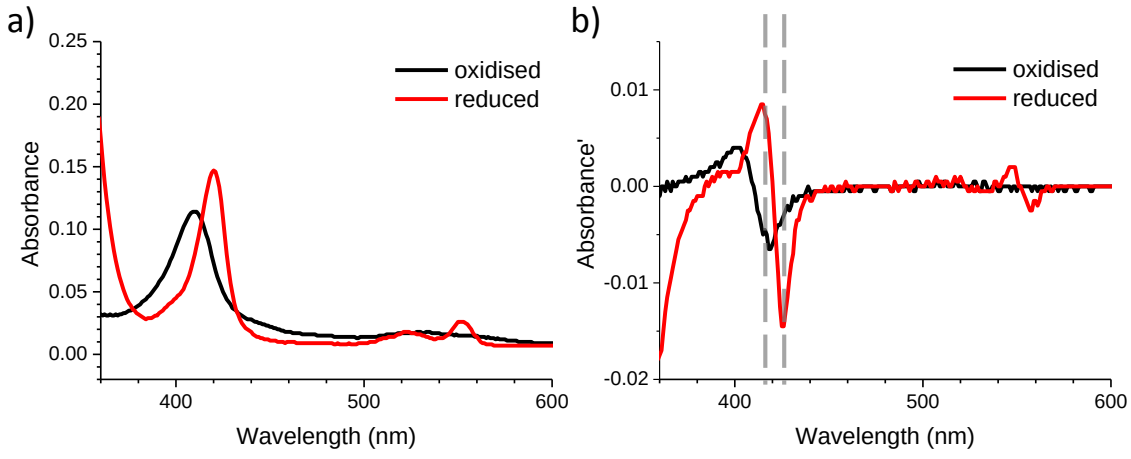

Figure 4.3: MtrCAB absorbance (a) and the 1st derivative of MtrCAB absorbance (b). Black – oxidised MtrCAB, Red – MtrCAB reduced by dithionite. Dashed lines indicate wavelengths selected to assess haem reductionby calculating the difference between them (*i.e.*, ΔA' = A'418 - A'426)). In this case ΔA' is -0.0035 and 0.02 for oxidised and reduced MtrCAB, respectively.

4.1.1 Summary of previous work, which led to the optimisation and creation of the MtrCAB compartment described in this chapter.

The work described in this chapter builds on the long-term collaboration and work with between previous members of the Jeuken group (*i.e.*, Dr Ee Taek Hwang, Dr Theodoros Laftsoglou), members of Prof. Julea Butt's group in the University of East Anglia (*i.e.*, Dr Emma Ainsworth, Dr Samuel Rowe and Sam Piper), and members of Prof. Erwin Reisner's group in the University of Cambridge. Many of the decisions concerning material selection and experimental procedures were thus taken based on conversations and meetings between these groups and building on the previous published and unpublished work. A lot of this work resulting from close collaboration between Dr Ee Taek Hwang and Dr Emma Ainsworth is described in the doctoral thesis of Dr Emma Ainsworth (see reference [85]). This dissertation describes studies of MtrC, OmcA and MtrCAB photoreduction using various different types of photosensitisers (*e.g.*, ruthenium complexes, Eosin Y, fluorescein, flavins) as well es experiments designing and optimising protocol for simultaneous liposome formation and MtrCAB incorporation through rapid dilution. This work also included testing encapsulation of various potential compounds that could be used as internal redox indicators and identified RR120 as a suitable indicator, which can be encapsulated in optimal amount within the liposomes and optimisation of lipid composition choosing to use *E. coli* lipids over chicken egg phosphatidylcholines, as *E. coli* lipids yielded better liposome formation in the presence of RR120. [85] This resulting protocol has been used for work presented in this chapter with minor modifications as described in section 2.2.1. The main reported difference is to exclude liposome extrusion step, which involves passing liposomes through nanoporous membrane (*e.g.*, pore size of 200 nm) to improve the homogeneity of liposome samples (*i.e.*, making liposomes to be more uniform in their size). This decision was made as a precaution as liposome extrusion might lead to temporary damage to liposome membrane and increase leakage of the encapsulated content and after experiments comparing liposome concentration and size distribution using nanoparticle tracking analysis (NTA) showed no meaningful difference between samples undergoing extrusion or without it (data not shown).

In terms of choosing LHNPs, I would also like to emphasize work by Dr Ee Taek Hwang, who tested electronic coupling between MtrC protein film and various TiO_2 NPs (see reference [63, 146]). This work led to identification of **RuP**-TiO_2 as a good candidate for light-harvesting step. And as it is discussed in the previous chapter (Chapter 3), TiO_2 nanoparticles seem to be able to directly bind MtrC, thus facilitating a close contact required for electron transfer from **RuP**-TiO_2

to MtrCAB. In addition, Prof. Erwin Reisner's group came to synthesize carbon dots showing promising light-harvesting properties and excellent water dispersion properties. [86, 88, 89] Two of these carbon dots, *i.e.*, amorphous carbon dots (*a*-CD) [86] and graphitic carbon dots with core nitrogen doping (*g*-N-CDs) [88, 89] were tested in experiments described in this chapter. As these carbon dot particles show excellent water solubility, it is assumed here that they do not form stable complexes with MtrCAB. However, the nature of this interaction still remains to be characterized (*e.g.*, by quartz crystal microbalance with dissipation (QCM-D) analysis or isothermal titration calorimetry).

4.2 Characterization of MtrCAB liposomes

MtrCAB proteoliposomes loaded with the dye RR120 were prepared as described in section 2.2.1. This proteoliposome protocol is based on spontaneous, stochastic liposome formation, where detergent-solubilised lipids and MtrCAB are injected in a higher (50x) volume solution to rapidly dilute the detergent below its critical micelle concentration (*i.e.*, concentration, where detergent forms self-assembled micelles within solution, which are able to solubilise lipid structures). As this is stochastic process every liposome preparation will yield a batch-to-batch variation due to small differences in the sample injection step and even small differences in lipid and detergent concentrations. These could be attempted to minimise by constructing a robotised version for the protocol, but that was beyond the scope of this project. The highest variation was for samples containing MtrCAB, where the success of MtrCAB reconstitution within liposomes varied from one reconstitution to another. Thus all the liposome estimates (*e.g.*, average liposome size and volume, amount of MtrCAB per liposome, amount of LHNP per liposome, speed of RR120 reduction) were calculated and compared within each liposome preparation. Only then the results which were independent of amount of MtrCAB (or had been normalised against variation in MtrCAB reconstitution) were compared between different liposome preparations.

(Proteo)liposomes from each preparation were characterized to determine their size, concentration and amount of reconstituted MtrCAB and encapsulated RR120 as described in sections 2.2.1 and 2.3. Although the size of MtrCAB proteoliposomes showed some batch-to-batch variation, the majority of proteoliposomes were consistently between 100 and 200 nm in diameter (Figure 4.4). The reconstitution protocol generated about 10^{13} liposomes/mL and thus an estimated total lumen volume in the order of 10-30 μL per mL of sample. Approximately 43% (SD = 13%, n =3 different liposome preparations) of initial MtrCAB was present in the reconstituted proteoliposomes with an estimated ratio of 10-50 MtrCAB proteins per liposome

(depending on liposome size) assuming an even distribution across the liposomes.

Estimation of the amount of RR120 encapsulated in MtrCAB proteoliposomes was performed spectroscopically using optical absorbance at 534 nm ($\epsilon_{534nm} = 31.83\ \mathrm{mM^{-1}cm^{-2}}$ was determined using titration). It was estimated that, on average RR120 concentration in liposome lumen was 10 mM, *i.e.*, the same order of magnitude as during liposome formation.

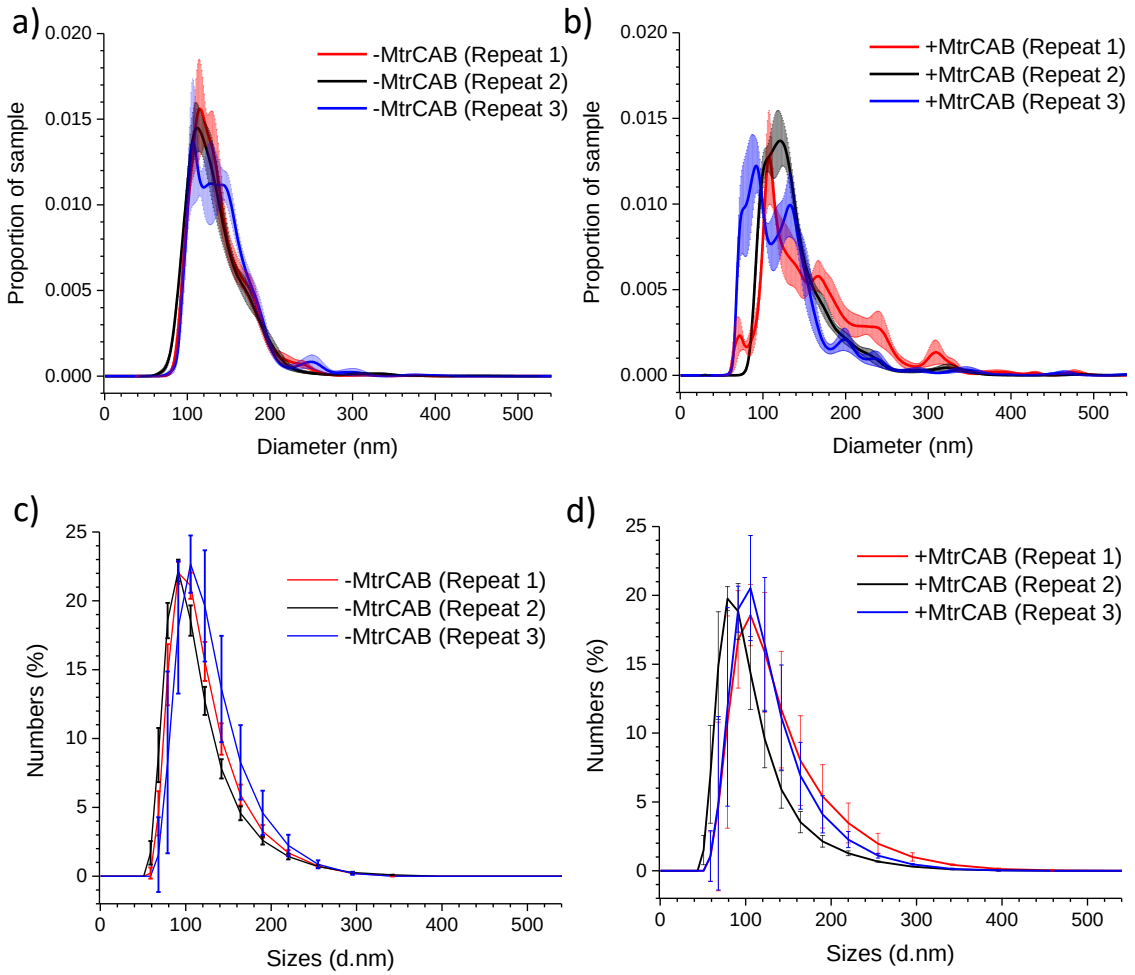

Figure 4.4: Size distribution of liposomes without MtrCAB (control) and liposomes with MtrCAB (a, c and b, d, respectively) determined from nanoparticle tracking analysis (NTA) (a,b) and dynamic light scattering (DLS) (c, d). Shaded area in NTA data represents the standard error for each sample, whereas the error bars in DLS represent the standard deviation (n=3) for each sample. Bin size for NTA is 0.5 nm. Repeats 1 - 3 represent liposomes from three separate sample preparations.

4.3 MtrCAB provides electron transfer across the bilayer

The ability of MtrCAB to transfer electrons across the membrane and reductively degrade RR120 was confirmed using an excess chemical reductant (dithionite, DT; Figure 4.5). DT (Em ≈ -0.41 V vs SHE at pH 7.4) [178] reduced MtrCAB (haem potential window ranging from -0.45 to 0 V vs SHE) [179] within the time resolution of the experiment ($<$ 20 s), as indicated by a shift of MtrCAB Soret peak due to haem absorbance (from 410 to 420 nm, Figure 4.5 b). This is followed by a slower (minutes) decrease of RR120 absorbance (450-570 nm, RR120 becomes reductively bleached at ≤ -0.4 V vs SHE [180]), confirming the destructive reduction of the encapsulated RR120. Only ≈10% of RR120 was reduced in control experiments using liposomes without MtrCAB, indicating that RR120 is protected from reductive bleaching when inside liposomes and that reduction of encapsulated RR120 proceeds only if MtrCAB is present (Figure 4.5 a). As a positive control, detergent (Triton X100, TX) was added at the end of the experiment to lyse the liposomes. This is followed by the immediate reductive bleaching of any remaining and now released RR120 (Figure 4.5 a and b, green lines). The rates of reduction of encapsulated RR120 were observed to vary between MtrCAB proteoliposome preparations, likely due to the fact that MtrCAB recovery yields varied (see section 4.2). For this reason, (photo)reduction of encapsulated RR120 by different reductants (*i.e.*, DT, LHNPs) was compared using proteoliposomes from the same preparation. In such studies the relative rates of RR120 reduction by the different LHNPs are as reported by the representative data. The chemical reduction using DT was used as indicator for the rate of electron transfer across the membrane, where electron supply to MtrCAB is not limited.

As mentioned earlier, the amounts of MtrCAB incorporated within liposomes varied between different liposome preparations. As MtrCAB is key for electron transfer across the membrane (and thus the reduction of encapsulated RR120), this batch-to-batch variability limited options to quantitatively and reliably compare the chemical reduction of RR120 between samples from different liposome preparations. Thus the data shown in Figure 4.5 is a representative example. For this same reason, reduction of encapsulated RR120 by different reductants (*i.e.*, DT, LHNPs) was compared primarily using proteoliposomes from the same preparation. In addition, Figure 4.5 also includes an exponential ($y=e^{-Ax}$) and a linear (y=kx+b) fit to the data, which are primarily meant to be guides for the eye. Having said this, these could also be used as very primitive data representations of the RR120 absorbance decay over time. In such case these fits can be use to extract a rate constant for RR120 decay, which in turn could be normalised to the amount of

MtrCAB per sample and lead to data, which could be compared across liposome samples from different MtrCAB proteoliposome preparations. This approach will be further discussed later in section 4.4.1.

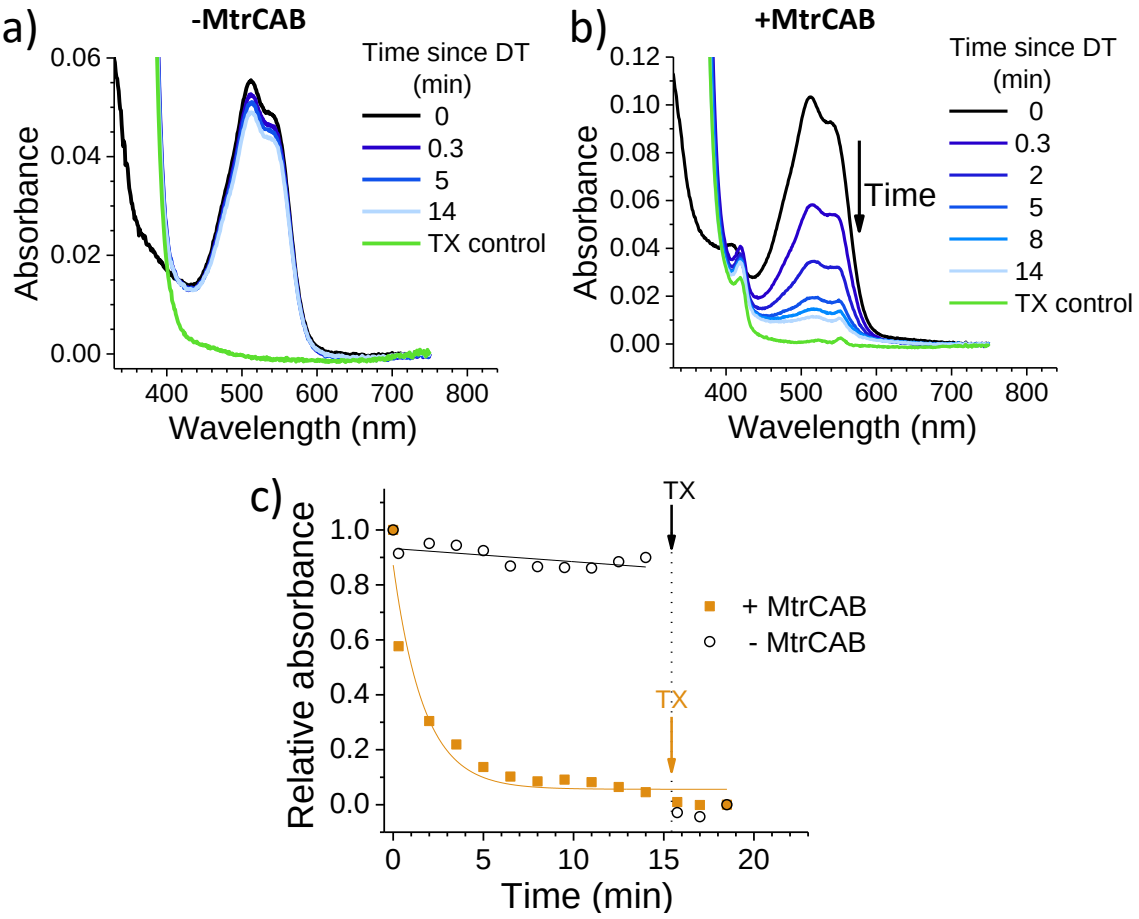

Figure 4.5: A representative example of chemical reduction of encapsulated RR120 by sodium dithionite (DT) in control liposomes without MtrCAB (a) and with MtrCAB (b) Reduction is followed optically by monitoring absorbance of MtrCAB haems (oxidised peak at 410 nm, reduced peak at 420 nm) and RR120 (oxidised 450-570 nm region). Black – oxidized sample; Blue – intact liposomes after addition of sodium dithionite; Green - sample after disruption of proteoliposome bilayer by detergent (Triton X100, TX). Time points indicate the time passed since the addition of DT. (**c**) Decrease of RR120 absorption (λ = 539 nm) over time using liposomes with and without MtrCAB. Yellow and black lines show exponential ($y=e^{-Ax}$) and linear (y=kx+b) fits to the data, respectively. These fits serve primarily as guides to the eye and are very primitive data representations of the RR120 absorbance decay over time.

4.4 Photoreduction across the membrane

Three different photosensitisers, *i.e.*, **RuP** dye sensitized TiO_2 nanoparticles (**RuP**-TiO_2) [63], amorphous carbon dots (*a*-CD) [86] and graphitic carbon dots with core nitrogen doping (*g*-N-CDs) [88, 89], were tested for photoreduction of RR120 encapsulated in liposomes with and without MtrCAB (Figure 4.6). All LHNPs have been previously shown to have sufficiently low reducing potential ($<$ -0.45 V vs SHE) [57, 89] to be able to reduce methyl viologen, and thus MtrCAB and RR120. Consistent with the data above, in the absence of MtrCAB, the majority ($> 70\%$) of RR120 was protected from photoreduction inside the liposome compartments (Figure 4.6 a). However, subsequent addition of DT to all samples showed that slightly more RR120 was reduced in samples exposed to *g*-N-CD and **RuP**-TiO_2 compared to 'DT only' control (compare black open circles to blue data points in Figure 4.6 a). This could suggest that small amounts of RR120 are released from liposomes due to interactions between **RuP**-TiO_2/*g*-N-CD and the liposomes. To further quantify this, well-established vesicle leakage assays were performed using a self-quenching dye, carboxyfluorescein (see publication on this method in reference [181]). No significant leakage was observed upon addition of any of the LHNPs, indicating no or very limited damage is incurred to the vesicles by the LHNPs (data not shown).The association of **RuP**-TiO_2 and liposomes was also probed using cryo-TEM (Figure 4.7), which indicated that **RuP**-TiO_2 particle self-agglomeration within the liposome sample without clear association with liposome in the presence and absence of the MtrCAB.

In the presence of MtrCAB, all three LHNPs photo-reduced the encapsulated RR120 (Figure 4.6 b). As before, photoreduction of encapsulated RR120 by different LHNPs was compared using proteoliposomes from the same preparation to limit influence of the variations of the amount of MtrCAB being reconstituted in different liposome preparations. The following discusses the example dataset presented in Figure 4.6 b). These experiments used 1 μM LHNPs, with an estimated ratio of 45 $\pm$ 2 LHNP per MtrCAB. **RuP**-TiO_2 and *g*-N-CD showed the fastest photoreduction, but with a rate lower compared to DT. Both *g*-N-CDs and *a*-CD showed a short 1–2 min delay from the start of irradiation till the onset of RR120 photoreduction. This delay is further referred as the 'lag phase' throughout this chapter. The name of the 'lag phase' is a reference to term used to describe bacterial growth characteristics, where cells are metabolically active and adapting to environmental conditions, but do not multiply. This is then followed by the active growth phased called 'log phase', when cells numbers grow in exponential fashion. Here, I use the term 'lag phase' to describe observed lack of initial photo-activity of carbon dots defined as period of time from the onset of sample illumination till the first signs of RR120 photoreduction.

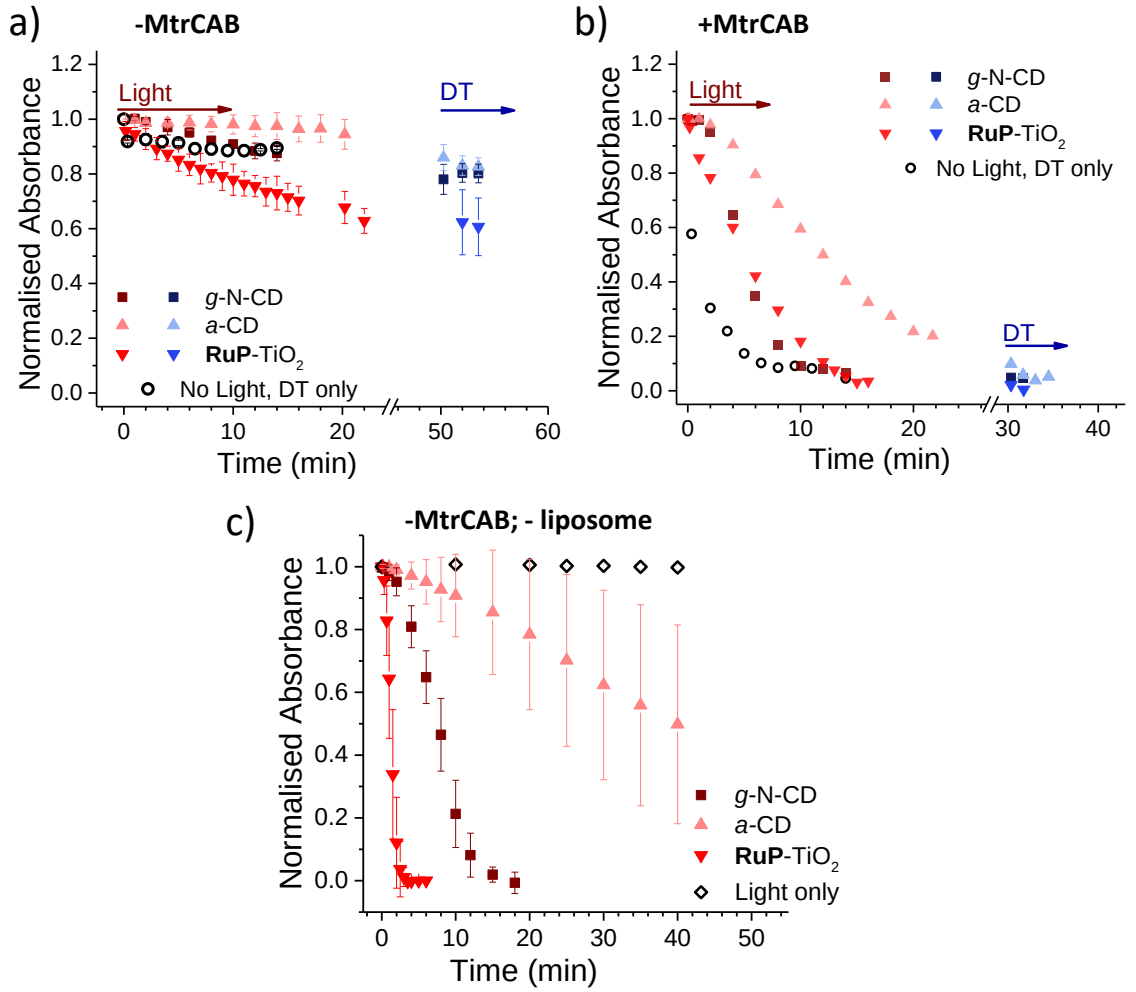

Figure 4.6: Photoreduction of RR120 encapsulated in control liposomes without MtrCAB (a, error bars indicate standard deviation for liposomes without MtrCAB from 3 different preparations), in MtrCAB proteoliposomes (b, representative sample using liposomes from the same preparation), and in control sample without liposomes and MtrCAB (c, error bars represent standard deviation, n=3). RR210 photoreduction is followed by a decrease in the RR120 absorbance at 539 nm. Squares – *g*-N-CD; Upward triangles – *a*-CD; Downward triangles – **RuP**-TiO_2; Red – sample after irradiation; Blue – sample after addition of DT; Black circles – chemical reduction using DT added at t=0 and without irradiation. Time points indicate cumulative time of irradiation. In case of DT, the time of DT addition is arbitrarily set to 50 and 30 min for (**a**) and (**b**), respectively, and following time points indicate time passed since addition of DT. (**c**) Direct photo-reduction of 10 μM RR120 in solution by LHNPs. White rhombus – irradiation of RR120 without LHNPs.

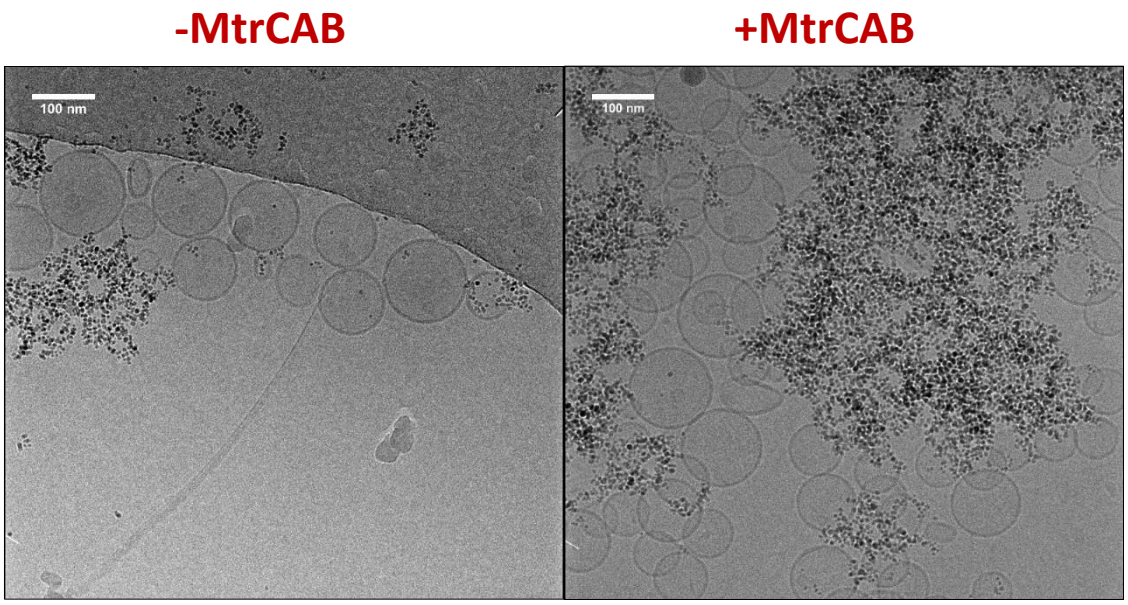

Figure 4.7: Cryo-TEM of *E. coli* liposomes without reconstituted MtrCAB (control) and with reconstituted MtrCAB mixed with RuP-TiO_2 NPs. RuP-TiO_2 agglomerates formed within 2-5 min after transfer from water to liposome sample.

Such initial period of carbon dot inactivity has been also observed by our collaborators in Prof. Erwin Reisner's lab, where they attribute this to surface heterogeneity or contamination that must be first reduced before achieving full activity of carbon dots (information shared through verbal communication).

The quantification of MtrCAB haem photoreduction by all three LHNPs was also attempted. Unfortunately, haem difference spectra could not be used due to spectral overlap with changes in RR120 and DT absorbance. Instead the first derivatives of all spectra were used as this is less sensitive to the background absorbance (Figures 4.3 and 4.8). This approach showed that DT immediately and fully reduces MtrCAB (4.8 a). Most MtrCAB is photoreduced by **RuP**-TiO_2 within the first minute of irradiation (4.8 b). In case of *g*-N-CDs and *a*-CD (4.8 c and d, respectively), it appeared that MtrCAB became reduced after several minutes, a time that coincides with the initial 'lag phase' of RR120 reduction (*i.e.*, initial carbon dot inactivity). After the lag phase, MtrCAB appeared to be fully reduced by *g*-N-CDs, whereas only partial MtrCAB photo-reduction seem to be observed by *a*-CDs. This suggest that with *a*-CD, photo-reduction of RR120 is in part rate-limited by the photo-reduction of MtrCAB. Thus the data shown in Figure 4.8 allows to observe the electron transfer function of MtrCAB in action, showing that electron supply to MtrCAB from **RuP**-TiO_2 and *g*-N-CDs is sufficient and the rate of RR120 reduction depends mainly on the number of MtrCAB present and the electron transfer from MtrCAB to RR120. In contrast, *a*-CDs were not able to fully reduce MtrCAB and further work on optimising the photo-

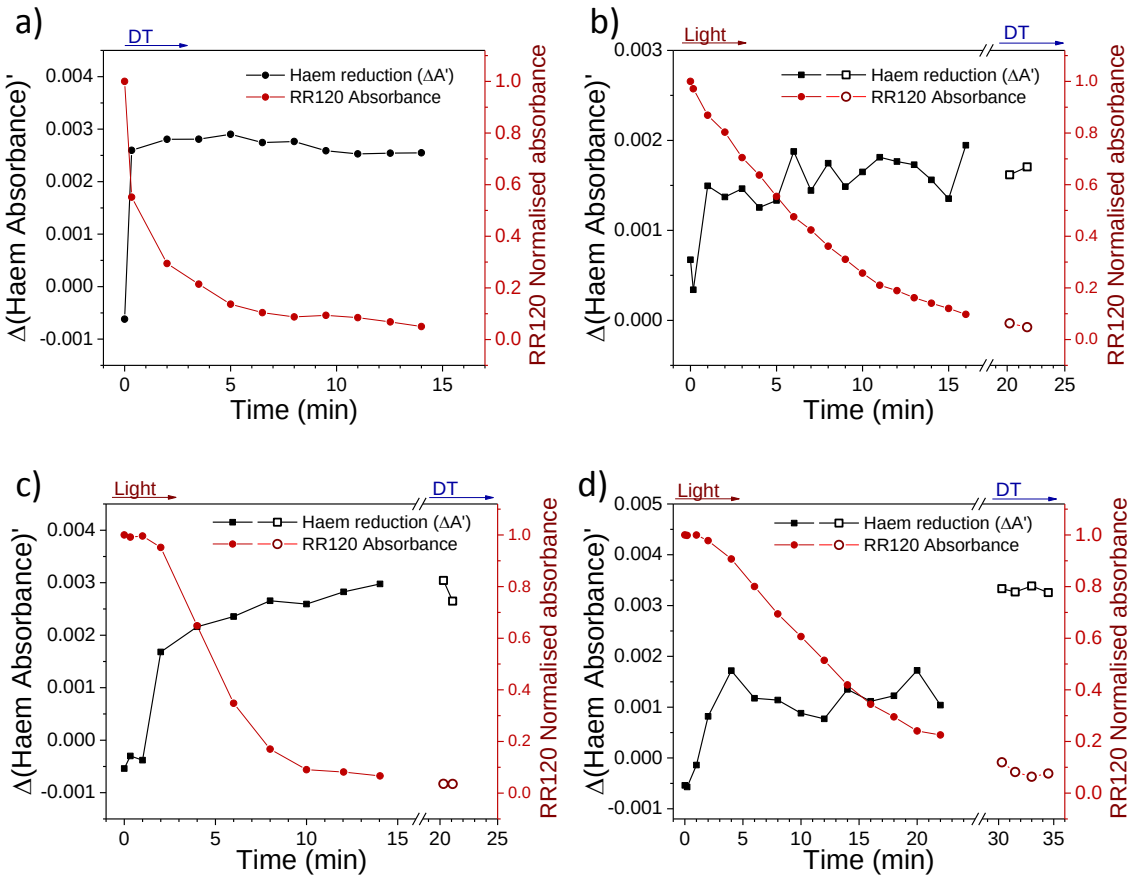

Figure 4.8: Reduction of MtrCAB haems and RR120 by DT (a), RuP-TiO_2 (b, *g*-N-CD (c) and *a*-CD (d)). (**a** - **d**) Photoreduction of MtrCAB haems as observed by changes in the 1st derivative of haem absorbance (scale on the left, black) and photoreduction of RR120 encapsulated in MtrCAB proteoliposomes (scale on the right, red). Time indicates duration of total illumination. DT – dithionite is included as indicator of fully reduced haems.

activity of *a*-CDs and the interaction (*i.e.*, binding) between MtrCAB and *a*-CDs could help to improve electron transfer from *a*-CDs to MtrCAB.

Finally, photo-reduction of RR120 in the MtrCAB proteoliposomes was compared to the direct photo-reduction of non-encapsulated RR120 (Figure 4.6 c). **RuP**-TiO_2 showed faster photoreduction compared to the MtrCAB proteoliposomes, clearing $> 90\%$ in less than 2 min, in line with conclusion that reduction in proteoliposomes is rate limited by the interaction between RR120 and MtrCAB. In contrast, *g*-N-CDs and *a*-CDs took significantly longer to directly photo-reduce RR120 compared to MtrCAB proteoliposomes, *i.e.*, about 20 minutes for *g*-N-CDs and for *a*-CDs it took more than 40 min to reduce even 50% of RR120. Both LHNPs also showed longer and more variable kinetics, with lag phases up to 5 min for *g*-N-CDs and 10-20 min for *a*-CDs. These variations in photo-reduction could reflect heterogeneity within carbon dots, as observed before. [182, 183]

4.4.1 Fitting and comparison between different liposome preparations

As discussed earlier the major limitation for comparing experimental data across samples is the high variation of MtrCAB reconstitution from one preparation to another. One way to overcome this is to estimating the rate of RR120 reduction by approximating the data of RR120 absorbance decay over time to a mathematical model (fitting data). An example of this is shown in chemical reduction of RR120 encapsulated in MtrCAB proteoliposomes as seen in Figure 4.5 c. In this case RR120 reduction via MtrCAB proteoliposomes was estimated to proceed as simple exponential decay (y=A^{-Ax}). The control sample without MtrCAB showed slow linear decrease (y=b-kx) in RR120, which is likely due to passive RR120 leakage out of the liposomes. Although this approach works for the chemical reduction of MtrCAB proteoliposomes (*i.e.*, assay using excess amount of DT as electron source), this can not be extrapolated easily to the photo-reduction experiments involving LHNPs, as these are more complex processes which do not reliably follow the rules of simple exponential decay. This is due to the RR120 photo-reduction reaction being influenced by:

- RR120 reduction being potentially limited by electron availability at 3 different stages: 1) photo-electron generation at LHNP; 2) electron transfer from LHNP to MtrCAB; 3) electron transfer from MtrCAB to RR120 (requires 4 electrons per azo-bond; 2 bonds per molecule);
- heterogeneity within carbon dot stock. Although the data was corrected for different 'lag

phases', it was observed that carbon dots exhibiting longer 'lag phase' were also photo-reducing RR120 slower;

- increased RR120 leakage from liposomes using **RuP**-TiO_2 and *g*-N-CD (as observed in control liposome experiments without MtrCAB);

- presence of some non-encapsulated RR120 on the outside of liposomes;

- liposome heterogeneity, where MtrCAB distribution per liposome was observed to vary between 10 and 50 (across different preparations) and a sub-population of liposomes might lack any MtrCAB;

- changes in RR120 reduction reaction by depletion of RR120 and accumulation of RR120 reduction products.

Given the complexity of the underlying process for RR120 photo-reduction, it was beyond the scope of this PhD to come up with a reasonable mathematical model to fit the data. Instead, I decided to estimate the initial rate of RR120 reduction using linear fit to the longest linear range after the onset of RR120 reduction (*i.e.*, after any determined 'lag phases' of carbon dots). This allows to estimate the initial rate of electron transfer from electron source (DT, LHNP) to MtrCAB and RR120 under optimal conditions for the reaction (*e.g.*, maximum electron supply and RR120 present in abundance). The results from control samples (*i.e.*, control liposomes without MtrCAB and direct photoreduction of RR120) were then directly compared across different sample preparations (see Table 4.1). The initial rate estimates for MtrCAB proteoliposome samples were then normalised to the number of MtrCAB present per liposome (calculated for each sample preparation) and then multiplied to the average amount of MtrCAB per liposome across all sample preparations (27± 17; SD, n=3). This approach provided a relatively simple way to compare initial RR120 reduction rate across different sample (and liposome) preparations and electron sources. The main caveat for this approach is that this method is itself error-prone as it imposes fitting a line to a subset of data which is not linear. This is seen in the error estimates for the final RR120 reduction rates (relative errors reach 70 and even 80%). The resulting data is shown in Table 4.1.

Table 4.1: Initial rate of RR120 reduction (%/min) using with MtrCAB proteoliposomes, control liposomes without MtrCAB and directly in control samples without MtrCAB and liposomes.

Electron source	**MtrCAB proteoliposomes (%/min±SD)**	**Control liposomes (%/min±SD)**	**Direct reduction in solution (%/min±SD)**
Dithionite (DT)	18±13	0.35±0.28	n/a (too fast to measure; <30 sec)
RuP-TiO_2	6.4± 4.2	1.35±0.10	60±12
g-N-CD	8.3±6.8	0.76±0.35	8.4±1.7
a-CD	2.7±1.8	0.24±0.19	0.93±0.39

n = 3; number of experimental repeats (different liposome prepations)

The estimates of the initial RR120 reduction rate in Table 4.1 neatly summarize what has been discussed before. **RuP**-TiO_2 showed the fastest direct RR120 photo-reduction, followed by *g*-N-CD and *a*-CD. However none of the LHNP were able to achieve as efficient reduction of MtrCAB as by chemical reduction with DT. This indicate that this system could potentially be optimised further by engineering better interaction between LHNPs and the MtrCAB. In addition, data on RR120 reduction control liposomes without MtrCAB in Table 4.1 confirms that **RuP**-TiO_2 does interact with the integrity of liposomes and seem to increase the leakiness of RR120. *g*-N-CD also increase the leakiness of liposomes, but does it half-as much as **RuP**-TiO_2.

4.5 Discussion

In plant photosynthesis, a lipid membrane is used as a scaffolding to arrange and spatially separate photosynthetic components between the different environments of thylakoid lumen and stroma. [50] In this chapter, liposome based nanocompartments are used to mimic such physical separation and show a biomimetic photo-reduction across an insulating lipid membrane, where energy generated by external LHNP is transferred across the lipid membrane via MtrCAB conduits to reduce electron acceptors located in the lumen of liposomes.

This system has several inter-facial electron transfer steps: 1) LHNP to MtrCAB, 2) MtrCAB to RR120 and 3) SED to LHNP (Figure 1.6 c). All experiments used excess amounts of SED (50 mM EDTA) and it has been previously shown that the SED is not rate limiting for photo-reduction of MtrC by **RuP**-TiO_2. [63] As MtrCAB provided the electron relay across the membrane,

the observed rate of RR120 reduction within liposomes will be dependent on the amount and distribution of MtrCAB within the liposome population. Chemical reduction of MtrCAB with DT was fast and instantaneous with respect to the time resolution of the experiments reported here. MtrCAB reduction by DT thus represent the fastest possible RR120 reduction within each liposome sample. The photoreduction by all three LHNPs was slower than reduction by DT, confirming that the overall rate of RR120 reduction was at least partly limited by the electron supply from LHNP to MtrCAB. However, for **RuP**-TiO_2 and *g*-N-CD, MtrCAB was almost fully reduced during the photo-reduction experiments, suggesting the reductive bleaching kinetics of RR120 were also rate limited by reduction of RR120 by MtrCAB. It is possible that electron transfer across the MtrCAB itself is influenced by the electron supply and demand on both sides of the membrane. MtrCAB orientation in liposomes is not known and likely random, possibly further complicating the observed kinetics.

TiO_2 has high affinity for Glu/Asp protein residues [184–186], and **RuP**-TiO_2 has been shown before to bind strongly to MtrC and MtrCAB [97]. In addition, **RuP**-TiO_2 showed the best direct photo-reduction of non-encapsulated RR120. Despite this, photoreduction of RR120 in MtrCAB liposomes with **RuP**-TiO_2 was slower compared to chemical reduction with DT. The faster photoreduction of non-encapulated RR120 is likely due to improved interaction between **RuP**-TiO_2 and RR120, where RR120 can interact with the whole surface area of **RuP**-TiO_2, which forms the interface for intermolecular transfer of light-excited electrons. In addition, RR120 contains several sulphate groups, which are known to bind to TiO_2 surface [187], thus **RuP**-TiO_2 and RR120 can establish close proximity facilitating intermolecular electron transfer. In the MtrCAB preteoliposome system electron transfer to RR120 occurs through the limited number of MtrCAB present in the liposomes (on average 27 MtrCAB per liposome; SD=17, n=3). (For context, LHNPs were in excess with 1206 LHNP per liposome; SD= 819, n=3.) In addition, **RuP**-TiO_2 self-agglomerate or aggregate within buffered solutions, as observed with cryo-electron microscopy analysis (Figure 4.7). Hence, the particle ratio and interaction between MtrCAB and **RuP**-TiO_2 might have been impaired further.

In contrast, the interaction between MtrCAB and both *g*-N-CDs and *a*-CDs is likely to be transient as no aggregation was detected upon mixing of the particles with MtrCAB liposomes. Nevertheless, for both carbon dots, relaying the electrons via MtrCAB improved total bleaching time of RR120 remarkably, which took up to four times faster in MtrCAB proteoliposomes compared to the direct photoreduction of RR120. This was also seen in the comparison between the initial RR120 photo-reduction rates shown in Table 4.1. As described earlier light-excited electrons are transferred from LHNP to other molecules (*e.g.*, RR120 or MtrCAB) from the surface

of LHNP, thus introduction of MtrCAB compartment limits the routes of electron transfer through the available amount of MtrCAB (as opposed to anywhere from LHNP surface; on average there were ≈50 times more LHNPs than MtrCAB). Interestingly, *g*-N-CD showed pretty much the same initial RR120 reduction rate in direct photo-reduction as with MtrCAB proteoliposomes (*i.e.*, 8.4±1.7 and 8.3±6.8, respectively). This suggests that MtrCAB improves the reaction rate to the levels that offset the MtrCAB 'bottleneck' within the electron flow path. *a*-CD, in turn, showed about 3 times more efficient RR120 photo-reduction within MtrCAB proteoliposomes than directly in solution. Encapsulation of RR120 at mM concentration in the small lumen of the liposomes (compared to 10 μM RR120 in the control experiments with direct photoreduction) will enhance reduction kinetics by MtrCAB and, indeed, reduction of RR120 by MtrCAB was not observed to be rate limiting for *a*-CD (where MtrCAB haems were partially reduced throughout the illumination, Figure 4.8). The enhanced photobleaching kinetics in the proteoliposome are thus due to a faster reduction of MtrCAB (at concentrations $\ll$ 10 μM) compared to free RR120. This enhancement is likely due to the MtrCAB conduit, which can accumulate multiple electrons on its 20 haems, improving the rate of the multi-electron reduction required to bleach each RR120 molecule. In this respect, MtrCAB is able to stabilise the charge separated intermediate for the photo-reduction of RR120, mimicking the role of the chlorophyl/pheophytin/QA electron relay of the natural photosystems I and II.

4.6 Chapter conclusion

This chapter demonstrated and assessed the proof-of-concept of using the transmembrane MtrCAB conduit for compartmentalized photo-reduction. The initial aims behind this work were to assess: 1) the ability to improve electron separation from LHNP by using MtrCAB as a route for electron relay away from LHNP and 2) the ability to use the environmental separation by liposomes (*i.e.*, interior and exterior environment) to optimise such light-harvesting oxidation-reduction reactions. Both of these aims were assessed testing three LHNPs. All three LHNPs showed efficient photo-reduction of a liposome-encapsulated dye using MtrCAB as an electron relay. Furthermore, MtrCAB improved the rate with which *a*-CD photo-reduced the encapsulated dye in the liposome system (as opposed to the non-encapsulated system). This example demonstrated how incorporation of a scaffolding material to separate photo-oxidation and reduction reactions can be beneficial for overall efficiency of solar energy harvest both in terms of using MtrCAB as electron relay (and accumulate electrons for such multi-electron reactions as reduction of RR120 azo-bonds) and using liposomal compartments for creating separate environments (and separate

and concentrate incompatible reactants of the reaction). In particular, it can be proposed that MtrCAB can aid in the stabilisation of the charge separated state, improving quantum efficiency. Such component could be beneficial to further advance artificial photosynthesis strategies and other (bio)nanocatalysis applications.

This bio-mimetic compartment for solar energy capture was intended to explore features of photosystem (*e.g.*, providing route for electron relay and environmental separation across the membrane) and proved to be able to change the dynamics of the photo-reduction reaction. Thus it is important to further explore strategies on how to physically arrange molecules and materials, which is not a simple task. Evolution has taken many billion years to perfect the composition of natural photosystems. The work described in this chapter illustrates some of the difficulties and the increasing complexity for assembling this system and assessing interactions between different molecular partners. Each of the molecular partners have their own properties, which can negatively interfere with the system. For example, **RuP**-TiO_2 tends to agglomerate and increase liposome leakiness. In contrast, both carbon dots were better for liposome membrane integrity, but also very soluble and thus are suspected to interact with MtrCAB only transiently.

The next step for exploring the potential use of MtrCAB conduit and nano-compartments is to test MtrCAB compartments for photosynthetic production of solar fuels or solar chemicals. In this case, a catalyst can be encapsulated in the liposomes, which enables a PS/LHNP to function in a separate environment from the fuel-generating catalyst. Chapter 5 summarizes work on trying to encapsulate such catalysts to produce hydrogen.

Chapter 5

Towards encapsulation of hydrogen evolving catalyst in lipid compartments

5.1 Chapter introduction

Chapter 4 describes how light energy is used to drive photo-electron transfer across the membrane for reductive bleaching of the encapsulated dye RR120. In short light energy was used to excite electrons at LHNPs. Then these electrons were transferred across a membrane via MtrCAB conduit and used to reduce an encapsulated azo-dye RR120 (Figure 5.1 a). The next step for demonstrating genuine compartmentalised photocatalysis within the lumen of the compartment is to change the final electron acceptor from RR120 (*i.e.*, using photo-excited electrons to reduce azo-bonds in the dye) to a fuel-producing catalyst (Figure 5.1 b). Such catalyst is required to complete the energy transformation from photons through photo-induced electron transfer to storing these electrons into chemical bonds of a synthesized compound such as producing gaseous H_2 as was discussed in the Chapter 1, section 1.5.3. In this case electrons transferred by MtrCAB reduce hydrogen/hydronium ions which are present within the lumen of the liposome due to the self-ionization of water (*i.e.*, $2H_O \rightleftharpoons H_3O + OH^-$) .

The aim of this chapter is to demonstrate a compartmentalised photo-catalysis of hydrogen production. In order to attempt this three different hydrogen evolving catalysts (HEC) were used: two types of platinum nanoparticles (*i.e.*, Pt_{syn} and Pt_{com}) and a hydrogenase HydA1. As introduced in Chapter 1, section 1.5.3, both Pt and hydrogenases are currently the benchmarks for showing the highest activity for hydrogen evolution. This chapter starts by determination of the catalytic and photocatalytic activity of the selected catalysts. The catalytic activity was measured

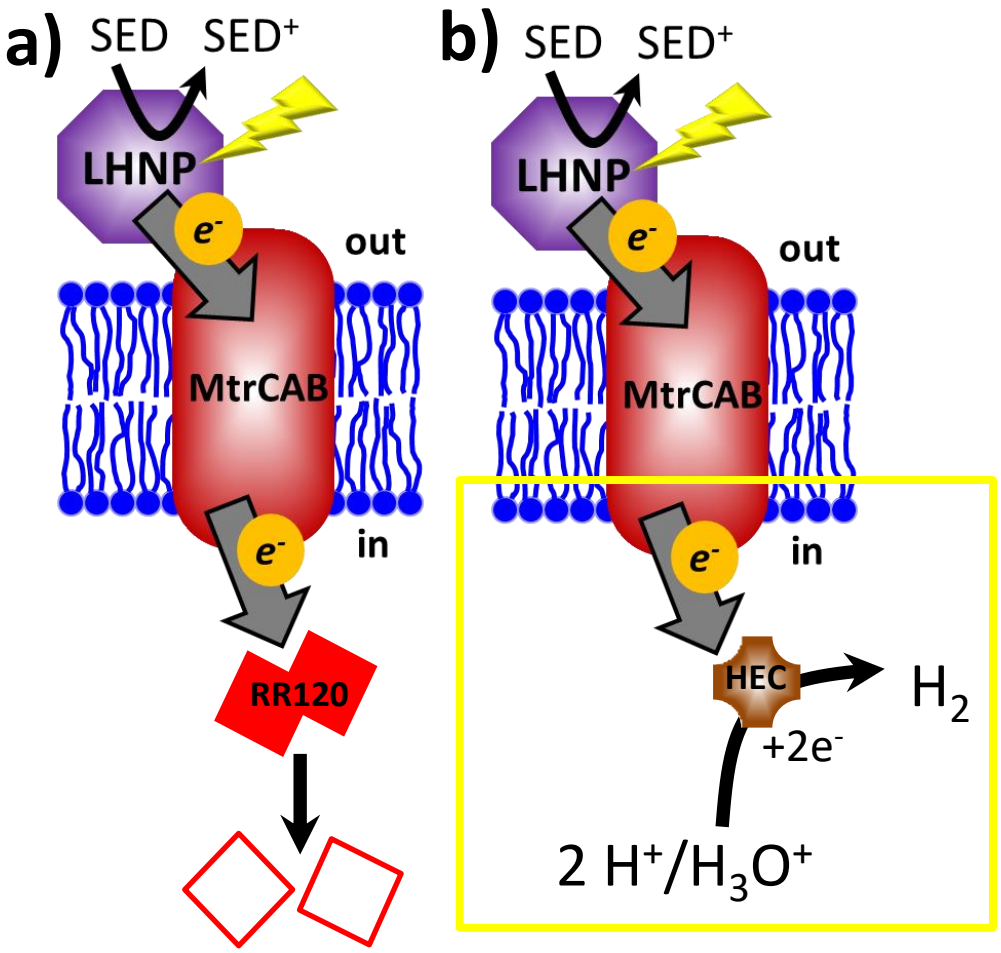

Figure 5.1: Schematic of light-driven electron transfer across the lipid membrane as was demonstrated in Chapter 4 (a) and as intended for work in this chapter(b). **a**) External electrons are supplied photo-chemically from a light-harvesting nanoparticle (LHNP) and then transferred across the lipid bilayer via transmembrane protein complex MtrCAB. This reaction is monitored following reductive bleaching of an internalised red azo dye, Reactive Red 120 (RR120). **b**) Electron electrons are relayed across the membrane via MtrCAB to a hydrogen evolving catalyst (HEC) leading to reduction of hydrogen/hydronium ions (present by self-ionization of water) and generation of gaseous H_2 within the compartment. SED – sacrificial electron donor. Figure adapted from [67].

using dithionite (DT) as chemical reductant and the photocatalytic activity was achieved after sample illumination with *g*-N-CD LHNPs. These experiments also tested how the H_2 evolution activity changes over time and whether addition of an electron mediator (*e.g*, methyl viologen, MV) improves or hinders the electron transfer from the electron source (*i.e.*, DT or *g*-N-CD) to the catalyst resulting in production of more H_2.

The chapter then describes the results for two different strategies employed to encapsulate HEC within the interior of liposomes. At first, liposomes are prepared by rapid dilution by adapting a liposome preparation protocol that was used previously for RR120 experiments in Chapter 4. This method of liposome formation by rapid dilution creates liposomes, reconstitutes MtrCAB and simultaneously encloses HEC catalysts present within the surrounding solution. However, rapid dilution is a stochastic process, thus it is difficult to control and reproduce the amount of catalysts that are encapsulated.

In order to gain better control over the catalyst loading within the compartment, a different strategy was explored using porous support material. In this case, HECs are trapped within a porous material (*e.g.*, porous silica), which is then enclosed by a supported lipid bilayer. This approach could provide higher control over catalyst loading (*e.g.*, the amount and reproducibility) by opening up the chemical space for manipulation (*e.g.*, pH, temperature, manipulation techniques) before introducing the fragile biological components to the system. Many studies have explored the use of silica as a solid support for such cargoes as chemical catalysts and pharmaceuticals. [188] Similarly, HEC could be trapped within silica nanoparticle, after which the HEC could be encapsulated by self-assembly of a membrane around the entire silica (SiO_2) nanoparticle. [18, 188, 189] Formation of a supported lipid bilayer containing functional membrane proteins has also been reported. [144, 190] In fact, Nordlund and colleagues have reconstituted functional cytochrome c oxidase in supported lipid membrane on porous silica and established proton-tight electrochemical gradient across these membranes. [190] This chapter explores use of two different types of supporting silica material. First, I test loading of Pt NPs into pre-formed commercial NPs. Then, I test the potential to achieve higher loading of Pt NPs by incorporating these during the synthesis of silica NPs.

Finally, the chapter concludes with a discussion of the results and the diversity of challenges that must be overcome to achieve reliable encapsulation of HECs within MtrCAB liposomes.

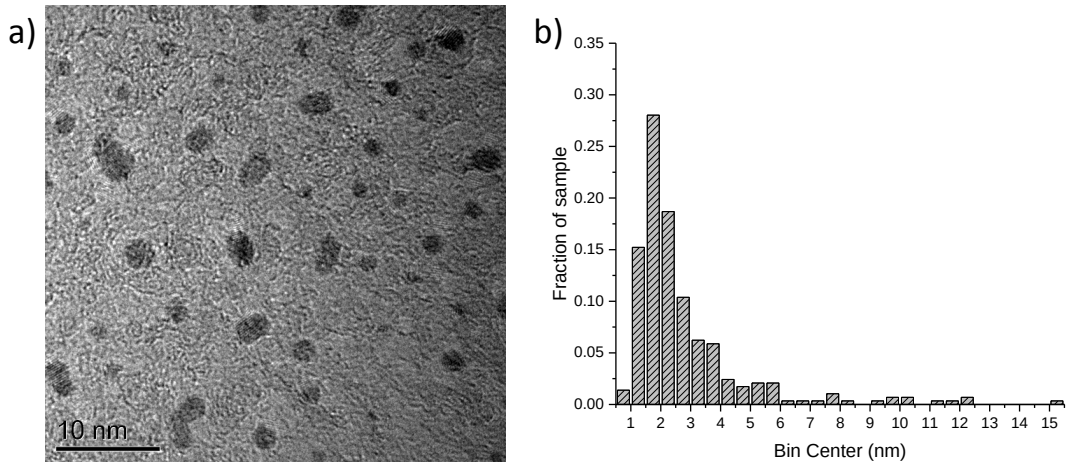

Figure 5.2: A representative TEM image (a) and the size distribution (b) of Pt$_{syn}$ NP observed by the TEM. n = 289, bin width = 0.5 nm, was chosen as a compromise between keeping sensitivity to the different sizes of NPs present in the sample and limiting the human error while performing manual particle measurements. (In these TEM images, 0.5 nm was around the level of reliable resolution by eye of Pt$_{syn}$ NPs vs. the background.)

5.2 Catalyst characterisation

5.2.1 Characterisation of the Pt NP size

Two types of Pt NPs were obtained - commercially purchased Pt NPs (Pt$_{com}$) and in-house synthesized Pt NPs (Pt$_{syn}$).The Pt$_{com}$ consists of 99.9% pure Pt and have an average particle size of 3 nm (specified by the manufacturer). Pt$_{syn}$ were synthesized as described in section 2.1 following previous work by Eklund and Cliffel, where glutathione was used as a capping agent to inhibit particle overgrowth and aggregation, and yield soluble NPs with an average size of about 2.5 nm. [111]

Both Pt$_{com}$ and Pt$_{syn}$ were imaged by the TEM as described in section 2.1. Pt$_{syn}$ are well dispersed particles with an average particle size of 2 nm (*i.e.*, diameter was measured for two different synthesis batches by TEM as 2.2 ± 0.3 nm, n=157 and 2.0 ± 0.3 nm, n=289; Figure 5.2).

TEM of the Pt$_{com}$ sample was performed by Dr Sunjie Ye. TEM revealed that although the individual particle size is ≈3 nm as specified by the manufacturer, many particles are present in much larger agglomerates (Figure 5.3 **a**). DLS of Pt$_{com}$ water dispersion confirmed the presence of particle aggregates between 100 - 200 nm (Figure 5.3 **b**).

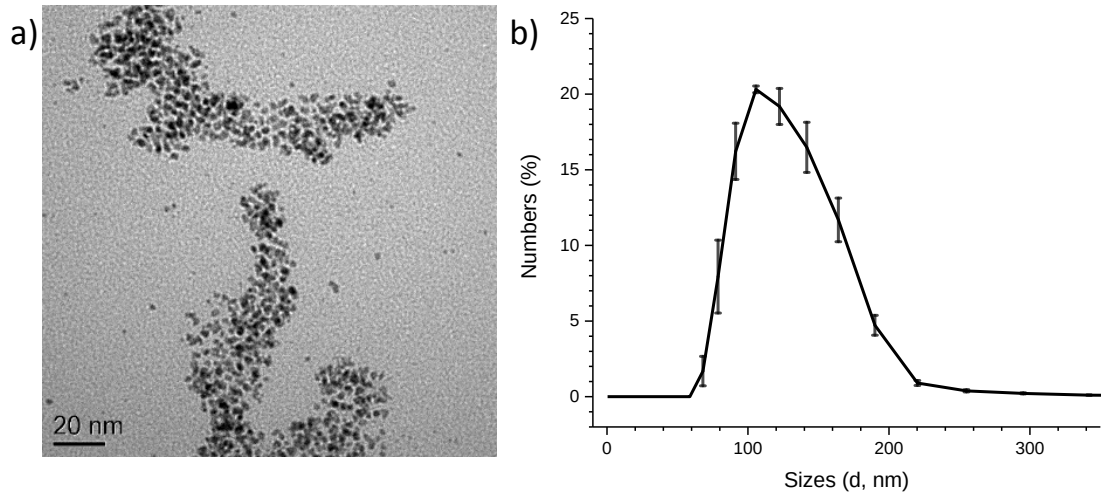

Figure 5.3: A representative TEM image (a) and the size distribution (b) of Pt_{com} NPs determined by DLS.

5.2.2 Characterizing the activity of Hydrogen evolution reaction (HER)

H_2 evolution of both Pt NPs and HydA were tested using a Clark-type electrode set-up as described in section 2.6. In brief, H_2 diffuses from the reaction chamber across a plastic (PTFE) membrane and is oxidised at the Pt anode (not to be confused with Pt_{com}/Pt_{syn}) kept at a constant potential of 0.6 V vs Ag/AgCl. [140] The resulting current is proportional to the concentration of dissolved H_2.

The activity of Pt_{com} was observed using excess amount of DT as the reductant (Figure 5.4). No current was observed from Pt_{com} until DT was added, which led to an immediate increase in current indicating H_2 production (Figure 5.4a). HER activity was estimated by a linear fit to the initial current increase and was recorded as ≈0.2 μmol H_2 min^{-1} mg^{-1} Pt_{com}. Over time, the current indicating H_2 evolution saturates and starts to decline. This might indicate poisoning of Pt_{com} surfaces by reaction by-products. It is well-known that Pt can be poisoned by CO and sulphur compounds such as SO_2, COS and H_2S. [107, 191] The products of dithionite decomposition contain HS^- and various sulphur-oxoacid salts, which could adsorb onto Pt_{com}. [192] Figure 5.4**b** explores how the activity of Pt_{com} changes upon adding electron mediator (methyl viologen, MV), which could further improve electron transfer from DT to Pt surface and improve H_2 production. And indeed, the presence of electron mediator (MV) increases the initial "burst" of activity, but it also leads to much quicker saturation and subsequent decline of H_2 evolution, suggesting that increased HER might lead to quicker accumulation of the Pt poisoning

by-products.

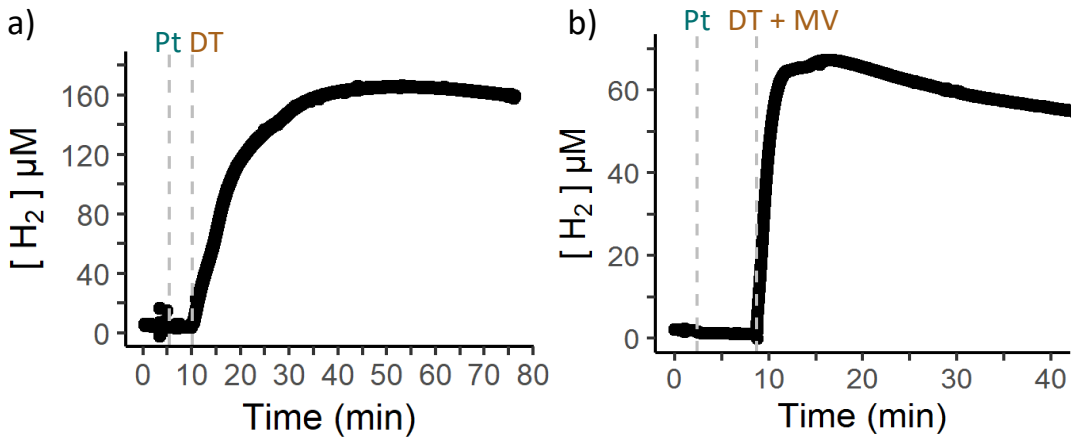

Figure 5.4: HER activity of Pt_{com} NPs using excess DT as electron source. Dashed lines indicate time-points when PtNPs, dithionite (DT) or methyl viologen (MV) were added to the reaction chamber. All experiments used 1 ml of 20 mM MOPS and 30 mM Na_2SO_4 buffer (pH 7.4) and 0.04 mg Pt_{com} . **a**) Experiment used 29 mM DT. **b)** Experiment involved 13 mM DT and 2 mM MV as additional electron mediator.

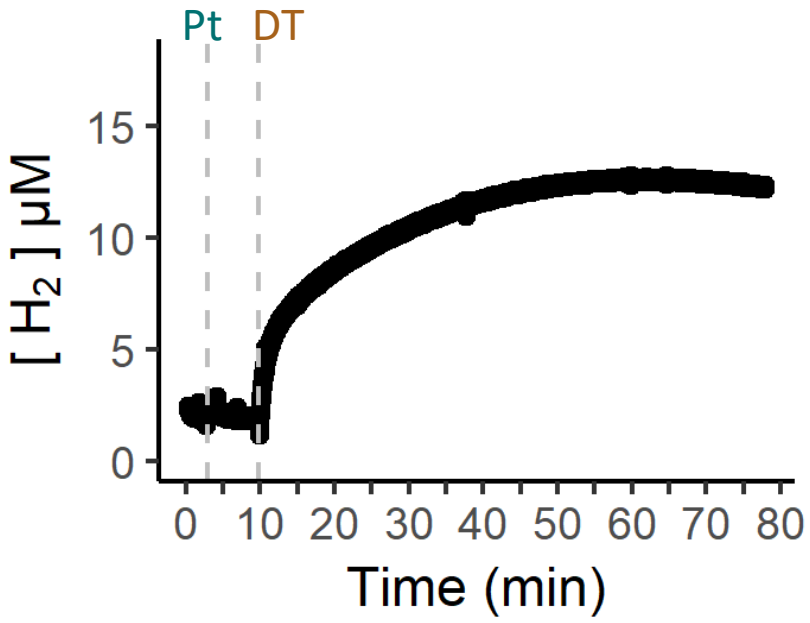

Figure 5.5: HER activity of Pt_{syn} NPs using excess DT as electron source. Dashed lines indicate time-points when PtNPs or dithionite (DT) were added to the reaction chamber. Experiments used 1 ml of 20 mM MOPS and 30 mM Na_2SO_4 buffer (pH 7.4) and ≈ 0.02 mg Pt_{syn} with 11 mM DT.

The activity of Pt_{syn} was determined as described above and is shown in Figure 5.5. Pt_{syn} showed lower HER activity (*i.e.*, ≈0.09 μmol H_2 min^{-1} mg^{-1} Pt_{syn}) than Pt_{com}, which is likely a trade-off for using glutathione as a capping agent to increase particle solubility and to prevent particle aggregation, and while doing so blocking the surface-active sites of Pt. [106] As seen with Pt_{com}, the H_2 evolution by Pt_{syn} also saturated and started to decline over time, indicating poisoning of Pt_{syn} surface. In order to test whether this surface poisoning depends on the activity of Pt_{syn} NP themselves or is purely influenced by the reaction conditions (*e.g.*, concentration of the breakdown products of DT), an experiment of stepwise addition of Pt_{syn} was performed (Figure 5.6). This showed that once H_2 evolution starts to saturate, it is not recovered by more Pt NPs indicating that the surface of freshly added Pt NP becomes immediately poisoned. In addition, further addition of even more electron source (DT) also did not help to restore HER even for short-term. Thus detection of the HER activity of Pt NPs using DT as an electron source is time sensitive and perhaps only reliable as a qualitative but not a quantitative method.

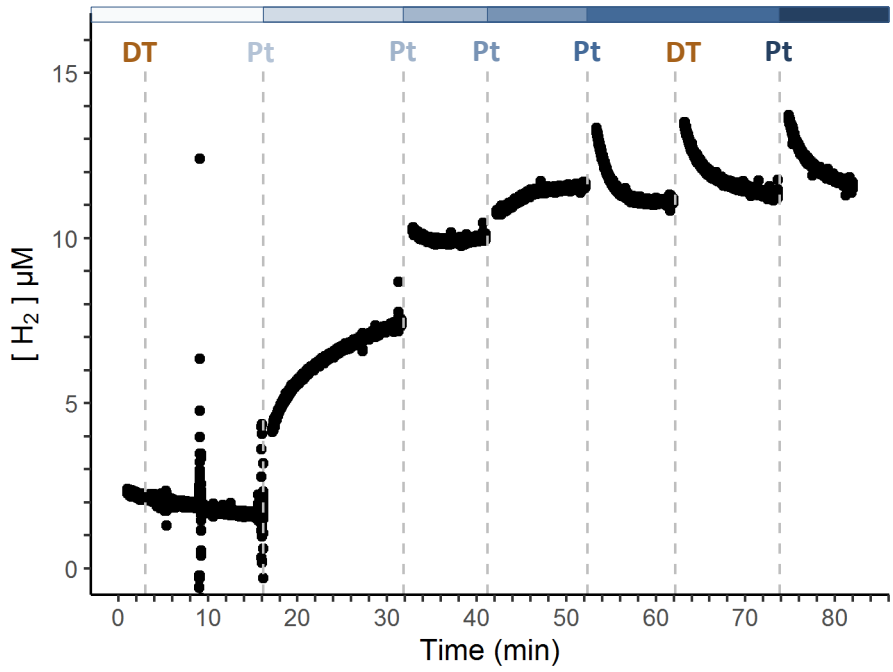

Figure 5.6: HER activity of increasing amounts of Pt_{syn}. The blue bar indicates increasing Pt amount corresponding to 0, 2.5, 3.5, 4.5, 5.5 and 6.5 arbitrary units of Pt. The precise amounts of Pt were not determined in this case, as the synthesized particles were subjected to additional cleaning step of particle precipitation using 1 : 2.5 v/v ethanol and re-suspension in water without measuring final amount of recovered Pt. Dashed lines indicate time-points when Pt NPs or dithionite (DT) were added to the reaction chamber. DT was added in two increments of 20 μl, 0.57 M resulting in concentrations of 11 mM and 19.5 mM. Experiment used 1 ml of 20 mM MOPS and 30 mM Na_2SO_4 buffer (pH 7.4)

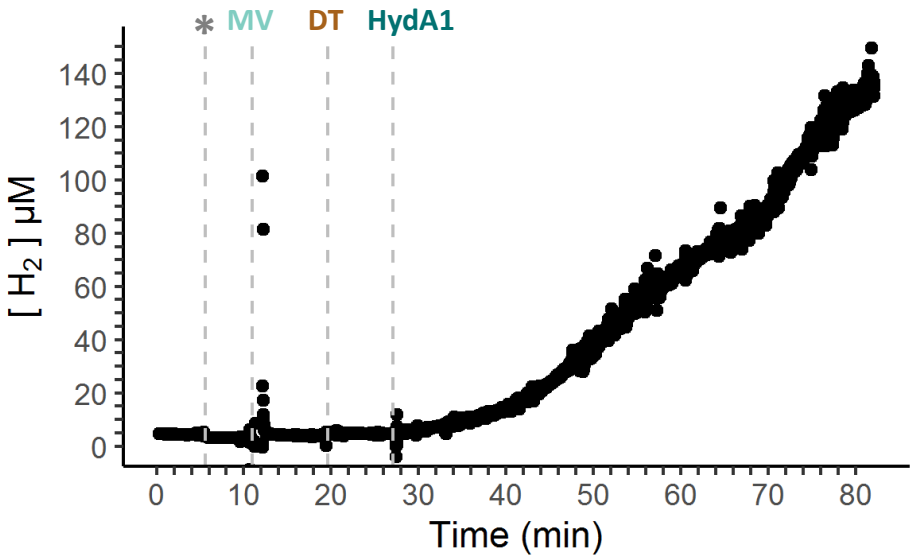

Figure 5.7: HER activity of HydA1 hydrogenase using excess DT as electron source and methyl viologen (MV) as electron mediator. Lines indicate time, when stated reaction components were added to the reaction chamber. The experiment involved 0.5 ml of 100 mM K-Pi buffer (pH 7.4), 10 mM MV, 100 mM DT, 4 nM HydA1. The asterisk indicates removal of some buffer.

The activity of HydA1 was observed using excess amount of methyl viologen (MV) and DT as an electron mediator and the electron donor, respectively (Figure 5.7). MV is typically used for measuring activity of hydrogenases, as the electron mediator often helps to ensure electron supply to the buried catalytic centre of the enzyme. [68, 107, 193] No H_2 was recorded after addition of MV and DT alone, until the addition of the HydA1. HER started as a slower initial phase (≈14 minutes), followed by a long linear increase. The region of this linear increase was used to estimate the catalytic activity of HydA1 as ≈13.0±7.8 μmol H_2 min^{-1} mg $HydA1^{-1}$ (n = 2). The recorded activity is about an order of magnitude lower than the activity reported for this particular protein batch received from Dr. Gustav Berggren (≈160 μmol H_2 min^{-1} mg $HydA1^{-1}$ measured at 28°C, 120 rpm, 10 mM methyl viologen, 100 mM Na-DT in 100 mM KPi pH 6.8, 15 minutes after Na-DT addition). This particular batch of HydA1 preparation had itself lower specific HER activity than was previously obtained by Dr. Gustav Berggren (700 - 800 μmol H_2 min^{-1} mg^{-1}) [112]. The lower activity most likely represents the difficulties to transport and preserve HydA1 in conditions that provide sufficient shielding from O_2 in the buffers, containers and atmosphere that might come in contact with the protein, as well as exposure to residual oxygen present in the experimental equipment (*e.g.*, the electrode set-up or solutions) despite working within the glovebox (O_2 < 0.01 ppm). The decreased catalytic activity might also be influenced by the lower temperature (room

temperature vs. 28°C used by Dr. Berggren group) and protein loss during sample transportation.

The photocatalytic activity of HECs

The photocatalytic activity of all three HECs were tested using the same electrochemical set-up supplemented with a light source as described in section 2.6 (Figure 5.8). *g*-N-CD was the most active LHNP in RR120 photo-reduction experiments in Chapter 4, and thus was selected for measuring photocatalytic HER by both Pt NPs and the HydA1 hydrogenase. All experiments used surplus *g*-N-CD and the initial HER activity (*i.e.*, before addition of MV or other components) was used to estimate the specific catalyst HER activity as 0.02, 0.005 and 2 μmol H_2 min^{-1} mg HEC^{-1} for Pt_{com}, Pt_{syn} and HydA1, respectively. Thus the HydA1 had the highest activity and, as noted previously, Pt_{com} was more active than Pt_{syn}. In these experiments electrons for H_2 evolution are supplied by *g*-N-CD, and to account for varying concentration of *g*-N-CDs the observed photocatalytic HER activity was estimated as 1, 0.07 and 200 μmol H_2 min^{-1} mg HEC^{-1} mg *g*-N-CD^{-1} for Pt_{com}, Pt_{syn} and HydA1, respectively. Due to time constraints, full characterisation and optimisation of the reaction kinetics was not performed (*i.e.*, optimisation of particle ratios between HEC and *g*-N-CD, determination how quickly Pt surface gets poisoned, determination if inclusion of electron mediator, *e.g.*, MV, improves or hinders HER initially and/or in long term). Some of these aspects are illustrated in Figure 5.8. Panel **b** attempts to observe change in the hydrogen evolution activity of Pt_{syn} after addition of electron mediator (MV), which did not seem to influence the activity significantly. The more Pt_{syn} and more *g*-N-CD were added, which did seem to result in a marginal increase in the rate of H_2 production (*i.e.*, steepness of the slope). MV was also tested for photo-catalytic HER by HydA1 (Figure 5.8 **c**). Presence of electron mediator (MV) also led to marginal increase in H_2 production, which is likely due to MV being able to improve electron transfer between *g*-N-CD and the catalytic site of HydA1. Overall, these observations confirm that photocatalytic HER is thermodynamically possible by combining these catalysts with *g*-N-CD as LHNP.

Illumination of the Clark electrode also generates a photocurrent, observed as an increase in the detected current, which then saturates (Figure 5.8, **d**). The observed photocurrent varies between repeated illuminations and experiments in terms of both the slope (average increase of 0.32 nA/min, SD 0.2 nA/min, n = 21) and duration of the current increase (6.3 min, SD 3.7 min, n = 21). This complicates data analysis of photocatalytic HER, as any detected increase in signal has to be higher or has to demonstrate longer increase in current than the one of the photocurrent.

The following sections of this chapter describe attempts to encapsulate HECs (Pt NPs and

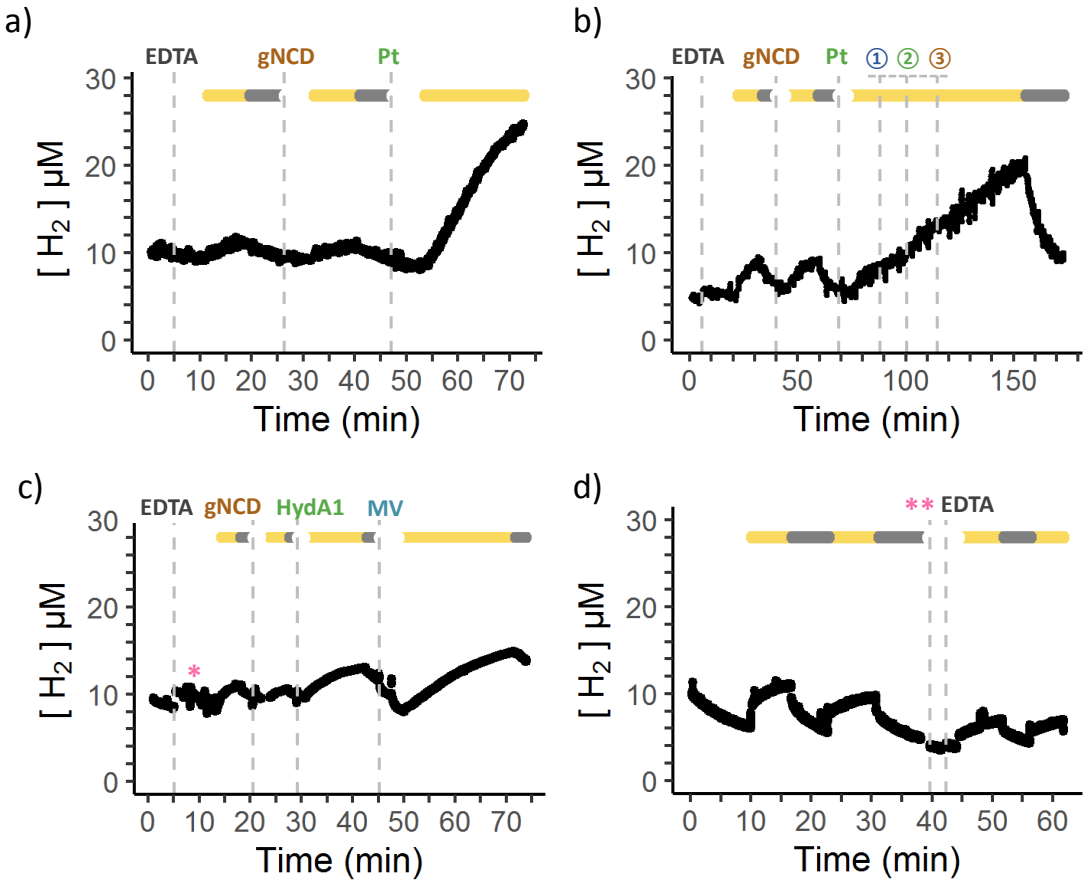

Figure 5.8: Photocatalytic HER activity of Pt_{com} (a), Pt_{syn} (b) and HydA1 hydrogenase (c), using carbon dots (*g*-N-CDs) as LHNPs and a control photo-current of the electrode (d). Lines indicate time, when stated reaction components were added to the reaction chamber. Yellow bars indicate sample illumination, and grey bars indicate time periods immediately after illumination. All experiments were performed in about 0.5 ml of 20 mM MOPS, 30 mM Na_2SO_4 (pH 7.4) buffer and 50 mM EDTA. **a**) Experiment involved 2 μM *g*-N-CD, 20 μg Pt_{com} (≈0.11 nmol NP). **b**) Experiment involved 2 μM *g*-N-CD, 19 μg Pt_{syn} (≈0.34 nmol NP). ① - addition of 0.2 μM MV, ② - addition of 15 μg more Pt_{syn} and more *g*-N-CD NPs (end concentration: 4 μM *g*-N-CD), ③ - addition of more *g*-N-CD NPs (end concentration: 6 μM *g*-N-CD). **c**) Experiment involved 1 μM *g*-N-CD, 4 nM HydA1 (2 pmol HydA1), 1 mM MV. The asterisk indicates noise due to loose electrode connection. **d**) The double asterisk (∗∗) indicates a removal of some buffer, before addition of EDTA.

HydA1) in compartments (liposomes and silica nanoparticles). To determine encapsulated catalyst qualitatively, DT was used as the electron source.

5.3 Attempts to trap HECs in liposome compartment by rapid dilution

The simplest way to attempt introducing a fuel-producing catalyst within the lumen of a compartment presented in Chapter 4 is to modify the existing protocol by substituting the RR120 for a HER catalyst. The main advantage for this approach is the ability to simultaneously encapsulate the catalyst and reconstitute MtrCAB while forming liposomes. The main disadvantage for this approach is the large volume sample gets diluted to, thus resulting in very low theoretical yields of HEC encapsulation.

Encapsulation of all three catalysts by rapid dilution was studied. Liposomes were prepared as described in section 2.2.2 and HEC activity was observed electrochemically as before. Liposomes were mixed with DT as a reducing reagent and H_2 evolution was monitored. In case of successful encapsulation, no changes in the recorded signal should be recorded as the DT cannot diffuse through the lipid membrane and proton permeability is low. However, once the the lipid bilayer is solubilised by a detergent (*e.g.*, Triton X100), an increase in detected current (and H_2 concentration) should be recorded, .

The liposome sample with Pt_{com} showed a significant H_2 evolution even before the detergent was added (Figure 5.9). This indicates that most of the Pt NPs are present on the outside of liposomes. The TEM of the Pt_{com} showed that most NPs are aggregating and these aggregates are likely being sedimented together with the reconstituted liposomes during the ultra-centrifugation step used for liposome recovery. In addition, the Pt_{com} agglomerates are comparable in size with the lipsomes (100 - 200 nm), making them less likely to be trapped within a liposome. It is also possible that Pt NPs interact with the liposomal membrane as this has been observed for other metal nanoparticles. [189] Attempts to separate liposomes and Pt_{com} using gel filtration (*e.g.*, Illustra NAP-5 column) were unsuccessful.

Pt_{syn} nanoparticles are more soluble than their Pt_{com} counterparts, and thus it should be easier to trap these within liposomes. Figure 5.10 shows a liposome sample showing a promising response for a successful encapsulation of Pt_{syn}. No increase in H_2 concentration was observed for liposomes without MtrCAB until detergent was added, and the liposome membrane was

solubilised. The same liposomes were also tested for photocatalytic HER using g-N-CD as a LHNP, however the amount of encapsulated Pt NPs was not enough to distinguish a photocatalytic HER from background photocurrent (Figure 5.10 **c**). Unfortunately, encapsulation of Pt_{syn} by rapid dilution showed very low reproducibility (*i.e.*, positive encapsulation was only confirmed for 18% of preparations, n = 11) and thus was discontinued. Perhaps, the amount of the trapped Pt NPs was too small to see any signal, especially taken into account that the Pt_{syn} had the lowest catalytic activity out of all three catalyst tested. Furthermore, a few times (3 preparations) H_2 production was observed before the lysis of the lipid membrane, indicating that Pt NPs were sometimes also present on the outside of the liposomes.

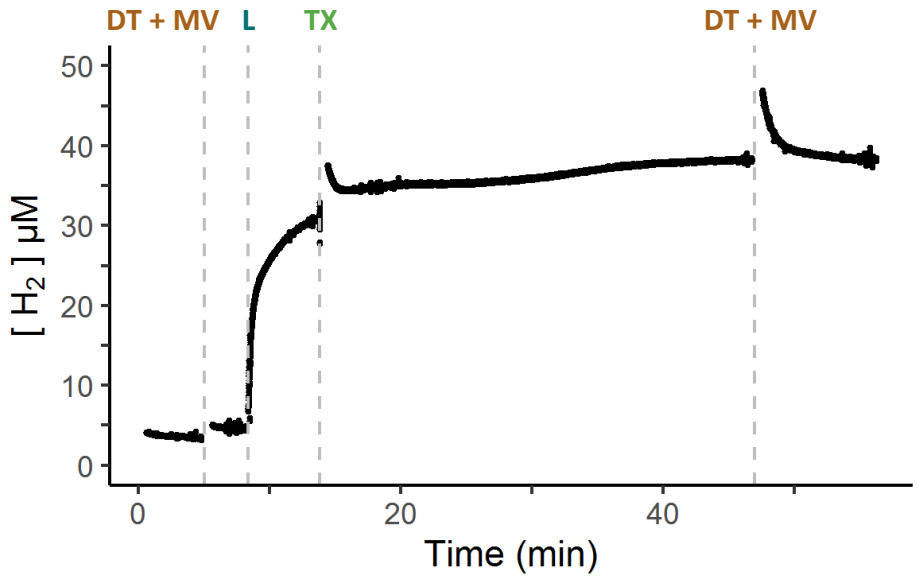

Figure 5.9: HER activity of *E. coli* polar lipid and 1% DOPE-CF liposomes (L) after an attempted encapsulation of Pt_{com} nanoparticles by rapid dilution. Excess dithionite (DT) was used as an electron source, methyl viologen (MV) as electron mediator and Triton X100 (TX) to solubilise the lipid bilayer. Lines indicate time, when stated reaction components were added to the reaction chamber. The experiment involved 1 ml of MOPS buffer (20 mM MOPS, 30 mM Na_2SO_4, pH 7.4), 2 mM MV, 14 mM DT, 0.1% v/v TX.

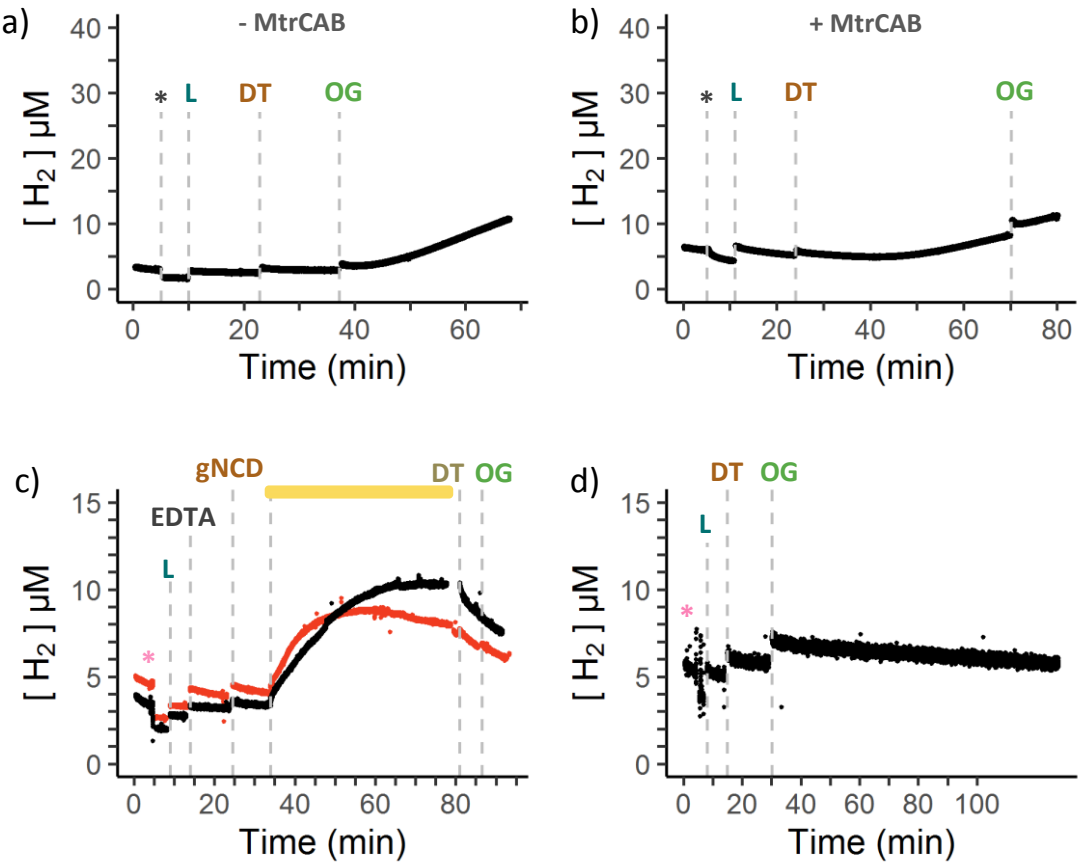

Figure 5.10: HER activity of *E. coli* polar lipid liposomes after encapsulation attempts of Pt_{syn} by rapid dilution. (**a**) Control liposomes without MtrCAB, (**b**) MtrCAB proteoliposomes. (**c**) photoactivity of MtrCAB proteoliposomes+Pt_{syn} (red) and control liposomes+Pt_{syn} (black), using carbon dots (*g*-N-CD, 2 μM) as a LHNP. Yellow bar indicate sample illumination. (**d**) A representative experiment of unsuccessful Pt_{syn} encapsulation in liposomes by rapid dilution. Lines indicate time, when stated reaction components were added to the reaction chamber. L - liposome samples, DT - dithionite (57 mM), OG - octyl glucoside (50 mM), EDTA - sacrificial electron donor (55 mM. All experiments were performed in ≈ 0.5 ml of 20 mM MOPS, 30 mM Na_2SO_4 (pH 7.4) buffer.

Finally, an attempt was made to encapsulate HydA1 using rapid dilution (Figure 5.11). Unfortunately, no HER activity was associated with the liposomes before or after addition of the detergent. This might be due to lack of success to trap any HydA1 within the liposome cavity, or lack of success in keeping sample protected from oxygen, which is the main challenge working with this extremely oxygen sensitive enzyme. The work was carried out in collaboration with Samuel Piper from the University of East Anglia and is currently continued here in Leeds by Dr Huijie Zhang.

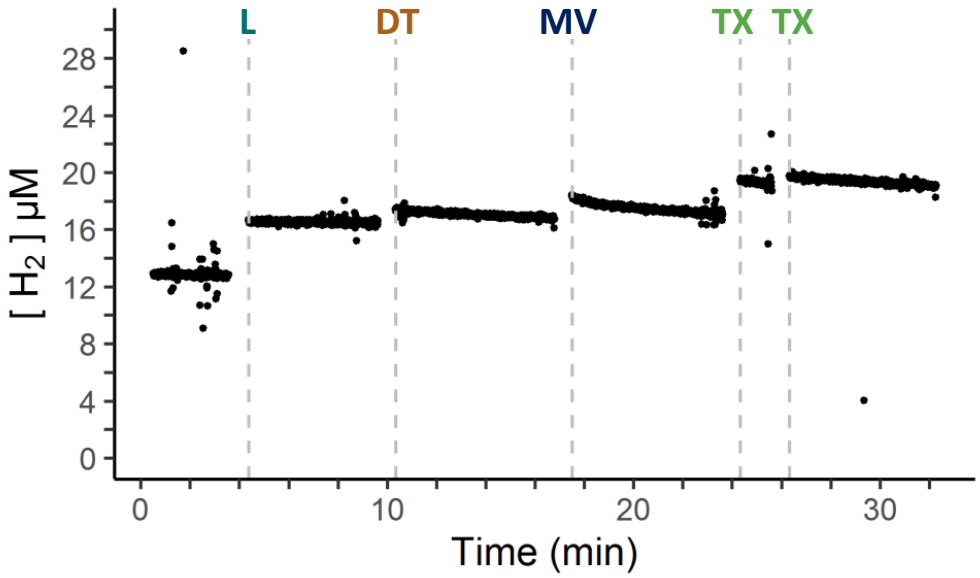

Figure 5.11: HER activity of *E. coli* polar lipid liposomes (L) with attempted encapsulation of HydA1 by rapid dilution. Excess dithionite (DT) was used as an electron source, methyl viologen (MV) as electron mediator and Triton X100 (TX) to solubilise the lipid bilayer. Lines indicate time, when stated reaction components were added to the reaction chamber. The experiment involved 0.5 ml of MOPS buffer (20 mM MOPS, 30 mM Na_2SO_4, pH 7.4), 1 mM MV, 11 mM DT, 0.1% v/v TX (0.11% v/v after second addition of TX).

5.4 Attempts to trap Pt_{syn} in porous silica nanoparticles

Two types of silica were used for testing catalyst encapsulation and the formation of supported lipid bilayers in this study. First, commercial mesoporous silica nanoparticles ($meSiO_2$, 200 nm particle size, pore size 4 nm) were obtained, and tested for Pt NP loading within the pre-formed pores of the silica (Figure 5.12 a). Secondly, bio-inspired silica ($gSiO_2$) were synthesized in collaboration with Prof. Siddharth V. Patwardhan from the University of Sheffield. Patwardhan and colleagues have developed a rapid, environmentally friendly way to form silica nanoparticles by silica precipitation using small amine polymers such as pentaethylenehexamine (PEHA) and diethylenetriamine (DETA). [194, 195] Their designed method allows trapping of Pt_{syn} within the porous $gSiO_2$ NP during particle synthesis (Figure 5.12 b).

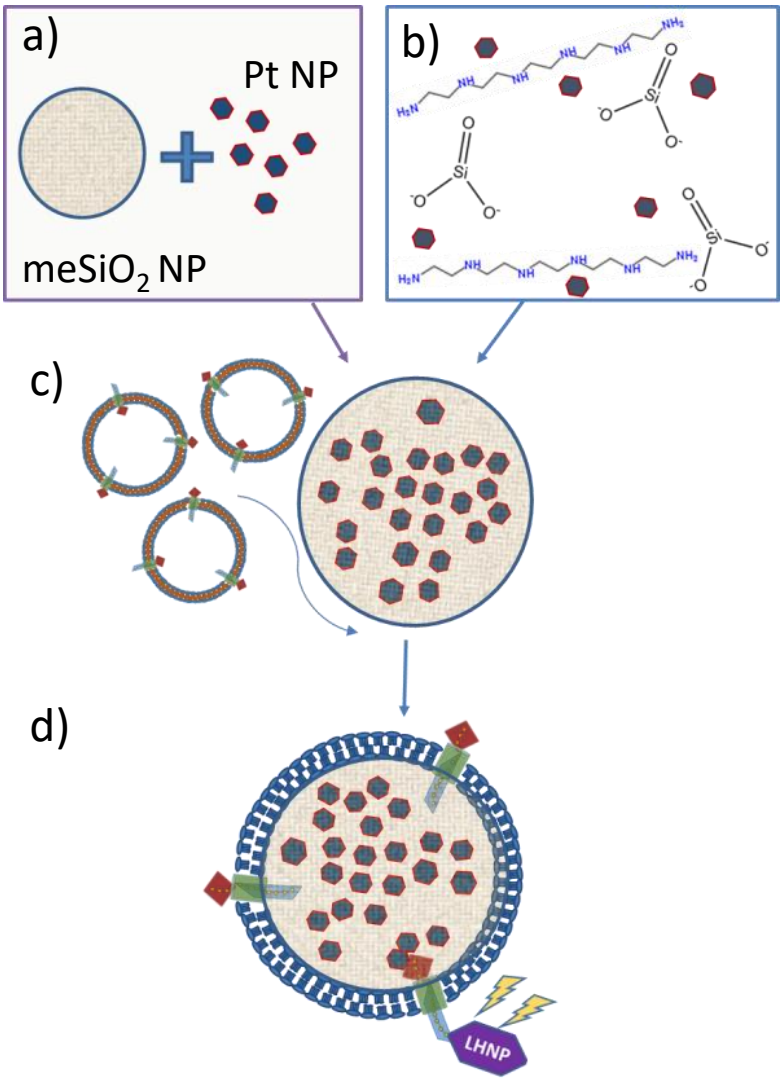

Figure 5.12: A diagram of formation of liposome compartment using porous silica support. **a**) Commercial silica nanoparticles (meSiO$_2$) are mixed with Pt nanoparticles, which enter the porous meSiO$_2$. **b**) Alternatively, Pt$_{syn}$ are trapped within the porous gSiO$_2$ NP during particle synthesis. Pt$_{syn}$ are mixed with the silica precursor and amine. The solution then gets acidified, which causes precipitation of the silica nanoparticles. **c**) Silica nanoparticles containing Pt catalyst are then mixed with liposomes, which form supported lipid bilayer around these particles, as shown in **d**).

5.4.1 Characterisation of the silica particles

The size distributions of both meSiO$_2$ and gSiO$_2$ NPs (Figure 5.13) were measured by nanoparticle tracking analysis (NTA) and also by imaging particles with the TEM as described in section 2.1. Both meSiO$_2$ and gSiO$_2$ ranged in size from 50 - 400 nm. In addition, Pt-loading did not seem to

significantly change the size distribution of $gSiO_2$. The TEM revealed that commercial $meSiO_2$ NPs were present as uniform spherical particles with a dense lattice-like structure, whereas the shape of the $gSiO_2$ NPs varied significantly. TEM of $gSiO_2$ NPs also indicated heterogeneous Pt loading, where some particles contained large clusters of Pt_{syn} and others had fewer and more dispersed Pt. This could be due to interaction of Pt_{syn} with the PEHA amine, resulting in exchange of Pt surface ligands from glutathione to PEHA. The resulting amine capped Pt NPs would also have a higher tendency to agglomerate. [196]

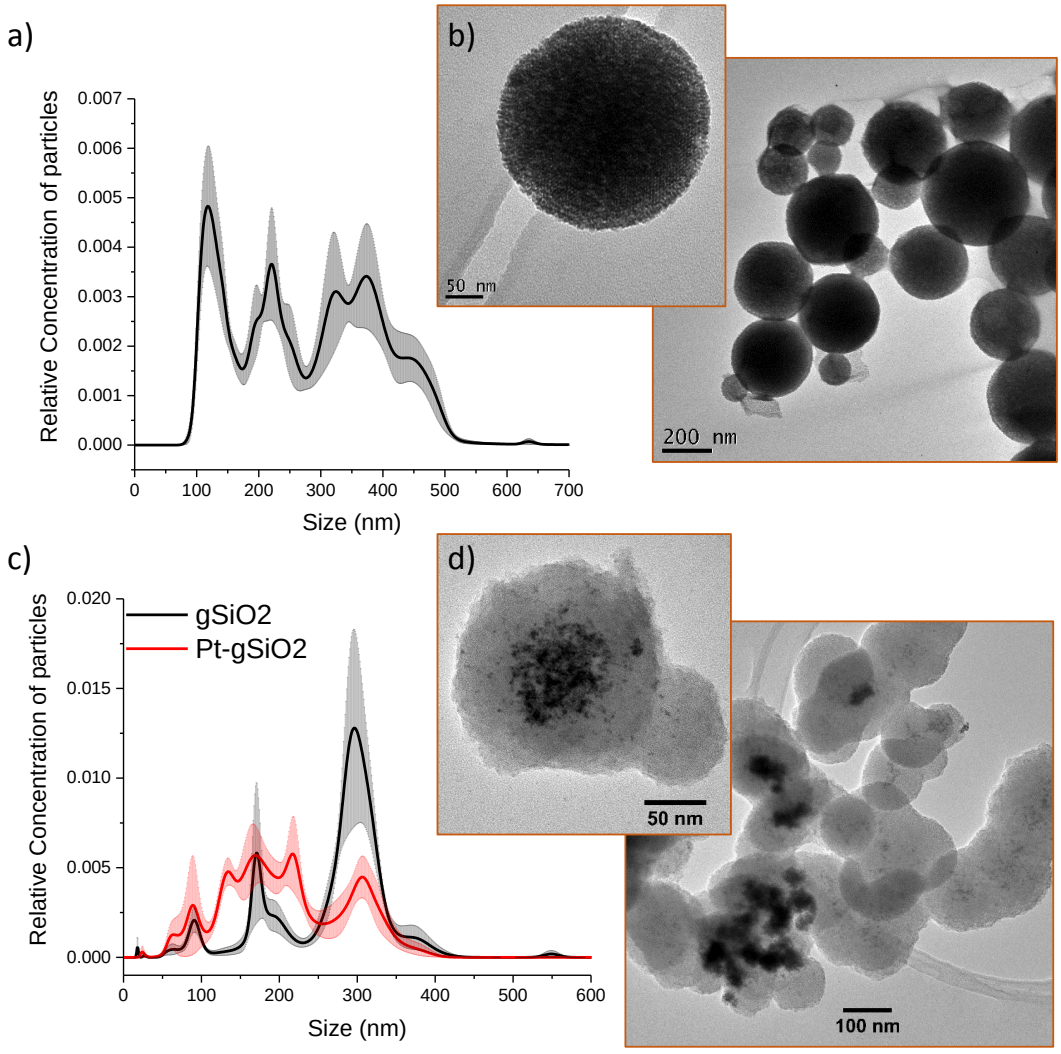

Figure 5.13: Representative size distributions and TEM images of $meSiO_2$ (a,b) and $gSiO_2$ NPs (c,d). a) NTA analysis of $meSiO_2$ NP dispersion based on analysis of 33083 tracked particles. **c** NTA analysis of $gSiO_2$ NPs loaded with Pt (Pt-$gSiO_2$) and without (n = 2987 Pt-$gSiO_2$ NPs and 1030 $gSiO_2$ NPs). NTA was performed in MOPS buffer (20 mM MOPS, 30 mM Na_2SO_4, pH 7.4) and the size distribution is represented using a bin size of 0.5 nm.

5.4.2 Supported lipid bilayer on porous silica support

The work in Chapter 4 used *E. coli* polar lipids to mimick the lipid mixture present in the outer membrane of the *S. oneidensis* and thus the native environment for the MtrCAB. Most reports on the formation of supported lipid bilayers, however, use synthetic lipids (*e.g.*, POPC, 1-palmitoyl-2-oleoyl-sn-glycero- 3-phosphocholine and DPPC, 1,2-dipalmitoyl-sn-glycero-3-phosphocholine) and mixtures of these such as 9:6:4:1 DOPE:DOPC:DOPG:CA (where DOPE stands for 1,2-Dioleoyl-sn-glycero-3-phosphoethanolamine, DOPC - 1,2-dioleoyl-sn-glycero-3-phosphocholine, DOPG - 1,2-dioleoyl-sn-glycero-3-phospho-(1'-rac-glycerol) and CA - cardiolipin). [18, 144, 190] In fact, there has been reports indicating difficulties to form supported lipid bilayer from *E. coli* total extract lipids, which could be partially solved by using 68:32 molar ratio of *E. coli* : POPC lipids. [197] Thus several lipid combinations were tested for supported lipid bilayer formation on $meSiO_2$. These were 100% POPC, 100% E. coli polar lipids, 68%-32% E. coli polar lipids- POPC and 5:3:1:1 E. coli polar lipids : POPC : POPG : POPE (where POPG stands for 1-Palmitoyl-2-Oleoyl-sn-Glycero-3-Phosphoglycerol and POPE - 1-palmitoyl-2-oleoyl-sn-glycero-3-phosphoethanolamine). All 4 lipid mixtures also contained 1% w/w fluorescent carboxyfluorescein-conjugated DOPE (DOPE-CF). The supported lipid bilayers were formed as described in section 2.7.3, washed by centrifugation and the fluorescence of the pellet (lipids associated with the silica) and the supernatant (free liposomes) was recorded (Figure 5.14). These experiments were performed using 12% wt/wt ratio of lipid to $meSiO_2$ (rough estimate of 2:1 lipid bilayer to silica surface ratio) as has been reported in [144]. The data confirms that out of the 4 tested lipid compositions POPC was the best at forming supported lipid bilayers, whereas pure *E. coli* polar lipids showed the least association with silica. Both mixtures containing $\approx$ 30% POPC showed $\approx$ 60% of the association of $meSiO_2$ seen for 100% POPC. Thus these lipid mixtures show a potential to both mimic the lipid composition of the bacterial outer membrane and to enclose silica. In addition, the dependency of lipid (POPC) concentration on the formation of supported lipid bilayers on $gSiO_2$ was also tested (Figure 5.15). These results show that particles get saturated with lipids already at 0.5 - 1 relative w/w ratios. Similar experiment, comparing the lipid concentration dependency on the formation of supported lipid bilayers on $meSiO_2$, were not performed, but would be advantageous to better estimate success of lipid bilayer formation.

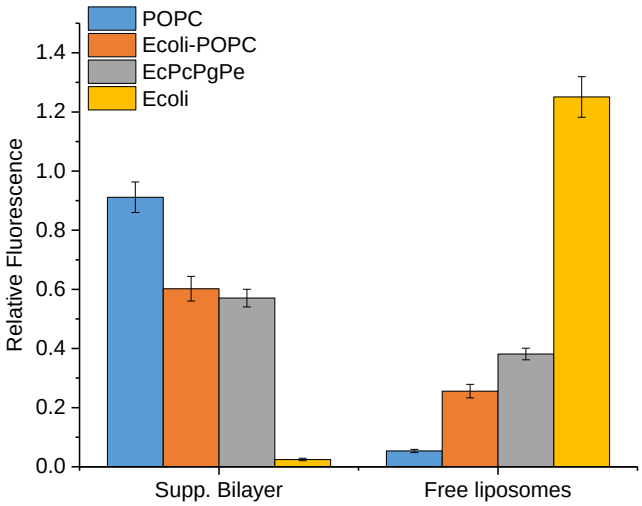

Figure 5.14: Formation of the supported lipid bilayer on meSiO$_2$ using different lipid compositions. Blue, 100% POPC; Orange, 68% *E. coli* polar lipids - 32% POPC, Grey, 5:3:1:1 *E. coli* polar lipids : POPC : POPG : POPE (EcPcPgPe); Yellow, 100% *E. coli* polar lipids. All lipid mixtures contained 1% w/w DOPE-CF and the recorded fluorescence values were normalised against the fluorescence of the original lipid sample. The experiment used 12% wt/wt ratio of lipid to meSiO$_2$ (rough estimate of 2:1 bilayer to silica surface ratio) in MOPS buffer (20 mM MOPS, 30 mM Na_2SO_4, pH 7.4).

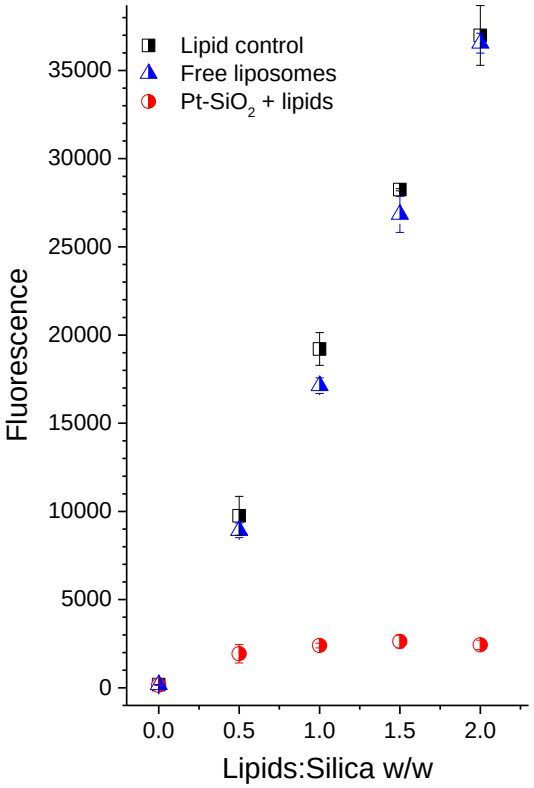

Figure 5.15: Formation of supported lipid bilayer on Pt-gSiO$_2$ NPs using increasing concentrations of POPC liposomes containing 1% w/w DOPE-carboxyfluorescein. Red - Pt-SiO$_2$ sample with the supported lipid layer, Blue - non-attached liposomes separated from the reported Pt-SiO$_2$ samples, Black - lipid control.

5.4.3 Trapping PtNPs in porous silica particles

Current attempts to load catalyst within porous silica tested only Pt_{syn} as these were smaller and better dispersed than their commercial counterparts. Pt_{syn} also allowed experimentation in aerobic conditions, which would not be possible if HydA1 was used. Pt_{syn} loaded $meSiO_2$ and $gSiO_2$ with attempted supported lipid bilayer were formed as described in section 2.7.3. The resulting particles were tested for H_2 evolution and were compared to lipid-free control samples using the same Clark-electrode type system as before (Figure 5.16).

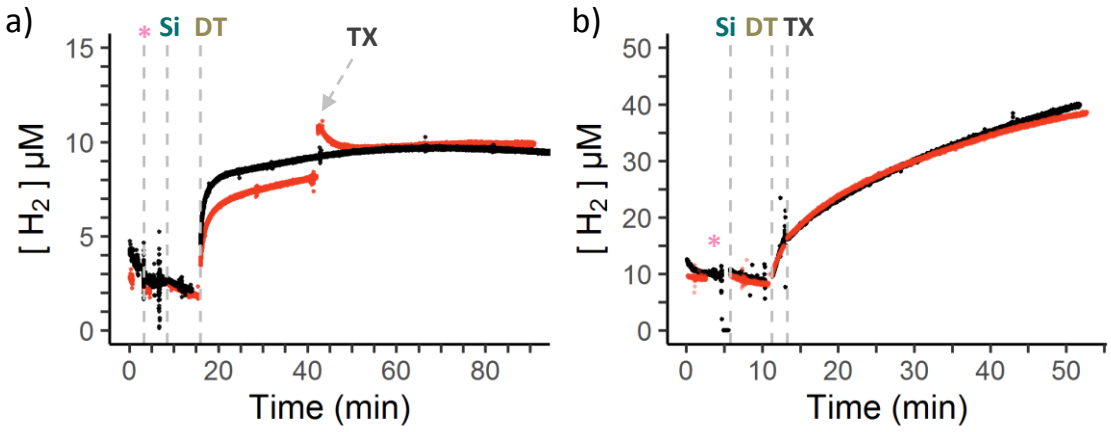

Figure 5.16: HER activity of Pt_{syn} loaded $meSiO_2$ (a) and $gSiO_2$ (b) covered with a supported lipid bilayer and using excess dithionite (DT) as the electron source. Black - lipid-free control sample, Red - sample with supported lipid bilayer. Si - addition of Pt-loaded SiO_2 nanoparticles; TX - Triton X100 detergent. Lines indicate time, when stated reaction components were added to the reaction chamber. The time data of the compared experiments (black and red) have been modified so that time and the signal changes associated with adding the stated components would be the same. The asterisk indicates removal of some buffer. Both experiments were performed in MOPS buffer (20 mM MOPS, 30 mM Na_2SO_4, pH 7.4). **a**) Experiments involved 1 ml sample containing ≈0.4 mg $meSiO_2$ loaded with Pt_{syn} and 0.2 mM MV, 68% *E.coli* polar lipid - 38% POPC liposomes, 11 mM DT and 0.1% v/v TX. **b**) Experiments involved 0.5 ml sample containing ≈0.4 mg $gSiO_2$ loaded with Pt_{syn}, liposomes containing 99.6% POPC - 0.4% Texas red labelled DHPE lipids (DHPE, 1,2-Dihexadecanoyl-sn-Glycero-3-Phosphoethanolamine), 57 mM DT and 0.1% v/v TX.

Both lipid-free controls showed clear change in HER upon introduction of the reducing agent (DT). Thus both silica NPs contained sufficient amounts of Pt_{syn}. The HER activity with $gSiO_2$ was significantly higher than $meSiO_2$. Regretfully, no clear difference was seen between silica

with supported lipid bilayers and the corresponding control samples. This is most likely an indication of an incomplete encapsulation of the silica by the supported lipid bilayers. All experimental conditions were estimated to contain surplus lipids. The experiments with $gSiO_2$ used 1.5 w/w lipid to silica ratio, which has been shown to saturate $gSiO_2$ particles in Figure 5.15. The experiments with $meSiO_2$ used 17% w/w ratio of lipids to $meSiO_2$ (rough estimate of 3:1 bilayer to silica surface ratio). Interestingly, Pt_{syn} loaded $meSiO_2$ with supported bilayer showed reduced HER activity compared to the lipid-free control. Lipid solubilisation by the detergent (TX) caused a "jump" in H_2 concentration, suggesting that some fraction of the $meSiO_2$ NPs might have been successfully encapsulated. This however is a very low change in the recorded H_2 concentration and should be optimised in future work.

5.5 Discussion

In this chapter, a study on encapsulation of three different catalysts (Pt_{com}, Pt_{syn} and HydA1 hydrogenase) within liposomes and in lipid-bilayer coated silica is described. The work was carried out with the ultimate goal of encapsulating the catalyst within separate compartment that would be coupled to an external light-harvesting nanoparticle by the membrane haem protein MtrCAB. This would create a first proof-of-concept system for demonstrating compartmentalized photo-catalysis. Unfortunately, none of the attempted methods so far have provided robust and reproducible results for successful catalyst encapsulation within lipid covered compartment. Main difficulties lie in combining the different materials (*i.e.*, lipids, protein, inorganic nanoparticles), whose properties restrict the range of methods available to assemble the compartment and gain spatial control over the assembly.

First, catalyst encapsulation was attempted with simultaneous MtrCAB reconstitution and liposome formation by rapid dilution. Although this approach was successful for experiments with RR120 azo-dye (reported in Chapter 4), it has limitations when dealing with larger and more valuable cargoes such as precious metal nanoparticles like Pt, and sensitive-enzymes like HydA1. Liposome formation by rapid dilution is a stochastic process, trapping only a small fraction of the relatively large sample volume within the liposome lumen (*i.e.*, cumulative liposome volume of ≈10 μl in 50 ml). Further difficulties arise, if the cargo to be encapsulated (*i.e.*, Pt NPs) itself form large agglomerates as was observed with Pt_{com}. Stochastic encapsulation of well-dispersed nanoparticles (3 nm in size) within 100-200 nm large liposomes is easier than encapsulation of particle agglomerates ranging in size of 100-200 nm. These Pt_{com} aggregates are very diverse in shape, which further impairs formation of continuous lipid bilayer around

them. Pt_{syn} are more water-soluble than Pt_{com} and remain small (≈2 nm), because their surface is modified by glutathione. Thus, it is more likely to encapsulate Pt_{syn} than Pt_{com} within MtrCAB proteoliposomes. And indeed, successful though unreliable encapsulation of Pt_{syn} was observed. However, the improved water solubility of Pt_{syn} comes at a catalytic cost, as the surface modification by glutathione also reduce the available Pt surface for H_2 evolution. As the result Pt_{syn} had half the catalytic activity as Pt_{com}. HydA1 seemed as the most suited catalyst for encapsulation by rapid dilution as it showed superior catalytic activity than both Pt NPs and is also very soluble. Unfortunately, the catalytic centre of HydA1 is extremely oxygen sensitive, which makes it very difficult to provide sufficiently anaerobic environment and work with this enzyme. This also makes it difficult to discriminate whether lack of HER activity is due to unsuccessful encapsulation of HydA1 or whether the enzyme has lost its activity.

Another issue upon observing HER activity was that the activity of both Pt NPs were time-limited by what appeared to be Pt surface poisoning with the end products of dithionite (DT) reduction. This meant that any enquiry of the catalytic activity of Pt NPs with chemical reductant (DT) as electron source was time-sensitive. In addition, a build-up of reaction by-products might even mask HER activity, when trying to determine whether any Pt NPs have been encapsulated within liposomes or not. Liposome assays relay on the assumption that no HER signal should be observed of liposomes with encapsulated catalyst till the liposome bilayer is solubilised by a detergent. The experiment in Figure 5.6 showed that addition of catalyst after the initial saturation of H_2 evolution reaction did not yield any increase in the observed signal. If this is caused by build-up of DT by-products that poison the catalytic Pt surface, than similar build-up might occur during the observation of liposome samples. In this situation, subsequent release of Pt NPs from liposomes by detergent would not yield any signal as Pt might get immediately poisoned by DT by-products. Thus it might be a better strategy to use LHNPs and photo-reduction as the electron source as it seemed to provide a less time-sensitive observation of HER activity.

The attempts to encapsulate the chosen HER catalysts (*i.e.*, Pt_{com}, Pt_{syn} and HydA1) exposed some of the challenges to be overcome. Firstly, sufficient amounts of catalyst have to be loaded within liposomes to record a clear signal. Secondly, the testing conditions for the catalytic activity should be optimised to prevent catalyst deterioration (*e.g.*, oxygen sensitivity, surface poisoning of Pt). Thirdly, greater control over the liposome preparation is required to achieve robust and reproducible liposome loading. Rapid dilution is a stochastic process with respect to HEC encapsulation. Increasing the concentration of catalyst should increase the catalyst loading within the liposomes. However, increasing the concentration of catalyst can also cause complications such as Pt NP aggregation, as well as raise the concentration of non-encapsulated catalyst in

the final sample. Thus, the liposome preparation mechanism should include a step to efficiently remove non-encapsulated catalyst from the exterior of liposomes. This could be based on size separation (*e.g.*, size exclusion, gel filtration, differential centrifugation) or employment of a catalyst specific approach. For example, Pt NPs could be precipitated (*e.g.*, by increasing salt concentration, which, in turn, can subject liposomes to osmotic shock) or nickel-nitrilotriacetic acid (Ni-NTA) resin can be used to bind the His-tag of non-encapsulated HydA1. Any potential preparation or cleaning step, however, has to be compatible with the fragile nature of liposomes and proteins (*e.g.*, MtrCAB and HydA1, if used). Thus, the space for sample manipulation is constrained to low and mild temperatures, neutral pH and strictly anaerobic environment in case of HydA1. Perhaps, further liposome engineering is required to expand the range of available methods and facilitate sample preparation. For example, another membrane protein (such as aquaporin [45] or self-inserting α-haemolysin [6]) engineered to have an affinity tag could be introduced and used to isolate purified liposomes. Other methods could be used to form liposomes and encapsulate catalysts. Edwards *et al.* encapsulated small tetraheme cytochrome (STC) by rehydrating within lipid membranes followed by sample sonication and freeze-thaw cycles. [93] This approach allows use of smaller sample volumes (and thus hopefully better yield of encapsulation), but it also exposes sensitive proteins (*i.e.*, HydA1 and MtrCAB) to harsher conditions, such as sonication and temperature changes. Additional washing steps to remove non-encapsulated catalyst are also still required.

A different approach would be to trap catalyst within a support material. This chapter describes work on loading Pt_{syn} in silica NPs (*i.e.*, $meSiO_2$ and $gSiO_2$), which loaded silica with Pt NPs during sample preparation allowing more flexibility of chemical conditions before the formation of solid supported lipid bilayers (SLB) in later steps. Thus the range of chemical approaches for material manipulation and catalyst loading can be expanded. For the work reported in this chapter, preformed $meSiO_2$ NPs were loaded with Pt_{syn} using extensive sonication, while Pt_{syn} were entrapped within $gSiO_2$ during the synthesis of $gSiO_2$. As the result, the $gSiO_2$ showed better catalyst loading than $meSiO_2$. Both $meSiO_2$ and $gSiO_2$ showed better and more reliable catalyst loading compared to previous catalyst encapsulation within liposomes formed by rapid dilution. Unfortunately, this approach was then stalled by observation that formation of supported lipid bilayers resulted in limited or only partial silica enclosure with both silica materials. Further work is required to optimise silica surface and lipids for the formation of SLB.

Solid-supported lipid bilayer formation on silica has been studied in detail [198–200] and is believed to proceed in stepwise mechanism: first, liposomes adsorb onto the surface of silica, which induce liposome deformation (Figure 5.17). The liposomes then either rupture and form a

SLB patch, which grows by fusion of other liposomes (self-spreading process), or reach a critical coverage of adsorbed liposomes, where rupture of one liposome triggers rupture of neighboring vesicles and a fusion of SLB patches (vesicle fusion). [198]

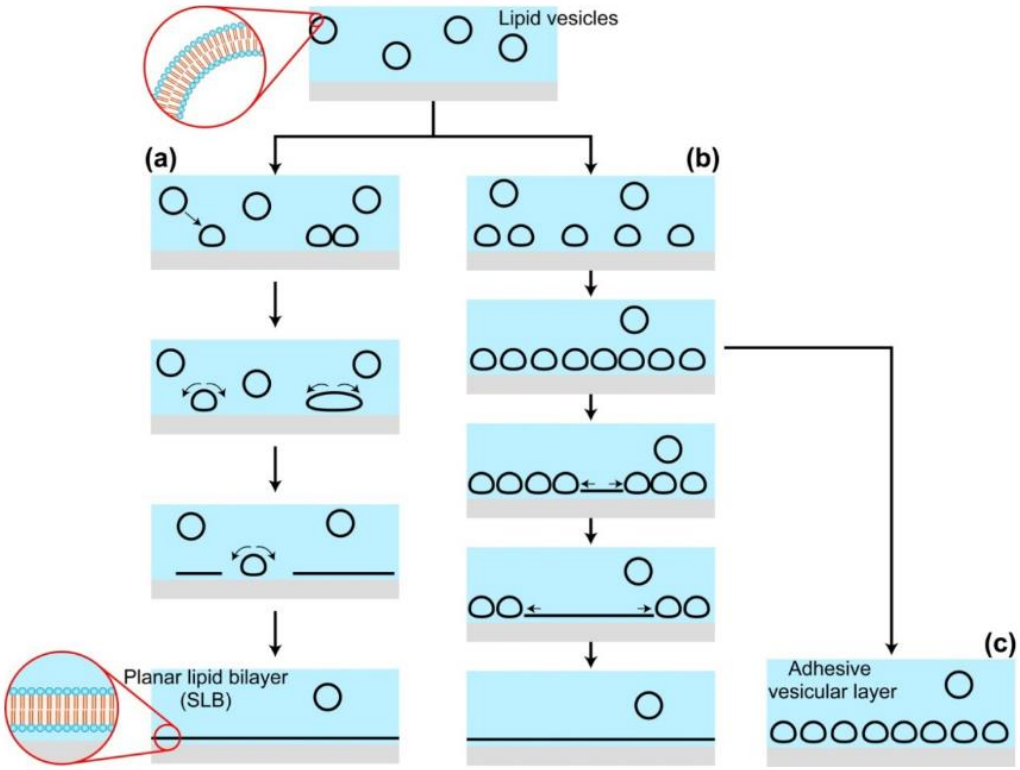

Figure 5.17: Diagram showing SLB formation by vesicle fusion. SLB formation proceeds in a stepwise mechanism: at first, liposomes adsorb onto the surface of silica, which induce liposome deformation. The liposomes then either rupture and form a SLB patch (**a**), which grows by fusion of other liposomes (self-spreading process), or reach a critical coverage of adsorbed liposomes, where a liposome rupture triggers rupture of neighbouring vesicles and a fusion of SLB patches (vesicle fusion)(**b**). Liposomes might also just adsorb onto silica without rupturing, but forming adhesive vesicular layer (**c**). Figure from reference [198].

Multiple parameters such as the physical and chemical composition of silica, liposomes and the environment (*e.g.*, temperature, pH, ionic strength of buffer) can influence lipid interactions with silica, and thus the formation of SLB. [198–200] This was briefly explored in experiments assessing the choice of lipids between *E. coli* polar lipid extract, pure POPC and various lipid mixes (Figure 5.14). In addition, membrane proteins within proteoliposomes can also affect the formation of SLBs, as been seen by Granéli *et al.*, where the hydrophilic domains of a membrane protein hindered SLB formation. [201] Thus, further work optimising the electrostatic interactions, Van der Waals forces and surface hydrophilicity/hydrophobicity is required to achieve a proton

tight SLBs on a porous silica support as reported by Nordlund *et al*. [190, 202]

5.6 Chapter conclusion

The work described in this chapter aimed to demonstrate a compartmentalised system for photo-catalytic evolution of H_2. Several strategies were attempted to trap Pt NPs and HydA within lipid-shielded space and to mimic the spatial separation aspect of natural photosynthesis. In order to achieve this catalytic and photo-catalytic performance of HER was assessed, showing that photo-catalytic evolution of H_2 is thermodynamically possible using *g*-N-CDs as photo-electron source. In addition, it was observed that the chemical electron source (DT), which is commonly used for reduction experiments, might lead to Pt poisoning and thus should only be used for initial, qualitative observation of catalytic activity. The catalyst encapsulation itself is technically very challenging. This study explored two strategies: liposome formation by rapid dilution and catalyst-loading within porous silica, which then could be covered with a supported lipid bilayer. Both strategies were met by issues caused by material incompatibility. For example, as liposome formation by rapid dilution is a very stochastic process, which yields very variable results. Its success is further limited by nanoparticle aggregation as seen by Pt_{com} and difficulties to ensure sufficiently anaerobic environment during rapid dilution, which is required for encapsulation of HydA1. Due to the high variability and unpredictably of the encapsulation process via rapid dilution, other methods for liposome preparation should be explored instead. In contrast, catalyst loading within silica showed more promising results in terms of control over catalyst loading within the supporting material (especially, for Pt loading during synthesis of $gSiO_2$). This strategy, however, highlighted a different challenge to gain control and achieve reproducible formation and complete coverage of $gSiO_2$ by supported lipid bilayers. This should be addressed by gaining better control on the shape and surface of the synthesised silica particles, as well as the lipid composition of liposomes used for supported lipid bilayer.

Although the completion of the original aim has not been successful so far, this chapter illustrated some of the challenges that must be addressed to gain spatial control over the compartment assembly. Further work is needed to design strategies to combine and manipulate different materials (*e.g.*, lipids, membrane proteins, organic and inorganic fuel-evolving catalysts *etc.*). Many of the highlighted issues could be addressed by developing new synthetic analogues to such labile bio-materials as lipids and proteins. Future work building on ongoing progress within fields focused on polymer self-assembly, microfluidics and nanoparticle engineering should help to address these challenges.

Chapter 6

Discussion and Future work

Micro- and nano-compartmentalization provides a framework to explore the role molecule organization plays in a wide variety of biological, chemical and physical processes. As such it supports a very interdisciplinary environment, where bottom-up synthetic compartments are used as model systems for cellular processes and engineering concepts (*e.g.*, interfacing different biological and inorganic materials, localising chemical reactions), as well as the resulting practical applications (*e.g.*, drug delivery in medicine and development of chemical microreactors). The work described within this thesis focuses on establishing an electron transfer (ET) functionality within a biomimetic lipid compartment for compartmentalised photo-catalysis, and thus in itself brings together several fields including solar fuels, molecular interactions and material engineering.

A key aspect for the envisioned compartment is efficient electron transfer between molecules: LHNP (light-harvesting nanoparticles), MtrCAB and HEC (hydrogen-evolving catalysts). Each of these molecular components is already known individually for their ability to harvest light energy for photocatalysis purposes (LHNP, dye-sensitized TiO_2 [82, 203, 204] and carbon dots [86, 88, 89]), to transfer electrons across membrane (MtrCAB [91, 173, 179]) and to use electrons for fuel synthesis (HEC, Pt [76, 205], HydA1 hydrogenase [107, 112]). Therefore, the main challenge for this study was to assemble these within a compartmentalised system and ensure electron transfer from one component to the other, where MtrCAB helps to transfer electrons across the membrane. It has also been indicated previously, that the rate of electron transfer across MtrCAB is more likely to be limited by electron transfer to and from MtrCAB than electron transfer between the MtrCAB haems [91, 94, 163]. Optimal electron transfer between different molecules requires both molecules to be in close proximity. Thus it is important to study and optimise the molecular interactions leading to photo-electron transfer from LHNP to MtrCAB

and to the reductive reaction within the compartment. For most of the components used in this study, their interactions and electron transfer are presumed to be governed by diffusion. However, it was known that TiO_2 nanoparticles can bind MtrC [146], and this interaction was further explored in Chapter 3. This showed how structural biology approaches like protein footprinting can be used to identify the molecular interfaces between MtrC and a-TiO_2. These results also added to the growing evidence about the role complementary electrostatic interactions and protein structure play to facilitate interaction between MtrC and TiO_2. This knowledge can now be used to further study molecular mechanisms for biological and metal binding (*e.g.*, nature of interaction, localisation of key residues and mutations) and be used to inform how to engineer direct contact between MtrC and TiO_2 nanoparticles (*i.e.*, by protein mutations, different surface modification of TiO_2 nanoparticles).

As the binding between MtrC and TiO_2 NPs is based on complementary electrostatic interactions, it is very likely to be affected by such environmental conditions as temperature, pH, ionic strength of buffer. [206] Thus a vast array of different buffers and conditions could be screened to improve electron transfer from TiO_2 to MtrCAB. Such screening of wider buffer conditions could also help to identify conditions, where aggregation of dye-sensitized TiO_2 NP would be reduced. Improvement of particle stability in sample buffer is likely to improve NP interaction with MtrCAB proteoliposomes by increasing the effective ratio between available TiO_2 NP and MtrCAB in proteoliposomes. In fact, the MtrCAB and RR120 proteoliposomes, which were demonstrated in Chapter 4, could be used as a simple indirect optical screening system to determine whether changes in buffer conditions result in improved electron transfer and thus reduction of RR120 by MtrCAB or not. In addition, use of MtrCAB proteoliposomes would allow to test electron transfer through the whole protein complex of MtrCAB and not just MtrC as was done for the protein footprinting assay.

Chapter 3 focused on the molecular interface between TiO_2 and MtrC, but the envisioned compartment for photo-catalysis contains other types of electron transfer interfaces, which could be explored similarly. These include: interface between both types of carbon dots and MtrCAB and the interface between MtrCAB and HECs (*i.e.*, Pt NPs, HydA1 and Pt loaded silica nanoparticles). In the context of the light-harvesting nanocompartments demonstrated in Chapter 4, no stable interaction has been observed between MtrCAB and both light-harvesting carbon dots. Thus engineering of complementary interactions between MtrC and *a*-CDs or *g*-N-CDs could be exploited to optimise ET from these LHNPs to MtrCAB. Both of these particles showed better reduction of RR120 within the MtrCAB proteoliposomes than directly in solution. The mechanism for this improvement in RR120 reduction could also be probed by engineering a

binding interaction between both types of CDs and MtrCAB. This would help to answer questions how does MtrCAB proteoliposome improve the reaction efficiency. For example, is MtrCAB driving the reduction of RR120 by accumulating electrons from several different CDs or helping to reduce charge-recombination from individual carbon dots? Or maybe the improved efficiency of RR120 reduction by CDs using MtrCAB proteoliposoms, is purely due to RR120 concentration within smaller compartmentalised spaces? Finally, interface of MtrCAB and fuel-generating catalysts should also be studied and engineered. This study focused primarily on the challenges leading to catalyst encapsulation within lipid coated compartment (see Chapter 5). Thus no experiments were performed to assess electron transfer from MtrCAB to HECs. Nevertheless, the electron transfer interface should be studied using similar methods to the protein footprinting used in Chapter 3, as also other instrumentations like quartz-crystal microbalance and isothermal titration calorimetry.

Ability to understand and engineer this interface could also help with the challenge to gain control for reliable nano-assembly of all the components (as described in Chapter 5). For example, nano-assembly of the photo-catalytic compartment could be improved by tethering catalyst to close proximity of MtrCAB, which could facilitate catalyst incorporation within the liposomal cavity. This could help to improve the catalyst loading and reproducibility using and exploring various methods for liposome formation. Chapter 4 and 5 relied on liposome formation by rapid dilution, however other methods could also be tested. For example, Edwards *et al.* encapsulated small tetraheme cytochrome (STC) by rehydrating within lipid membranes followed by sample sonication and freeze-thaw cycles. [93]

Similar strategy could be used to engineer interaction between MtrCAB proteoliposomes and porous silica, that could help with forming proton-tight supported lipid bilayer around the silica nanoparticle. Nordlund *et al* reports that formation of a proton tight SLBs on a porous silica support could be improved by optimising the electrostatic interactions, Van der Waals forces and surface hydrophilicity/hydrophobicity between silica and lipid bilayer [190, 202]. Another way to minimise the effect of the silica substrate properties could be by forming a tethered lipid bilayer, where linker molecules (such as covalently bound polymers or avidin interacting with biotinylated lipids) are used to bind the support material with lipid bilayers. [198] Alternatively, silica could be replaced by other supporting materials, such as polyelectrolyte coacervates, which have been used to trap functional enzymes (*e.g.*, glucose oxidase and horseradish peroxidase) in polymer-stabilized compartments. [207, 208] Recently, coacervates have also been coated by lipid vesicles, which did not however fused to form a continuous bilayer. [209]

Other approaches for encapsulating catalysts within compartments use polymersomes and

microfluidic devices. Enzyme encapsulation within polymersomes has been reported for such biocatalysts as superoxide dismutase, horse-radish peroxidase, catalase, glucose oxidase, urease and hemoglobin. [210–214] Generally, these approaches are similar to liposome preparations, where lipids are substituted to polymer blocks. For example, polymersomes have been formed by rehydration of polymer film followed by sample extrusion through a polymer membrane [211, 213]. Other preparations use polymersome formation by injection of polymer dissolved in organic solvent (*e.g.*, tetrahydrofuran or ethanol), followed by solvent removal (*e.g.*, by dialysis). [210, 212, 214] The main advantages for these approaches arise from substituting lipids for chemically more controlled and stable polymers, which would extend the life-time of the compartment as well as permit use of harsher conditions for polymersome recovery. For example, polymersomes could survive being subjected to higher osmotic shock to precipitate non-encapsulated Pt NPs. Main foreseeable challenges for using polymersomes to build the MtrCAB compartment for light energy harvest as envisioned in this PhD thesis, are necessities to further develop these techniques for reconstituting membrane proteins (such as MtrCAB) in the thicker non-native polymer membranes. In addition, many polymersome preparations still rely on a rather stochastic entrapment of the catalyst inside the polymersome lumen.

Microfluidic devices aim to provide higher control over sample loading within compartments, as the aqueous catalyst-containing phase is mixed with oil emulsions, and the droplet interface is stabilised by surfactants or polymers. This approach was used by Peng *et al.* to load Pt NPs within a polymersome cavity [215] and similar principles have been used to encapsulate proteins such as benzaldehyde lyase [80] and even protein expression systems demonstrating GFP production [39]. However, further improvements are necessary to build photo-synthetic compartments as the ones aimed in this chapter. First, methods for incorporating membrane proteins within these microfluidic water-oil-water emulsion systems have to be developed. Possible solutions could be developed inspiring from work by Kawano and colleagues, who demonstrated use of the osmotic pressure to promote fusion of pre-made proteoliposomes in droplet chamber [216] or by Biner and colleagues, who used charge-mediated fusion of proteoliposomes and preformed target liposomes for liposome functionalisation with membrane proteins [217]. The main challenge here then lies in liposome fusion without breaking and releasing the encapsulated catalyst from the target vesicles. Another feature of the current microfluidic devices is that they generally produce large cell-sized vesicles termed giant unilamellar vesicles (GUVs) [39, 218–220], where the bulk mass transport within the vesicle could limit the potential gains of using membrane-bound compartment for bringing together light-harvest nanoparticles and fuel generating catalysts.

Observations made within this thesis have significance to research areas outside the field of bio-

compartments. For example, mapping of the MtrC areas binding TiO_2 adds on the available information of protein-inorganic interfaces, which can help to design tools for determining and predicting processes at bio-inorganic interfaces. These in turn could aid the development of nanoparticles for diagnostic and therapeutic applications, or help to estimate the role of NP pollution within the environmental and biogeochemical processes. [174] Besides, indication of a putative conserved mineral-binding interfaces (*i.e.*, area 2 in MtrC and MtrF), can augment the biochemical understanding of metabolic processes within the *Shewanella oneidensis*, which serves as a model organism for microbial electrochemistry and biogeochemical reactions. [97, 163] In addition, quantitative and mechanistic understanding of electronic coupling between light-harvesting materials and *S. oneidensis* are relevant for such applications as microbial electrosynthesis and microbial fuel cells, which involve coupling between bacterial cells and an electrode. In case of microbial electrosynthesis, electricity is used to drive specific chemical conversions within microbial metabolism, whereas microbial fuel cells use microbial metabolic activity for generating electricity. [97, 148, 221]

Finally, such physical and engineering concepts and the knowledge how spatial arrangement can be used to modulate molecular interactions (*e.g.*, protein binding to LHNP) or processes (*e.g.*, electron transfer) can also help in the development and the scale-up of synthetic industrial systems, such as optimising physical arrangement of molecular components for more efficient solar cells and solar-fuel generators. Results in Chapter 4 provide an insight into how control over the nano-device organization and assembly can be used in artificial photosynthesis and solar-fuel catalyst design to enhance catalytic efficiency and the external quantum efficiency (*i.e.*, measuring how much of the applied light energy results in the final reaction product [57]). This adds to the ongoing research in which the organisation of different photosynthetic components is exploited for (bio-)nanocatalysis. [58] For example, stacked multilayers of lipid membranes containing PSII [83] have been shown to increase production of ATP due to highly efficient exchange of substrates, while limiting diffusion of photo- and catalytic centres. Besides lipid membranes, various other template materials such as viruses, graphene and peptide fibres have been used to gain control over precise physical distribution of porphyrin PSs and catalytic reaction centres (*e.g.*, Pt, TiO_2 and IrO_2 clusters). [222–227] A 10-times higher yield for selective CO_2 conversion into methanol was reported using hollow graphene-doped nanofibers (G-fibers). [227] In this case, multiple enzymes required for methanol generation were confined within the nanofibers, and the photo-excited electrons were transported through the graphene fibers from photosensitizers located on the outside. [227] In a similar approach, photo-oxidation was separated from photo-reduction reactions by employing hierarchical cobalt oxide – silica core-shell nanotube arrays, where

water oxidation and photo-reduction was confined to the inner and outer surface of nanotubes, respectively. [228]

6.1 Summary of directions for future research

Several directions were discussed within this chapter on how to take this research further. These are summarized below:

- exploration and engineering of the molecular interface between LHNP and MtrCAB;
- exploration and engineering of the molecular interface between MtrCAB and HydA1;
- using molecular anchoring to encapsulate HEC or fully cover porous silica nanoparticles containing Pt;
- forming MtrCAB proteoliposomes using microfluidics approach (main challenge lies in reconstitution of membrane proteins and the resulting size of liposomes);
- building synthetic analogue compartments to MtrCAB proteoliposomes using chemically more stable materials (*e.g.*, polymerosomes instead of liposomes).

Appendix

A Peptide fragments analysed using XFMS

Table 1: List of peptides identified to have XFMS modifications and their subsequent analysis. (Peptides without +16, +32 or +48 modifications are not included.)

Peptide position	Native peptide		Modified peptide				Rate constant k±SE (s^{-1})		Ratio (MtrC/MtrC:a-TiO_2)
	Peptide	*m/z*	Δmass (Da)	ΔRT ± SD (min)[a]	Assignment	Assignment criteria	MtrC control	+ a-TiO_2	
37-50	DGGEPAGSIQTLNL	686.34 (2+)	+16	-0.59 ± 0.07	PAGSIQTL	(1) Overlapping peaks in EIC (2) MS/MS narrows down to PAGSIQTL, further identification not reliable	1.1±0.2	0.042±0.007	25±7
51-58	DITKVSYE	*not analysed yet*							
51-71	DITKVSYEN*GAPMVTVFATNE	1144.04 (2+) 763.02 (3+)	+16	-2.03 ± 0.06	M63	1) MS/MS narrows down to PMV 2) Met is 13x and 10x more reactive to •OH than Pro and Val, respectively. [129]	11±1	12±2	1.0±0.2
51-72	DITKVSYEN*GAPMVTVFATNEA	*not analysed yet*							
52-71	ITKVSYEN*GAPMVTVFATNE	*not analysed yet*							
59-71	N*GAPMVTVFATNE	*not analysed yet*							
59-72	N*GAPMVTVFATNEA	*not analysed yet*							
72-83	ADMPVIGLANLE	*not analysed yet*							
73 - 83	DMPVIGLANLE	583.30 (2+)	+16	-2.53 ± 0.04	M74	MS/MS	21±6	9±3	2.4±1.0
			+32	-1.60 ± 0.05		MS/MS			
94 - 114	GATGPGNSANWQGLGSSKSYV	1019.48 (+2) 679.99 (+3)	+16, +32	-2.1± 0.1		MS/MS	*data too noisy for a reliable fit*[b]		
			+32	-1.9 ± 0.1	W104	MS/MS	0.27±0.15	0.11±0.03	2.4±1.5[b]
			+32	-0.8 ± 0.2		MS/MS	0.50±0.18	0.07±0.03	7±4.1[b]
			+16, +32	-0.7 ± 0.1		MS/MS	1.4±0.4	0.38±0.15	3.7±1.9
			+16, +32	from -0.41 to 0.00	PGNSANWQ-GLGSSKSYV	1) MS/MS identifies peptide; 2) very likely W104, as W is among the top 3 most reactive residues [129]; but peak also overlaps native peptide, thus can not exclude in source oxidation	5.3±1.6	1.2±0.4	4.4±1.9
115 - 125	DNKN*GSYTFKF	661.308 (2+), 441.21 (3+)	+16	from -0.1 to in source	DNKN*GSYTF	1) modified peptide elutes immediately before the native, thus it also overlaps with the in source oxidised peaks; 2) MS/MS resolution very low; 3) potentially oxidised Lys, 4) K124 has been identified in related peptide below and shows similar rates of modification.	2.7±0.6	0.7±0.3	4.0±1.8
118 - 125	N*GSYTFKF	482.72 (2+)	+16	from -0.1 to in source	K124	1) modified peptide elutes immediately before the native peptide and thus overlaps with the signal from in source oxidised peptide; 2) Y121, T122 or K124 have been identified by MS/MS; 3) peptides with oxidised Lys typically elute just before the native peptide [130]	2.2±0.7	0.4±0.2	5.6±2.8

(Table continues on next page.)

(Continued from overleaf.)

Peptide position	Native peptide		Modified peptide				Rate constant k±SE (s^{-1})		Ratio
	Peptide	*m/z*	△mass (Da)	△RT ± SD (min)[a]	Assignment	Assignment criteria	MtrC control	+ a-TiO_2	(MtrC/MtrC:a-TiO_2)
129 - 152	DSNKVFNAQLTQRFNAQLTQRFN-VVSAAGKLA	860.13 (3+), 645.35 (4+)	+16	-1.8 ± 0.08	L151	MS/MS	0.086±0.038	0.027±0.0062	3.2±1.6
				-1.55 ± 0.04	L138, V145	1) high noise in MS/MS so potentially contains unresolved peaks, 2) both Leu and Val have similar reactivities [129]	0.57± 0.18	0.070± 0.005	8.1±2.6
				-0.99 ±0.07	V145	MS/MS	0.25± 0.10	0.073±0.008	3.5±1.4
				-0.74±0.05	DSNKVFNAQ	MS/MS very noisy and allows identification only to peptide level for both modified peaks	0.72±0.09	0.091±0.007	7.9±1.2
				-0.49±0.05	F134 and whole peptide	1) Overlapping peaks in EIC; 2) MS/MS indicating F134, and the beginning and end of the peptide, *i.e.*, peptides 'DSNKVFN' and 'SAAGKLA', thus it's impossible to reliably assign peaks	4.5±1.1	0.53±0.11	8.6±2.7
153 - 164	DGTTVPVAEMVE	*not analysed yet; the unmodified peptide is absent, as modification at M has prevented proteolysis*							
241 - 253	DNKIPTVAQNIVQ	720.40 (2+)	+16	from -1.52 to -0.98[a]	I244	MS/MS	2.1±0.3	0.04±0.02	50±24
		480.60 (3+)	+16	-0.20 ± 0.08	K243, (P)TV	1) Overlapping peaks in EIC 2) MS/MS narrows down to DNK and PTV 3) Pro, Thr and Val have similar reactivities; Pro is buried within the protein structure, Thr and Val are exposed 4) Lys is 4.7x and 7.1x more reactive than D and N, respectively 5) peptides with modified Lys have previously shown RT very close to that of the native peptide [130]	0.8 ± 0.2	0.09 ± 0.01	8.6 ± 2.6
269 - 278	AKNWSRIPTM	602.31 (2+)	+16	-1.9±0.2	M278	MS/MS	5.9±1.5	4.7±1.7	1.25±0.55
		407.21 (3+)	+16	-1.01 ± 0.13	W272	MS/MS	4.1±1.9	2.1±1.5	1.9±1.6[b]
			+32	-1.28 ± 0.13					
269 - 279	AKNWSRIPTME	666.84 (2+)	+16	-1.4±0.1	M278	MS/MS	9.4±2.7	5.4±2.1	1.73±0.83
		444.89 (3+)	+16	-0.91 ± 0.12	W272	MS/MS	1.9±1.1	3.7±1.5	0.52±0.36[b]
			+32	-1.18 ± 0.11					
317 - 335	LHTAKTTATKNLIN*YGIE	1059.07 (2+), 706.38 (3+)	+16	from -1.6 to -0.5	TAKTTATKNLIN	noisy MS/MS, reliable identification only to peptide level	0.23±0.13	0.14±0.04	1.6±1.1[b]
		530.03 (4+)	+16	from -0.1 to in source	AKTTAT	noisy MS/MS, reliable identification only to peptide level; likely K321 as elutes immediately before the 'native' peptide [130]	2.4±1.5	0.5±0.2	4.5±3.0[b]
344 - 354	TKAATISVQVV	1116.67 (1+)	+16	from -1.45 to -1.13	V354	MS/MS	0.40±0.10	0.030±0.006	13.5±4.2
		558.84 (2+)	+16	from -0.1 to in source	K345	1) to overlapping peaks mixed with the in source oxidised native peptide; 2) MS/MS identify to TK, TKAATISV, SVQ; 3) T and K are similarly reactive, but K typically elutes just before the native peptide	2.0±0.3	0.3±0.1	5.9±2.1

(Table continues on next page.)

(Continued from overleaf.)

Peptide position	Native peptide		Modified peptide				Rate constant k±SE (s^{-1})		Ratio (MtrC/MtrC:a-TiO_2)
	Peptide	*m/z*	△mass (Da)	△RT ± SD (min)[a]	Assignment	Assignment criteria	MtrC control	+ a-TiO_2	
362 - 374	DLKTILPKVQRLE	776.97 (2+) 518.31 (3+) 388.99 (4+)	+16	-2.44 ± 0.09	L367	MS/MS	0.21±0.06	0.024±0.001	8.9±2.4
			+16	from -1.13 to -0.74[a]	I366; P368	1) Overlapping peaks in EIC 2) MS/MS identified both residues	0.36±0.07	0.054±0.003	6.58±1.33
			+16	from -0.30 to +0.04[a]	K364; P368	1) Potentially overlapping peaks in EIC 2) MS/MS, potentially include also in source oxidation	1.8±0.6	0.16±0.02	11.0±4.1
375 - 391	IITNVGPNNATLGYSGK	859.96 (2+) 573.64 (3+)	+16	-1.22 ± 0.12	L386	MS/MS	0.18±0.04	0.009±0.002	19.5±6.0
			+16	-0.72 ± 0.07	I376, GYSGK(391)	1) Overlapping peaks in EIC 2) MS/MS identify I376 and narrows down to GYSG 3) Tyr about 40x more reactive than Ser and Lys, and about 760x more reactive than Gly, but Tyr already assigned below; Ser and Lys about 20x more reactive than Gly [129]; K typically has short RT [130]	0.20±0.05	0.13±0.05	1.5±0.6
			+16	-0.36 ± 0.04	Y388	1) MS/MS narrows down to GY 2) Tyr about 760x more reactive than Gly [129]	0.20±0.03	0.014±0.002	6.0±1.4
392 - 402	DSIFAIKNGAL	574.82 (2+) 383.55 (3+)	+16	-3.11 ± 0.09	F395, L402	1) Overlapping peaks in EIC 2) MS/MS	0.7 ± 0.1	0.10±0.01	7.0±1.7
			+16	-2.27 ± 0.04	I394, F395	1) Overlapping peaks in EIC 2) MS/MS	0.70 ± 0.09	0.09±0.01	7.6±1.4
			+16	-1.14 ± 0.04	F395	MS/MS	0.6 ± 0.1	0.05±0.01	12.3±4.5
			+16	-0.14 ± 0.07	K398	MS/MS	1.1 ± 0.1	0.07±0.03	15.6±6.2
410 - 420	DAGKLVYTTTK	598.83 (2+) 399.55 (3+)	+16	-0.26 ± 0.05	V415	MS/MS	1.5 ± 0.3	0.11±0.02	14.1±3.6
			+16	-0.02 ± 0.03	Y416, K420	1) Overlapping peaks in EIC 2) MS/MS	2.4 ± 0.5	0.6±0.2	3.8±1.3
421-429	DLKLGQN*GA	*not analysed yet*							
421-431	DLKLGQN*GADS	1118.54 (1+)	+16	from -0.1 to in source	Q426	1) overlapping peak with an in source oxidised peak 2) MS/MS identifies peak eluting immediately before the native peptide as Q426	2.8±0.5	0.51±0.12	5.5±1.6
432-442	DTAFSFVGWSM	*not analysed yet*							

(Table continues on next page.)

(Continued from overleaf.)

Peptide position	Native peptide		Modified peptide				Rate constant k±SE (s^{-1})		Ratio
	Peptide	*m/z*	△mass (Da)	△RT ± SD (min)[a]	Assignment	Assignment criteria	MtrC control	+ a-TiO_2	(MtrC/MtrC:a-TiO_2)
]] 432-446	DTAFSFVGWSMC*SSE	855.84(2+) 570.89(3+)	+48	-4.67 ± 0.15	W440 and M44	MS/MS	3.0±0.5	0.67±0.32	4.5±2.3
			+16, +32	from -3.9 to -3.3	W440 and M442	1) overlapping peaks; 2) MS/MS	*data too noisy for a reliable fit* [b]		
			+48	-3.37 ± 0.04	W440 and M442	1) MS/MS narrows to GW and SM; 2) W and M more reactive [129]	0.35±0.30	0.18±0.096	1.9±1.9[b]
			+32	from -3.13 to -2.51	W440	MS/MS	*data too noisy for a reliable fit* [b]		
			+16	-2.16 ± 0.12	M442	MS/MS	*data too noisy for a reliable fit* [b]		
			+16	from -2.1 to -1.67	W440 and M442	1) two overlapping peaks; 2) MS/MS narrows to GW and SMCS; 3) W and M more reactive	*data too noisy for a reliable fit* [b]		
			+16	from -1.43 to -1.06	W440 and M442	1) two overlapping peaks; 2) MS/MS narrows to GW and SM; 3) W and M more reactive	*data too noisy for a reliable fit* [b]		
458-470	DGVDVTKYTGMKA	692.84 (2+) 462.23 (3+)	+16	from -1.52 to -1.2	V462, M468	1) overlapping peaks; 2) MS/MS not very clear but identify to peptides GVD and YTGMKA; 3) V462 and M468 more reactive and both identified in individual samples [129]	2.33±1.17	2.52±0.76	0.9±0.5[b]
			+16	-0.95±0.05	V460	MS/MS	0.92±0.35	0.34±0.045	2.7±1.1
461-470	DVTKYTGMKA	*not analysed yet*							
471-482	DLAFATLSGKAP	*not analysed yet*							
471-487	DLAFATLSGKAPSTRHV	590.98 (3+)	+16	from -1.71 to -1.22	L477	MS/MS	1.46±0.52	0.12±0.03	12.3±5.2
			+32	from -1.38 to -1.16	F474 and TLSGKA	1) overlapping peaks; 2) MS/MS identify to F474 and TLSGKA	0.10±0.03	0.016±0.003	6.4±2.3
		443.49 (4+) 885.98 (2+)	+16, +32	from -0.38 to native	K480, F474, APSTRH	1) several overlapping peaks; 2)MS/MS identify to K480 and K typically elutes close to native peptide; 3) MS/MS also narrows to DLAF, FAT and APSRTH; 4) F more reactive than D,L,A,T [129]	3.3±0.5	0.76±0.21	4.3±1.4
471-488	DLAFATLSGKAPSTRHVD	*not analysed yet*							
525-534	DAN*GKAIVGL	*not analysed yet*							
544-556	DGTYSFANRGALE	*not analysed yet*							

[a] - In cases where overlapping peaks of multiple peptides were detected within EIC, these were processed cumulatively and the corresponding range of ΔRT is reported.

[b] - Inconclusive result due to high noise caused by atypical or noisy data causing data fitting to be unreliable. Is some cases reliable fit was not achieved. In others, the ratio between conditions (MtrC/MtrC:a-TiO_2) yielded error that was more than 60%.

* - Asn deamidation was detected

Bibliography

[1] Neha P. Kamat, Joshua S. Katz, and Daniel A. Hammer. Engineering Polymersome Protocells. *The Journal of Physical Chemistry Letters*, 2(13):1612–1623, jul 2011.

[2] Hans-Peter M. de Hoog, Madhavan Nallani, and Nikodem Tomczak. Self-assembled architectures with multiple aqueous compartments. *Soft Matter*, 8(17):4552, 2012.

[3] Helen R Saibil. Chaperone machines in action. *Current opinion in structural biology*, 18(1):35–42, feb 2008.

[4] Xiaofeng Liu and Elizabeth C Theil. Ferritins: Dynamic Management of Biological Iron and Oxygen Chemistry. *Accounts of Chemical Research*, 38(3):167–175, mar 2005.

[5] Geoffrey M Cooper. Lysosomes. In *The Cell: A Molecular Approach*. Sinauer Associates, Sunderland (MA), 2nd editio edition, 2000.

[6] Rona Chandrawati, Martin P. van Koeverden, Hannah Lomas, and Frank Caruso. Multicompartment Particle Assemblies for Bioinspired Encapsulated Reactions. *The Journal of Physical Chemistry Letters*, 2(20):2639–2649, oct 2011.

[7] Maïté Marguet, Colin Bonduelle, and Sébastien Lecommandoux. Multicompartmentalized polymeric systems: towards biomimetic cellular structure and function. *Chem. Soc. Rev.*, 42(2):512–529, 2013.

[8] Nick Lane and William F. Martin. The Origin of Membrane Bioenergetics. *Cell*, 151(7):1406–1416, 2012.

[9] Kyeong Kyu Kim, Rosalind Kim, and Sung-hou Kim. Crystal structure of a small heat-shock protein. 394(August):595–599, 1998.

[10] Masaki Uchida, Sebyung Kang, Courtney Reichhardt, Kevin Harlen, and Trevor Douglas. The ferritin superfamily: Supramolecular templates for materials synthesis. *Biochimica et Biophysica Acta (BBA) - General Subjects*, 1800(8):834–845, aug 2010.

[11] Pierre Baudhuin, Henri Beaufay, and Christian de Duve. COMBINED BIOCHEMICAL AND MORPHOLOGICAL STUDY OF PARTICULATE FRACTIONS FROM RAT LIVER. *The Journal of Cell Biology*, 26(1):219–243, jul 1965.

[12] Stijn F. M. van Dongen, Hans-Peter M. de Hoog, Ruud J R W Peters, Madhavan Nallani, Roeland J M Nolte, and Jan C. M. van Hest. Biohybrid Polymer Capsules. *Chemical Reviews*, 109(11):6212–6274, nov 2009.

[13] Rupa R. Sawant and Vladimir P. Torchilin. Liposomes as 'smart' pharmaceutical nanocarriers. *Soft Matter*, 6(17):4026, 2010.

[14] Qiang He, Yue Cui, and Junbai Li. Molecular assembly and application of biomimetic microcapsules. *Chemical Society reviews*, 38(8):2292–303, 2009.

[15] Markus Antonietti and Stephan Förster. Vesicles and Liposomes: A Self-Assembly Principle Beyond Lipids. *Advanced Materials*, 15(16):1323–1333, 2003.

[16] E. Kaler, A. Murthy, B. Rodriguez, and J. Zasadzinski. Spontaneous vesicle formation in aqueous mixtures of single-tailed surfactants. *Science*, 245(4924):1371–1374, sep 1989.

[17] Dan D. Lasic. Novel applications of liposomes. *Trends in Biotechnology*, 16(7):307–321, 1998.

[18] A L Troutier and C Ladaviere. An overview of lipid membrane supported by colloidal particles. *Adv Colloid Interface Sci*, 133(1):1–21, 2007.

[19] Stefan Egli, Helmut Schlaad, Nico Bruns, and Wolfgang Meier. Functionalization of Block Copolymer Vesicle Surfaces. *Polymers*, 3(1):252–280, 2011.

[20] Katarzyna Kita-Tokarczyk, Julie Grumelard, Thomas Haefele, and Wolfgang Meier. Block copolymer vesicles - Using concepts from polymer chemistry to mimic biomembranes. *Polymer*, 46(11):3540–3563, 2005.

[21] Ozana Onaca, Ramona Enea, David W. Hughes, and Wolfgang Meier. Stimuli-Responsive Polymersomes as Nanocarriers for Drug and Gene Delivery. *Macromolecular Bioscience*, 9(2):129–139, 2009.

[22] Pascal Tanner, Patric Baumann, Ramona Enea, Ozana Onaca, Cornelia Palivan, and Wolfgang Meier. Polymeric Vesicles: From Drug Carriers to Nanoreactors and Artificial Organelles. *Accounts of Chemical Research*, 44(10):1039–1049, oct 2011.

[23] Weijun Tong and Changyou Gao. Multilayer microcapsules with tailored structures for bio-related applications. *Journal of Materials Chemistry*, 18(32):3799, 2008.

[24] Anchao Feng and Jinying Yuan. Smart Nanocontainers: Progress on Novel Stimuli-Responsive Polymer Vesicles. *Macromolecular Rapid Communications*, 35(8):767–779, apr 2014.

[25] Zhikang Fu, Mirjam Andreasson Ochsner, Hans-Peter M. de Hoog, Nikodem Tomczak, and Madhavan Nallani. Multicompartmentalized polymersomes for selective encapsulation of biomacromolecules. *Chemical Communications*, 47(10):2862, 2011.

[26] André H Gröschel and Axel H E Müller. Self-assembly concepts for multicompartment nanostructures. *Nanoscale*, 7(28):11841–76, 2015.

[27] Lise Schoonen and Jan C.M. Van Hest. Compartmentalization Approaches in Soft Matter Science: From Nanoreactor Development to Organelle Mimics. *Advanced Materials*, 28(6):1109–1128, 2016.

[28] Peter Walde. Building artificial cells and protocell models: Experimental approaches with lipid vesicles. *BioEssays*, 32(4):296–303, 2010.

[29] Young Rok Kim, Sungho Jung, Hyunil Ryu, Yeong Eun Yoo, Sun Min Kim, and Tae Joon Jeon. Synthetic biomimetic membranes and their sensor applications. *Sensors (Switzerland)*, 12(7):9530–9550, 2012.

[30] S. Zhang, H.-J. Sun, A. D. Hughes, R.-O. Moussodia, A. Bertin, Y. Chen, D. J. Pochan, P. A. Heiney, M. L. Klein, and V. Percec. Self-assembly of amphiphilic Janus dendrimers into uniform onion-like dendrimersomes with predictable size and number of bilayers. *Proceedings of the National Academy of Sciences*, 111(25):9058–9063, 2014.

[31] Enrico G Bellomo, Michael D Wyrsta, Lisa Pakstis, Darrin J Pochan, and Timothy J Deming. Stimuli-responsive polypeptide vesicles by conformation-specific assembly. *Nature Materials*, 3(4):244–248, apr 2004.

[32] Mazda Rad-Malekshahi, Koen M. Visscher, João P. G. L. M. Rodrigues, Renko de Vries, Wim E. Hennink, Marc Baldus, Alexandre M. J. J. Bonvin, Enrico Mastrobattista, and Markus Weingarth. The Supramolecular Organization of a Peptide-Based Nanocarrier at High Molecular Detail. *Journal of the American Chemical Society*, 137(24):7775–7784, jun 2015.

[33] Dindyal Mandal, Amir Nasrolahi Shirazi, and Keykavous Parang. Self-assembly of peptides to nanostructures. *Organic & biomolecular chemistry*, 12(22):3544–61, 2014.

[34] Aya Koide, Akihiro Kishimura, Kensuke Osada, Woo Dong Jang, Yuichi Yamasaki, and Kazunori Kataoka. Semipermeable polymer vesicle (PICsome) self-assembled in aqueous medium from a pair of oppositely charged block copolymers: Physiologically stable micro-/nanocontainers of water-soluble macromolecules. *Journal of the American Chemical Society*, 128(18):5988–5989, 2006.

[35] Daniel A. Balazs and WT. Godbey. Liposomes for Use in Gene Delivery. *Journal of Drug Delivery*, 2011(January 2011):1–12, 2011.

[36] Francis Szoka and Demetrios Papahadjopoulos. Comparative properties and methods of preparation of lipid vesicles (liposomes). *Ann. Rev. Biophys. Bioeng.*, 9:467–508, 1980.

[37] *The Future of Solar Energy*. Number 3. MIT, 2015.

[38] Scott A Walker, Michael T Kennedy, and Joseph A N Zasadzinski. Encapsulation of bilayer vesicles by self-assembly. *Nature*, 387(6628):61–64, may 1997.

[39] Sadao Ota, Satoko Yoshizawa, and Shoji Takeuchi. Microfluidic Formation of Monodisperse, Cell-Sized, and Unilamellar Vesicles. *Angewandte Chemie International Edition*, 48(35):6533–6537, aug 2009.

[40] a L Klibanov, K Maruyama, V P Torchilin, and L Huang. Amphipathic polyethyleneglycols effectively prolong the circulation time of liposomes. *FEBS letters*, 268(1):235–237, 1990.

[41] Joseph a. Zasadzinski, Benjamin Wong, Natalie Forbes, Gary Braun, and Guohui Wu. Novel methods of enhanced retention in and rapid, targeted release from liposomes. *Curr. Opin. Colloid IN.*, 16(3):203–214, 2011.

[42] T Oberholzer, M Albrizio, and P L Luisi. Polymerase chain reaction in liposomes. *Chemistry & biology*, 2(10):677–682, 1995.

[43] Yuchen Fan and Qiang Zhang. Development of liposomal formulations: From concept to clinical investigations. *Asian Journal of Pharmaceutical Sciences*, 8(2):79–90, 2013.

[44] Peter Walde and Sosaku Ichikawa. Enzymes inside lipid vesicles: preparation, reactivity and applications. *Biomolecular Engineering*, 18(4):143–177, 2001.

[45] Ozana Onaca, Madhavan Nallani, Saskia Ihle, Alexander Schenk, and Ulrich Schwaneberg. Functionalized nanocompartments (Synthosomes): Limitations and

prospective applications in industrial biotechnology. *Biotechnology Journal*, 1(7-8):795–805, 2006.

[46] Anna Grochmal, Luba Prout, Robert Makin-Taylor, Rafel Prohens, and Salvador Tomas. Modulation of Reactivity in the Cavity of Liposomes Promotes the Formation of Peptide Bonds. *Journal of the American Chemical Society*, 137(38):12269–12275, 2015.

[47] T Kaneko, T J Itoh, and H Hotani. Morphological transformation of liposomes caused by assembly of encapsulated tubulin and determination of shape by microtubule-associated proteins (MAPs). *Journal of molecular biology*, 284(5):1671–81, 1998.

[48] Vincent Noireaux and Albert Libchaber. A vesicle bioreactor as a step toward an artificial cell assembly. *Proceedings of the National Academy of Sciences of the United States of America*, 101(51):17669–74, 2004.

[49] Kazuya Nishimura, Saburo Tsuru, Hiroaki Suzuki, and Tetsuya Yomo. Stochasticity in Gene Expression in a Cell-Sized Compartment. *ACS Synthetic Biology*, 4(5):566–576, may 2015.

[50] Nathan Nelson and Adam Ben-Shem. The complex architecture of oxygenic photosynthesis. *Nature Reviews Molecular Cell Biology*, 5(12):971–982, dec 2004.

[51] G Steinberg-Yfrach, J L Rigaud, E N Durantini, A L Moore, D Gust, and T A Moore. Light-driven production of ATP catalysed by F0F1-ATP synthase in an artificial photosynthetic membrane. *Nature*, 392(6675):479–482, 1998.

[52] Hyo-Jick Choi and Carlo D Montemagno. Artificial organelle: ATP synthesis from cellular mimetic polymersomes. *Nano Letters*, 5(12):2538–2542, 2005.

[53] Wei Qi, Li Duan, Kewei Wang, Xuehai Yan, Yue Cui, Qiang He, and Junbai Li. Motor protein CF0F1 reconstituted in lipid-coated hemoglobin microcapsules for ATP synthesis. *Advanced Materials*, 20(3):601–605, 2008.

[54] Devens Gust, Thomas A. Moore, and Ana L. Moore. Mimicking Photosynthetic Solar Energy Transduction. *Accounts of Chemical Research*, 34(1):40–48, jan 2001.

[55] David P Summers and David Rodoni. Vesicle Encapsulation of a Nonbiological Photochemical System Capable of Reducing NAD + to NADH. *Langmuir*, 31(39):10633–10637, oct 2015.

[56] Vincenzo Balzani, Alberto Credi, and Margherita Venturi. Photochemical Conversion of Solar Energy. *ChemSusChem*, 1(1-2):26–58, feb 2008.

[57] Janina Willkomm, Katherine L Orchard, Anna Reynal, Ernest Pastor, James R Durrant, and Erwin Reisner. Dye-sensitised semiconductors modified with molecular catalysts for light-driven H 2 production. *Chem. Soc. Rev.*, 45(1):9–23, jan 2016.

[58] Jae Hong Kim, Dong Heon Nam, and Chan Beum Park. Nanobiocatalytic assemblies for artificial photosynthesis. *Current Opinion in Biotechnology*, 28:1–9, 2014.

[59] Sahng Ha Lee, Jae Hong Kim, and Chan Beum Park. Coupling Photocatalysis and Redox Biocatalysis Toward Biocatalyzed Artificial Photosynthesis. *Chemistry - A European Journal*, 19(14):4392–4406, apr 2013.

[60] Martin A Green. Commercial progress and challenges for photovoltaics. *Nature Energy*, 1:15015, jan 2016.

[61] Shane Ardo, David Fernandez Rivas, Miguel A. Modestino, Verena Schulze Greiving, Fatwa F. Abdi, Esther Alarcon Llado, Vincent Artero, Katherine Ayers, Corsin Battaglia, Jan-Philipp Becker, Dmytro Bederak, Alan Berger, Francesco Buda, Enrico Chinello, Bernard Dam, Valerio Di Palma, Tomas Edvinsson, Katsushi Fujii, Han Gardeniers, Hans Geerlings, S. Mohammad H. Hashemi, Sophia Haussener, Frances Houle, Jurriaan Huskens, Brian D. James, Kornelia Konrad, Akihiko Kudo, Pramod Patil Kunturu, Detlef Lohse, Bastian Mei, Eric L. Miller, Gary F. Moore, Jiri Muller, Katherine L Orchard, Timothy E. Rosser, Fadl Hussein Saadi, Jan-Willem Schüttauf, Brian Seger, Stafford W. Sheehan, Wilson A. Smith, Joshua Spurgeon, Maureen H. Tang, Roel van de Krol, Peter C K Vesborg, and Pieter Westerik. Pathways to electrochemical solar-hydrogen technologies. *Energy & Environmental Science*, 11(10):2768–2783, 2018.

[62] D. Lips, J. M. Schuurmans, F. Branco Dos Santos, and K. J. Hellingwerf. Many ways towards 'solar fuel': Quantitative analysis of the most promising strategies and the main challenges during scale-up. *Energy and Environmental Science*, 11(1):10–22, 2018.

[63] Ee Taek Hwang, Khizar Sheikh, Katherine L. Orchard, Daisuke Hojo, Valentin Radu, Chong-Yong Lee, Emma Ainsworth, Colin Lockwood, Manuela A. Gross, Tadafumi Adschiri, Erwin Reisner, Julea N. Butt, and Lars J. C. Jeuken. A Decaheme Cytochrome as a Molecular Electron Conduit in Dye-Sensitized Photoanodes. *Advanced Functional Materials*, 25(15):2308–2315, apr 2015.

[64] Aaron M. Collins, Christine Kirmaier, Dewey Holten, and Robert E. Blankenship. Kinetics and energetics of electron transfer in reaction centers of the photosynthetic

bacterium Roseiflexus castenholzii. *Biochimica et Biophysica Acta (BBA) - Bioenergetics*, 1807(3):262–269, mar 2011.

[65] Dmitry V Matyushov. Protein electron transfer: is biology (thermo)dynamic? *Journal of physics. Condensed matter : an Institute of Physics journal*, 27(47):473001, 2015.

[66] Melih Şener, Johan Strümpfer, Jen Hsin, Danielle Chandler, Simon Scheuring, C. Neil Hunter, and Klaus Schulten. Förster energy transfer theory as reflected in the structures of photosynthetic light-harvesting systems. *ChemPhysChem*, 12(3):518–531, 2011.

[67] Anna Stikane, Ee Taek Hwang, Emma V. Ainsworth, Samuel E. H. Piper, Kevin Critchley, Julea N. Butt, Erwin Reisner, and Lars J. C. Jeuken. Towards compartmentalized photocatalysis: multihaem proteins as transmembrane molecular electron conduits. *Faraday Discussions*, 215:26–38, 2019.

[68] Wei Wei, Peiqing Sun, Zhen Li, Kuisong Song, Wenyin Su, Bao Wang, Yangzhong Liu, and Jing Zhao. A surface-display biohybrid approach to light-driven hydrogen production in air. *Science Advances*, 4(2):eaap9253, feb 2018.

[69] Mrinal Kumar Sarma, Sharbani Kaushik, and Pranab Goswami. Cyanobacteria: A metabolic power house for harvesting solar energy to produce bio-electricity and biofuels. *Biomass and Bioenergy*, 90:187–201, jul 2016.

[70] Lærke Münter Lassen, Agnieszka Zygadlo Nielsen, Bibi Ziersen, Thiyagarajan Gnanasekaran, Birger Lindberg Møller, and Poul Erik Jensen. Redirecting Photosynthetic Electron Flow into Light-Driven Synthesis of Alternative Products Including High-Value Bioactive Natural Compounds. *ACS Synthetic Biology*, 3(1):1–12, jan 2014.

[71] David J Vinyard, Javier Gimpel, Gennady M Ananyev, Stephen P Mayfield, and G Charles Dismukes. Engineered Photosystem II reaction centers optimize photochemistry versus photoprotection at different solar intensities. *Journal of the American Chemical Society*, 136(10):4048–55, mar 2014.

[72] Elshan Musazade, Roman Voloshin, Nathan Brady, Jyotirmoy Mondal, Samaya Atashova, Sergey K. Zharmukhamedov, Irada Huseynova, Seeram Ramakrishna, Mohammad Mahdi Najafpour, Jian-Ren Shen, Barry D. Bruce, and Suleyman I. Allakhverdiev. Biohybrid solar cells: Fundamentals, progress, and challenges. *Journal of Photochemistry and Photobiology C: Photochemistry Reviews*, 35:134–156, jun 2018.

[73] Mariko Miyachi, Shu Ikehira, Daiki Nishiori, Yoshinori Yamanoi, Masato Yamada, Masako Iwai, Tatsuya Tomo, Suleyman I. Allakhverdiev, and Hiroshi Nishihara. Photocurrent Generation of Reconstituted Photosystem II on a Self-Assembled Gold Film. *Langmuir*, 33(6):1351–1358, 2017.

[74] Fangyuan Zhao, Felipe Conzuelo, Volker Hartmann, Huaiguang Li, Marc M. Nowaczyk, Nicolas Plumeré, Matthias Rögner, and Wolfgang Schuhmann. Light Induced H2 Evolution from a Biophotocathode Based on Photosystem 1–Pt Nanoparticles Complexes Integrated in Solvated Redox Polymers Films. *The journal of physical chemistry. B*, 119(43):13726–31, oct 2015.

[75] Mariko Miyachi, Kyoko Okuzono, Daiki Nishiori, Yoshinori Yamanoi, Tatsuya Tomo, Masako Iwai, Suleyman I. Allakhverdiev, and Hiroshi Nishihara. A Photochemical Hydrogen Evolution System Combining Cyanobacterial Photosystem I and Platinum Nanoparticle-terminated Molecular Wires. *Chemistry Letters*, 46(10):1479–1481, oct 2017.

[76] Lisa M. Utschig, Nada M. Dimitrijevic, Oleg G. Poluektov, Sergey D. Chemerisov, Karen L. Mulfort, and David M. Tiede. Photocatalytic hydrogen production from noncovalent biohybrid Photosystem I/Pt nanoparticle complexes. *Journal of Physical Chemistry Letters*, 2(3):236–241, 2011.

[77] Sunshine C. Silver, Jens Niklas, Pingwu Du, Oleg G. Poluektov, David M. Tiede, and Lisa M. Utschig. Protein delivery of a Ni catalyst to photosystem i for light-driven hydrogen production. *Journal of the American Chemical Society*, 135(36):13246–13249, 2013.

[78] Tomoyasu Noji, Hiroyuki Suzuki, Toshiaki Gotoh, Masako Iwai, Masahiko Ikeuchi, Tatsuya Tomo, and Takumi Noguchi. Photosystem II–Gold Nanoparticle Conjugate as a Nanodevice for the Development of Artificial Light-Driven Water-Splitting Systems. *The Journal of Physical Chemistry Letters*, 2(19):2448–2452, 2011.

[79] Katarzyna P. Sokol, William E. Robinson, Julien Warnan, Nikolay Kornienko, Marc M. Nowaczyk, Adrian Ruff, Jenny Z. Zhang, and Erwin Reisner. Bias-free photoelectrochemical water splitting with photosystem II on a dye-sensitized photoanode wired to hydrogenase. *Nature Energy*, 57(33):10595–10599, sep 2018.

[80] Fangyuan Zhao, Steffen Hardt, Volker Hartmann, Huijie Zhang, Marc M. Nowaczyk, Matthias Rögner, Nicolas Plumeré, Wolfgang Schuhmann, and Felipe Conzuelo. Light-induced formation of partially reduced oxygen species limits the lifetime of photosystem 1-based biocathodes. *Nature Communications*, 9(1):1973, dec 2018.

[81] Sahng Ha Lee, Da Som Choi, Su Keun Kuk, and Chan Beum Park. Photobiocatalysis: Activating Redox Enzymes by Direct or Indirect Transfer of Photoinduced Electrons. *Angewandte Chemie - International Edition*, 57(27):7958–7985, 2018.

[82] Janina Willkomm, Nicoleta M. Muresan, and Erwin Reisner. Enhancing H 2 evolution performance of an immobilised cobalt catalyst by rational ligand design. *Chemical Science*, 6(5):2727–2736, 2015.

[83] Yue Li, Jinbo Fei, Guangle Li, Haiming Xie, Yang Yang, Jieling Junbai Li, Youqian Xu, Bingbing Sun, Jiarui Xia, Xueqi Fu, and Jieling Junbai Li. Supramolecular Assembly of Photosystem II and Adenosine Triphosphate Synthase in Artificially Designed Honeycomb Multilayers for Photophosphorylation. *ACS Nano*, 12(2):1455–1461, 2018.

[84] Mingming Wang, Jinquan Chen, Tianquan Lian, and Wei Zhan. Mimicking Photosynthesis with Supercomplexed Lipid Nanoassemblies: Design, Performance, and Enhancement Role of Cholesterol. *Langmuir*, 32(29):7326–7338, 2016.

[85] Emma Victoria Ainsworth. *Photoreduction of Outer Membrane Cytochromes : Solution and Proteoliposome Nanocompartment Studies*. Phd thesis, Univeristy of East Anglia, 2017.

[86] Benjamin C M Martindale, Georgina A M Hutton, Christine A. Caputo, and Erwin Reisner. Solar Hydrogen Production Using Carbon Quantum Dots and a Molecular Nickel Catalyst. *Journal of the American Chemical Society*, 137(18):6018–6025, may 2015.

[87] Youfu Wang and Aiguo Hu. Carbon quantum dots : synthesis , properties and applications. *Journal of Materials Chemistry C: Materials for optical and electronic devices*, 2:6921–6939, 2014.

[88] Georgina A.M. Hutton, Benjamin C.M. Martindale, and Erwin Reisner. Carbon dots as photosensitisers for solar-driven catalysis. *Chemical Society Reviews*, 46(20):6111–6123, 2017.

[89] Benjamin C. M. Martindale, Georgina A. M. Hutton, Christine A. Caputo, Sebastian Prantl, Robert Godin, James R. Durrant, and Erwin Reisner. Enhancing Light Absorption and Charge Transfer Efficiency in Carbon Dots through Graphitization and Core Nitrogen Doping. *Angewandte Chemie International Edition*, 56(23):6459–6463, jun 2017.

[90] Marian Breuer, Kevin M Rosso, Jochen Blumberger, and Julea N Butt. Multi-haem cytochromes in Shewanella oneidensis MR-1: structures, functions and opportunities. *Journal of the Royal Society, Interface / the Royal Society*, 12(102):20141117, jan 2015.

[91] Gaye F White, Zhi Shi, Liang Shi, Zheming Wang, Alice C Dohnalkova, Matthew J Marshall, James K Fredrickson, John M Zachara, Julea N Butt, David J Richardson, and Thomas A Clarke. Rapid electron exchange between surface-exposed bacterial cytochromes and Fe(III) minerals. *Proceedings of the National Academy of Sciences of the United States of America*, 110(16):6346–51, 2013.

[92] James K Fredrickson, Margaret F Romine, Alexander S Beliaev, Jennifer M Auchtung, Michael E Driscoll, Timothy S Gardner, Kenneth H Nealson, Andrei L Osterman, Grigoriy Pinchuk, Jennifer L Reed, Dmitry a Rodionov, Jorge L M Rodrigues, Daad a Saffarini, Margrethe H Serres, Alfred M Spormann, Igor B Zhulin, and James M Tiedje. Towards environmental systems biology of Shewanella. *Nature reviews. Microbiology*, 6(8):592–603, aug 2008.

[93] Marcus J. Edwards, Gaye F. White, Colin W. Lockwood, Matthew C. Lawes, Anne Martel, Gemma Harris, David J. Scott, David J. Richardson, Julea N. Butt, and Thomas A. Clarke. Structural modeling of an outer membrane electron conduit from a metal-reducing bacterium suggests electron transfer via periplasmic redox partners. *Journal of Biological Chemistry*, 293(21):8103–8112, may 2018.

[94] Marcus J. Edwards, Gaye F. White, Julea N. Butt, David J. Richardson, and Thomas A. Clarke. The Crystal Structure of a Biological Insulated Transmembrane Molecular Wire. *Cell*, 181(3):665–673.e10, 2020.

[95] Chong-Yong Lee, Bertrand Reuillard, Katarzyna P Sokol, Theodoros Laftsoglou, Colin W. J. Lockwood, Sam F. Rowe, Ee Taek Hwang, Juan-Carlos C. Fontecilla-Camps, Lars J C Jeuken, Julea N. Butt, and Erwin Reisner. A decahaem cytochrome as an electron conduit in protein–enzyme redox processes. *Chemical Communications*, 52(46):7390–7393, 2016.

[96] Bertrand Reuillard, Khoa H. Ly, Peter Hildebrandt, Lars J. C. Jeuken, Julea N. Butt, and Erwin Reisner. High Performance Reduction of H 2 O 2 with an Electron Transport Decaheme Cytochrome on a Porous ITO Electrode. *Journal of the American Chemical Society*, 139(9):3324–3327, mar 2017.

[97] Emma V. Ainsworth, Colin W. J. Lockwood, Gaye F. White, Ee Taek Hwang, Tsubasa Sakai, Manuela A. Gross, David J. Richardson, Thomas A. Clarke, Lars J. C. Jeuken,

Erwin Reisner, and Julea N. Butt. Photoreduction of Shewanella oneidensis Extracellular Cytochromes by Organic Chromophores and Dye-Sensitized TiO 2. *ChemBioChem*, 17(24):2324–2333, dec 2016.

[98] Gisèle F. White, Kathleen I. Racher, André Lipski, F.Ross Hallett, and Janet M. Wood. Physical properties of liposomes and proteoliposomes prepared from Escherichia coli polar lipids. *Biochimica et Biophysica Acta (BBA) - Biomembranes*, 1468(1-2):175–186, sep 2000.

[99] W. Dowhan. MOLECULAR BASIS FOR MEMBRANE PHOSPHOLIPID DIVERSITY:Why Are There So Many Lipids? *Annual Review of Biochemistry*, 66(1):199–232, jun 1997.

[100] L O Ingram. Changes in lipid composition of escherichia coli resulting from growth with organic solvents and with food additives. *Applied and Environmental Microbiology*, 33(5):1233–1236, 1977.

[101] Rosalba Passalacqua, Siglinda Perathoner, and Gabriele Centi. Semiconductor, molecular and hybrid systems for photoelectrochemical solar fuel production. *Journal of Energy Chemistry*, 26(2):219–240, mar 2017.

[102] N. S. Lewis and D. G. Nocera. Powering the planet: Chemical challenges in solar energy utilization. *Proceedings of the National Academy of Sciences*, 103(43):15729–15735, oct 2006.

[103] Nikolay Kornienko, Jenny Z. Zhang, Kelsey K. Sakimoto, Peidong Yang, and Erwin Reisner. Interfacing nature's catalytic machinery with synthetic materials for semi-artificial photosynthesis. *Nature Nanotechnology*, 13(10):890–899, oct 2018.

[104] Xiaoxin Zou and Yu Zhang. Noble metal-free hydrogen evolution catalysts for water splitting. *Chem. Soc. Rev.*, 44:5148–5180, 2015.

[105] J. K. Nørskov, T. Bligaard, A. Logadottir, J. R. Kitchin, J. G. Chen, S. Pandelov, and U. Stimming. Trends in the exchange current for hydrogen evolution. *Journal of the Electrochemical Society*, 152(3):J23, 2005.

[106] Changhong Wang, Feng Hu, Hongchao Yang, Yejun Zhang, Huan Lu, and Qiangbin Wang. 1.82 wt.% Pt/N, P co-doped carbon overwhelms 20 wt.% Pt/C as a high-efficiency electrocatalyst for hydrogen evolution reaction. *Nano Research*, 10(1):238–246, 2017.

[107] Erwin Reisner. Solar hydrogen evolution with hydrogenases: From natural to hybrid systems. *European Journal of Inorganic Chemistry*, (7):1005–1016, 2011.

[108] Kylie A. Vincent, Alison Parkin, and Fraser A. Armstrong. Investigating and exploiting the electrocatalytic properties of hydrogenases. *Chemical Reviews*, 107(10):4366–4413, oct 2007.

[109] Claire Wombwell, Christine A. Caputo, and Erwin Reisner. [NiFeSe]-Hydrogenase Chemistry. *Accounts of Chemical Research*, 48(11):2858–2865, 2015.

[110] Jia Wei Wang, Wen Ju Liu, Di Chang Zhong, and Tong Bu Lu. Nickel complexes as molecular catalysts for water splitting and CO2 reduction. *Coordination Chemistry Reviews*, 378:237–261, 2019.

[111] Sven E. Eklund and David E. Cliffel. Synthesis and Catalytic Properties of Soluble Platinum Nanoparticles Protected by a Thiol Monolayer. *Langmuir*, 20(14):6012–6018, jul 2004.

[112] G. Berggren, A. Adamska, C. Lambertz, T. R. Simmons, J. Esselborn, M. Atta, S. Gambarelli, J. M. Mouesca, E. Reijerse, W. Lubitz, T. Happe, V. Artero, and M. Fontecave. Biomimetic assembly and activation of [FeFe]-hydrogenases. *Nature*, 499(7456):66–69, 2013.

[113] Christina Kamp, Alexey Silakov, Martin Winkler, Edward J. Reijerse, Wolfgang Lubitz, and Thomas Happe. Isolation and first EPR characterization of the [FeFe]-hydrogenases from green algae. *Biochimica et Biophysica Acta (BBA) - Bioenergetics*, 1777(5):410–416, may 2008.

[114] Patricia Rodríguez-Maciá, Leonie Kertess, Jan Burnik, James A. Birrell, Eckhard Hofmann, Wolfgang Lubitz, Thomas Happe, and Olaf Rüdiger. His-Ligation to the [4Fe-4S] Subcluster Tunes the Catalytic Bias of [FeFe] Hydrogenase. *Journal of the American Chemical Society*, 141(1):472–481, 2019.

[115] T Happe and J D Naber. Isolation, characterization and N-terminal amino acid sequence of hydrogenase from the green alga Chlamydomonas reinhardtii. *European journal of biochemistry*, 214(2):475–81, jun 1993.

[116] George R. Heath, Mengqiu Li, Isabelle L. Polignano, Joanna L. Richens, Gianluca Catucci, Paul O'Shea, Sheila J. Sadeghi, Gianfranco Gilardi, Julea N. Butt, and Lars J. C. Jeuken. Layer-by-Layer Assembly of Supported Lipid Bilayer Poly-L-Lysine Multilayers. *Biomacromolecules*, 17(1):324–35, jan 2016.

[117] Paul E. Thomas, Dene Ryan, and Wayne Levin. An improved staining procedure for the detection of the peroxidase activity of cytochrome P-450 on sodium dodecyl sulfate polyacrylamide gels. *Analytical Biochemistry*, 75(1):168–176, sep 1976.

[118] Robert S. Hartshorne, Brian N. Jepson, Tom A. Clarke, Sarah J. Field, Jim Fredrickson, John Zachara, Liang Shi, Julea N. Butt, and David J. Richardson. Characterization of Shewanella oneidensis MtrC: A cell-surface decaheme cytochrome involved in respiratory electron transport to extracellular electron acceptors. *Journal of Biological Inorganic Chemistry*, 12(7):1083–1094, 2007.

[119] *Physical Principles*, chapter 2, pages 63–102. John Wiley & Sons, Ltd, 1998.

[120] A K Mallia, M D Frovenzano, E K Fujimoto, B J Olson, D C Klenk, and Pierce Chemical Company. Measurement of Protein Using Bicinchoninic Acid '. 85:76–85, 1985.

[121] Xiaoli Zhu and Tao Gao. Chapter 10 - spectrometry. In Genxi Li, editor, *Nano-Inspired Biosensors for Protein Assay with Clinical Applications*, pages 237 – 264. Elsevier, 2019.

[122] Fanny Varenne, Ali Makky, Mireille Gaucher-Delmas, Frédéric Violleau, and Christine Vauthier. Multimodal Dispersion of Nanoparticles: A Comprehensive Evaluation of Size Distribution with 9 Size Measurement Methods. *Pharmaceutical Research*, 33(5):1220–1234, 2016.

[123] Vasco Filipe, Andrea Hawe, and Wim Jiskoot. Critical Evaluation of Nanoparticle Tracking Analysis (NTA) by NanoSight for the Measurement of Nanoparticles and Protein Aggregates. *Pharmaceutical Research*, 27(5):796–810, may 2010.

[124] JLS Milne, MJ Borgnia, and A Bartesaghi. Cryo-electron microscopy–a primer for the non-microscopist. *Febs J.*, 280(1):28–45, 2013.

[125] Caroline A Schneider, Wayne S Rasband, and Kevin W Eliceiri. NIH Image to ImageJ: 25 years of image analysis. *Nature Methods*, 9(7):671–675, jul 2012.

[126] Kyle C. Dent, Rebecca Thompson, Amy M. Barker, Julian A. Hiscox, John N. Barr, Peter G. Stockley, and Neil A. Ranson. The Asymmetric Structure of an Icosahedral Virus Bound to Its Receptor Suggests a Mechanism for Genome Release. *Structure*, 21(7):1225–1234, jul 2013.

[127] Yunjun Cao, Min Yu, Shandong Qi, Tingting Wang, Shiming Huang, Zhengfeng Ren, Shishen Yan, Shujun Hu, and Mingchun Xu. CO2 adsorption on anatase TiO2(101)

surfaces: A combination of UHV-FTIRS and first-principles studies. *Physical Chemistry Chemical Physics*, 19(46):31267–31273, 2017.

[128] Chi Lun Pang, Robert Lindsay, and Geoff Thornton. Chemical reactions on rutile TiO2(110). *Chemical Society Reviews*, 37(10):2328–2353, 2008.

[129] Guozhong Xu and Mark R. Chance. Hydroxyl radical-mediated modification of proteins as probes for structural proteomics. *Chemical Reviews*, 107(8):3514–3543, 2007.

[130] Owen Cornwell, Sheena E. Radford, Alison E. Ashcroft, and James R. Ault. Comparing Hydrogen Deuterium Exchange and Fast Photochemical Oxidation of Proteins: a Structural Characterisation of Wild-Type and ΔN6 β2-Microglobulin. *Journal of The American Society for Mass Spectrometry*, 29(12):2413–2426, dec 2018.

[131] V. N. Bavro, S. Gupta, and C. Ralston. Oxidative footprinting in the study of structure and function of membrane proteins: current state and perspectives. *Biochemical Society Transactions*, 43(5):983–994, 2015.

[132] Sayan Gupta, Jun Feng, Leanne Jade G. Chan, Christopher J. Petzold, and Corie Y. Ralston. Synchrotron X-ray footprinting as a method to visualize water in proteins. *Journal of Synchrotron Radiation*, 23(5):1056–1069, sep 2016.

[133] Sayan Gupta, Richard Celestre, Christopher J. Petzold, Mark R. Chance, and Corie Ralston. Development of a microsecond X-ray protein footprinting facility at the Advanced Light Source. *Journal of Synchrotron Radiation*, 21(4):690–699, jul 2014.

[134] Tatsuya Fukushima, Sayan Gupta, Behzad Rad, Jose A. Cornejo, Christopher J. Petzold, Leanne Jade G. Chan, Rena A. Mizrahi, Corie Y. Ralston, and Caroline M. Ajo-Franklin. The Molecular Basis for Binding of an Electron Transfer Protein to a Metal Oxide Surface. *Journal of the American Chemical Society*, 139(36):12647–12654, sep 2017.

[135] Jen Bohon, Rhijuta D'Mello, Corie Ralston, Sayan Gupta, and Mark R. Chance. Synchrotron X-ray footprinting on tour. *Journal of Synchrotron Radiation*, 21(1):24–31, jan 2014.

[136] Sayan Gupta, Michael Sullivan, John Toomey, Janna Kiselar, and Mark R. Chance. The beamline X28C of the center for synchrotron biosciences: A national resource for biomolecular structure and dynamics experiments using synchrotron footprinting. *Journal of Synchrotron Radiation*, 14(3):233–243, 2007.

[137] Maolian Chen and Kelsey D. Cook. Oxidation artifacts in the electrospray mass spectrometry of Aβ peptide. *Analytical Chemistry*, 79(5):2031–2036, 2007.

[138] Richard Wang, F. P. Healey, and Jack Myers. Amperometric Measurement of Hydrogen Evolution in Chlamydomonas . *Plant Physiology*, 48(1):108–110, jul 1971.

[139] Dino Mislov, Mario Cifrek, Igor Krois, and Hrvoje Dzapo. Measurement of dissolved hydrogen concentration with clark electrode. In *2015 IEEE Sensors Applications Symposium (SAS)*, pages 1–5. IEEE, apr 2015.

[140] S.C. Chang, J.R. Stetter, and C.S. Cha. Amperometric gas sensors. *Talanta*, 40(4):461–477, apr 1993.

[141] L. W. Winkler. Die Löslichkeit der Gase in Wasser. *Berichte der deutschen chemischen Gesellschaft*, 24(1):89–101, jan 1891.

[142] R. Sander. Compilation of Henry's law constants (version 4.0) for water as solvent. *Atmospheric Chemistry and Physics*, 15(8):4399–4981, 2015.

[143] Joseph R H Manning, Eleni Routoula, and Siddharth V Patwardhan. Preparation of Functional Silica Using a Bioinspired Method. *JoVE*, (138):e57730, 2018.

[144] V. Vasilca, A. Sadeghpour, S. Rawson, L. E. Hawke, S. A. Baldwin, T. Wilkinson, D. Bannister, V. L.G. Postis, M. Rappolt, S. P. Muench, and L. J.C. Jeuken. Spherical-supported membranes as platforms for screening against membrane protein targets. *Analytical Biochemistry*, 549(March):58–65, 2018.

[145] R. A. Marcus and Norman Sutin. Electron transfers in chemistry and biology. *BBA Reviews On Bioenergetics*, 811(3):265–322, 1985.

[146] Ee Taek Hwang, Katherine L. Orchard, Daisuke Hojo, Joseph Beton, Colin W.J. Lockwood, Tadafumi Adschiri, Julea N. Butt, Erwin Reisner, and Lars J.C. Jeuken. Exploring Step-by-Step Assembly of Nanoparticle:Cytochrome Biohybrid Photoanodes. *ChemElectroChem*, 4(8):1959–1968, 2017.

[147] Brian H. Lower, Liang Shi, Ruchirej Yongsunthon, Timothy C. Droubay, David E. McCready, and Steven K. Lower. Specific bonds between an iron oxide surface and outer membrane cytochromes MtrC and OmcA from Shewanella oneidensis MR-1. *Journal of Bacteriology*, 189(13):4944–4952, 2007.

[148] Marcus J Edwards, Gaye F White, Michael Norman, Alice Tome-fernandez, Emma Ainsworth, Liang Shi, Jim K Fredrickson, John M Zachara, Julea N Butt, David J Richardson, and Thomas A Clarke. Redox Linked Flavin Sites in Extracellular Decaheme Proteins Involved in Microbe-Mineral Electron Transfer . *Nature Publishing Group*, (July):1–11, 2015.

[149] A. Johs, L. Shi, T. Droubay, J. F. Ankner, and L. Liang. Characterization of the decaheme c-type cytochrome OmcA in solution and on hematite surfaces by small angle x-ray scattering and neutron reflectometry. *Biophysical Journal*, 98(12):3035–3043, 2010.

[150] Yoshihide Tokunou and Akihiro Okamoto. Geometrical Changes in the Hemes of Bacterial Surface c-Type Cytochromes Reveal Flexibility in Their Binding Affinity with Minerals. *Langmuir*, 35(23):7529–7537, 2019.

[151] Brian H. Lower, Roberto D. Lins, Zachery Oestreicher, Tjerk P. Straatsma, Michael F. Hochella, Liang Shi, and Steven K. Lower. In vitro evolution of a peptide with a hematite binding motif that may constitute a natural metal-oxide binding archetype. *Environmental Science and Technology*, 42(10):3821–3827, 2008.

[152] Alexander S. Beliaev and Daad A. Saffarini. Shewanella putrefaciens mtrB encodes an outer membrane protein required for Fe(III) and Mn(IV) reduction. *Journal of Bacteriology*, 180(23):6292–6297, 1998.

[153] J. M. Myers and C. R. Myers. Role for outer membrane cytochromes OmcA and OmcB of Shewanella putrefaciens MR-1 in reduction of manganese dioxide. *Applied and Environmental Microbiology*, 67(1):260–269, 2001.

[154] Wesley Carpentier, Lina De Smet, Jozef Van Beeumen, and Ann Brigé. Respiration and growth of Shewanella oneidensis MR-1 using vanadate as the sole electron acceptor. *Journal of Bacteriology*, 187(10):3293–3301, 2005.

[155] Marion J. Limo, Anna Sola-Rabada, Estefania Boix, Veeranjaneyulu Thota, Zayd C. Westcott, Valeria Puddu, and Carole C. Perry. Interactions between Metal Oxides and Biomolecules: From Fundamental Understanding to Applications. *Chemical Reviews*, 118(22):11118–11193, 2018.

[156] Haibin Chen, Xiaodi Su, Koon Gee Neoh, and Woo Seok Choe. Probing the interaction between peptides and metal oxides using point mutants of a TiO2-binding peptide. *Langmuir*, 24(13):6852–6857, 2008.

[157] Y. Randika Perera, Rebecca A. Hill, and Nicholas C. Fitzkee. Protein Interactions with Nanoparticle Surfaces: Highlighting Solution NMR Techniques. *Israel Journal of Chemistry*, page ijch.201900080, sep 2019.

[158] Silvia H. De Paoli Lacerda, Jung Jin Park, Curt Meuse, Denis Pristinski, Matthew L. Becker, Alamgir Karim, and Jack F. Douglas. Interaction of gold nanoparticles with common human blood proteins. *ACS Nano*, 4(1):365–379, 2010.

[159] Yan Ling Zhao, Cui Hong Wang, Ying Zhai, Rui Qin Zhang, and Michel A. Van Hove. Selective adsorption of l-serine functional groups on the anatase TiO2(101) surface in benthic microbial fuel cells. *Physical Chemistry Chemical Physics*, 16(38):20806–20817, 2014.

[160] P. A. Connor and A. J. McQuillan. Phosphate adsorption onto TiO2 from aqueous solutions: an in situ internal reflection infrared spectroscopic study. *Langmuir*, 15(8):2916–2921, 1999.

[161] Eunyoung Bae and Wonyong Choi. Effect of the anchoring group (carboxylate vs phosphonate) in Ru-complex-sensitized TiO2 on hydrogen production under visible light. *Journal of Physical Chemistry B*, 110(30):14792–14799, 2006.

[162] Willem Norde and Carla E. Giacomelli. BSA structural changes during homomolecular exchange between the adsorbed and the dissolved states. *Journal of Biotechnology*, 79(3):259–268, 2000.

[163] David J. Richardson, Julea N. Butt, Jim K. Fredrickson, John M. Zachara, Liang Shi, Marcus J. Edwards, Gaye White, Nanakow Baiden, Andrew J. Gates, Sophie J. Marritt, and Thomas A. Clarke. The 'porin-cytochrome' model for microbe-to-mineral electron transfer. *Molecular Microbiology*, 85(2):201–212, 2012.

[164] Feng Yang, Bogdan Bogdanov, Eric F. Strittmatter, Andrey N. Vilkov, Marina Gritsenko, Liang Shi, Dwayne A. Elias, Shuisong Ni, Margaret Romine, Ljiljana Paša-Tolić, Mary S. Lipton, and Richard D. Smith. Characterization of purified c-type heme-containing peptides and identification of c-type heme-attachment sites in Shewanella oneidenis cytochromes using mass spectrometry. *Journal of Proteome Research*, 4(3):846–854, 2005.

[165] Sayan Gupta, Jin Chai, Jie Cheng, Rhijuta D'Mello, Mark R. Chance, and Dax Fu. Visualizing the kinetic power stroke that drives proton-coupled zinc(ii) transport. *Nature*, 512(1):101–104, 2014.

[166] Sayan Gupta, Miklos Guttman, Ryan L. Leverenz, Kulyash Zhumadilova, Emily G. Pawlowski, Christopher J. Petzold, Kelly K. Lee, Corie Y. Ralston, and Cheryl A. Kerfeld. Local and global structural drivers for the photoactivation of the orange carotenoid protein. *Proceedings of the National Academy of Sciences*, 112(41):E5567–E5574, 2015.

[167] Elizabeth Jurrus, Dave Engel, Keith Star, Kyle Monson, Juan Brandi, Lisa E. Felberg, David H. Brookes, Leighton Wilson, Jiahui Chen, Karina Liles, Minju Chun, Peter Li, David W. Gohara, Todd Dolinsky, Robert Konecny, David R. Koes, Jens Erik Nielsen, Teresa Head-Gordon, Weihua Geng, Robert Krasny, Guo-Wei Wei, Michael J. Holst, J. Andrew McCammon, and Nathan A. Baker. Improvements to the apbs biomolecular solvation software suite. *Protein Science*, 27(1):112–128, 2018.

[168] Schrödinger, LLC. The PyMOL molecular graphics system, version 1.8. November 2015.

[169] Ersin Emre Oren, Rebecca Notman, Il Won Kim, John Spencer Evans, Tiffany R. Walsh, Ram Samudrala, Candan Tamerler, and Mehmet Sarikaya. Probing the molecular mechanisms of quartz-binding peptides. *Langmuir*, 26(13):11003–11009, 2010.

[170] John Spencer Evans. 'Apples' and 'oranges': comparing the structural aspects of biomineral- and ice-interaction proteins. *Current Opinion in Colloid & Interface Science*, 8(1):48–54, mar 2003.

[171] Zihao Liu, Shiqing Ma, Shun Duan, Deng Xuliang, Yingchun Sun, Xi Zhang, Xinhua Xu, Binbin Guan, Chao Wang, Meilin Hu, Xingying Qi, Xu Zhang, and Ping Gao. Modification of Titanium Substrates with Chimeric Peptides Comprising Antimicrobial and Titanium-Binding Motifs Connected by Linkers to Inhibit Biofilm Formation. *ACS Applied Materials and Interfaces*, 8(8):5124–5136, 2016.

[172] Marian Breuer, Piotr Zarzycki, Jochen Blumberger, and Kevin M. Rosso. Thermodynamics of electron flow in the bacterial deca-heme cytochrome MtrF. *Journal of the American Chemical Society*, 134(24):9868–9871, 2012.

[173] Frauke Kracke, Igor Vassilev, and Jens O. Krömer. Microbial electron transport and energy conservation - The foundation for optimizing bioelectrochemical systems. *Frontiers in Microbiology*, 6(JUN):1–18, jun 2015.

[174] D. Docter, D. Westmeier, M. Markiewicz, S. Stolte, S. K. Knauer, and R. H. Stauber. The nanoparticle biomolecule corona: lessons learned - challenge accepted? *Chemical Society Reviews*, 44(17):6094–6121, 2015.

[175] Feifang Zhang, Ayfer Yediler, Xinmiao Liang, and Antonius Kettrup. Ozonation of the purified hydrolyzed azo dye Reactive Red 120 (CI). *Journal of Environmental Science and Health - Part A Toxic/Hazardous Substances and Environmental Engineering*, 37(4):707–713, may 2002.

[176] André B. dos Santos, Francisco J. Cervantes, and Jules B. van Lier. Review paper on current technologies for decolourisation of textile wastewaters: Perspectives for anaerobic biotechnology. *Bioresource Technology*, 98(12):2369–2385, 2007.

[177] Mayara Carantino Costa, Francisco Suetônio B Mota, André Bezerra Dos Santos, Glaydson Leandro Farias Mendonça, and Ronaldo Ferreira do Nascimento. Effect of dye structure and redox mediators on anaerobic azo and anthraquinone dye reduction. *Química Nova*, 35(3):482–486, 2012.

[178] Stephen G. Mayhew. The Redox Potential of Dithionite and SO-2 from Equilibrium Reactions with Flavodoxins, Methyl Viologen and Hydrogen plus Hydrogenase. *European Journal of Biochemistry*, 85(2):535–547, apr 1978.

[179] Robert S Hartshorne, Catherine L Reardon, Daniel Ross, Jochen Nuester, Thomas a Clarke, Andrew J Gates, Paul C Mills, Jim K Fredrickson, John M Zachara, Liang Shi, Alex S Beliaev, Matthew J Marshall, Ming Tien, Susan Brantley, Julea N Butt, and David J Richardson. Characterization of an electron conduit between bacteria and the extracellular environment. *Proceedings of the National Academy of Sciences*, 106(52):22169–22174, dec 2009.

[180] CCI Guarantini, A. G. Fogg, and Maria Valnice Boldrin Zanoni. Electrochemical reduction of azo-based chlorotriazine reactive dyes. In A. J. Ricco, P. Vanyek, G. Horvai, and A. F. Silva, editors, *Proceedings of the Symposium on Chemical and Biological Sensors and Analytical Electrochemical Methods*, pages 467–476. Electrochemical Society Series, 1997.

[181] John N Weinstein, Robert Blumenthal, and Richard D. Klausner. [38] Carboxyfluorescein leakage assay for lipoprotein-liposome interaction. In *Methods Enzymology*, volume 128, pages 657–668. Academic Press, 1986.

[182] Yiqun Zhou, Piumi Y. Liyanage, Daniel L. Geleroff, Zhili Peng, Keenan J. Mintz, Sajini D. Hettiarachchi, Raja R. Pandey, Charles C. Chusuei, Patricia L. Blackwelder, and Roger M. Leblanc. Photoluminescent Carbon Dots: A Mixture of Heterogeneous Fractions. *ChemPhysChem*, 19(19):2589–2597, oct 2018.

[183] Jeremy B. Essner, Jennifer A. Kist, Luis Polo-Parada, and Gary A. Baker. Artifacts and Errors Associated with the Ubiquitous Presence of Fluorescent Impurities in Carbon Nanodots. *Chemistry of Materials*, 30(6):1878–1887, mar 2018.

[184] Erwin Reisner, Juan C. Fontecilla-Camps, and Fraser A. Armstrong. Catalytic electrochemistry of a [nifese]-hydrogenase on tio2 and demonstration of its suitability for visible-light driven h2 production. *Chem. Commun.*, pages 550–552, 2009.

[185] Erwin Reisner, Daniel J. Powell, Christine Cavazza, Juan C. Fontecilla-Camps, and Fraser A. Armstrong. Visible Light-Driven H 2 Production by Hydrogenases Attached to Dye-Sensitized TiO 2 Nanoparticles. *Journal of the American Chemical Society*, 131(51):18457–18466, dec 2009.

[186] Yu Kang, Xin Li, Yaoquan Tu, Qi Wang, and Hans Ågren. On the mechanism of protein adsorption onto hydroxylated and nonhydroxylated TiO2 surfaces. *Journal of Physical Chemistry C*, 114(34):14496–14502, 2010.

[187] Charith E. Nanayakkara, Whitney A. Larish, and Vicki H. Grassian. Titanium Dioxide Nanoparticle Surface Reactivity with Atmospheric Gases, CO 2 , SO 2 , and NO 2 : Roles of Surface Hydroxyl Groups and Adsorbed Water in the Formation and Stability of Adsorbed Products. *The Journal of Physical Chemistry C*, 118(40):23011–23021, oct 2014.

[188] Kyoung Taek Kim, Silvie A. Meeuwissen, Roeland J. M. Nolte, and Jan C. M. van Hest. Smart nanocontainers and nanoreactors. *Nanoscale*, 2(6):844, 2010.

[189] Juewen Liu. Interfacing zwitterionic liposomes with inorganic nanomaterials: Surface forces, membrane integrity, and applications. *Langmuir*, 32(18):4393–4404, 2016.

[190] Gustav Nordlund, Jovice Boon Sing Ng, Lennart Bergström, and Peter Brzezinski. A membrane-reconstituted multisubunit functional proton pump on mesoporous silica particles. *ACS Nano*, 3(9):2639–2646, sep 2009.

[191] Benjamin D. Gould, Olga A. Baturina, and Karen E. Swider-Lyons. Deactivation of Pt/VC proton exchange membrane fuel cell cathodes by SO2, H2S and COS. *Journal of Power Sources*, 188(1):89–95, 2009.

[192] Katherine Telfeyan, Artas A. Migdisov, Sachin Pandey, Velimir V. Vesselinov, and Paul W. Reimus. Long-term stability of dithionite in alkaline anaerobic aqueous solution. *Applied Geochemistry*, 101(December 2017):160–169, 2019.

[193] Sam F. Rowe, Gwénaëlle Le Gall, Emma V. Ainsworth, Jonathan A. Davies, Colin W.J. Lockwood, Liang Shi, Adam Elliston, Ian N. Roberts, Keith W. Waldron, David J. Richardson, Thomas A. Clarke, Lars J.C. Jeuken, Erwin Reisner, and Julea N. Butt. Light-Driven H 2 Evolution and C=C or C=O Bond Hydrogenation by Shewanella oneidensis: A Versatile Strategy for Photocatalysis by Nonphotosynthetic Microorganisms. *ACS Catalysis*, 7(11):7558–7566, 2017.

[194] Joseph R.H. Manning, Thomas W.S. Yip, Alessia Centi, Miguel Jorge, and Siddharth V. Patwardhan. An Eco-Friendly, Tunable and Scalable Method for Producing Porous Functional Nanomaterials Designed Using Molecular Interactions. *ChemSusChem*, 10(8):1683–1691, 2017.

[195] Siddharth V. Patwardhan, Graham E. Tilburey, and Carole C. Perry. Interactions of amines with silicon species in undersaturated solutions leads to dissolution and/or precipitation of silica. *Langmuir*, 27(24):15135–15145, 2011.

[196] Patricia Wand, Johannes D. Bartl, Ueli Heiz, Martin Tschurl, and Mirza Cokoja. Functionalization of small platinum nanoparticles with amines and phosphines: Ligand binding modes and particle stability. *Journal of Colloid and Interface Science*, 478:72–80, sep 2016.

[197] Angélique Coutable, Irina Randrianjatovo, Vincent Noireaux, Christophe Vieu, Christophe Thibault, Emmanuelle Trévisiol, and Jean M. François. A Comparative Study of α-Hemolysin Expression in Supported Lipid Bilayers of Synthetic and Enriched Complex Bacterial Lipid. *BioNanoScience*, 4(2):104–110, jun 2014.

[198] Ryugo Tero. Substrate effects on the formation process, structure and physicochemical properties of supported lipid bilayers. *Materials*, 5(12):2658–2680, 2012.

[199] Ralf P. Richter, Rémi Bérat, and Alain R. Brisson. Formation of solid-supported lipid bilayers: An integrated view. *Langmuir*, 22(8):3497–3505, 2006.

[200] Xiaoshun Wang, Xiaoqiu Li, Hui Wang, Xiaohan Zhang, Lei Zhang, Feng Wang, and Juewen Liu. Charge and Coordination Directed Liposome Fusion onto SiO 2 and TiO 2 Nanoparticles. *Langmuir*, 35(5):1672–1681, 2019.

[201] Annette Granéli, Jan Rydström, Bengt Kasemo, and Fredrik Höök. Formation of supported lipid bilayer membranes on SiO2 from proteoliposomes containing transmembrane proteins. *Langmuir*, 19(3):842–850, 2003.

[202] Juewen Liu, Alison Stace-Naughton, Xingmao Jiang, and C. Jeffrey Brinker. Porous nanoparticle supported lipid bilayers (protocells) as delivery vehicles. *Journal of the American Chemical Society*, 131(4):1354–1355, 2009.

[203] Scott A. Trammell, John A. Moss, John C. Yang, Bassam M. Nakhle, Cheryl A. Slate, Fabrice Odobel, Milan Sykora, Bruce W. Erickson, and Thomas J. Meyer. Sensitization of TiO ₂ by Phosphonate-Derivatized Proline Assemblies. *Inorganic Chemistry*, 38(16):3665–3669, 1999.

[204] Erwin Reisner, Daniel J. Powell, Christine Cavazza, Juan C. Fontecilla-Camps, and Fraser A. Armstrong. Visible Light-Driven H ₂ Production by Hydrogenases Attached to Dye-Sensitized TiO ₂ Nanoparticles. *Journal of the American Chemical Society*, 131(51):18457–18466, 2009.

[205] Wenchao Sheng, Hubert a. Gasteiger, and Yang Shao-Horn. Hydrogen Oxidation and Evolution Reaction Kinetics on Platinum: Acid vs Alkaline Electrolytes. *Journal of The Electrochemical Society*, 157(11):B1529, 2010.

[206] Graham A. Rance and Andrei N. Khlobystov. Nanoparticle-nanotube electrostatic interactions in solution: The effect of pH and ionic strength. *Physical Chemistry Chemical Physics*, 12(36):10775–10780, 2010.

[207] Alexander F. Mason, Bastiaan C. Buddingh', David S. Williams, and Jan C. M. van Hest. Hierarchical Self-Assembly of a Copolymer-Stabilized Coacervate Protocell. *Journal of the American Chemical Society*, 139(48):17309–17312, dec 2017.

[208] N. Amy Yewdall, Bastiaan C. Buddingh, Wiggert J. Altenburg, Suzanne B. P. E. Timmermans, Daan F. M. Vervoort, Loai K. E. A. Abdelmohsen, Alexander F. Mason, and Jan C. M. van Hest. Physicochemical Characterization of Polymer-Stabilized Coacervate Protocells. *ChemBioChem*, pages 1–11, 2019.

[209] Fatma Pir Cakmak, Alex T. Grigas, and Christine D. Keating. Lipid Vesicle-Coated Complex Coacervates. *Langmuir*, 35(24):7830–7840, 2019.

[210] Fabian Axthelm, Olivier Casse, Willem H. Koppenol, Thomas Nauser, Wolfgang Meier, and Cornelia G. Palivan. Antioxidant nanoreactor based on superoxide dismutase encapsulated in superoxide-permeable vesicles. *Journal of Physical Chemistry B*, 112(28):8211–8217, 2008.

[211] Lisanne M.P.E. Van Oppen, Loai K.E.A. Abdelmohsen, Sjenet E. Van Emst-De Vries, Pascal L.W. Welzen, Daniela A. Wilson, Jan A.M. Smeitink, Werner J.H. Koopman, Roland Brock, Peter H.G.M. Willems, David S. Williams, and Jan C.M. Van Hest. Biodegradable Synthetic Organelles Demonstrate ROS Shielding in Human-Complex-I-Deficient Fibroblasts. *ACS Central Science*, 4(7):917–928, 2018.

[212] Dennis M. Vriezema, Paula M.L. Garcia, Núria Sancho Oltra, Nikos S. Hatzakis, Suzanne M. Kuiper, Roeland J.M. Nolte, Alan E. Rowan, and Jan C.M. Van Hest. Positional assembly of enzymes in polymersome nanoreactors for cascade reactions. *Angewandte Chemie - International Edition*, 46(39):7378–7382, 2007.

[213] Dominik Dobrunz, Adriana C. Toma, Pascal Tanner, Thomas Pfohl, and Cornelia G. Palivan. Polymer nanoreactors with dual functionality: Simultaneous detoxification of peroxynitrite and oxygen transport. *Langmuir*, 28(45):15889–15899, 2012.

[214] Hailong Che, Shoupeng Cao, and Jan C.M. Van Hest. Feedback-Induced temporal control of "breathing" polymersomes to create self-adaptive nanoreactors. *Journal of the American Chemical Society*, 140(16):5356–5359, 2018.

[215] Fei Peng, Nan Nan Deng, Yingfeng Tu, Jan C.M. Van Hest, and Daniela A. Wilson. Continuous fabrication of polymeric vesicles and nanotubes with fluidic channels. *Nanoscale*, 9(15):4875–4880, 2017.

[216] Ryuji Kawano, Yutaro Tsuji, Koji Sato, Toshihisa Osaki, Koki Kamiya, Minako Hirano, Toru Ide, Norihisa Miki, and Shoji Takeuchi. Automated parallel recordings of topologically identified single ion channels. *Scientific Reports*, 3(Dcm):1–7, 2013.

[217] Olivier Biner, Thomas Schick, Yannic Müller, and Christoph von Ballmoos. Delivery of membrane proteins into small and giant unilamellar vesicles by charge-mediated fusion. *FEBS Letters*, 590:2051–2062, 2016.

[218] Supramaniam, Ces, and Salehi-Reyhani. Microfluidics for Artificial Life: Techniques for Bottom-Up Synthetic Biology. *Micromachines*, 10(5):299, 2019.

[219] Jeanne C Stachowiak, David L Richmond, Thomas H Li, Allen P Liu, Sapun H Parekh, and Daniel a Fletcher. Unilamellar vesicle formation and encapsulation by microfluidic jetting. *Proceedings of the National Academy of Sciences of the United States of America*, 105(12):4697–702, 2008.

[220] Kei Funakoshi, Hiroaki Suzuki, and Shoji Takeuchi. Formation of giant lipid vesiclelike compartments from a planar lipid membrane by a pulsed jet flow. *Journal of the American Chemical Society*, 129(42):12608–12609, 2007.

[221] Michaela A. Teravest and Caroline M. Ajo-Franklin. Transforming exoelectrogens for biotechnology using synthetic biology. *Biotechnology and Bioengineering*, 113(4):687–697, 2016.

[222] Yoon Sung Nam, Taeho Shin, Heechul Park, Andrew P Magyar, Katherine Choi, Georg Fantner, Keith A Nelson, and Angela M Belcher. Virus-Templated Assembly of Porphyrins into Light-Harvesting Nanoantennae. *Journal of the American Chemical Society*, 132(5):1462–1463, feb 2010.

[223] Yoon Sung Nam, Andrew P Magyar, Daeyeon Lee, Jin-woong Kim, Dong Soo Yun, Heechul Park, Thomas S. Pollom, David A Weitz, and Angela M Belcher. Biologically templated photocatalytic nanostructures for sustained light-driven water oxidation. *Nature Nanotechnology*, 5(5):340–344, may 2010.

[224] Kai Liu, Ruirui Xing, Yongxin Li, Qianli Zou, Helmuth Möhwald, and Xuehai Yan. Mimicking Primitive Photobacteria: Sustainable Hydrogen Evolution Based on Peptide-Porphyrin Co-Assemblies with a Self-Mineralized Reaction Center. *Angewandte Chemie International Edition*, 55(40):12503–12507, sep 2016.

[225] Kai Liu, Manzar Abass, Qianli Zou, and Xuehai Yan. Self-assembly of biomimetic light-harvesting complexes capable of hydrogen evolution. *Green Energy & Environment*, 2(1):58–63, 2017.

[226] Jae Hong Kim, Minah Lee, Joon Seok Lee, and Chan Beum Park. Self-Assembled Light-Harvesting Peptide Nanotubes for Mimicking Natural Photosynthesis. *Angewandte Chemie International Edition*, 51(2):517–520, jan 2012.

[227] Xiaoyuan Ji, Yong Kang, Zhiguo Su, Ping Wang, Guanghui Ma, and Songping Zhang. Graphene Oxide and Polyelectrolyte Composed One-Way Expressway for Guiding Electron Transfer of Integrated Artificial Photosynthesis. *ACS Sustainable Chemistry & Engineering*, 6(3):3060–3069, mar 2018.

[228] Wooyul Kim, Beth Anne McClure, Eran Edri, and Heinz Frei. Coupling carbon dioxide reduction with water oxidation in nanoscale photocatalytic assemblies. *Chemical Society Reviews*, 45(11):3221–3243, 2016.